

## ABSTRACT

Title of dissertation: SOOT OXIDATION IN FLAMES:  
NANOSTRUCTURE, MORPHOLOGY,  
AND CHEMICAL KINETICS

Paul M. Anderson  
Doctor of Philosophy, 2019

Dissertation directed by: Professor Peter B. Sunderland  
Department of Mechanical Engineering

Soot produced from the combustion of hydrocarbons is of immense scientific interest owing to its deleterious effects on human health and the environment. Despite decades of research, existing soot models are accurate across only a narrow range of combustion conditions. A substantial portion of this inaccuracy is rooted in the multitude of factors affecting soot oxidation that remain ill-understood.

In the current work, a novel flame system allowed soot oxidation to be observed in isolation from competing soot formation processes. Measurements tracked evolving soot structures, oxidation rates, temperatures and gas species concentrations. Transmission electron microscopy (TEM) was used to characterize soot structure at aggregate, primary particle, and nanostructural scales. For this, a program called Aerosol Image Analyzer was developed, incorporating new algorithms for processing and measuring TEM images of mass-fractal aerosols, like soot. For the first time, TEM image measurement uncertainties incorporating sample, operator, and random effects, were quantified through gage repeatability and reproducibility anal-

ysis. Successful methods for reducing operator bias were presented, and automated measurement methods from literature were tested and found to be unreliable. Measurements of surface area by N<sub>2</sub> adsorption validated TEM as a technique for determining soot specific surface area, provided that the polydispersity and partial sintering of primary particles is taken into account.

TEM measurements of soot undergoing oxidation showed continuously decreasing primary particle size distributions and increasing specific surface area. Measurements of soot aggregate morphology found a fractal dimension of 1.74 that was unchanged by oxidation. The breakup of aggregates by oxidative fragmentation was observed for the first time using methods that combined TEM analysis with laser extinction. Soot nanostructure was characterized through high resolution TEM measurements of lattice fringe length, tortuosity, orientation, and separation distance. It was observed that primary particles could be divided into an inner 80%, where lattice fringes showed greater graphitic order with increasing radial location, and an outer 20%, where this trend was reversed. While oxidation proceeded in a shrinking-sphere manner at the particle surface, the interior underwent thermal and oxidation-induced graphitization, challenging the assumption that the nanostructure of mature soot is “locked-in.” This results in a surface nanostructure that is effectively unchanging from the perspective of the oxidizing gases and corresponds to a constant collision efficiency kinetics model.

SOOT OXIDATION IN FLAMES: NANOSTRUCTURE,  
MORPHOLOGY, AND CHEMICAL KINETICS

by

Paul Marcus Anderson

Dissertation submitted to the Faculty of the Graduate School of the  
University of Maryland, College Park in partial fulfillment  
of the requirements for the degree of  
Doctor of Philosophy  
2019

Advisory Committee:

Professor Peter B. Sunderland, Chair/Advisor

Professor Christopher Cadou, Dean's Representative

Professor Elaine S. Oran

Professor Arnaud Trouvé

Associate Professor Michael J. Gollner

© Copyright by  
Paul Marcus Anderson  
2019

## Acknowledgments

I am filled with deep gratitude for the many individuals who made this work possible. A big thank you to my advisor, Dr. Peter Sunderland, for his unflagging support and positivity throughout this processes. Thank you to Dr. Elaine Oran, Dr. Christopher Cadou, and Dr. Michael Gollner for giving me the chance to work with and learn from you in many ways beyond just this dissertation, and to Dr. Arnaud Trouvé for many helpful discussions and encouragement. Thank you to Dr. Wen-An Chiou, Dr. Sz-Chian Liou, and the support of the Maryland NanoCenter and its AIMLab.

Thank you to my kitchen cabinet of advisors: Ajay Singh, Haiqing Guo, and Ahmed Khalil. You kept me from going off plenty of cliffs, and were an ever-present source of good ideas, or at least good laughs. For as miserable as we were, we definitely laughed a lot. Playing with lasers helps.

Thank you to the many people in the Mechanical Engineering Department and my adoptive Fire Protection Engineering Department at Maryland who made this a great place be each day: Evan, Xuan, Ram, Raquel, Isaac, Cara, Sara, Fernando, Colin, Andrés, Ahmed, Conor, Yan, Dennis, Mark, Zhengyang, Yasser, Yaqoub, Hannes, Vivek, Ryan, Ford, Kerri, Nicole, Christine, Rosa, Antoine, Mary Lou, Sharon, and Dr. Milke.

Thank you to Sheryl Duff and James Stankevitz for giving me the inspiration and tools early on to pursue a life of science.

Thank you for the love and support of my incredible family. Mom and Dad,

you've given me the firm foundation. Rachel, Gene, Jacob, and Edith, you have been a wind in my sails. Lora, Armin, David, Ryan, Emily, and Evan, you have been an unbelievable cheering section.

Most of all, thank you to my wonderful wife, Jennifer. There is no way I can express my gratitude that would not be an absurd understatement. You're my favorite, and there's no one else I'd rather stumble through life with. Thank you Marcus and Matthew for being my biggest, littlest fans, and for bringing joy to each day. Never lose your sense of wonder and adventure. Not only will it serve you well, it is what you were made for.

# Table of Contents

Acknowledgments	ii
List of Tables	vii
List of Figures	viii
Nomenclature	xi
1 Introduction	1
1.1 Motivation . . . . .	1
1.2 General Background . . . . .	2
2 Literature Review	5
2.1 Soot Oxidation . . . . .	5
2.1.1 Oxidation by O <sub>2</sub> . . . . .	5
2.1.2 Oxidation by OH . . . . .	8
2.1.3 Oxidation Model . . . . .	10
2.2 Soot Morphology . . . . .	12
2.2.1 Aggregates . . . . .	12
2.2.1.1 Aggregate Measurement Methods: Non-TEM . . . . .	13
2.2.1.2 Aggregate Measurement Methods: TEM . . . . .	14
2.2.2 Primary Particles . . . . .	18
2.2.2.1 Primary Particle Size Distribution . . . . .	18
2.2.2.2 Sintering and Overlap of Primary Particles . . . . .	20
2.2.2.3 Attempts to Automate Primary Particle Measurement . . . . .	21
2.2.3 Uncertainty of TEM Morphological Measurements . . . . .	23
2.3 Soot Fragmentation . . . . .	24
2.4 Soot Nanostructure . . . . .	26
2.4.1 Description of Nanostructure . . . . .	26
2.4.2 Dependence on Heat Treatment and Fuel Type . . . . .	28
2.4.3 Nanostructure Diagnostic Methods . . . . .	29
2.4.3.1 Non-TEM Methods . . . . .	29
2.4.3.2 Selected-Area Electron Diffraction (SAED) . . . . .	30

2.4.3.3	High Resolution Transmission Electron Microscopy (HRTEM) Lattice Fringe Analysis . . . . .	33
2.4.4	Role of Nanostructure in Soot Oxidation . . . . .	38
3	Experimental Methods . . . . .	46
3.1	Ternary Flame System . . . . .	46
3.2	Axial Flame Velocity Measurement . . . . .	48
3.3	Temperature, Soot Volume Fraction, and Gas Species Measurements . . . . .	50
3.3.1	Soot Flame Temperature . . . . .	51
3.3.2	Soot Volume Fraction . . . . .	52
3.3.3	Major Species Concentrations . . . . .	54
3.3.4	Estimation of OH Radical Concentrations . . . . .	55
3.4	Thermophoretic Sampling of Flame Soot . . . . .	55
3.5	TEM Measurements . . . . .	57
3.5.1	Aerosol Image Analyzer Program . . . . .	58
3.5.2	Primary Particle Measurement . . . . .	60
3.5.2.1	Measurement Bias Controls . . . . .	60
3.5.2.2	Center-Selected Edge Scoring (CSES) Algorithm . . . . .	61
3.5.2.3	Primary Particle Overlap . . . . .	63
3.5.3	Soot Surface Area . . . . .	64
3.5.4	Soot Aggregate Morphology . . . . .	69
3.5.5	Soot Fragmentation . . . . .	73
3.5.6	Selected Area Electron Diffraction . . . . .	73
3.5.7	HRTEM Lattice Fringe Analysis . . . . .	76
3.5.7.1	HRTEM Image Processing Procedure . . . . .	76
3.5.7.2	HRTEM Fringe Measurement . . . . .	83
3.6	Soot Oxidation Rate . . . . .	88
3.7	Uncertainty Analysis . . . . .	92
4	Repeatability and Reproducibility of TEM Measurements and Surface Area Validation . . . . .	94
4.1	Non-Bias-Controlled Results and Study Motivation . . . . .	95
4.2	Methods . . . . .	97
4.2.1	Bias-controlled measurements . . . . .	97
4.2.2	Gage R & R Analysis . . . . .	98
4.2.3	A simplified approach to obtaining sample confidence intervals . . . . .	101
4.2.4	Automated Measurements . . . . .	102
4.2.4.1	Circular Hough Transform . . . . .	102
4.2.4.2	Euclidean Distance Mapping . . . . .	104
4.2.5	TEM-Derived Mass Specific Surface Area . . . . .	105
4.2.6	BET-Derived Mass Specific Surface Area . . . . .	106
4.3	Results . . . . .	108
4.3.1	Gage R & R Results . . . . .	108
4.3.2	Automated Results . . . . .	111
4.3.3	Mass Specific Surface Area Results . . . . .	113

4.4	Conclusions	117
5	Results	120
5.1	Axial Flame Velocity Results	120
5.2	Temperature, Soot Volume Fraction, and Gas Species Concentration Results	121
5.2.1	Temperature and Soot Volume Fraction	121
5.2.2	Gas Species Concentrations	123
5.3	TEM Measurement Results	124
5.3.1	Primary Particle Measurements	124
5.3.2	Soot Surface Area	130
5.3.3	Soot Aggregate Morphology	132
5.3.4	Soot Fragmentation	137
5.3.5	Primary Particle Number Flow Rate	139
5.3.6	Selected Area Electron Diffraction	143
5.3.7	HRTEM Lattice Fringe Analysis Results	145
5.3.7.1	Fringe Length	147
5.3.7.2	Fringe Tortuosity	151
5.3.7.3	Fringe Orientation	155
5.3.7.4	Fringe Separation Distance	159
5.3.7.5	Nanostructure at the Particle Surface	163
5.4	Soot Oxidation Rate Expressions	166
6	Conclusions and Recommendations	170
6.1	Summary and Conclusions	170
6.2	Recommendations for Future Study	177
A	MATLAB Code	179
A.1	Center-Selected Edge Scoring	179
A.2	SAED Image Analysis Code	183
A.3	Lattice Fringe Analysis Code	189
A.3.1	BridgeGaps Function	189
A.3.2	SeverBranches Function	192
A.3.3	MeasureFringes Function	195
A.3.4	GetFringeSeps Function	199
B	Mathematical Derivations	202
B.1	Expressions for the Diameters of Average Surface Area and Volume	202
B.2	Expressions for Spherical Cap Height	205
C	Supplemental Figures	207
C.1	Fractal Dimension and Pre-factor from Fitted Data	208
C.2	Additional Fringe Measurements at the Primary Particle Surface	209
	Bibliography	210

## List of Tables

2.1	Summary of literature reporting OH collision efficiencies with soot, under various experimental conditions. . . . .	10
4.1	Components of variance in the measurement of primary particle diameter mean and standard deviation as quantified by Gage R & R analysis. . . . .	109
4.2	Primary particle diameter mean and standard deviation of each sample using two methods for combining operator measurements. Intervals are at the 95% confidence level. . . . .	111
4.3	Components of variance in the skewness of the primary particle size distribution and the mean projected overlap coefficient, as quantified by Gage R & R analysis. . . . .	114
5.1	Comparison of oxidation mechanism predictions with measured oxidation rates. . . . .	168

## List of Figures

2.1	Common measurements on binary soot aggregate images . . . . .	16
2.2	Structure of crystalline graphite . . . . .	27
2.3	HRTEM image showing internal burning . . . . .	42
3.1	Ternary flame system . . . . .	46
3.2	Soot column disruption apparatus for velocity measurement . . . . .	49
3.3	Velocity measurement video analysis method . . . . .	49
3.4	Laser extinction system schematic . . . . .	53
3.5	Thermophoretic soot sampling apparatus . . . . .	56
3.6	Aerosol Image Analyzer GUI . . . . .	58
3.7	Screenshot of primary particles measured using the CSES algorithm . . . . .	61
3.8	Steps in the CSES algorithm . . . . .	62
3.9	Spherical cap and overlapping primary particle schematic . . . . .	68
3.10	Procedure for creating binary images of soot aggregates . . . . .	71
3.11	SAED image measurement process . . . . .	75
3.12	Fringe image: ROI and contrast enhancement . . . . .	78
3.13	Fringe image: processing and skeletonization . . . . .	79
3.14	Fringe segment connection . . . . .	82
3.15	Fringe branch severing . . . . .	83
3.16	Lattice fringe measurement . . . . .	85
3.17	Lattice fringe separation measurement . . . . .	86
3.18	Differing reciprocal fringe separation distances . . . . .	87
3.19	Final fringe measurements in the Aerosol Image Analyzer . . . . .	87
3.20	Soot flame control volume for oxidation rate analysis . . . . .	89
4.1	Preliminary measurements of $\overline{d_p}$ without bias controls. . . . .	96
4.2	Soot collection apparatus for BET measurement . . . . .	107
4.3	Gage R & R results for $\overline{d_p}$ and $s_{d_p}$ . . . . .	109
4.4	Comparison of automated and Gage R & R results for $\overline{d_p}$ and $s_{d_p}$ . . . . .	112
4.5	Comparison of MSSA results from various methods . . . . .	115
5.1	Soot flame velocity vs. height above burner . . . . .	120
5.2	Radial temperature and soot volume fraction . . . . .	122

5.3	Temperature and integrated soot volume fraction vs. HAB . . . . .	122
5.4	Concentrations of major species and radicals vs. HAB . . . . .	124
5.5	Representative images of primary particles obtained at HABs of 10, 15, 25, and 50 mm . . . . .	125
5.6	Primary particle size distributions at HAB = 10 to 30 mm . . . . .	127
5.7	Primary particle size distributions at HAB = 35 to 50 mm . . . . .	128
5.8	Primary particle measurements vs. HAB . . . . .	129
5.9	Soot specific surface area vs. HAB . . . . .	131
5.10	Specific surface area overlap factor vs. HAB . . . . .	131
5.11	Aggregate size distributions at HAB = 10 to 45 mm . . . . .	134
5.12	Radius of gyration geometric mean vs. HAB . . . . .	135
5.13	Fractal dimension and pre-factor vs. HAB . . . . .	136
5.14	Distribution of primary particles per aggregate at each HAB . . . . .	137
5.15	Geometric mean number of primary particles per aggregate and num- ber flow rate of aggregates vs. HAB . . . . .	138
5.16	Primary particle number flow rate vs. HAB . . . . .	141
5.17	Representative SAED images obtained at HAB = 10, 15, 25, and 50 mm	143
5.18	SAED d-spacings and integral breadths at HAB = 10, 15, 25, and 50 mm . . . . .	144
5.19	Diameters of primary particles used for fringe analysis at each HAB .	145
5.20	HRTEM images of soot obtained at HABs 10, 15, 20, and 50 mm . .	146
5.21	(a) Fringe length distribution; (b) Median fringe length vs. HAB . . .	148
5.22	Median fringe length vs. fringe radial location . . . . .	149
5.23	Change in fringe length with primary particle size, inner 80% of pri- mary particles . . . . .	151
5.24	(a) Fringe tortuosity distribution; (b) Median fringe tortuosity vs. HAB	152
5.25	Median fringe tortuosity vs. fringe radial location . . . . .	154
5.26	Change in fringe tortuosity with respect to primary particle size, inner 80% of primary particles . . . . .	155
5.27	(a) Fringe Non-concentricity distribution; (b) Std Dev. of fringe non- concentricity vs. HAB . . . . .	156
5.28	Standard deviation of fringe non-concentricity vs. fringe radial location	157
5.29	Change in std. dev. of fringe non-concentricity with respect to pri- mary particle size, inner 80% of primary particles . . . . .	158
5.30	(a) Fringe separation distance distribution; (b) Mean of fringe sepa- ration vs. HAB . . . . .	160
5.31	Mean fringe separation distance vs. fringe radial location . . . . .	161
5.32	Change in mean fringe separation distance with respect to primary particle size, inner 80% of primary particles . . . . .	162
5.33	Fringe length measurements within the outer 20% of primary particles	164
5.34	Change in fringe length with respect to primary particle size, outer 2 nm of the primary particle . . . . .	165
5.35	Measured and predicted soot oxidation rates vs. HAB . . . . .	167
B.1	Spherical cap and overlapping primary particle schematic . . . . .	205

C.1	Fitted data to obtain fractal dimension and pre-factor at HAB = 10 to 45 mm . . . . .	208
C.2	Additional fringe measurements within the outer 20% of the primary particle . . . . .	209

## Nomenclature

### *Physical constants*

$c$	Speed of light in a vacuum ( $3.0 \times 10^8$ m/s)
$h$	Planck's constant ( $6.63 \times 10^{-34}$ J-s)
$k_B$	Boltzmann's constant ( $1.38 \times 10^{-23}$ J/K)
$R_u$	Ideal gas constant ( $R_u = 8.314$ J/mol-K)

### *Latin symbols*

$a_1, a_2$	Limits of a bias correction distribution
$A_a$	Projected area of an aggregate
$A_i$	Arrhenius pre-factor for species $i$
$A_p$	Cross-sectional area of a primary particle of mean diameter
$B$	Expected value of a bias correction
$C$	Empirical constant for determining radius of gyration
$C_{ov}$	3-dimensional primary particle overlap coefficient
$C_{ov,p}$	Projected (2D) primary particle overlap coefficient
$C_s$	Surface concentration of active sites
$C_\lambda$	Calibration constant for bandpass filter centered at wavelength $\lambda$
$CM_i$	The $i^{\text{th}}$ central moment of a size distribution
$d$	Scale diameter in Eq.4.9
$d_f$	Fringe separation distance
$d_{hkl}$	Distance between Bragg planes specified by Miller indices $hkl$
$d_{ij}$	Distance between primary particles $i$ and $j$
$d_p$	Primary particle diameter
$\overline{d_p}$	Mean primary particle diameter of a sample
$d_{p,\min}$	Specified minimum primary particle diameter
$d_{p,\max}$	Specified maximum primary particle diameter

$\overline{d_{pg}}$	Geometric mean primary particle diameter
$d_{ps}$	Primary particle diameter of average surface area
$d_{pv}$	Primary particle diameter of average volume
$D_f$	Fractal dimension of an aggregate
$E_{A,i}$	Activation energy of species $i$
$E_{ijk}$	Measured difference from the mean due to random effects
$E(m)$	Refractive index absorption function
$F_{ov}$	Specific surface area overlap factor
$f_s$	Local soot volume fraction
$F_s$	Sectional integrated soot volume fraction
$F_S$	Lost surface area factor due to primary particle overlap
$F_V$	Lost volume factor due to primary particle overlap
$ G_i $	Magnitude of image intensity gradient at pixel $i$
$GS$	Grayscale intensity of a soot flame image
$h_i$	Spherical cap height of primary particle $i$
$I$	The set of overlapping primary particle pairs in an image
$k$	Coverage factor
$k(T)$	Temperature dependent reaction rate
$k_a$	Projected area pre-factor
$k_f$	Fractal pre-factor
$K_e$	Dimensionless extinction coefficient
$L$	Maximum projected length of an aggregate (i.e. maximum caliper length)
$L_a$	Crystallite layered plane diameter
$L_c$	Crystallite layered plane stacking height
$L_{cam}$	TEM camera length
$L_f$	Fringe length
$\tilde{L}_f$	Median fringe length

$m$	mass
$M_i$	Molar mass of species $i$
$n$	Sample size
$N$	Population size
$\dot{N}_a$	Number flow rate of aggregates
$\dot{N}_p$	Number flow rate of primary particles
$N_p$	Number of primary particles in a soot population
$N_{p,a}$	Number of primary particles per aggregate
$N_{px}$	Number of pixels
$o$	Number of operators
$O_j$	Measured difference from the mean due to operator effects
$p_i$	Partial pressure of species $i$
$P_i$	Measured difference from the mean due to sample effects
$(PO)_{ij}$	Measured difference from the mean due to sample-operator interaction effects
$r$	Number of replicate measurements
$r_f$	Radial fringe location
$r_f^*$	Normalized radial fringe location
$r_i$	Radius of primary particle $i$
$r_{ox}$	Oxidation rate per unit mass of soot
$\bar{r}_p$	Mean primary particle radius
$r_{px,i}$	Distance between the $i^{\text{th}}$ pixel and the aggregate centroid
$R$	Radius of a diffraction ring <i>or</i> soot flame radius
$R_g$	Radius of gyration of an aggregate
$R_{g,2D}$	The 2D image radius of gyration of an aggregate
$s_Y$	Sample standard deviation of measurand $Y$
$S$	Surface area of a soot population
$S_a$	Surface area of an aggregate

$S_{cap}$	Surface area of a spherical cap
$S_m$	Mass specific surface area
$S_{m,0}$	Initial mass specific surface area
$S_V$	Volume specific surface area
$S_V^\circ$	Volume specific surface area of non-overlapping primary particles
$S_{V,mono}^\circ$	Volume specific surface area of monodisperse non-overlapping primary particles
$t$	Time
$T$	Temperature
$u$	Standard uncertainty
$\bar{v}_i$	Mean molecular velocity of species $i$
$v_s$	Soot velocity
$V_{cap}$	Volume of a spherical cap
$V_s$	Volume of a soot population
$w$	Statistical weight equaling the inverse variance
$\dot{w}_{ox}$	Soot oxidation rate per unit surface area
$W$	Maximum projected width normal to $L$ in an aggregate
$x$	Order of the reaction in carbon <i>or</i> horizontal coordinate in the object plane
$x_i$	Independent variable in a data reduction equation
$y$	The calculated result of a data reduction equation
$Y$	A measurand
$Y_{A,C}$	The combined weighted mean of measurements of $Y$ for sample $A$
$Y_{ijk}$	A measured value of measurand $Y$ from sample $i$ , by operator $j$ , the $k^{\text{th}}$ time
$z$	Height above burner

*Greek symbols*

$\alpha$	Projected area exponent, <i>or</i> statistical significance level
$\beta$	An equation constant

$\gamma$	Skewness of a distribution
$\hat{\gamma}$	Point estimator of population skewness
$\zeta_1, \zeta_2$	Regression constants relating $C_{ov}$ to $C_{ov,p}$
$\eta_i$	Collision efficiency between species $i$ and the soot surface
$\theta_B$	Bragg angle
$\theta_{f,c}$	Fringe angle of deviation from concentricity (i.e. non-concentricity)
$\theta_i$	Difference in intensity gradient orientation from that of a perfect circle, at pixel $i$
$\lambda$	Bandpass filter wavelength <i>or</i> laser wavelength
$\lambda_e$	DeBroglie wavelength of an electron
$\mu_Y$	True mean of measurand $Y$
$\hat{\mu}$	Point estimator of population mean
$\xi$	Oxidized fraction of the original carbon mass
$\rho_s$	Soot density
$\rho_{sa}$	Ratio of scattering-to-absorption cross section
$\sigma_Y^2$	True variance of measurand $Y$
$\hat{\sigma}^2$	Point estimator of population variance
$\sigma_\varepsilon^2$	True variance due to effect $\varepsilon$
$\sigma_{pg}$	Geometric standard deviation of primary particle diameter
$\tau_f$	Fringe tortuosity
$\tilde{\tau}_f$	Median fringe tortuosity
$\phi_s$	Surface area coefficient in Eq. 2.10
$\Omega$	Calibration constant in Eq.4.9

### *Subscripts*

$a$	Aggregate
$CV$	Control Volume
$f$	Fringe <i>or</i> Fractal

<i>g</i>	Geometric mean <i>or</i> gyration radius
<i>m</i>	Mass
<i>ov</i>	Overlap
<i>ov, p</i>	Projected image overlap
<i>ox</i>	Oxidation
<i>p</i>	Primary particle
<i>px</i>	Pixel
<i>s</i>	Soot
<i>sa</i>	Scattering and absorption
<i>S</i>	Surface area
<i>V</i>	Volume
<i>Y</i>	Pertaining to measurand <i>Y</i>

#### *Abbreviations*

AIA	Aerosol Image Analyzer
ANOVA	Analysis of Variance
BET	Brunauer-Emmett-Teller method
BSU	Basic Structural Unit (of nanocrystalline carbon)
CSES	Center-Selected Edge Scoring algorithm
CHT	Circular Hough Transform
CPC	Condensation Particle Counter
CV	Control Volume
DMA	Differential Mobility Analyzer
EDM	Euclidian Distance Mapping
EELS	Electron Energy Loss Spectroscopy
FWHM	Full-Width at Half-Maximum
FT	Fourier Transform

FTIR	Fourier-Transform Infrared spectroscopy
Gage R & R	Gage Repeatability and Reproducibility
GUI	Graphical User Interface
HAB	Height Above Burner
HRTEM	High Resolution Transmission Electron Microscopy
LIF	Laser-Induced Fluorescence
LII	Laser-Induced Incandescence
MCM	Monte Carlo Method of uncertainty propagation
MSSA	Mass Specific Surface Area
NSC	Nagle and Strickland-Constable model of soot oxidation by O <sub>2</sub>
PAH	Polycyclic Aromatic Hydrocarbons
PPSD	Primary Particle Size Distribution
RDG-PFA	Rayleigh-Debye-Gans Polydisperse Fractal Aggregate theory
ROI	Region of Interest
SAED	Selected-Area Electron Diffraction
SMPS	Scanning Mobility Particle Sizer
TEM	Transmission Electron Microscopy
TGA	Thermogravimetric Analysis
TSM	Taylor Series Method of uncertainty propagation
VSSA	Volume Specific Surface Area
XPS	X-ray Photoelectron Spectroscopy
XRD	X-ray Diffraction spectroscopy

## Chapter 1: Introduction

### 1.1 Motivation

Soot is carbon particulate formed through the incomplete combustion of carbonaceous fuels. It is the byproduct of modern combustion systems including gas and diesel engines, boilers, and coal-fired power plants. Soot produced by these processes is enormously detrimental to human health and the environment. Anthropogenic soot is responsible for cardiopulmonary, lung cancer, and ischemic heart disease mortality [1–4]. The World Health Organization estimated that in 2012, one in eight deaths worldwide resulted from air pollution exposure, of which soot is a major contributor [5]. Similarly, in 2012 the U.S. Environmental Protection Agency estimated that a 20% reduction in the soot emission limit from coal-fired power plants and diesel vehicles would result in over 1,000 fewer premature deaths and would avoid as much as \$9 billion in health related costs annually [6].

In addition, atmospheric soot is a major contributor to climate change. It is the strongest absorber of shortwave radiation in the atmosphere, resulting in a warming effect that is second only to carbon dioxide [7, 8]. Additionally, soot deposits on snow and ice reduce reflectivity, resulting in positive climate forcing [9, 10].

A thorough understanding of how soot is produced and consumed in com-

bustion environments is therefore of great interest to the broad fields of energy, health, and the environment. However, current models of soot processes in flames are incapable of predicting sooting behavior across more than a targeted set of combustion environments. Improving these models will require improved models of soot oxidation.

## 1.2 General Background

Soot oxidation is a heterogeneous reaction between gas-phase oxidizers and the soot particle surface. Soot oxidation studies have been performed across a variety of experimental conditions including premixed and diffusion flames, shock tubes, and flow reactors. Unfortunately, as one review observed, the oxidation rates reported by these studies vary by over 2 orders of magnitude [11]. In flames, soot formation processes compete simultaneously with soot oxidation, making it difficult to isolate the effects of either phenomenon.

Soot formation research has generally received greater attention than oxidation. Leading models include those by Kazakov et al. [12] and Appel et al. [13] for laminar premixed flames and those by Smooke et al. [14] and Dworkin et al. [15] for laminar diffusion flames. The model predictions generally compare well with the experimental environments targeted by each model. However, in a study by Mehta and coworkers in which 36 different detailed models of gas and soot kinetics were compared with 8 different laminar premixed and diffusion flames, no model could accurately match the experimental soot volume fractions for all eight flames within

a factor of five [16]. An improved understanding of soot oxidation might enhance the predictive capabilities of such models, and might also contribute to improved soot formation models due to the competition between soot formation and oxidation in flames.

In addition to oxidation kinetics, an accurate understanding of the physical structure of soot and how it evolves in various oxidative environments is critical to a full description of the oxidation process. Soot formation in a flame is a complex process involving particle inception, condensation, surface growth and aggregation. The resulting particles are chain-like aggregates of partially sintered spherules referred to as primary particles, and the morphology is described as fractal-like [17].

The structural description of soot occurs on three scales. The largest scale pertains to the size and shape of the aggregate, or what is often simply referred to as the soot "particle." Below that are the primary particles: spherules that group together to form the aggregate. The aggregate and its constituent primary particles together comprise what in most literature is referred to as the soot morphology. The third and smallest scale deals with forms and features at the sub-primary particle level down to the atomic scale, and is most often referred to as the soot nanostructure. The nanostructure mediates how soot carbon atoms are presented to the attacking gas-phase oxidizers, and hence is vital to understanding variations in oxidation behavior.

The high level of attention paid to the study of soot formation over many decades may in part be due to its truly puzzling nature. At its core, the challenge is in identifying a pathway for gas-phase polycyclic aromatic hydrocarbons

(PAHs) to cluster and grow into a condensed phase without violating the second law of thermodynamics [18]. The recently proposed mechanism involving chain reactions of resonance-stabilized hydrocarbon radicals capable of producing growing PAH clusters is a promising approach [19].

If the problem of soot formation is gaining focus, the question of oxidation is becoming more complex. In addition to gas-phase kinetics, factors affecting the rate and pathways of soot oxidation have grown to encompass: the presence of surface oxygenates, aliphatic C-H groups, and other heteroatoms in the carbon matrix [20–27], pore size distribution [22, 28–30], aggregate morphology and fragmentation [31–34], the size, curvature, and stacking of carbon planes [11, 35–37], and degree of amorphousness [38]. As one longtime researcher of soot phenomena recently noted, “The mechanism [of soot oxidation] appears to be complex, perhaps even more so than that of soot growth” [39]. The present work hopes to help untangle the skein of factors affecting soot oxidation and gain deeper insight into the phenomenon.

## Chapter 2: Literature Review

### 2.1 Soot Oxidation

Studies of soot oxidation have been summarized in the reviews of Howard [40] Kennedy [41], and Stanmore [30]. Soot oxidation in flames has been found to be dominated by molecular oxygen,  $O_2$ , and the hydroxyl radical, OH. Contributions by other oxidizers including O,  $CO_2$ ,  $H_2O$ , and NO have generally been observed to be minor, although a recent study by Frenklach et al. [39] suggests a greater role for oxidation by O.

#### 2.1.1 Oxidation by $O_2$

One of the earliest studies to isolate the oxidation of carbon by  $O_2$  was that of Nagle and Strickland-Constable (NSC) [42]. The study measured the removal of carbon from a heated pyrographite rod by an impinging oxygen jet. The resulting semi-empirical model defined two types of active sites on the carbon surface with different reactivities. The model was first order in  $O_2$  partial pressure at low oxygen concentrations but approached zeroth order at high  $O_2$  partial pressures. Despite little experimental resemblance to flame conditions, the NSC correlation remains a

widely-used model, and has become a benchmark against which new experimental oxidation results are compared (e.g., [11, 43–46]).

Another popular model of oxidation by  $O_2$  comes from Lee et al. [47] who measured oxidation in the lean regions of a hydrocarbon diffusion flame. Unlike NSC, their results showed a first-order dependence on  $O_2$  partial pressure. The study did not account for oxidation by other species such as OH, or O and was limited to a narrow range of  $O_2$  partial pressures.

Park and Appelton [48] performed shock tube measurements which generally agreed with NSC between 1500 - 2000 K, however above 2000 K, oxidation was underpredicted by the NSC expression. The study required short test times and considered temperatures much higher than those of a typical flame. Roth et al. [49] also performed shock tube experiments and obtained results comparable to Park and Appelton.

At lower temperatures, Chan et al. [50] measured  $O_2$  oxidation between 770-1250 K in both a post flame region similar to Lee et al., and with thermogravimetric analysis (TGA). Their results generally agreed with Lee et al. and showed first order  $O_2$  dependence. Neeft et al. [29] flowed oxygen over fixed-temperature (near 775 K) beds of Printex-U and diesel soot and measured the carbon mass loss rate. They found a reaction order in  $O_2$  partial pressure between 0.76–0.94 that depended on the degree of burnout and sample type.

Flow reactors in combination with mobility analysis has been another technique more recently employed. Higgins et al. [51] and Ma et al. [52] extracted soot from an ethylene coflow diffusion flame and measured the change in mobility di-

ameter of size-selected particles as they passed through an oxygen-filled reactor. In both studies, the apparent kinetic rate parameters depended on the size of the soot particles. Although a definitive reason for this could not be established, the authors offered various possibilities including different effective densities, different particle compositions, or different surface areas due to primary particle sintering. More recently, Camacho et al. [53] used a similar configuration to study the O<sub>2</sub> oxidation of nascent soot. They observed oxidation rates an order of magnitude higher than those predicted by NSC, and attributed this to the difference in nascent soot's structure and higher concentration of active sites as compared to mature soot.

Some researchers have noted the dependence of O<sub>2</sub> soot oxidation rates on soot nanostructure. Vander Wal and Tomasek [11] synthesized soot from benzene, acetylene, and ethanol in a tube furnace, and then oxidized it in the post flame region of a fuel lean methane/air flame on a McKenna burner. They attributed different oxidation rates among the three soot types to their differing nanostructures. The oxidation rates exceeded those predicted by NSC by as much as a factor of 5, although the researchers ignored any oxidation by OH, assuming its concentration was negligible due to the fuel lean condition. Song and co-workers [54] went further and derived an empirical modification to the pre-factor in the NSC model that was a function of fringe lengths measured from HRTEM soot images. The mathematical form of the empirical factor has no physical significance, and its numerical values have limited utility outside of the specific study from which it was derived. Nonetheless, the work serves as a proof-of-concept as to how nanostructure can be taken into consideration in predicting soot oxidation rates.

### 2.1.2 Oxidation by OH

In many cases, especially in fuel rich flames, OH is the principal soot oxidizer. Studies of soot oxidation by OH are fewer in number than those of O<sub>2</sub>, most likely because quantifying the short-lived radical is notoriously difficult. Most studies that have measured OH in sooting flames have used laser-induced fluorescence (LIF) [55–58], although others have used absorption spectroscopy [59], or Li atom absorption [60–62]. Another approach has been to forgo direct measurement altogether and infer OH concentrations based on partial equilibrium assumptions [43, 63, 64], full equilibrium [65], or some other kinetic model [49]. All of these methods carry substantial uncertainties.

Owing to its high reactivity, the activation energy of OH with soot is generally considered to be zero. This was supported recently in a comprehensive review of experiments investigating OH oxidation of soot [46]. Consequently, the oxidation rate by OH is typically expressed as a temperature-independent collision efficiency, denoted  $\eta_{OH}$ . Fenimore and Jones [66] were the first to measure oxidation by OH. They used a two-stage burner where soot generated in a rich premixed ethylene flame was oxidized in a secondary lean hydrogen premixed flame. They reported a collision efficiency of 0.1. The most commonly used collision efficiency is that of Neoh et al. [43], who also used a premixed two-stage burner configuration. They subtracted the O<sub>2</sub> oxidation rate as predicted by the mechanism of NSC from the total oxidation rate and attributed the balance to OH, whose concentrations were calculated from partial equilibrium considerations. Flame velocities were not mea-

sured and oxidation was measured across a height of only 5 mm. In addition, soot deposition prevented longer-term observations of steady flames. They measured a collision efficiency of 0.27 when using an apparent optical diameter of the soot aggregates and 0.13 when the actual particle size as determined by transmission electron microscopy (TEM) was used.

Oxidation of soot by OH was investigated by Roth and co-workers [49] in shock tube experiments in which soot particles were suspended in mixtures of O<sub>2</sub>/H<sub>2</sub>/Ar gas. The group used time-resolved CO and CO<sub>2</sub> measurements to infer the progress of soot oxidation and in situ laser extinction to determine particle size and number density. Combined with OH concentrations computed from the kinetic model of Warnatz [67], the group found a collision efficiency ranging from 0.13 to 0.34 depending on the gas phase mixture used, and an overall mean of 0.21. The group concluded that these results principally agreed with the observations of Fenimore and Jones [66] and Neoh et al. [43], despite being higher and more widely scattered.

Oxidation by OH was also examined in a number of studies in laminar hydrocarbon diffusion flames at atmospheric pressure [56, 60, 68–70]. Though largely supporting the OH findings by Neoh et al. and the O<sub>2</sub> findings by NSC, the range of collision efficiencies was wide both within and among these studies, ranging from 0.01 to 0.38, with many authors suggesting that particle reactivity and/or density of active sites changed with time. Studies by Kim and coworkers [61, 62] examined oxidation over pressures ranging from 0.1 - 8.0 atm, and found the OH collision efficiency to be nearly independent of pressure. Table 2.1 lists the OH collision efficiencies reported in all the known experimental studies of soot oxidation by OH.

Table 2.1: Summary of literature reporting OH collision efficiencies with soot, under various experimental conditions.

Study	Condition	$\eta_{OH}$
Fenimore and Jones, 1967 [66]	premixed flame	0.1
Mulcahy and Young, 1975 [71]	graphite in low temp flow reactor	0.04 - 0.08
Neoh, 1980 [43]	premixed flame	0.13
Garo et al., 1990 [68]	diffusion flame	0.01 - 0.1
Roth et al., 1991 [49]	shock tube	0.13 - 0.34
Puri, et al., 1994, 1995 [69, 70]	diffusion flame	0.03 - 0.38
Haudiquert, et al., 1997 [56]	diffusion flame	0.01 - 0.11
Xu, et al., 2003 [60]	diffusion flame	0.14
Kim, et al., 2004 [61]	diffusion flame	0.13
Kim, et al., 2004 [61]	diffusion and partially premixed flames	0.12
Guo, et al., 2016 [46]	meta-analysis of past experiments	0.10

### 2.1.3 Oxidation Model

Kinetic models of soot oxidation are often reported in the following form:

$$r_{ox} = S_m C_s k(T) f(p_{O_2}, p_{OH}, \dots) \quad (2.1)$$

where  $r_{ox}$  is the oxidation rate per unit mass of soot,  $S_m$  is the specific surface area,  $C_s$  is the surface concentration of active sites,  $k(T)$ , is a temperature dependent reaction rate usually in an Arrhenius form, and  $f(p_{O_2}, p_{OH}, \dots)$  is a function describing the dependence of the reaction rate on the partial pressures on the various reactants. It is clear from this expression that knowing the available surface area and active site concentration at a given moment is just as important as choosing the correct Arrhenius parameters in predicting oxidative behavior.

As oxidation proceeds, the change in the available mass specific surface area,

$S_m$ , is most simply expressed as a function of the conversion,  $\xi$ , or the fraction of the original amount of carbon which has been oxidized:

$$S_m = S_{m,0}(1 - \xi)^x \quad (2.2)$$

Here  $S_{m,0}$  is the initial specific surface area (i.e. when  $\xi = 0$ ) and  $x$  is the reaction order in carbon. The simplest application of the above expression is what is variously referred to as the shrinking sphere or shrinking core model for which the value of  $x$  is  $2/3$ . (A value of  $1/3$  is used if consumed material is computed using diameter rather than surface area). The model assumes all oxidation occurs on the smooth outer surface of spherical particles of constant density which shrink isotropically. This model has been used to derive oxidation rates by several groups (e.g. [11, 51, 72]). However, apart from some notable exceptions [29, 73], most studies to evaluate this model, have observed effects such as surface porosity and burning from the interior of the particle outward, that cannot be accounted for by the shrinking sphere model [22, 23, 28, 74, 75].

A more nuanced approach considers three regimes of soot oxidation: full penetration of the oxidizer into soot pores resulting in reactions on all surfaces (regime I), partial penetration and internal burning by the oxidizer (regime II), and reactions only at the outer surface of the soot particles (regime III). The circumstances under which each of these regimes applies has been the subject of some debate. Stanmore et al. [30] found that a regime II situation applied to a study oxidizing diesel soot in a 500°C dry-air furnace [76]. Ma et al. [52] studied soot oxidation by O<sub>2</sub> in a flow reactor from 600 - 900°C and found a regime change from I to II above about 675°C.

On the other hand, several groups have suggested that internal burning (regime I) is present at significantly higher temperatures ( $T=1500^{\circ}\text{C}$ ) [77, 78]. The above studies also discussed additional factors affecting specific surface area, including the opening of occluded pore space after removal of surface layers and the reduction of surface area due to sintering of primary particles.

## 2.2 Soot Morphology

Soot morphology affects a wide array of properties including light scattering, absorption, and radiation [79–84], particle mobility [85–88], and reactive surface availability [89–92]. It comes as no surprise then that the structure of soot and its measurement methods have been the topic of considerable research for many decades.

### 2.2.1 Aggregates

The fractal description of aerosols formed by diffusion limited cluster aggregation, such as soot, was first introduced in 1979 by Forrest and Wittan [93]. Fractal aggregates are scale-invariant and can be mathematically described by the relationship:

$$N_{p,a} = k_f \left( \frac{R_g}{\bar{r}_p} \right)^{D_f} \quad (2.3)$$

where  $N_{p,a}$  is the number of primary particles per aggregate,  $k_f$  is the fractal pre-factor,  $R_g$  is the radius of gyration of the aggregate,  $\bar{r}_p$  is the mean primary particle radius, and  $D_f$  is the fractal dimension of the aggregate.

### 2.2.1.1 Aggregate Measurement Methods: Non-TEM

Researchers have employed a variety of methods to measure the terms found in expression 2.3 above. Angular light scattering has seen widespread use and has the major advantages of being unobtrusive and able to be performed in-situ [43, 94–97]. A disadvantage is that it requires optical access to the flame, which is not always available in combustion environments of interest. In addition, light scattering measurements are affected by the distribution of primary particle and aggregate sizes as well as fractal dimension [98]. Mobility analysis is an increasingly common aerosol measurement approach, especially within the last decade [52, 53, 86, 99–102]. A major advantage of this method is that freshly generated flame soot can be sampled, processed, and analyzed continuously in a single in-line system. The downside is that the technique only directly measures the mobility diameter of a soot particle. Mobility measurements are related to other morphological parameters of interest by empirical expressions that require assumptions about the dispersity of primary particle sizes, and degree of sintering [103]. In addition, mobility measurements must be coupled with primary particle measurements obtained from an alternative technique (e.g. TEM) to accurately estimate soot surface area; (see for example Refs [52, 88]).

For studies of oxidation, soot surface area is the structural quantity of greatest interest since the heterogeneous reaction is mediated by the particulate surface. Gas adsorption techniques are commonly employed to measure soot specific surface area as well as surface porosity. The Brunauer-Emmett-Teller (BET) method [104]

has been used extensively [76, 77, 105, 106]; thermogravimetric analysis (TGA) less so [107–109]. BET is the more accurate of the two but requires soot quantities in excess of 100 mg, while TGA requires substantially less ( $\sim 30$  mg) [107]. Still, collecting even this smaller amount is often impractical in many combustion environments, especially for experiments examining oxidation where soot burnout is expected.

### 2.2.1.2 Aggregate Measurement Methods: TEM

The use of transmission electron microscopy (TEM) to quantify soot morphological details was spurred forward by Dobbins and Megaridis who pioneered the technique of thermophoretic sampling of soot directly from a flame onto a copper TEM grid [110]. Thermophoretic deposition is driven by the temperature gradient between the hot soot-laden gases and the relatively cold surface presented by the probe carrying the TEM grid. Contact with the cold probe effectively freezes the chemistry of the soot particles. The probe must remain in-flame long enough for sufficient soot deposition to occur, but not so long as to cause significant heating of the probe. Typical sampling times are on the order of 10-100 ms. Sample grids are then imaged using TEM.

In many cases, TEM is the preferred method for measuring soot morphology, as it allows features to be directly assessed from the soot aggregate images. However, since TEM images are 2-dimensional projections, techniques are required to extract the desired 3-dimensional characteristics. From both theoretical considerations [111]

and experiments using stereo-pair imaging and different viewing angles [90,98,112], the following expression, first proposed by Medalia and Heckman [113], relates the number of primary particles in an aggregate,  $N_{p,a}$ , and the aggregate’s projected area  $A_a$ :

$$N_{p,a} = k_a \left( \frac{A_a}{A_p} \right)^\alpha \quad (2.4)$$

The term  $A_p$  is the projected area of a primary particle of mean diameter. The projected area pre-factor,  $k_a$  and projected area exponent  $\alpha$  are empirically derived either from simulation or experiment. For soot, values in the literature for  $k_a$  range from 1.0 - 1.44, while  $\alpha$  ranges from 1.08 - 1.15 [90,96,98,112,114–116].

Recently, Moran et al. [117] performed simulations of soot aggregates comprised of polydisperse primary particles and found that Eq. 2.4 is more accurate when  $A_p$  is replaced with cross-sectional area of a particle of average surface area. Since the latter is larger than  $A_p$ , this implies that using  $A_p$  in Eq. 2.4 will overestimate  $N_{p,a}$ . However, this finding is in direct conflict with another recent study of simulated aggregates by Martos et al. [116], which found that  $N_{p,a}$  was consistently underpredicted when literature values for the parameters in Eq. 2.4 were used. This led them to suggest a higher value for  $\alpha$  than is common. Notably, Martos and co-workers did not consider the effect of polydispersity. Nonetheless, the lack of consensus for how Eq. 2.4 should be adjusted leads the current author to apply it in its unaltered form.

Several methods have been put forth for determining an aggregate’s radius of gyration from its TEM projection. The 2-dimensional radius of gyration,  $R_{g,2D}$  can

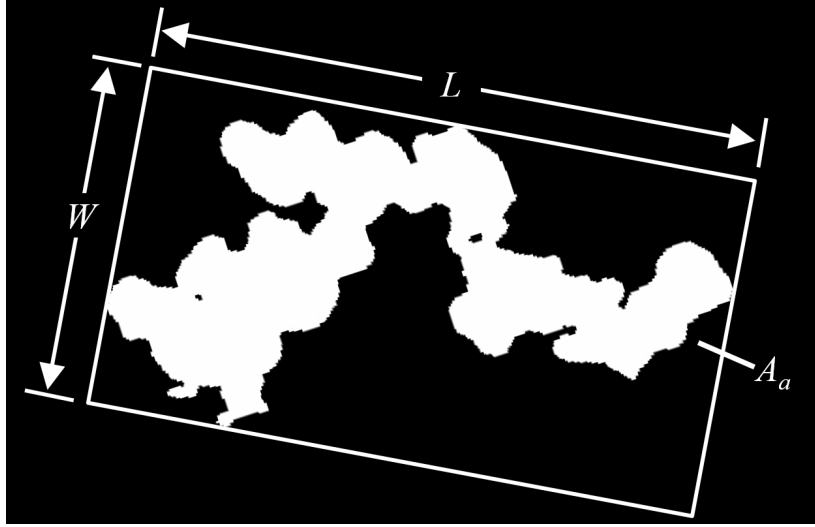


Figure 2.1: Morphological measurements commonly performed on binary soot aggregate images: Projected area,  $A_a$ , maximum projected length,  $L$ , and maximum projected width normal to  $L$ ,  $W$ .

be computed directly from a binary aggregate image, such as that shown in Fig. 2.1 using:

$$R_{g,2D} = \sqrt{\frac{1}{N_{px}} \sum_{i=1}^{N_{px}} r_{px,i}^2} \quad (2.5)$$

where  $r_{px,i}$  is the distance between the  $i^{\text{th}}$  pixel and the aggregate centroid, and  $N_{px}$  is the number of pixels in the aggregate. Several authors have uncritically assumed an equivalence of  $R_{g,2D}$  with  $R_g$  [81, 118]. However this has been demonstrated to be an poor assumption. Using simulated aggregates, Köylü et al. [90] found  $R_g$  to be greater than  $R_{g,2D}$  by a factor of 1.24. Similarly, simulations by Martos et al. [116] suggested the relationship:  $R_g = R_{g,2D} + AR_{g,2D}^B$ , where  $A = 3.73 \times 10^{-5}$  and  $B = 2.79$ .

As an alternative characteristic length, several authors have suggested using the geometric mean of  $L$ , the aggregate's maximum projected length, and  $W$ , the

maximum projected width normal to  $L$ , (i.e.  $\sqrt{LW}$ ) [90, 119, 120]. This could be directly substituted for  $R_g$  in Eq. 2.3. In principal, this would not affect the derived value of  $D_f$ , only the pre-factor, which would then be designated  $K_{LW}$ . Alternatively,  $\sqrt{LW}$  could be related back to  $R_g$  with the relationship suggested by Köylü et al. [90]:

$$R_g = \frac{\sqrt{LW}}{\beta} \quad (2.6)$$

where  $\beta$  is a constant equal to 2.34. However, caution should be exercised in the application of the above equation, since  $\beta$  is not truly constant, but has a complicated dependence on both the aggregate fractal dimension and number of primary particles [90, 121].

The final approach to deriving an aggregate's radius of gyration requires measuring only the maximum projected length,  $L$ , from the TEM image. Both experimental [90, 122] and numerical studies [111, 114, 117, 121] have indicated that  $R_g$  can be inferred from  $L$  using:

$$R_g = \frac{L}{2C} \quad (2.7)$$

Although the empirical constant  $C$  varies from 1.39 to 1.78 in these papers,  $C = 1.5$  appears to be a consensus value [89, 117, 118, 123, 124]. Köylü et al. [90] found that the scaling of  $R_g$  with  $L$  was less sensitive to changes in  $N_{p,a}$  than was the scaling of  $R_g$  with  $\sqrt{LW}$ . Similarly, Moran et al. [117] performed simulations of soot that were polydisperse at both the aggregate and primary particle level, and found that  $C$  remained nearly constant around 1.5 (maximum deviation  $< 10\%$ ) across a wide range polydispersity levels. A similar maximum deviation around a mean value of

$C = 1.45$  was observed in simulated aggregates of monodisperse primary particles by Wozniak et al. [121].

Regardless of the method used to obtain  $R_g$ , once it and  $N_{p,a}$  have been calculated for a large number of aggregates, the fractal dimension and pre-factor in Eq. 2.3 can be obtained by applying a least-squares fit to a plot of  $\ln(N_{p,a})$  vs.  $\ln(R_g/\bar{r}_p)$ , where  $D_f$  corresponds to the slope, and the intercept corresponds to  $\ln(k_f)$ . Values of  $D_f$  for combustion soot as determined by this method have ranged from 1.47 to 1.93 [96, 98, 112, 115, 118, 123, 125–127], which encompasses the theoretical value of 1.78 for diffusion limited cluster aggregation [103]. It should be noted that this method does not determine the fractal parameters for individual aggregates, but rather yields a global fractal dimension and pre-factor for an entire sample.

## 2.2.2 Primary Particles

### 2.2.2.1 Primary Particle Size Distribution

Accurate knowledge of the size distribution of the primary particles that make up soot aggregates is critical to quantifying a wide range of aerosol properties. Primary particle size is needed to derive optical properties from Rayleigh–Debye–Gans fractal aggregate theory [79–81], and charging efficiency in electrical mobility analysis depends on primary particle size [85, 88]. Morphological properties, such as fractal dimension, surface area, and volume, also depend on primary particle size distribution [89, 90, 128].

Manual analysis of TEM images is the most common method for measuring

primary particle size, and the results are often used to calibrate or validate other measurements. De Iuliis et al. [97] employed manual TEM measurements to validate the results of three-angle scattering and extinction. Laser induced incandescence (LII) measurements of primary particle size have often relied on manual TEM measurements to calibrate [129] or validate results [130, 131]. However, a recent comparison of TEM and LII primary particle measurements by Kholghy et al. [132] showed that additional factors such as shielding and bridging of particles due to high aerosol concentration can complicate validation. Attempts at automating the TEM measurement process have also relied on manual measurements to calibrate [133] or validate results [134, 135].

Despite its importance, knowledge of the distribution of primary particle sizes may not be readily available. This may be due to small sample sizes resulting from the manual nature of the TEM measurement (see for example [98, 112]), or because other methods (e.g. mobility analysis) were used instead. In these cases, simplifications such as monodisperse primary particles in single point contact with one another are common [49, 52, 61, 62, 119, 136–138]. However, when measured, the distribution of soot primary particles has generally been found to approach either a normal [22, 115, 118, 127, 138–140] or lognormal [97, 119, 130, 133, 134] distribution. Not accounting for this polydispersity can greatly alter surface area estimates [141, 142].

### 2.2.2.2 Sintering and Overlap of Primary Particles

Likewise, in most combustion environments, substantial sintering, or overlap, between primary particles makes the point-contact assumption difficult to justify. This can have a substantial impact on the estimation of surface area and aggregate fractal parameters. Neoh and coworkers observed that assuming single-point contact between primary particles overestimated the total surface area by 60% as compared to the BET external surface area [77]. Using simulated aggregates, Oh and Sorensen found that both fractal dimension ( $D_f$ ) and prefactor ( $k_f$ ) increased with the degree of primary particle overlap [111]. Lapuerta et al. [143], similarly saw a significant increase in  $k_f$  as overlap increased in simulated aggregates, but at the same time found  $D_f$  to decrease. Johnsson et al. [144] showed that not accounting for overlap could result in as much as a 51% overestimation of primary particle size derived from LII measurements. Simulations by Yon et al. [145] demonstrated that scattering and absorption properties of soot are significantly affected by primary particle overlap.

To account for the effect of primary particle overlap in extracting morphology from TEM images, Brasil et al. [114] introduced a parameter  $C_{ov,p}$ , which they termed the projected image overlap coefficient and defined it:

$$C_{ov,p} = \frac{\bar{d}_p - d_{ij}}{\bar{d}_p} \quad (2.8)$$

The term  $d_{ij}$  is the distance between primary particles  $i$  and  $j$ , and  $\bar{d}_p$  is their average diameter. Unfortunately, a 2D TEM image cannot distinguish between partially sintered primary particles and those that appear overlapped due to shad-

owing by primary particles on a different vertical plane. Using simulated aggregates with monodisperse primary particles and a fractal dimension of 1.78, Brasil and co-workers established the following relationship between the projected overlap and the true three dimensional particle overlap  $C_{ov}$ :

$$C_{ov} = \zeta_1 \overline{C_{ov,p}} - \zeta_2 \quad (2.9)$$

Values of  $\zeta_1 = 1.1 \pm 0.1$  and  $\zeta_2 = 0.2 \pm 0.02$  were shown to hold for  $C_{ov}$  values between 0 and 0.33. Wozniak et al. [121] arrived at the same linear relationship from their own simulations, with similar regression constants of  $\zeta_1 = 1.27 \pm 0.01$  and  $\zeta_2 = 0.27 \pm 0.01$ .

To find the true aggregate surface area accounting for overlap,  $S_a$ , Brasil et al. [114] suggested the following correction to the surface area with no overlap,  $S_{a,0}$ :

$$S_a = [1 - \phi_s C_{ov} (1 - 1/N_{p,a})] S_{a,0} \quad (2.10)$$

where a value of  $\phi_s = 1.3$  comes from a fit of the group's simulation results. Gwaze and coworkers [115] employed the method of Brasil et al. on soot aggregates from wood combustion. While the results were reasonable, they were not validated against other techniques. Bau et al. [89] also applied the method to estimate the surface areas of various solid oxide nanoparticles and found good agreement with BET values.

### 2.2.2.3 Attempts to Automate Primary Particle Measurement

Given the large number of measurements needed to quantify morphological properties with statistical significance, and the laborious nature of manually obtain-

ing them, there is a strong incentive to automate the TEM measurement process. Most attempts at automating measurement of primary particles have followed one of two approaches. The first is built around the Hough Transform [146], a well-known algorithm that identifies pre-defined geometries, such as a line or circle, by the strength of features in a parameter space. Grishin et al. [134] were the first to apply the Circular Hough Transform (CHT) to fractal aggregates. Because the algorithm relies on accurate edge detection, primary particle detection was restricted to the perimeter of a binarized aggregate image. Other studies [135,147], extended the technique to interrogate the interior of an aggregate using a combination of image self-subtraction and Canny edge detection [148]. Canny edge detection is known for its ability to detect weak edges and is therefore thought to be well-suited to discerning primary particles in the interior of a soot aggregate. A drawback of the CHT approach is that it requires accurate pre-knowledge of several input parameters, including the range of primary particle diameters and the CHT sensitivity level.

The second automation method is based upon Euclidean distance mapping (EDM) of a binarized aggregate image [133,149]. EDM is a technique whereby pixels within a binarized image object are assigned grayscale intensities corresponding to their distance from the object's nearest edge. The procedure outlined by Bescond et al. [133] involves thresholding the EDM image of an aggregate at a specific pixel intensity, then inverting and repeating the EDM-threshold sequence. Repeating this process across all possible threshold levels, a sigmoidal function emerges relating the number of white pixels remaining after processing, to threshold value. Following

calibration, this can be translated into a primary particle size distribution function.

The EDM approach has the advantage of not requiring an assumed geometry or size range for detection. However, its results must be calibrated against manual TEM measurements, and the shape of the size distribution must be assumed. Additionally, one must assume that the calibration holds across samples with potentially dissimilar morphologies.

### 2.2.3 Uncertainty of TEM Morphological Measurements

Despite its importance and use as a calibration/validation source, uncertainties associated with manual TEM soot measurements have received little attention. If reported at all, the standard uncertainty of the mean primary particle diameter is typically  $< 3\%$  and represents the standard deviation of the mean of a single measurement replicate by a single operator on a single sample (e.g., [22, 119, 126, 133]). A study by Kondo, Aizawa, Kook, & Pickett [150] observed that different operators, especially those with less experience, were the greatest source of fluctuation among primary particle measurements. However, to date there has been no formal attempt to quantify the uncertainty of TEM soot measurements resulting from different operators, samples, and measurement replicates. In addition, opportunities for bias are introduced at nearly every stage of the measurement process. These include bias in choosing which regions of the TEM grid to investigate, which aggregates to image from those regions, which images to select for measurement, which image areas and primary particles to consider, and how to best interpret the size of a given primary

particle. With a few exceptions [25, 121, 151, 152], studies rarely employ safeguards against operator bias.

## 2.3 Soot Fragmentation

More recently, increasing attention has been given to soot fragmentation as a controlling step in the prediction of soot burnout and particle size distributions [32]. While oxidation is the general process by which carbon atoms are subtracted from soot particles, fragmentation refers to the breakup of aggregates into smaller pieces. It is generally hypothesized that fragmentation is the result of oxidation by  $O_2$  either at the narrow bridging between primary particles or within the primaries where internal burning increases porosity and eventually breaks the particle apart [153].

Oxidation-induced soot fragmentation was first experimentally observed in the 2-stage burner studied by Neoh et al. [77]. Soot and exhaust gases generated by a  $CH_4$ - $O_2$  premixed flame were mixed with a secondary stream of  $O_2$  and then oxidized in a flat flame burner. Overall equivalence ratios were controlled by the amount of secondary gas supplied. Measurements were performed using light scattering and absorption techniques. They found that in fuel-lean and slightly fuel-rich flames, soot number concentrations increased as oxidation progressed, while they remained constant in more fuel-rich flames. They concluded that internal burning by the additional  $O_2$  in leaner flames resulted in breakup of aggregates at points of structural weakness. More recently, Echavarria et al. [78] and Ghiassi et al. [153] used an experimental configuration similar to Ref. [77] to study soot fragmentation.

Measurements were made using a scanning mobility particle sizer (SMPS), and a condensation particle counter (CPC) coupled to a differential mobility analyzer (DMA). Like Neoh and coworkers, the results of Echavarria's group linked increased fragmentation to greater  $O_2$  concentration. However, the results of Ghiassi et al. suggested that reduced temperature was more important to fragmentation than the amount of oxygen.

For diffusion flames, Garo et al. [68] used light scattering and extinction methods to measure soot in a  $CH_4$ -air laminar diffusion flame and observed an increased number density of soot aggregates near 75% of total soot burnout. Noting that this effect was more prevalent in regions with higher  $O_2/OH$  ratios, they concluded that fragmentation had occurred due to internal burning by molecular oxygen. In a different study, Zhang and Kook [154] analyzed in-cylinder diesel soot using TEM. They found that a drop in the radius of gyration of soot aggregates near cylinder walls was consistent with fragmentation due to flame-wall interactions.

Recent numerical studies have also investigated soot fragmentation. Harris and Maricq [155] modeled diesel exhaust soot and found that including fragmentation in the model significantly improved the soot size distribution prediction. Mueller and co-workers [156] modeled the premixed flames measured in Ref. [77] as well as the partially premixed counterflow diffusion flames studied in Ref. [157]. The fragmentation model agreed well with the premixed flame measurements, while no fragmentation was predicted in the counterflow flame. The authors concluded that this is because the soot is completely oxidized by OH before reaching  $O_2$  rich regions. Counterflow diffusion flames were both measured and modeled by Sirignano

et al. [32], who found that fragmentation greatly affects the particle size distribution by inhibiting coagulation and aggregate growth.

## 2.4 Soot Nanostructure

### 2.4.1 Description of Nanostructure

Seeking to explain the wide variability of soot oxidation rates reported in the literature, much recent research has focused on the role that nanostructure may play in the rates and modes of soot oxidation. The fine structure of mature soot is comprised of short segments of layered graphene planes, held together by van der Waals forces [41, 158, 159], and often seen grouped into short stacks, referred to as crystallites. The stacked carbon layers are randomly rotated with respect to each other along the c-axis (the axis normal to the layered planes), an arrangement referred to as turbostratic [76, 160–163]. This contrasts with polycrystalline graphite, whose layered planes are aligned with respect to each other. This results in a much closer interlayer  $d_{002}$  spacing for graphite (3.354 Å), than for soot which typically ranges from 3.5 Å- 3.9 Å [76, 161, 162, 164–170]. An illustration of this interlayer spacing within crystalline graphite is shown in Fig.2.2(a).

The crystallites within a soot primary particle are typically arranged in a core-shell structure. The central core, a region approximately 4-6 nm in diameter [158, 171], contains randomly oriented crystallites as well as more amorphous material, while the outer shell is comprised of crystallites whose layered planes are often preferentially oriented perpendicular to the radius of the primary par-

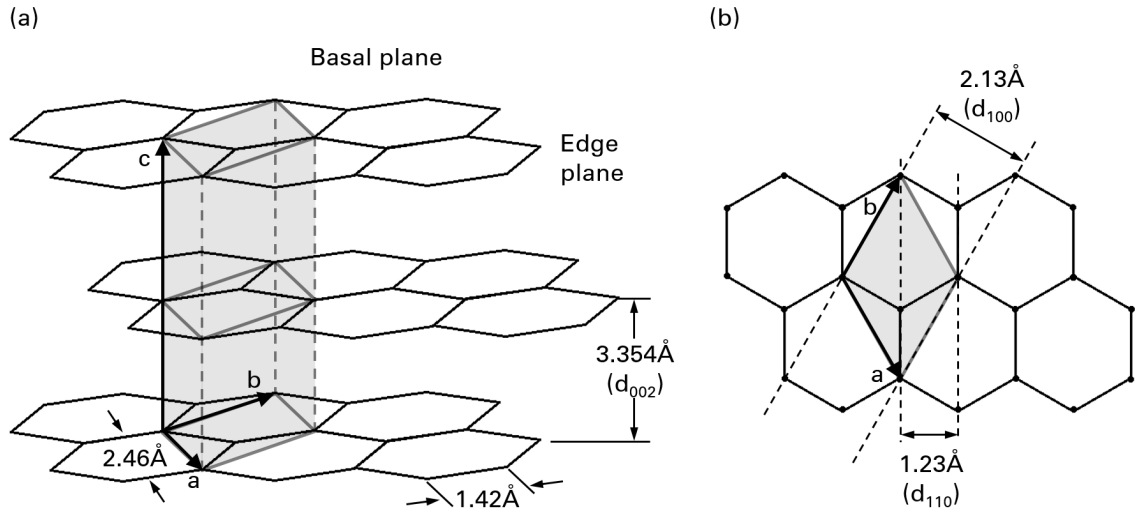


Figure 2.2: Structure of a crystalline graphite. The unit cell (shaded region) is defined by the primitive vectors  $a$ ,  $b$ , and  $c$ , where  $a = b$  in the case of a hexagonal structure. The  $c$  vector is twice the interlayer spacing because the ABA layering of graphite requires 3 planes to define the unit cell. (a) A 3-dimensional crystallite with interlayer spacing  $d_{002}$ . In a turbostratic configuration, layered planes will be rotated randomly about the  $c$ -axis and  $d_{002}$  will be greater than that of graphite. (b) A single layered plane showing lattice spacings between the (110) and (100) Bragg planes.

ticle [119, 158, 161, 162, 166, 172, 173]. This preference tends to become more pronounced with increasing radial distance [174, 175]. Curvature of the carbon layer planes, arising from five- and seven-membered rings within the aromatic matrix, is also a nanostructure feature of interest, and some have observed curvature to increase near the primary particle core [11]. Additional carbon material, not organized into any periodic structure, may also be present, helping to partially adjoin neighboring crystallites [176]. Discontinuities and misalignments between layers produce microporous voids which can substantially increase the surface area of a primary particle above that of a smooth surface [177]. Opening of these pores during oxidation can further increase the specific surface area beyond the smooth-surface model [76].

The nanostructural features of flame-generated soot are the result of a complicated process of soot formation that begins with the first appearance of polyaromatic hydrocarbons (PAH) clusters. These PAHs grow by various pathways such as hydrogen abstraction carbon addition (HACA) [178, 179], and form nucleated particles of nascent soot which further grow through surface reactions, PAH condensation and particle coalescence [18]. In the high temperatures of the flame, the nascent soot sheds hydrogen, and the carbon layer planes further carbonize and form graphitic crystallites [162, 180]. The resulting carbonized primary particles are conjoined within larger aggregates and are what is referred to as "mature" soot [181]. It is generally thought that once carbonization has occurred, the carbon layers are no longer able to reorganize at ordinary flame temperatures ( $<1800$  °C), and the nanostructure is essentially "locked in" [182]. As such, the mature soot nanostructure reflects the nucleation and growth environment.

#### 2.4.2 Dependence on Heat Treatment and Fuel Type

Within this general picture there is substantial variability in soot nanostructure that depends primarily on the thermal history of the particles and to a lesser degree, on fuel type. Various studies have demonstrated that thermal annealing of soots and carbon blacks, through heat treatment, reduces plane defects and promotes carbon plane layer growth. This latter structural change is most commonly referred to as graphitization [162, 164, 183]. As the temperature of the heat treatment increases, relative alignment between carbon layers improves, resulting in interlayer

spacings that decrease toward that of graphite [160,184]. Higher temperatures also cause crystallites to grow both in the size of their carbon layer planes and in the number of stacked layers [183]. Importantly, these thermally-induced structural changes are present even at the sub-microsecond time scales relevant to soot formation and oxidation in flames [185–187].

Fuel type has also been shown to affect soot nanostructure. Vander Wal et al. [182] found that fuel type influenced the curvature of the carbon layer planes, an effect that could be enhanced or suppressed depending on the temperature and duration of heat treatment. Alfé et al. [24] observed that cycloalkanes and aromatic fuels produced soot with a more ordered nanostructure than that produced by straight alkanes and ethylene. Lapuerta et al. [25] observed that the nanostructure of biodiesel soot exhibited greater order and a higher degree of graphitization than diesel soot produced under the same conditions. Apicella et al. [188] found that the carbon layer planes in soot from a methane flame were much smaller than what is typically found in ethylene and benzene flame soot [170].

## 2.4.3 Nanostructure Diagnostic Methods

### 2.4.3.1 Non-TEM Methods

A wide array of diagnostic techniques can be used to extract nanostructural features of soot. X-ray diffraction (XRD) is one of the most commonly used tools [23, 76, 160, 164, 167, 173, 189]. Using the positions and widths of peaks in an XRD pattern, one can estimate the average crystallite interlayer ( $d_{002}$ ) spacing, lay-

ered plane diameter,  $L_a$ , and stacking height,  $L_c$  [173]. Similar information can be obtained from Raman spectroscopy. Here the intensity ratio of spectral bands corresponding to graphitic and defect structures (G band and D bands, respectively), can be used to estimate  $L_a$  [190–193], as well as provide information about the degree of graphitic ordering within a specimen [22, 25, 27, 189, 194].

Other methods gage the degree of graphitization by probing the carbon bonding states. X-ray photoelectron spectroscopy (XPS) is used to measure the relative prevalence of carbon hybridization states  $sp^2$  and  $sp^3$ . The former bonding state is indicative of graphitic content while the latter is generally interpreted as defect sites within the graphitic network [73, 74, 195–197]. Likewise, electron energy loss spectroscopy (EELS) can assess graphitization based on the different energy losses of electrons passing through the sample, indicative of  $sp^2$  versus  $sp^3$  hybridization [37, 76, 188, 195, 198]. A similar task can be performed using Fourier Transform infrared spectroscopy (FTIR) on the basis of absorption by C=C bonds as opposed to hydrogenated or oxygenated bonds [76, 199, 200].

#### 2.4.3.2 Selected-Area Electron Diffraction (SAED)

As with morphology, TEM imaging is indispensable for revealing information about soot nanostructure. Different information may be obtained by operating the instrument in either diffraction mode, or in high resolution mode (HRTEM). In diffraction analysis, the incoming electron beam is thought of as a plane wave whose wavelength,  $\lambda_e$ , is the electron DeBroglie wavelength, which is a function of the

beam energy. The wave is elastically scattered by the atoms in the specimen. If the specimen possesses atomic planes at regular spacings,  $d_{hkl}$ , and the polar angle between the beam and the plane is at  $\theta_B$ , satisfying the Bragg condition,

$$2d_{hkl} \sin \theta_B = n\lambda_e \quad (2.11)$$

where  $n$  is an integer, then waves re-scattered at  $\theta_B$ , (the Bragg angle), will constructively interfere. In polycrystalline materials such as soots and carbon blacks, crystallites are oriented randomly with respect to the incoming electron beam. This ensures many crystalline domains will be oriented at the correct polar angle with respect to the beam to produce constructive interference. The random orientation will also ensure that the re-scattered waves will emanate equally over all  $2\pi$  azimuthal angles from the specimen. The diffracted waves will trace out a cone in space and arrive in a ringed pattern at the TEM projection plane. The distance from the specimen to the projection plane is referred to as the camera length. The relationship between the cone half-angle  $2\theta_B$ , the camera length  $L_{cam}$ , and the diffraction ring radius  $R$  at the projection plane is

$$\tan 2\theta_B = \frac{R}{L_{cam}} \quad (2.12)$$

Combining Eq. 2.11 & 2.12, and assuming  $R \ll L_{cam}$ , yields

$$d_{hkl} = \frac{\lambda_e L_{cam}}{R} \quad (2.13)$$

The d-spacing,  $d_{hkl}$ , is the distance between the Bragg planes specified by Miller indices  $hkl$ , which identify the direction normal to the plane with respect to the unit cell of the crystal lattice. If  $L_{cam}$  is known from calibration of a specimen

with known lattice spacings, the d-spacings of an unknown specimen are readily determined by measuring  $R$  from the diffraction image. The d-spacings  $d_{002}$ ,  $d_{100}$ , and  $d_{110}$  illustrated in Fig. 2.2 produce the most prominent rings in typical soot specimens.

In the technique of selected area electron diffraction (SAED), only the portion of the specimen that is visible through the selected area aperture (also called a field-limiting aperture) contributes to the diffraction pattern. In the case of soot, one can probe the crystalline structure within an area as small as a single primary particle. The average spacing between various Bragg planes is easily measured from the diffraction peaks and can be translated into first- and second-neighbor interatomic distances of the  $sp^2$  carbons [193, 201]. Distance between the (002) basal planes can be compared to known values of pure graphite (Fig. 2.2) to infer degree of graphitization [189]. A greater portion of the electron beam will be diffracted with increasing crystallinity, an effect observable in the integrated intensity of diffraction peaks [22, 162]. Similarly, diffraction peak broadness reflects the dispersity of diffracting layer spacings, and hence indicates relative amorphousness of the specimen [168, 176, 201–203]. Broadness of a diffraction peak is typically reported as the full-width at half maximum (FWHM) of a peak curve, or as the integral breadth, defined as ratio of the integrated intensity to the peak maximum.

The SAED technique is limited by a number of uncertainties affecting the terms found in Eq 2.13. The first originates from the energetic variability of the electrons, which are produced in a TEM by either field emission or thermionic emission. This variation in energy translates into an wavelength bandwidth that is

wider than what is typically seen from X-ray sources [162]. Electromagnetic lenses used in a TEM can produce elliptical distortions in diffraction rings, making the camera length non-uniform, and changes in lens currents can also affect the camera length value [202].

### 2.4.3.3 High Resolution Transmission Electron Microscopy (HRTEM)

#### Lattice Fringe Analysis

A commonality among all the nanostructure diagnostic techniques thusfar mentioned, is that they can only yield specimen-averaged quantities. In contrast, HRTEM provides nanostructural information that can be spatially resolved across the projected soot image. This information comes in the form of lattice fringes formed by the interference between the direct and scattered electron waves. It should be noted that the structures visible in an HRTEM image of soot are not the graphene planes themselves, but rather the fringes resulting from this phase contrast phenomenon [203]. Adding to the challenge of interpreting HRTEM images are the irregularities inherent to soot, such as overlapping and curved carbon layers, amorphous content, and contrast variations [204]. Nonetheless, on-axis lattice fringe images can provide information about the orientation, spacing, and extent of the local lattice structure [203]. For over 20 years, researchers have developed methods to process and extract quantitative structural information from the lattice fringe images of carbonaceous materials.

All methods of lattice fringe image analysis can be broadly organized into two

steps: An image processing procedure that identifies and isolates fringe objects, and algorithms to meaningfully quantify the size, shape, and arrangement of these fringes within the carbon nanomaterial. Davis et al. [21] were the first to apply quantitative lattice fringe analysis to pulverized coal during combustion. After applying a Fourier transform (FT) filter to remove structures lacking the characteristic periodicity of turbostratic carbons, the group measured average fringe lengths and relative amounts of crystalline structure. In the analysis of soot HRTEM images, Palotas et al. [205] obtained binary images of the fringe structure by similarly applying a bandpass filter in the frequency domain, followed by a reverse transform and then thresholding. Measurements including the length, orientation, and circularity of fringes as well as interplanar spacing were then extracted from the binary images.

Sharma et al. [206] argued that a bandpass filter removed information that had value but lacked periodicity. Using a step filter in Fourier space, they were able to remove noise while retaining both periodic stacks and non-periodic single layers. Following an inverse FT, binarization, and skeletonization, an algorithm was applied that removed Y and T shaped fringe linkages and then reconnected those fringes that conformed to a set of geometric parameters. Measurements of fringe length, stacking dimension, and interlayer spacing were obtained. Interlayer spacing calculations were restricted to fringe pairs within tolerances that included parallelism ( $\pm 10^\circ$ ), and perpendicular distance ( $0.355 \pm 0.025$  nm). Shim et al. [175] similarly used a process involving FT filtering, binarization, skeletonization, linkage separation and fringe reconnection. Fringes shorter than 1.5 nm were discarded and average fringe lengths, tortuosity, and apparent crystalline fraction were calculated. They defined

tortuosity as the fringe length divided by the diagonal length of a box bounding the fringe. Additionally, they developed a method to characterize the orientational order of the lattice fringes. Investigating the nanostructure of carbon particles formed by laser pyrolysis, Galvez et al. [199] followed a similar process, but applied a top-hat filter prior to binarization to reduce intensity variations, and threw out fringes shorter than the size of a single aromatic ring (0.25 nm). They also identified stacked crystallite structures, so-called basic structural units (BSUs) [207], on the basis of fringe spacing and similar fringe orientations and tortuosities.

Yehliu et al. [208], provided a very detailed description of their method for processing and measuring HRTEM images of soot. Following an inversion of the image grayscale, a region of interest (ROI) around a primary particle was manually selected. Defining an ROI improved operations that rely on image statistics, such as contrast enhancement, since areas outside the ROI were not included in the statistical treatment. After ROI selection, contrast was enhanced, high frequency noise was attenuated by a Gaussian lowpass filter in the frequency domain, and uneven illumination was ameliorated through a top-hat filter. After thresholding to binarize the image, a morphological opening and closing operation was performed in place of the linkage separation and fringe reconnection steps of previous works [175, 206]. Fringes touching the ROI border were removed, the image was skeletonized, and fringes shorter than 0.5 nm were eliminated. Following the work of Ref. [209], distributions of fringe length and tortuosity were automatically calculated while fringe separation distribution was determined from the manual selection of fringe pairs in the image. Here, as in most other studies, tortuosity was defined as the

fringe length divided by the distance between fringe endpoints.

Several researchers have since followed the process outlined by Yehliu et al. [208], with or without minor modifications [35, 74, 118, 210, 211]. Botero et al. [210], consolidated the steps of image inversion and top-hat filtering via a bottom-hat transformation, and they automated the fringe separation distance calculation while taking fringe orientations into account. They selected 0.483 nm as the minimum allowable fringe length as this corresponds to the length of two aromatic rings.

Other approaches include those by Wang et al. [212] who applied HRTEM analysis to coals. Rather than calculating tortuosity, they presented an image analysis method that measured the individual angles between fringe segments. From this they produced a distribution not only of fringe lengths, but of fringe curvatures as an accumulation of individual segment angles. In another approach, Pré and coworkers [213], attempted to glean surface nanopore information from HRTEM images of activated carbons. Extending the work of Refs. [199, 207], they merged nearby BSUs with similar orientations into what they termed continuous domains. They assumed that the non-organized regions separated from these domains were probable locations of nanopores, and then correlated the size distributions of spaces between ensembles of fringes, BSUs, and continuous domains, to the pore size distributions obtained from Nitrogen adsorption isotherms.

A number of studies have compared measurements obtained from lattice fringe analysis to those obtained from non-TEM methods. Taken in aggregate, one can observe several trends. First, unless the range of allowable fringe separation distances is restricted *a priori* to the characteristic range of turbostratic carbon (see

section 2.4.1)(e.g. by means of an FT filter or calculation window) the fringe separation distance obtained from HRTEM images is substantially higher than the  $d_{002}$  lattice spacing given by XRD. This discrepancy serves as a reminder to not confuse lattice fringes with the carbon layers themselves. Nonetheless, relative differences in fringe spacings can be used to distinguish between specimens possessing different lattice spacings and degrees of graphitization [209, 214]. Generally speaking, if separations between 0.3 and 0.6 nm are permitted, the fringe separation distance will follow a symmetric bell-shaped distribution with a mean between 0.38 and 0.45 nm [24, 118, 199, 207, 210, 215]. The 0.6 nm upperbound is often chosen because van der Waals forces are negligible beyond this distance (see [24, 169, 210]). Additionally, upperbounds below this value can often be seen to truncate the fringe separation distribution (see for example [209, 214]).

Comparison of HRTEM fringe analysis with Raman spectroscopy has shown mixed results. Sampling soot from premixed benzene and ethylene flames, Apicella et al. [192] saw excellent agreement between the mean fringe length determined by Raman spectroscopy and that found by HRTEM lattice fringe analysis. Their analysis assumed an equivalence between the Raman measured crystallite diameter,  $L_a$ , and HRTEM fringe length,  $L_f$ , an assumption of dubious validity. Parent et al. [193], also found reasonable agreement in the absolute values of  $L_a$  and  $L_f$  in aircraft soot produced at different engine thrusts, but noted that the two measurement techniques yielded trends in opposite directions. Studies by Vander Wal et al. [183] and Yehliu et al. [214] on various soots and carbon blacks did not attempt to extract crystallite size from Raman measurements. However, they did see a monotonic

relationship between the ratio of the graphitic and defect band intensities, and the mean or median fringe lengths measured by HRTEM. Song et al. [22] also measured both of these quantities for biodiesel soots. The general trend was similar but not monotonic.

Various other validations of the HRTEM method are scattered about the literature. Using XPS, Gaddam et al. [74] found a nearly constant  $sp^2/sp^3$  ratio during oxidation of a carbon black, which was consistent with the constant distribution breadth of fringe length measured by HRTEM. Yehliu et al. [214] observed that mean fringe separation distance increased with mean tortuosity. They took this both as evidence that curved structures inhibit stacked layer development and as validation of their tortuosity measurement method.

#### 2.4.4 Role of Nanostructure in Soot Oxidation

Broadly speaking, soot reactivity increases with nanostructural disorder as measured by the various techniques outlined in Section 2.4.3 (see, for example, trends in Refs. [22, 31, 35, 73, 211]). This is because the carbon atoms comprising a soot particle are not a homogeneous population, but rather participate in a variety of bonding structures affecting their reactivity. The rates and pathways of soot oxidation therefore depend on the relative prevalence and accessibility of differently bound carbons, which in turn is dictated by the nanostructure.

The most important reactivity variation is between the vastly more reactive carbons found on the edges of a layered plane than those lying on the basal

plane [216] (see Fig. 2.2). This bifurcation correlates to the empirically derived two-site model by Nagle and Strickland-Constable discussed in Section 2.1.1. An edge site carbon has an unpaired  $sp^2$  electron, which can facilitate the chemisorption of oxygen, a critical step in the transformation of soot carbon into a gaseous carbon oxide [20, 216]. Edge sites can also host impurities common in combustion environments such as Fe, Zn, and Cu that can catalyze the oxidation reaction [20, 27]. Surface edge sites are more likely to terminate in oxygenated or hydrogenated groups, both of which can enhance oxidation rates [22–24, 26, 217]. Lastly, edge site carbons are more prone to oxidative attack than basal plane carbons simply by virtue of their greater physical exposure to the gas phase.

Rosner and Allendorf [218] observed the reactivity of isotropic graphite to  $O_2$  was over 100 times that of pyrolytic graphite, and attributed this to the relative abundance of edge sites in the former. The reactivity of edge site carbons in graphene can be 100 - 1000 times that of basal plane carbons [216]. It follows then, that since the ratio of edge site to basal plane carbons decreases with increasing crystallite size, the overall soot reactivity should decrease as well.

Other nanostructural features will also increase carbon reactivity above that of a relatively inert graphene plane. The presence of 5- and 7-membered rings induces curvature in a carbon plane. This curvature creates bond strain, weakening the C-C bond and effectively reducing the oxidation activation energy [11]. The carbon planes, nominally  $sp^2$  hybridized, will also possess a small admixture of  $sp^3$  characterization due to curvature [74, 219]. The presence of  $sp^3$  hybridized amorphous carbon will also increase reactivity, owing to its lower C-C bond dissociation

energies [21, 73, 220].

Numerous studies have demonstrated the interdependence between soot nanostructure and oxidation. Ishiguro et al. [76] observed the progressive oxidation of diesel soot in a dry-air furnace at 500°C. Comparing BET surface areas with those measured by TEM, the group found porosity increased by over a factor of 4 as oxidation progressed. At the same time, the nanostructure became more ordered by certain measures. Using XRD, they detected an increase in crystallite size in the stacking dimension and a decrease in layered plane spacing during oxidation, while in-plane carbon layer growth was inferred from EELS and FTIR measurements. By considering the comparative weakness of inter-layer van der Waals forces to the covalent bonds holding edge-site carbons, and in light of the carbon layer plane growth, the researchers concluded that primary particle mass loss was due primarily to the stripping of outer shell crystallite segments, rather than the dissociation of carbon atoms from layer plane edges.

Palotas et al. [165] used HRTEM to analyze the nanostructure of commercial carbon blacks undergoing oxidation in a TGA at temperatures of 575°C and 680°C. They similarly observed a decrease in interlayer spacing as oxidation progressed, due mostly to the disappearance of the widest spacings in the distribution. The standard deviation of interlayer spacings also decreased with oxidation while the fraction of each primary particle containing crystallite structures increased. They interpreted all of these results as an increased order in the carbon structure due to oxidation.

Vander Wal and Tomasek [11] took soot synthesized from benzene, acetylene,

and ethanol in a tube furnace, and oxidized it in the 750°C post flame region of a McKenna burner. They used HRTEM to measure the different initial nanostructures of the three soots which then translated into different oxidation rates. Benzene soot was characterized by short, disordered fringes and few discernible crystallites. It showed an oxidation rate approximately 5 times that predicted by the NSC model. They attributed this to the high proportion of edge to basal plane sites in the short graphene segments. In contrast, acetylene soot displayed long, weakly curved, concentric lattice fringes and oxidized much more slowly (although still faster than NSC would predict). This, they concluded, was due to the fewer exposed edge sites and the minimal bond strain imposed on the basal plane carbons. Lastly, ethanol soot, which exhibited longer fringes than benzene soot but greater curvature than acetylene soot, showed an oxidation rate as high as that for the benzene soot. They concluded that weakly held carbons in the strain-inducing curved planes was the determining factor in the high reactivity.

Raj et al. [37] compared the oxidation of two different model soots: one composed primarily of planar PAH segments (Printex-U), and one composed mostly of curved PAHs (Fullerene soot). Using a TGA at air temperatures ranging from 200 - 800°C and different heating rates, they found the activation energy for the curved soot to be 26 kJ/mol lower than for the planar soot. This was true in spite of there being a higher H/C ratio in the planar soot, which normally correlates to higher oxidation rates. They interpreted this as showing the dominant role of PAH curvature in oxidative reactivity. This interpretation was bolstered by quantum chemistry calculations that demonstrated consistently lower energy barriers for the oxidation

pathways of curved PAH than for planar PAH.

Gaddam et al. [74] observed the changing nanostructure of 5 different model carbons oxidized in a flow reactor (400 - 550°C) and a TGA (490 - 650°C). Using various methods (XPS, HRTEM, BET, and Raman spectroscopy) they tracked how nanostructural changes impacted the mode and rate of oxidation. The initial nanostructure of R250 carbon black contained loosely concentric fringes of varying lengths with slightly more disorder near a primary particle's core. The nanostructure was largely unchanged by oxidation which proceeded at a nearly constant rate and progressed outward from the particle's core. As in Ref. [23], the internal burning mode was dramatically apparent from the HRTEM images as seen in Fig. 2.3.

Different behavior was observed in arc-generated soot owing to its largely amorphous initial structure. The amorphous carbon made for fast initial oxidation but also provided material for oxidation-induced graphitization, which in turn, slowed oxidation. (Oxidation-induced graphitization is understood to occur by the removal of cross-links, interstitial atoms such as non- $sp^2$  carbon, or strained bonds within the carbon matrix. This frees graphene segments to realign and create longer carbon planes [21, 221, 222]. Radicals produced during oxidation would also serve as sites for carbon plane growth [222]). M1300 carbon black, on the other hand, showed

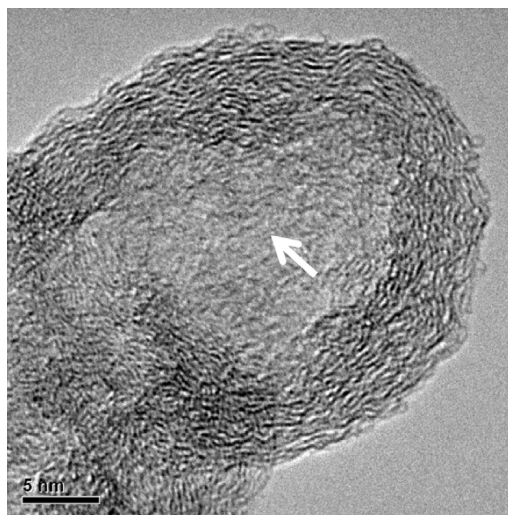


Figure 2.3: HRTEM image showing internal burning within a primary particle. (Image From Ref. [74])

different behavior was observed in arc-generated soot owing to its largely amorphous initial structure. The amorphous carbon made for fast initial oxidation but also provided material for oxidation-induced graphitization, which in turn, slowed oxidation. (Oxidation-induced graphitization is understood to occur by the removal of cross-links, interstitial atoms such as non- $sp^2$  carbon, or strained bonds within the carbon matrix. This frees graphene segments to realign and create longer carbon planes [21, 221, 222]. Radicals produced during oxidation would also serve as sites for carbon plane growth [222]). M1300 carbon black, on the other hand, showed

a highly curved but non-concentric fringe arrangement. Oxidation started at sites of curvature which then opened into pores, exposing ever greater numbers of reactive edge site carbons producing an exponentially increasing oxidation rate. Lastly, multi-walled carbon nanotubes and carbon onions, which began with highly graphitized nanostructures, oxidized more slowly than the other model carbons. Oxidation occurred almost exclusively at edge sites and did little to affect the nanostructure.

The presence of oxygenated functional groups and aliphatic C-H groups on the soot surface can greatly affect the way nanostructure evolves, especially during initial oxidation, which in turn impacts oxidation at later stages. Highlighting the importance of oxygenated surface functional groups, Song et al. [22] compared the oxidation of biodiesel soot with that of diesel produced by the Fischer-Tropsch process (F-T soot). The soot samples were oxidized in a TGA with 500°C air and were analyzed with a bevy of techniques including HRTEM, SAED, Raman spectroscopy, EELS, and FTIR. Biodiesel soot, initially exhibited shrinking sphere oxidation dominated by oxygenated surface functional groups. This gave way to internal burning made accessible by the opening of micropores while the remaining outer layers underwent oxidation-induced graphitization. By contrast, smaller presence of oxygen functional groups in F-T soot resulted in slower oxidation and no evidence of internal burning. The shrinking core model held throughout and there was little change in fringe lengths or reorganization of the carbon layers as oxidation progressed.

Other studies have shown the effect of surface oxygenates to be less important. Seong and Boehman [223] characterized soot from a turbocharged diesel engine using XPS, HRTEM, Raman spectroscopy, and XRD. In contrast to Song et al. [22], they

found surface oxygen content to have little impact on oxidation rates. Instead, reactivity was increased by the presence of metallic compounds from the engine lubricant, and also possibly by increasing nanostructural disorder. Wang et al. [26] similarly found oxygenated surface functional groups to be much less important to the reactivity of in-cylinder diesel soot than aliphatic C–H surface functional groups.

There is scarce literature exploring the link between soot oxidation and nanostructure in actual flames. Notwithstanding the work of Vander Wal and Tomasek [11], the papers surveyed here thus far, all oxidized soot in furnaces, TGA’s, or flow reactors at colder temperatures and longer times than are found in flames. Moreover, the only oxidizer considered has been O<sub>2</sub>. This is a major gap in the literature. Two very recent studies by Li et al. [118] and Botero et al. [215] tracked the evolution of soot within co-flow diffusion flames of varying fuels. Observations of oxidation effects were limited to regions near the flame tip where soot growth no longer dominated. Li and coworkers saw a slight increase in fringe length near the flame tip but offered no explanation. In this region, tortuosity increased due to the oxidation of straighter outer layers, which left behind a less-ordered core. Fringe separation distance was seen to fluctuate throughout the flame, for which several reasons were given, none as convincing to the present author as simple statistical variation.

In addition to measuring at different flame locations, Botero et al. [215] analyzed fringe structure at various radial locations within the primary particles. Once nascent particles had begun to coalesce and show surface growth, fringe length consistently increased and tortuosity decreased with radial location, indicating graphitization as the soot matured, even as oxidation began to dominate. Near the tip

of the flame, oxidation was concentrated on the particle surface. Fringe length and fringe stacking decreased, and fringe separation distance increased, but this was predominantly limited to the outer shell of the primary particles. Near the core, a slight decrease in tortuosity and increase in fringe stacking was observable, which the authors interpreted as evidence of heat-induced graphitization. Interestingly, elsewhere in the flame, the authors found that the nanostructure in the core changed very little, suggesting molecular immobility in this region.

## Chapter 3: Experimental Methods

### 3.1 Ternary Flame System

Measurements were performed in the ternary flame system shown in Fig. 3.1. Here, a column of soot generated by a propylene/air co-flowing diffusion flame, passes through the center of a ring burner supporting a hydrogen diffusion flame. The hydrogen flame supplies heat and oxidizing species to the soot column, producing a soot flame. This configuration enables soot oxidation, occurring within the soot flame, to be observed in a diffusion flame environment in a region far separated from competing soot formation processes.

The soot-generating propylene/air laminar diffusion flame was produced using a Santoro-style co-flow burner [94], consisting of concentric brass tubes with inner diameters of 14 and 101.6 mm. Propylene

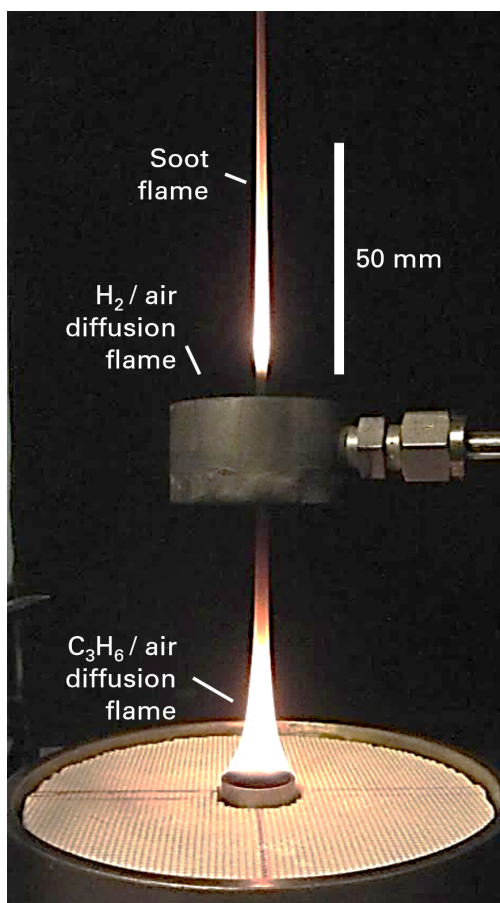


Figure 3.1: Ternary flame system.

(99.5% purity) flowed through the inner tube at 2.1 mg/s surrounded by a 1.18 g/s co-flow of air. Plug flow for the co-flowing air was achieved by injecting the air into the bottom of the outer brass tube where it flowed past 3 mm glass beads followed by a ceramic honeycomb with 1.5 mm square cells. The surface of the honeycomb sat 4 mm below the top of fuel port. The vertical column of soot produced by the co-flow flame was axisymmetric with a luminous length of  $\sim 50$  mm.

A brass ring burner with inner and outer diameter of 10.2 mm and 38.1 mm, and a height of 20.8 mm was centered over the soot column with its top face positioned 80 mm above the co-flow fuel port. Hydrogen (99.9995% purity) flowed at 1.48 mg/s into the ring burner plenum and exited through 41 jets measuring 0.41 mm in diameter encircling the ring center at a radius of 7.6 mm. As the soot column passed through the center of the ring burner and into the H<sub>2</sub> flame, it ignited, producing a soot flame that was steady, optically thin, and axisymmetric. The flow of gases supplied to the flame system were each controlled with a pressure regulator and need valve, and were measured with rotameters calibrated with a soap bubble meter. Additional details of the ternary flame system can be found in the dissertation work of Guo [224], and in work published by this group in [225].

Temperature measurements using a K-type thermocouple on the flame axis at the ring burner entrance were below 300°C, indicating that at this height, most of the gaseous products of the propylene flame had been diffusively replaced by N<sub>2</sub> and O<sub>2</sub>. This means that very few carbonaceous gas species were carried to the soot flame to that would otherwise have contributed to soot formation. Observations and measurements to characterize soot oxidation were performed in the soot flame,

which had a luminous length of  $\sim 70$  mm. The diameter of the soot flame ranged between 1 – 4 mm, narrowing as height above the ring burner increased. The open accessibility of the soot flame facilitated optical diagnostics and soot and gas sampling.

### 3.2 Axial Flame Velocity Measurement

Given the narrow width of the soot flame (1 - 4 mm), velocities were assumed to be radially uniform. It was also expected that the soot particles would follow the local gas velocities which are high enough to dominate over any thermophoresis effects in the axial direction.

The axial velocity of the flame was determined by using high frame rate video to track a brief disruption to the soot column as it traveled upward. To create a consistent, minimally obtrusive, but trackable perturbation, a device was constructed which quickly swung a small steel rod with a wedge-shaped profile ( $0.6 \times 3$  mm) through the upward-traveling soot column. The motion of the steel rod was actuated by a solenoid piston connected to a 4-bar linkage (See Fig. 3.2), and interrupted the column for  $\sim 2$  ms at a location 35 mm above the propylene fuel port. The resulting disturbance to the flame was recorded with video (Casio EX-FH100) at 420 frames per second with a 0.45 mm spatial resolution.

Flame velocity was determined by tracking the axial location of the point of minimum pixel intensity along the centerline of the soot flame. Video analysis was facilitated by a program developed in MATLAB and is depicted in Fig. 3.3. Video

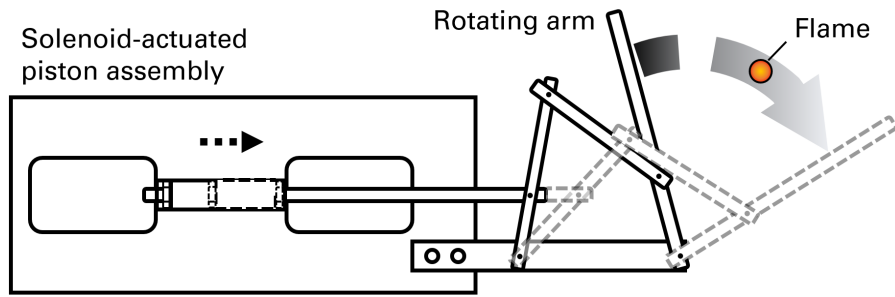


Figure 3.2: Soot column disruption apparatus for velocity measurement.

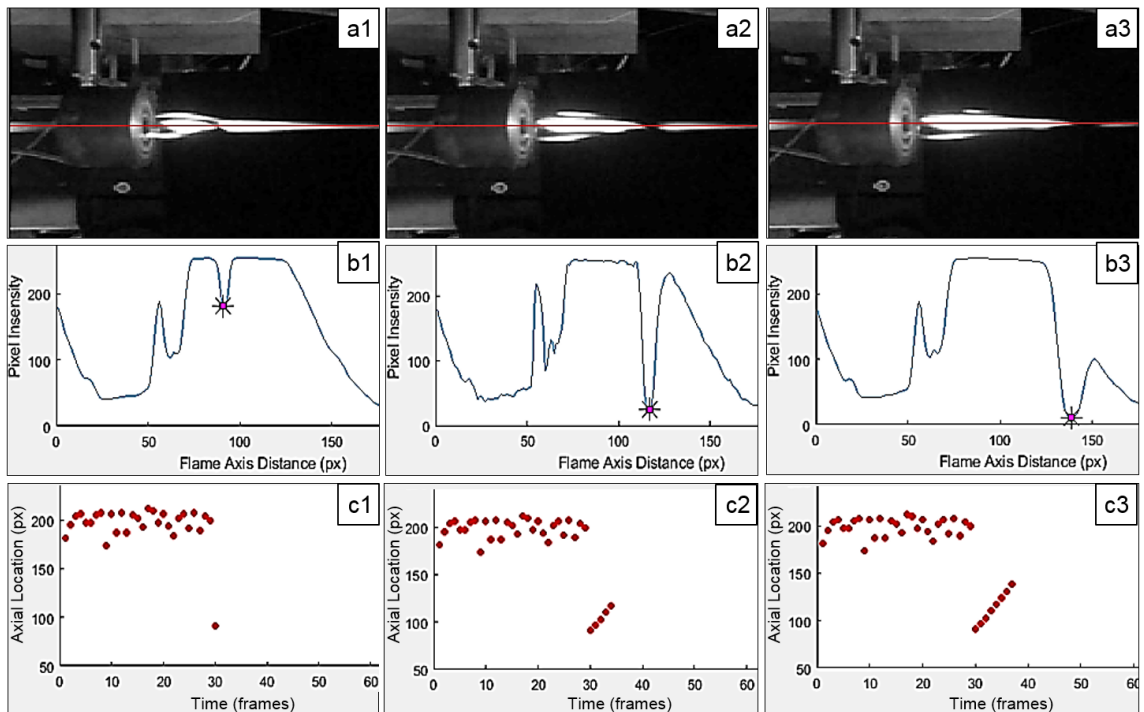


Figure 3.3: Velocity measurement video analysis method. (a1-a3) A perturbation to the soot flame is seen as a gap in the luminous soot traveling axially. (b1-b3) The perturbation, identified as the local minimum intensity along the soot flame centerline, is tracked in each frame. (c1-c3) The evolving plot of axial location of local minimum vs. time measured in frames.

was first converted from the RGB color format into 8-bit grayscale. The centerline of the soot flame was detected as the column of pixels oriented parallel to the flame axis with the maximum overall pixel intensity (Fig. 3.3 a1-a3). Gaussian smoothing was applied to the centerline intensities using a 5 pixel window to eliminate noise. Intensities along the centerline were displayed as a plot of intensity vs. axial height above burner. Upon detection of a disturbance to the flame, the program tracked the axial location of the point of minimum intensity along the smoothed centerline above the ring burner as it moved from one frame to the next (Fig. 3.3 b1-b3). The axial location of the local minimum was plotted against time (Fig. 3.3 c1-c3), to which a polynomial line was fit. First, 2nd, and 3rd order polynomial fits were considered. An expression for axial velocity vs. height above burner was then determined by taking the 1st derivative of the fitted lines.

### 3.3 Temperature, Soot Volume Fraction, and Gas Species Measurements

Measurements within the soot flame of temperature, soot volume fraction, and gas species concentrations were reported in detail in the dissertation of Guo [224]. The essential aspects of the methods used and additional details relevant to the present study are provided here.

### 3.3.1 Soot Flame Temperature

Temperatures in the soot flame were measured using ratio pyrometry as described by Guo et al. [226]. Images of the soot flame were obtained at wavelengths of 450, 650, and 900 nm using a modified Nikon D700 camera in combination with three bandpass filters. The camera was modified by removing both the infrared cut filter to reach the 900 nm wavelength, and the anti-aliasing filter to improve focus. Spatial resolution in the object plane was 21  $\mu\text{m}$ . The camera was calibrated using a blackbody furnace (Oriel 67032) at temperatures ranging 900 – 1200 °C, yielding a calibration constant,  $C_\lambda$ , for each bandpass filter. The line-of-sight images of the axisymmetric soot flame were averaged across the flame axis, and then processed by Abel deconvolution yielding radial grayscale intensities,  $GS$  at each wavelength. The local soot temperature,  $T$ , was then measured from each pairwise combination of wavelength filters (denoted here by subscripts 1 and 2), using:

$$T = \frac{hc(1/\lambda_1 - 1/\lambda_2)}{k_B \ln(C_{\lambda_1} GS_1 / C_{\lambda_2} GS_2)} \quad (3.1)$$

where  $c$  is the speed of light,  $h$  is Planck's constant,  $k_B$  is the Boltzmann constant, and  $\lambda$  is each filter's central wavelength. The soot temperature was assumed to be equal to the local gas temperature, which is reasonable for soot primary particle diameters within the typical 20 - 50 nm range [227]. Local temperatures were taken as the average of the three temperatures obtained from each line pair. The difference between the average temperature and any of the line pairs was lower than 50 K. Temperatures obtained using the ratio pyrometry method outlined here are

estimated to have an uncertainty of  $\pm 50$  K [226].

### 3.3.2 Soot Volume Fraction

Soot volume fraction was measured using the laser extinction method of Guo et al. [226], who validated the method against a well-studied reference flame. A schematic of the laser extinction system is given in Fig. 3.4. The beam from a 7 mW He-Ne laser (Melles Griot 25LHR171) at a 632.8 nm wavelength expands through a stationary diffuser (Thorlabs DG20-220), and then a vibrating diffuser (Thorlabs DG20-600) to reduce speckling. An off-axis parabolic mirror collimates the beam to 100 mm before it passes through the soot flame. After the flame, a filter (Andover ANDV12564) retains only light at the laser wavelength, the beam is decollimated, attenuated to avoid camera saturation, and sent through a pinhole to remove off-axis light. The camera, which is the same as that used for temperature measurements, was focused on the soot flame’s object plane and had a spatial resolution of  $34 \mu\text{m}$ . Abel deconvolution can be used to convert the line-of-site images of the laser, whose attenuation follows the Beer-Lambert law, to local radial soot volume fractions,  $f_s(r)$  [228]. Since radial soot transport was observed to be non-negligible in the soot flame, the sectional integrated soot volume fraction,  $F_s$ , defined as  $F_s = \int_0^\infty 2\pi r f_s(r) dr$  at each height, was used instead of the centerline soot volume fraction ( $f_s$ ). Fortunately,  $F_s$  can also be calculated directly from the line-of-site laser images, thereby avoiding noise introduced by deconvolution, using:

$$F_s = \frac{\lambda \int_{-R}^R \ln[GS^\circ(x)/GS(x)] dx}{K_e} \quad (3.2)$$

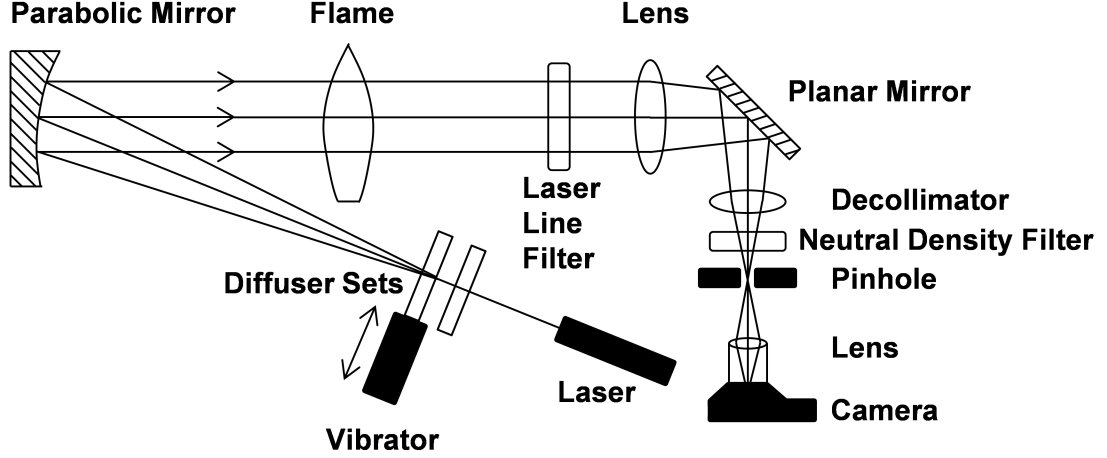


Figure 3.4: Schematic of the laser extinction system. Image taken from Ref [226].

Here  $\lambda$  is the laser wavelength,  $R$  is the soot flame radius,  $x$  is the horizontal coordinate in the object plane, and  $GS(x)$  is the line-of-site grayscale images divided by the camera shutter time. The superscript ( $^{\circ}$ ) denotes the reference image (i.e. the “flame off, laser on” image) which was approximated by linearly interpolating the grayscales of the soot free regions in the “flame on, laser on” image. The denominator in Eq. 3.2 is the volumetric dimensionless extinction coefficient, which can be represented as:

$$K_e = 6\pi E(m)(1 + \rho_{sa}) \quad (3.3)$$

where  $E(m)$  is the refractive index absorption function and  $\rho_{sa}$  is the ratio of scattering-to-absorption cross section [79, 229]. In modeling the extinction of light by soot, primary particles are commonly thought of as independent absorbers, for which scattering effects are negligible [230–232]. Hence, a value of  $\rho_{sa} = 0$ , was adopted for the present work. Soot was assumed to have a refractive index of

$m = 1.57 - 0.56i$  [233], which corresponds to  $E(m) = 0.26$  [81]. For the laser wavelength  $\lambda = 632.8$  nm, soot primary particles are significantly smaller ( $d_p \approx 30$  nm) than the Rayleigh limit ( $\pi d_p / \lambda < 0.3$ ) [234]. Therefore, both temperature and soot volume fraction calculations assume soot satisfies the Rayleigh scattering approximation. Uncertainties of  $\pm 5\%$  (95% confidence) are expected for values of  $F_s > 3 \times 10^{-5}$  mm<sup>2</sup>, and  $\pm 10\%$  otherwise.

### 3.3.3 Major Species Concentrations

Concentrations of the gases H<sub>2</sub>, O<sub>2</sub>, N<sub>2</sub>, CO, CO<sub>2</sub>, were measured in the soot flame using gas chromatography while concentrations of H<sub>2</sub>O were measured by desiccant gravimetry. Gas was sampled isokinetically at various axial locations within the flame using a radiatively cooled stainless steel probe with a 2.1 mm diameter, in a manner similar to Refs. [136, 137, 235]. The probe was connected to a vacuum pump regulated by a rotameter, and the flow rate required for isokinetic conditions was determined from the local measured temperature (Sec. 3.3.1) and flow velocity (Sec. 3.2).

Water concentration was determined by passing soot-filtered flame gases through a water-cooled stainless steel trap filled with Drierite desiccant, and then measuring the increase in water trap weight. For other stable species, filtered gases were drawn into a gas chromatograph (GC) (Hewlett-Packard 5890) with a thermal conductivity detector. Helium was used as the carrier gas for N<sub>2</sub>, O<sub>2</sub>, CO<sub>2</sub>, and CO, while argon was used as the carrier gas for H<sub>2</sub>, because helium and hydrogen have similar

thermal conductivities. The relative concentration of each gaseous compound was calculated by first calibrating the GC with different volumes of known gas mixtures. All concentration uncertainties were estimated at  $\pm 10\%$ .

### 3.3.4 Estimation of OH Radical Concentrations

For the purposes of analyzing the chemical kinetics of soot oxidation, radical concentrations were estimated based on an assumption of full equilibrium. This choice was prompted by two major considerations. First, it has been shown that diffusion flames approach full equilibrium in fuel lean regions, and the soot flame studied here is fuel lean at all heights [224]. Second, the presence of soot has been shown to reduce hydroxyl concentrations from superequilibrium by serving as a sink for the radical pool [69]. Using the measured temperatures and major species concentrations as inputs, concentrations of the radicals O, H, and OH were calculated using the equilibrium solver in CHEMKIN [236], assuming constant pressure and enthalpy. The thermodynamic properties of each species were taken from the default thermodynamic database in CHEMKIN Ver. 4.0.

## 3.4 Thermophoretic Sampling of Flame Soot

A schematic of the apparatus constructed for thermophoretic sampling is shown in Fig. 3.5 A double-acting pneumatic cylinder with a 7.9 mm (5/16 inch) bore and 7.62 cm (3 inch) stroke (Bimba 0073-DXP) was connected to 5-port solenoid-actuated control valve (Motion Industries LTV-115DD) with 60 psi sup-

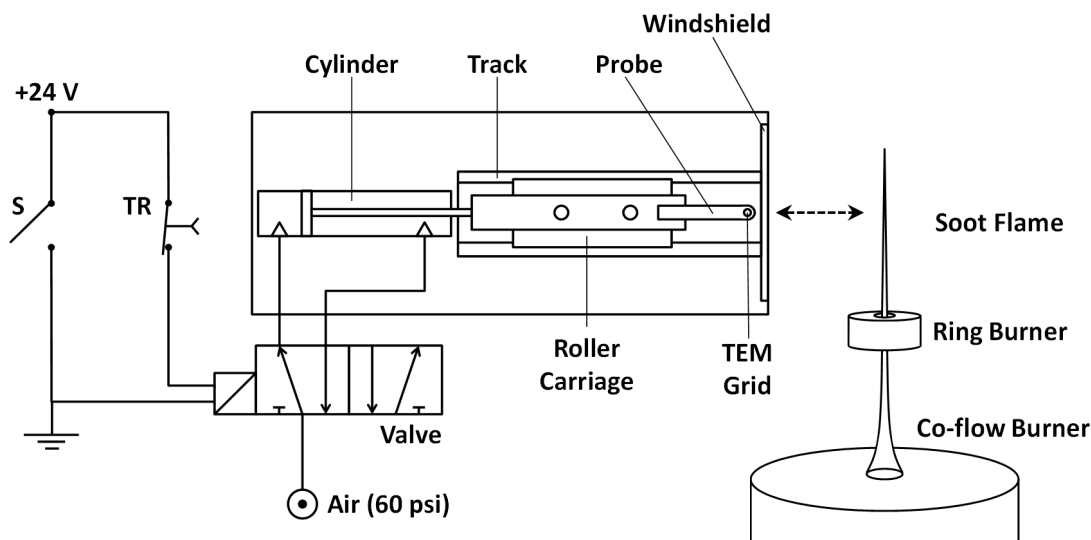


Figure 3.5: Pneumatic and electrical schematic of the thermophoretic soot sampling apparatus. (TR) is a normally-closed, timed-open relay, and (S) is a manual switch.

ply air. The control valve was switched by a normally-closed, timed-open relay (SSAC TRDU24A3), set to a time delay of 0.1 s. The cylinder piston was connected to a roller carriage ( $8.26 \times 3.18$  cm), shuttling it along a track while carrying the thermophoretic sampling probe to the flame. The brass probe measured  $53 \times 5 \times 0.65$  mm and had a rounded tip. The entire assembly was mounted to an aluminum plate with a stainless steel wind shield mounted on the end nearest the flame.

All soot sampled from the soot flame was collected on a 200 mesh copper grid with a lacey carbon support film (Electron Microscopy Sciences LC200-Cu). Attachment of the TEM grid to the probe was done by laying the grid flat against the probe's surface at its rounded end, and then applying a very small amount of rubber cement onto the edge of the grid farthest from the probe tip. Upon actuation, the roller carriage travels a distance of 7.62 cm along the track, inserting the TEM grid directly into the soot flame, and then retracting. The probe dwells a total of

about 90 ms in the flame. Soot samples were obtained within the soot flame at 10 different heights above the ring burner: 10, 13, 15, 20, 25, 30, 35, 40, 45, and 50 mm.

### 3.5 TEM Measurements

Soot images were obtained on a JEOL-2100 LaB<sub>6</sub> transmission electron microscope at the University of Maryland NanoCenter's AIMLab. For all measurements, the TEM was operated with an electron beam accelerating voltage of 200 kV. Coordinates on the TEM grid plane to be considered for analysis were randomly generated using MATLAB prior to imaging with the TEM. The coordinate generating program was constrained to produce equal numbers of coordinates in each grid quadrant. Imaging was only considered at regions centered at these coordinates. If no soot aggregates were present at the specified location, analysis simply continued with the next randomly generated coordinate. If soot was present, no attempt was made to center the viewing window on any particular image element. Both bright field and diffraction pattern images in the TEM were calibrated against a gold diffraction grating replica (Ted Pella, part no. 607). The standard uncertainty of the length scale was estimated to be 0.8% at magnifications between 2,000 and 200,000, and 0.2% at higher magnifications. Images were obtained with an Orius SC1000A1 CCD camera using Gatan Digital Micrograph V3.22 software and saved as 8-bit .tif files.

### 3.5.1 Aerosol Image Analyzer Program

The extensive use of TEM methods in the present work made the choice of software for quantitative image analysis critical. The NIH software ImageJ is commonly used and freely available [237]. Gatan Digital Micrograph is also widely used, especially in diffraction pattern analysis. Ultimately, these off-the-shelf softwares were found to be lacking for the unique and heavily quantitative needs of the present study. Instead, a custom software, named Aerosol Image Analyzer (AIA), was developed by the author using MATLAB. This choice was made based on MATLAB's extensive image processing functions and the author's long experience with the platform.

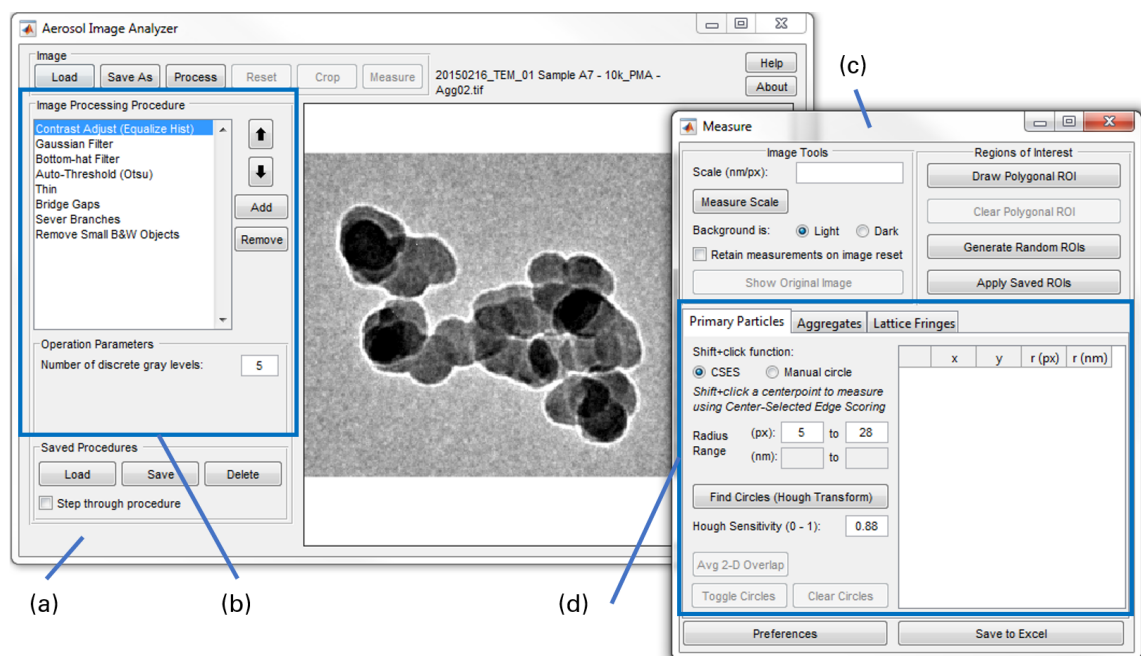


Figure 3.6: Aerosol Image Analyzer GUI. (a) Image viewing and processing GUI. (b) User-defined image processing procedure. (c) Measurements GUI. (d) Tabs for switching between measurement of primary particles, aggregates, and lattice fringes.

The graphical user interface (GUI) of the AIA program can be broken into two components: a image viewing and processing GUI, and a GUI for performing measurements. These components are shown in Fig. 3.6. In the image viewing and processing GUI (Fig. 3.6a) the user can perform typical file management functions (open, save, etc.), and can interact with the image in customary ways (pan, zoom, crop). The interface is designed to support the rapid creation and testing of complex image processing procedures, allowing the user to converge on an optimal set of image processing steps to achieve a consistent result (Fig. 3.6b). The user may select from 33 common image processing operations native to MATLAB along with 3 custom functions (detailed in Sec. 3.5.7). Individual parameters for each image processing operation can be changed directly within the GUI, and operations can be quickly added, removed, and re-ordered. When running the procedure, the user can elect to step through and see the effects of each operation, or simply run the procedure to completion. Procedures can be named and saved for use in future sessions.

The measurements GUI (Fig. 3.6c) contains a number of utilities, such as the ability to easily specify the image resolution by clicking the image scale bar, creating regions of interest that can be saved with the image, and changing program default settings. Other features include auto-detection of image polarity (i.e. whether the image foreground is light or dark with respect to the background), and the ability to toggle between original and processed images while holding measurements on-screen. The controls for measuring aggregates, primary particles, and lattice fringes are split into three tabs (Fig. 3.6d). Measurement results are displayed in tables

embedded within each tab and can be directly exported to Excel. The controls also allow measurements on the image to be individually or collectively displayed, hidden, or deleted. Past measurements of primary particles that have been saved elsewhere (as in Excel) can even be re-displayed on the current image by copying and pasting the past measurements into the embedded table.

## 3.5.2 Primary Particle Measurement

### 3.5.2.1 Measurement Bias Controls

The primary particle size distribution (PPSD) was measured from TEM images obtained at each sampled location within the soot flame. At least 20 images were obtained at each flame location and magnifications ranged between 6,000 and 60,000. To avoid image selection bias, 10 images were randomly drawn from each image set. To mitigate bias in selecting which primary particles to measure, the AIA program generated 5 randomly placed  $140 \times 140$  nm regions of interest (ROIs) on each image. The operator then measured every element within each ROI that could be reasonably deemed a primary particle using a semi-automated algorithm called center-selected edge scoring (CSES) which is detailed in Sec. 3.5.2.2. If not satisfied with the algorithm's output, the operator could reject it and remeasure with CSES by selecting a different pixel and/or restricting the diameter range. Alternatively, the operator could remeasure the primary particle manually by drawing the desired circle on the image.

This measurement procedure has several benefits. First, the semi-automation

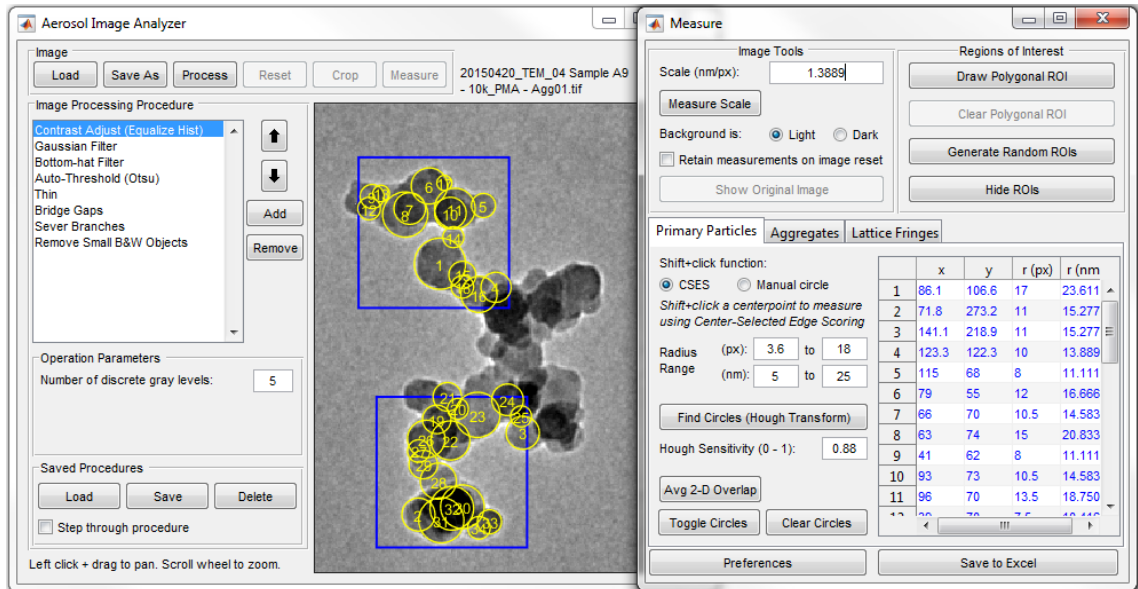


Figure 3.7: Screenshot of the Aerosol Image Analyzer program showing primary particles measured using the CSES algorithm within randomly generated ROIs.

speeds up the measurement process fivefold, as will be shown in following section. In addition, it is expected to reduce bias since it quantifies image features uniformly. At the same time, the operator’s best judgment is retained since the semi-automated results may be overridden. Figure 3.7 shows a typical soot aggregate, whose primary particles have been measured using the CSES algorithm within random ROIs.

### 3.5.2.2 Center-Selected Edge Scoring (CSES) Algorithm

Existing attempts at automating or semi-automating primary particle size measurement generally rely on Circular Hough Transform (CHT) or Euclidean distance mapping (EDM) algorithms as discussed in Sec. 2.2.2.3. As will be shown in Sec. 4.3.2, the available automation algorithms found in the literature do not accurately assess PPSD. In addition, they are incapable of measuring overlap among

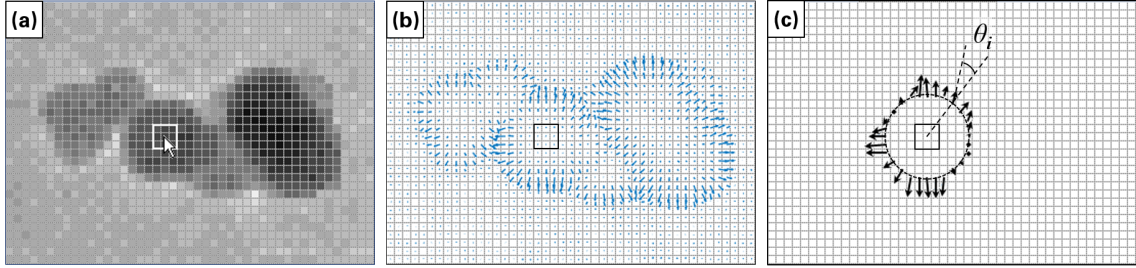


Figure 3.8: Steps in the CSES algorithm. A low magnification image is shown to clearly illustrate individual pixels. (a) Pixels of candidate center points around an operator-selected pixel. (b) Grayscale intensity gradient map with vectors denoting gradients. (c) The magnitude and orientation (shown by vectors) of the gradient of a candidate circle’s edge pixels.

primary particles.

One of the reasons that both CHT and EDM algorithms have performed poorly, is because they rely on detectable edges in an image to infer circular features. By contrast, center-selected edge scoring (CSES) begins from an estimate of a primary particle’s center point, and then, like a manual operator, considers image features over the entire circumference of a primary particle, not just those parts detectable as “edges.” Figure 3.8 outlines this process. The operator manually selects a point on the image that is judged to be the center of a primary particle. A square neighborhood of pixels around the selected point is calculated (Fig. 3.8a). Candidates for a best-fit circle are those within an operator-specified diameter range,  $d_{p,\min}$  to  $d_{p,\max}$ , centered at any pixel within this neighborhood. A neighborhood measuring  $1 + 2[\text{round}(0.025d_{p,\max} + 1)]$  on a side was found to match operators’ intuitive expectations for candidate center point tolerance. Using a  $3 \times 3$  Sobel filter, the algorithm computes a gradient map of the grayscale intensity at each image pixel (Fig. 3.8b). For each candidate circle, all pixels in the gradient map are eliminated

except those that comprise the candidate circle’s circumference (Fig. 3.8c). The fit of each circle is scored using the magnitude of the image intensity gradient,  $|G_i|$ , at each pixel  $i$ , and the difference in its gradient orientation from that of a perfectly circular primary particle,  $\theta_i$  according to:

$$\text{Score} = \frac{1}{N_{px}} \sum_{i=1}^{N_{px}} |G_i| \cos \theta_i \quad (3.4)$$

where  $N_{px}$  is the number of circumference pixels. The best-fit circle is chosen as that with the greatest score, according to Eq. 3.4. The CSES code is provided in Appendix A.1. Though developed using soot TEM images, the CSES algorithm has application to any aerosol that is spheroidal or comprised of spheroidal primary particles.

CSES also has the feature of being substantially faster than the traditional primary particle measurement. The time per primary particle needed to perform measurements using CSES was compared to a manual measurement on the same images in ImageJ. Twice measuring 100 primary particles on two randomly selected image sets, CSES was found to require a little less than 20% of the operator time required by manual measurement. This improvement comes from the fact that a pixel can be selected at a perceived center point much more quickly than a circle can be drawn to fit a perceived circumference.

### 3.5.2.3 Primary Particle Overlap

The partial sintering of primary particles reduces the overall volume and surface area of a soot population relative to the single-point-contact primary particle

model. Partial sintering is measured as overlap of adjacent primary particles in a 2-dimensional TEM image as described in Sec. 2.2.2.2. Once all the primary particles on a TEM image have been measured as outlined in Sec. 3.5.2.2, the AIA program evaluates each pair of primary particles on the 2D image. Particles are deemed overlapping if the distance between their two centerpoints is less than their combined radii. The projected overlap coefficient,  $C_{ov,p}$  is then calculated for each overlapping pair per Eq. 2.8.

### 3.5.3 Soot Surface Area

Soot surface area derived from the TEM images is calculated in terms of the volume specific surface area (VSSA). Ignoring the effect of overlap for the moment, the surface area of a population of  $N_p$  spherical primary particles in single point contact is:

$$S^\circ = N_p \pi d_{ps}^2 \quad (3.5)$$

where  $d_{ps}$  is the diameter of average surface area. Similarly, the population's volume can be expressed in terms of the diameter of average volume,  $d_{pV}$ :

$$V^\circ = \frac{N_p \pi d_{pV}^3}{6} \quad (3.6)$$

Combining Eq. 3.5 and 3.6 the volume specific surface area for a polydisperse population of primary particles in single point contact,  $S_V^\circ$ , can be expressed as:

$$S_V^\circ = \frac{6d_{ps}^2}{d_{pV}^3} \quad (3.7)$$

Determination of  $d_{ps}$  and  $d_{pV}$  will be discussed momentarily, however, they need not be calculated if the assumption of monodisperse primary particles is applied. In this

case Eq. 3.7 simply reduces to:

$$S_{V,\text{mono}}^{\circ} = 6/\overline{d_p} \quad (3.8)$$

A more thoroughgoing VSSA model takes both polydispersity and overlap of primary particles into consideration. The factors  $F_S$  and  $F_V$  are introduced to respectively account for surface area and volume lost to primary particle overlap. They may be combined into a single VSSA overlap factor,  $F_{ov}$ :

$$F_{ov} = F_S/F_V \quad (3.9)$$

Now the VSSA can be expressed as:

$$S_V = \frac{6F_{ov}d_{ps}^2}{d_{pv}^3} \quad (3.10)$$

If one assumes the distribution of  $d_p$  to be either normal or lognormal, expressions for  $d_{ps}$  and  $d_{pv}$  are readily obtained from the second and third moments of the distribution [117, 141, 142, 238–241]. However, while a lognormal size distribution for soot aggregates is generally a safe assumption [141, 241], primary particles have been observed with distributions of varying levels of symmetry and modality [18, 22, 97, 115, 118, 119, 127, 130, 133, 134, 138–140, 242, 243]. It would be valuable, therefore, to have expressions for  $d_{ps}$  and  $d_{pv}$  that hold regardless of the distribution. Such expressions may be derived from the so-called central moments (or moments about the mean) of the distribution. The general equation for the  $i^{\text{th}}$  central moment  $CM_i$ , of a continuous distribution of variable  $x$ , with probability density function  $f(x)$  and mean value  $\mu$  is:

$$CM_i = \int_{-\infty}^{\infty} (x - \mu)^i f(x) dx \quad (3.11)$$

The second central moment corresponds to the variance  $\sigma^2$ , of the distribution, while the third central moment is equal to the skewness of the distribution  $\gamma$ , multiplied by the cube of its standard deviation. For a sample population of primary particles with mean diameter  $\overline{d}_p$  and standard deviation  $s_{d_p}$ , the diameter of average surface area is found by:

$$d_{pS} = (s_{d_p}^2 + \overline{d}_p^2)^{1/2} \quad (3.12)$$

The diameter of average volume incorporates the skewness of the sampled population of primary particles,  $\gamma_{d_p}$ , and is given by the expression

$$d_{pV} = (\gamma_{d_p} s_{d_p}^3 + 3\overline{d}_p s_{d_p}^2 + \overline{d}_p^3)^{1/3} \quad (3.13)$$

The summary variables  $d_{pS}$  and  $d_{pV}$  are now defined in terms of known statistical parameters. Surprisingly, while expressions for  $d_{pV}$  are available in the literature for known distributions as mentioned above, the author has yet to encounter the distribution-agnostic Eq. 3.13. Hence, its derivation, along with that for  $d_{pS}$ , is presented in Appendix B.1.

At this point, the only remaining values needed for calculating the VSSA are  $F_S$  and  $F_V$ . One approach would be to assume that the volume lost to primary particle overlap is negligible, and then estimate the lost surface area factor from the coefficient of Eq. 2.10. Together these are:

$$F_S = 1 - \phi_s C_{ov} \quad (3.14a)$$

$$F_V = 1 \quad (3.14b)$$

where  $\phi_s = 1.3$  [114]. Note that unlike Eq. 2.10, the number of primary particles

in an aggregate,  $N_{p,a}$ , is not present in this expression for  $F_S$  because specific surface area at the population level rather than at the aggregate level is of interest. This approach has been taken by several researchers [89, 124], however there are drawbacks. For one, this expression for  $F_S$  comes from a simulation of aggregates comprised of monodisperse primary particles; the effect of polydispersity has never been investigated. Second, Eq. 3.14 assumes only surface area loss, however, volume lost to partial sintering may not be negligible.

To overcome many of these drawbacks, a methodology that accommodates a polydisperse primary particle population was developed for the present work. The approach begins by estimating the true 3D overlap,  $C_{ov}$ , from the 2D TEM image using the linear function  $C_{ov} = \zeta_1 \overline{C_{ov,p}} - \zeta_2$ , which was introduced earlier as Eq. 2.9. The values of  $\zeta_1 = 1.27 \pm 0.01$  and  $\zeta_2 = 0.27 \pm 0.01$  from Wozniak et al. [121] were chosen for the present study. The negative intercept of Eq. 2.9 reflects the fact that some of the overlap observed in the 2D image is due to shadowing by out-of-plane primary particles rather than to a true material overlap. In other words, a positive mean value of  $C_{ov,p}$  will be measured on a TEM image even at the limit of  $C_{ov} = 0$ . Hence, Eq. 2.9 is necessarily a population-averaged expression and cannot be applied to individual primary particle pairs, as doing so would lead to a non-physical, negative overlap for small values of  $C_{ov,p}$ . Therefore, the values of  $C_{ov,p}$ , obtained according to Sec. 3.5.2.3, are averaged to give  $\overline{C_{ov,p}}$  and then supplied to Eq. 2.9, yielding a global  $C_{ov}$  for the sample.

Using this sample-averaged  $C_{ov}$ , the lost surface area and volume can be calculated in terms of the size of the spherical cap consumed by the partial merger of

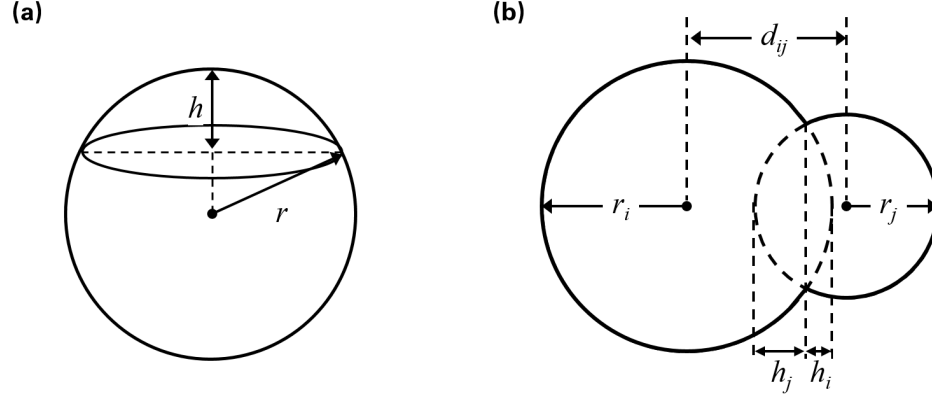


Figure 3.9: (a) Spherical cap (b) Overlapping primary particles of different sizes.

each overlapping pair. For a sphere of radius  $r$ , the surface area and volume of a spherical cap of height  $h$ , as depicted in Fig. 3.9a, are given respectively by:

$$S_{cap} = 2\pi r h \quad (3.15)$$

and

$$V_{cap} = \frac{1}{3}\pi h^2(3r - h) \quad (3.16)$$

To apply these relationships to overlapping primary particles, consider Fig. 3.9b. The spherical cap height  $h_i$  can be computed from the known terms  $r_i$ ,  $r_j$ , and  $C_{ov}$  according to:

$$h_i = \frac{C_{ov}^2(r_i + r_j) - 2r_j C_{ov}}{2(C_{ov} - 1)} \quad (3.17)$$

By swapping subscripts  $i$  and  $j$ , the value for  $h_j$  can be computed from the same expression, or from its relation to  $h_i$ :

$$h_j = C_{ov}(r_i + r_j) - h_i \quad (3.18)$$

Derivations of Eq. 3.17 and 3.18 are provided in Appendix B.2.

Combining Eq. 3.5 and 3.15,  $F_S$  can be calculated from:

$$F_S = 1 - \frac{2 \sum_{(i,j) \in I} (r_i h_i + r_j h_j)}{N_p d_{ps}^2} \quad (3.19a)$$

where  $I$  is the set of overlapping primary particle pairs. Similarly, by combining Eq. 3.6 and 3.16, an expression for  $F_V$  is obtained:

$$F_V = 1 - \frac{2 \sum_{(i,j) \in I} (h_i^2(3r_i - h_i) + h_j^2(3r_j - h_j))}{N_p d_{pv}^3} \quad (3.19b)$$

The approach embodied by Eqs. 3.15 - 3.19 is not without its limitations. For one, despite not relying on Eq. 3.14, which assumes monodisperse primary particles and aggregates with a 1.78 fractal dimension, it still depends on Eq. 2.9 to estimate  $C_{ov}$ , which is built on the very same assumptions. Additionally, the method shown here analyzes each overlapping pair in isolation. This does not take into consideration cases in which the overlapping region of multiple pairs occupy the same physical space. Such situations certainly exist in real aggregates, especially those with larger fractal dimensions (i.e. less chain-like). This simplification, therefore, would tend to overestimate the surface area and volume consumed by partially merged primary particles, resulting in a net effect of slightly underestimating the VSSA.

### 3.5.4 Soot Aggregate Morphology

At the scale of the aggregate, soot exhibits a mass fractal morphology, described by the power law relationship:  $N_{p,a} = k_f (R_g / \bar{r}_p)^{D_f}$ , which was introduced earlier as Eq. 2.3, and is sometimes termed the "fractal equation." This equation

relates the parameters most often used to quantify soot morphology: the number of primary particles in the aggregate,  $N_{p,a}$ , the radius of gyration,  $R_g$ , fractal dimension,  $D_f$ , and fractal pre-factor,  $k_f$ .

Formally identical to the fractal equation, Eq. 2.4,  $N_{p,a} = k_a(A_a/A_p)^\alpha$ , is used to extract  $N_{p,a}$  from the 2D TEM soot images. From a consideration of the reviewed literature (Sec. 2.2.1.2), the present analysis adopts the values of  $k_a = 1.15 \pm 0.04$  and  $\alpha = 1.09 \pm 0.36$ , from the work of Köylü et al. [90], which was found to be the most compelling. Likewise, for determination of  $R_g$  in the current study, the literature shows good evidence for the robustness of the expression  $R_g = L/2C$ , (Eq. 2.7), where  $C = 1.5 \pm 0.05$ .

At least 20 TEM images of soot aggregates were obtained at each sampled location within the soot flame. Magnifications ranged from 5,000 and 8,000. No fewer than 10 images were randomly selected from each image set for measurement. More images were chosen if 10 was insufficient to achieve a statistically significant number of aggregates (ideally  $> 250$ ). Soot deposition was so sparse on the TEM grid sampled at HAB = 50 mm that an insufficient number of aggregates could be imaged. Consequently, soot morphology was not analyzed at this flame location.

Before they can be measured, images of soot aggregates must first be binarized. This step is reasonably straight-forward if the image background is relatively homogeneous, as is the case with a TEM grid with a carbon film substrate. However, since carbon film interferes with HRTEM and SAED measurements, a lacey carbon substrate was used in the present study. Unfortunately, while a human operator can easily distinguish between a soot aggregate and a lacey carbon support, they

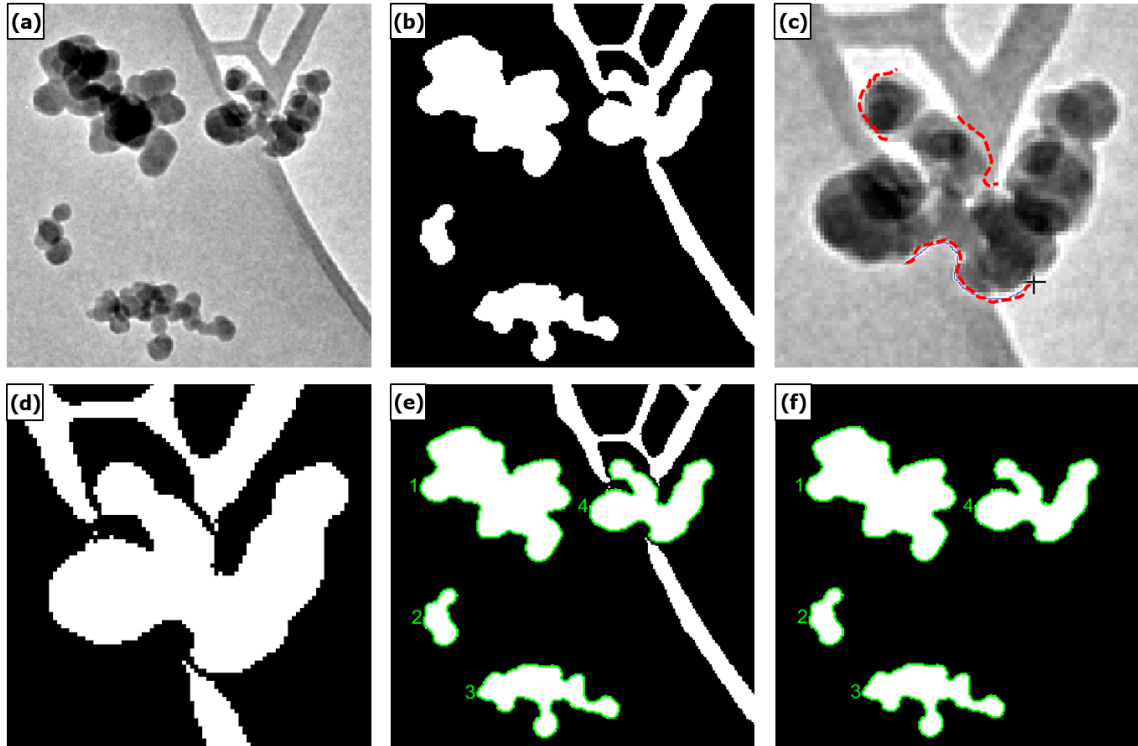


Figure 3.10: Procedure for creating binary images of soot aggregates. (a) Original TEM image. (b) Result of image background removal and binarization process. (c) Locations for aggregate - background separation are manually identified. (d) Result of manual separation of aggregate from background. (e) Measured aggregates. (f) Non-aggregate objects removed from image.

are virtually indistinguishable by background removal algorithms, especially near the dark edges of the carbon lace. To circumvent this difficulty, the AIA program was equipped with a tool that effectively allows the operator to manually snip the aggregate away from the carbon lace wherever this problem exists within the image.

The steps for producing binary images of discrete aggregates is illustrated in Fig. 3.10. Starting from the initial TEM image (Fig. 3.10a), a process is followed that removes as much of the image background as possible without deleting any portions of the aggregates themselves, and then performs image binarization (Fig. 3.10b).

Several methods for removing the background of TEM images have been suggested in the literature [134, 244], however the greatest success was achieved here using a general procedure of edge-preserved smoothing (e.g., median filtering), contrast enhancement followed by a rolling-ball transform, and lastly, manual thresholding. The size of the structural element used in the rolling ball transform and the manual thresholding level often had to be adjusted by trial and error to achieve optimal results. Even with optimized background removal, artifacts from the lacey carbon substrate were usually present in the binary image. The next step, therefore, was to cut away points of connection between aggregate and substrate. This was accomplished using the aforementioned manual cutting tool within the AIA program. The operator can mark the locations for the image cut on either the binary image or on the original image as shown in Fig. 3.10c. Once soot aggregates were adequately separated from non-aggregate objects (i.e. 8-pixel connectivity was severed), as in Fig. 3.10d, the operator could measure aggregates (Fig. 3.10e) and eliminate all non-aggregate objects in the image (Fig. 3.10f).

The AIA program performs the following measurements on each the binary aggregate object on the image resulting from the above procedure. The projected aggregate area,  $A_a$ , is simply determined from the number of pixels comprising the discrete binary object, and the maximum projected length,  $L$ , is calculated as the maximum Feret diameter. For comparison purposes, functions within the AIA program were also written to calculate the projected radius of gyration,  $R_{g,2D}$ , per Eq. 2.5, and the maximum width  $W$ , normal to  $L$ , for use in Eq. 2.6.

### 3.5.5 Soot Fragmentation

Soot fragmentation refers to the breakup of larger aggregates into smaller pieces. If this phenomenon is present within the soot flame, one should observe an increase in the overall number flow rate of aggregates as well as a decrease in the average number of primary particles per aggregate. Averaging the results of Eq. 2.4 across a large sample of TEM aggregate images will produce an estimate of the mean number of primary particles per aggregate,  $\overline{N_{p,a}}$ . If the size distribution of aggregates is lognormal, as is typical [241], the geometric mean number of primary particles in an aggregate,  $\overline{N_{pg,a}}$ , will be the statistic of interest.

Combining the sectional integrated soot volume fraction,  $F_s$ , and soot flame velocity,  $v_s$ , with the diameter of average primary particle volume found by Eq. 3.13, the total number flow rate of aggregates,  $\dot{N}_a$  can be calculated at any given height using:

$$\dot{N}_a = \frac{6v_s F_s}{\overline{N_{p,a}} F_V \pi d_{pV}^3} \quad (3.20)$$

Here  $F_V$  is the lost volume factor due to primary particle overlap, discussed in Sec. 3.5.3.

### 3.5.6 Selected Area Electron Diffraction

Soot aggregates considered for SAED analysis were identified at random locations on the TEM grid. For a chosen aggregate, a portion that was suspended away from the lacey carbon support structure was imaged at a magnification of 300,000. A 20 $\mu\text{m}$  diameter selected area aperture was inserted into the beam path, eliminat-

ing any possible diffraction signal from the amorphous lacey carbon film. To make comparisons of SAED measurements as meaningful as possible, similar volumes of soot were used to generate diffraction patterns from each sample. This was done by first centering the viewing window on a section of the aggregate in which primary particles were not stacked along the electron beam axis (i.e. at a location where the aggregate was only one primary particle thick). Additionally, the sample was also positioned such that soot occupied at least  $\sim 90\%$  of the area viewed through the aperture. Diffraction pattern images were captured over a 1 s exposure time at a scale of  $0.017036 \text{ nm}^{-1}/\text{px}$ .

For each diffraction pattern image (e.g. Fig 3.11a), the center point was determined using Digital Micrograph's Find Center tool, and a binary mask to exclude the beam blocker from image analysis (Fig. 3.11b) was generated using the PolyROI tool in the AIA program (Sec. 3.5.1). Quantitative analysis of the SAED images was performed using the following steps, which were executed using the MATLAB code given in Appendix A.2. Ignoring pixels covered by the beam blocker, the average intensity of the image as a function of radius was computed, producing a radial intensity profile (Fig. 3.11c). The profile was smoothed until two minima between the diffraction rings were identified. The first inflection point following the initial decay of the direct electron beam was chosen as starting location for diffraction analysis.

Labar [245] has observed that in the absence of amorphous material, the background signal of an SAED image will follow a lognormal curve. Hence, background illumination from the direct beam was first estimated by fitting a lognormal function to the background points, which were taken to be the first inflection point,

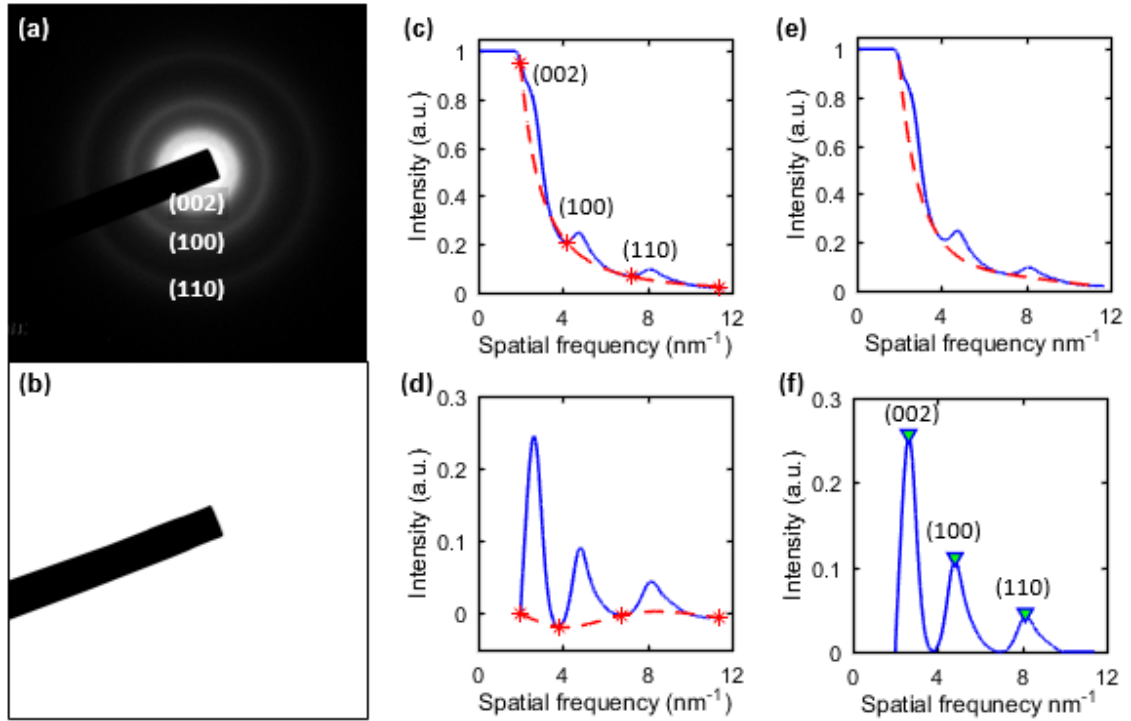


Figure 3.11: SAED image measurement process. (a) Original diffraction pattern image with lattice spacings identified by their Miller indices. (b) Beam blocker mask; only diffraction pattern pixels corresponding to white pixels on the mask are analyzed. (c) (—) Radially averaged diffraction pattern, (---) lognormal fit of the background signal, (\*) points used in lognormal curve fit. (d) (—) Diffraction peaks with first estimate of background removed, (---) spline fit to refine the background signal estimate, (\*) points used in the spline curve fit. (e) (—) Radially averaged diffraction pattern, (---) combined lognormal-spline fit of the background signal. (f) Final net diffraction peaks with noted locations of maxima ( $\blacktriangledown$ ).

the inter-ring minima, and the end point of the radial intensity profile (Fig. 3.11c).

The background estimate was subtracted from the original diffraction image and was then refined by fitting a spline curve to the local minima, inflection and end points on the net diffraction profile. (Fig. 3.11d). The lognormal and spline curves were combined into a final background estimate (Fig. 3.11e), which was subtracted from the original diffraction curve, leaving only the diffraction peaks produced by

the  $d_{002}$ ,  $d_{100}$ , and  $d_{110}$  lattice spacings. (Fig. 3.11f).

### 3.5.7 HRTEM Lattice Fringe Analysis

Capture of high resolution soot images was carried out using the general methodology outlined in Section 3.5. Images were obtained at magnifications of either 300,000 (0.0421 nm/px) or 400,000 (0.0307 nm/px). Each image was processed using a procedure that resulted in a binary image in which lattice fringes appeared as skeletonized segments. The procedure follows the general roadmap provided by Yehliu et al. [208] and Botero et al. [210], with some improved algorithms for connecting segments belonging to the same fringe and for breaking spurious fringe branches. The steps of the procedure are: ROI creation, contrast enhancement, Gaussian filtering, bottom-hat filtering, thresholding, skeletonization, fringe connection, branch severing, and removal of segments below a size threshold. The details of each step are given below. Once a skeletonized fringe image was obtained, analysis was performed yielding measurements of fringe length, tortuosity, inter-fringe separation distance, deviation from concentric orientation, and fringe radial location.

#### 3.5.7.1 HRTEM Image Processing Procedure

##### *ROI Creation*

In the first image processing step, a region of interest (ROI) was manually created by drawing a closed polygon (Fig. 3.12a) on the image using Aerosol Image

Analyzer's *Draw Polygonal ROI* tool. ROIs were drawn such that they encompassed only individual primary particles and excluded regions of overlap with neighboring primary particles. This was done because overlapping primaries tend to produce a complicated fringe pattern that is unrepresentative of either primary particle's fringe structure. In addition to restricting measurements to a desired region, creation of an ROI allows regions outside of it to be ignored, which quickens subsequent image processing steps and improves the results of operations relying on image statistics, such as contrast enhancement and thresholding.

#### *Contrast Enhancement*

Image contrast within the ROI was enhanced using the histogram equalization method and was implemented using MATLAB's *histeq* function. Histogram equalization enhances contrast by reducing an image's grayscale intensity histogram to a fewer number of discrete levels whose distribution is approximately flat. Experience found that a contrast-enhanced image containing only five discrete gray levels produced the best results. Figure 3.12 shows the grayscale histograms for the example image before and after contrast enhancement.

#### *Gaussian Filtering*

The next step, Gaussian low-pass filtering, removed high frequency noise from the image, and utilized the 2-D Gaussian filtering function *imgaussfilt* in MATLAB. The Gaussian filter is defined by two user-supplied parameters: The filter size is specified as an odd number of pixels and determines the size of the square Gaussian

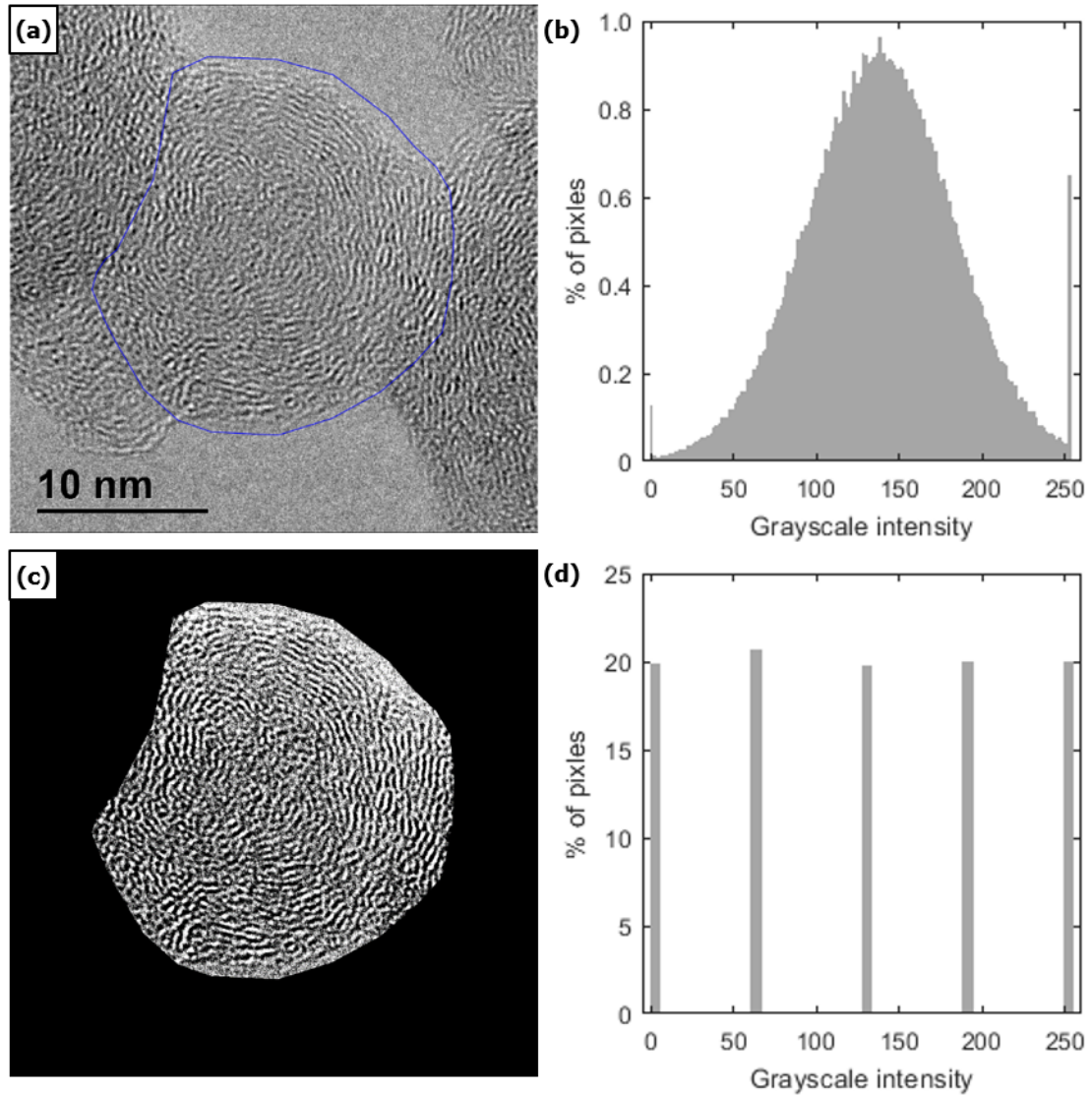


Figure 3.12: (a) Original image with user-drawn ROI. (b) Grayscale histogram of (a) (ROI only). (c) Fringe image after contrast enhancement. (d) Grayscale histogram of (c).

kernel, while the standard deviation effectively determines the cut-off frequency of the filter. Although the standard deviation is specified in the spatial domain, the filtering is performed in the frequency domain after Fourier transformation of the kernel. Best results were obtained with a filter sizes of 7 and 9 px for  $3 \times 10^5$  and

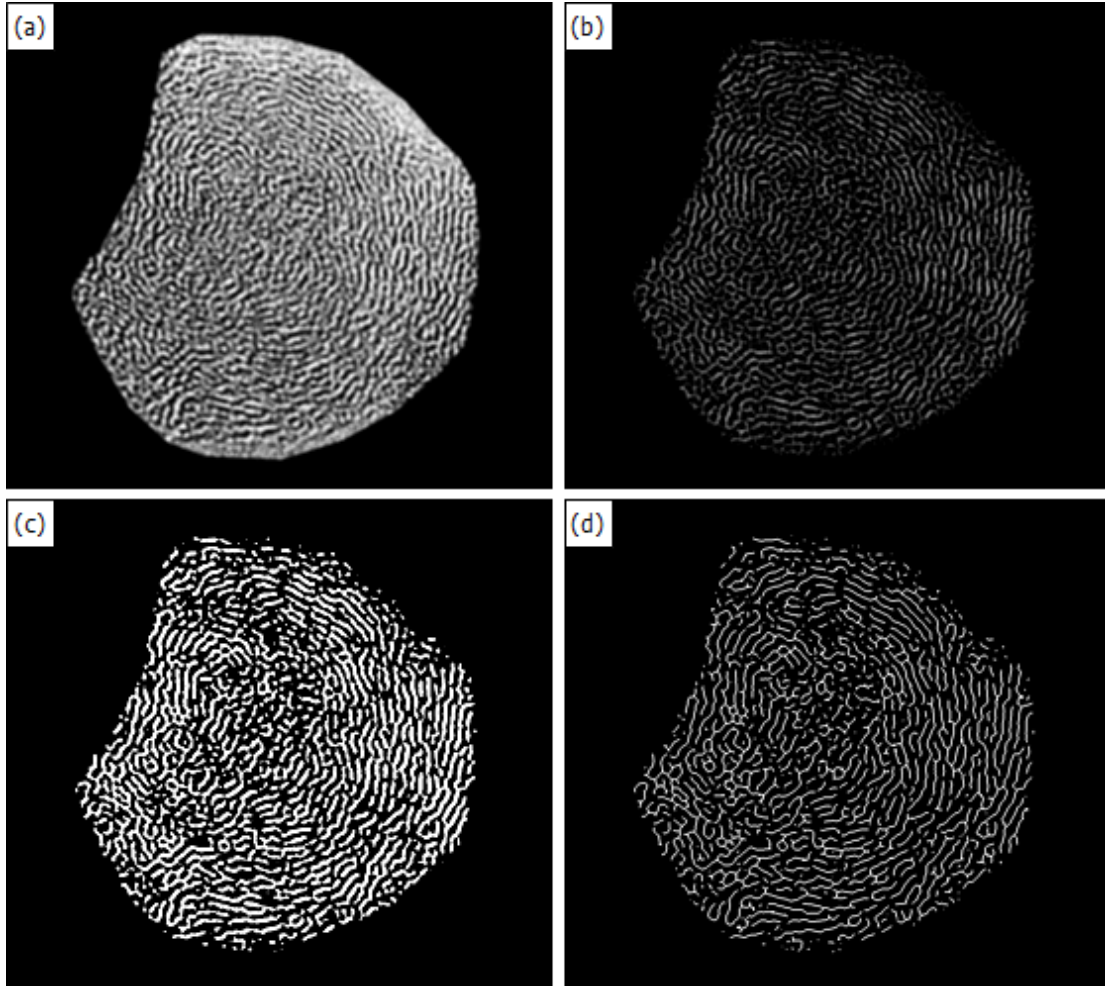


Figure 3.13: Lattice fringe image resulting from successive image processing operations: (a) Gaussian filtering, (b) Bottom-hat filtering, (c) Thresholding, (d) Skeletonization.

$4 \times 10^5$  magnifications, respectively (approximately 0.3 nm) and a standard deviation of 3 px. Results of the Gaussian filter for the example image are given in Fig. 3.13a.

#### *Bottom-hat Filtering*

Bottom-hat filtering, (also called black top-hat filtering) was used to correct uneven image illumination and bring fringes into greater relief against the back-

ground. It also had an inverting effect, so that lattice fringes, appearing dark in the raw image, are light against a dark background in the processed image. The filter operates by subtracting an image from its morphological closing using a structuring element [246]. This was implemented here using MATLAB's *imbothat* function. Best results were obtained using a 4 or 5 px ( $\sim 0.15$  nm) disk-shaped structuring element. Results of this operation for the example image are shown in Fig. 3.13b.

### *Thresholding*

Thresholding produces a binary image by setting all pixels with grayscale values above a certain threshold to 1, and all others to 0. Thresholding of the bottom-hat-filtered image was performed using Otsu's method (MATLAB functions *graythresh* and *im2bw*) which chooses a threshold based on the image's grayscale distribution [246]. The resulting binary image shows the lattice fringes as white objects of varying sizes, as seen in the example image in Fig. 3.13c.

### *Skeletonization*

Skeletonization reduces each binary object down to a single-pixel-width centerline. The operation preserves the positions and essential structures of each object. Skeletonization facilitates quantitative analysis of the fringe objects, as will be seen. Skeletonization was performed using MATLAB's *thin* morphological operation. The *skeletonize* operation, which uses a slightly different algorithm, was also tested but was more prone to producing spurious artifacts. Figure 3.13d shows the skeletonized example image.

### *Fringe Connection*

The series of operations leading to a skeletonized fringe image inevitably separates structures that would properly be interpreted as belonging to a single fringe object. To reunite such structures, a fringe connecting algorithm called *BridgeGaps* was developed. The function, whose code is provided in Appendix A.3.1, connects segments whose endpoints are within a user-defined proximity and orientation tolerance. After identifying the endpoints of each segment, the algorithm calculates the orientation of the two ends. Around a given endpoint, the algorithm evaluates a region whose radius equals the user-specified proximity (Fig. 3.14a). If a neighboring segment terminates within that region, its ending orientation is compared to that of the original segment. If the two orientations differ by  $180^\circ \pm$  the user-supplied tolerance, and the two endpoints are not part of the same segment, a line is drawn connecting the two segment endpoints (Fig. 3.14b). Best results were obtained with a 7 or 9 px proximity (for  $3 \times 10^5$  and  $4 \times 10^5$  magnifications, respectively), and a  $30^\circ$  orientation tolerance.

### *Branch Severing*

Fringes in the skeletonized image that are linked together or that branch in different directions, cannot be properly measured. Hence, all such linkages must be severed. The *SeverBranches* function was developed to accomplish this; (code in Appendix A.3.2). The function begins by identifying each branch point in the image. Then, a square interrogation window, whose size is specified by the user, is centered

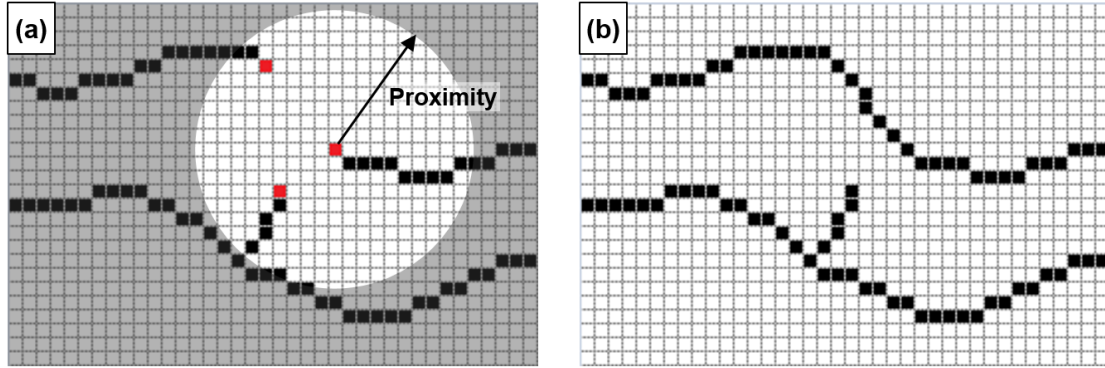


Figure 3.14: Connection of segments belonging to the same fringe. For clarity, pixel colors have been inverted. (a) Identification of segment endpoints (red pixels) within a user-defined proximity. (b) The two segments whose ends are oriented roughly opposite one another are connected. The orientation difference with the second segment within proximity did not meet a user-defined tolerance, so was not connected.

at each branch point (Fig. 3.15a). The orientation of each branching segment with respect to the branch point is defined by the location at which each segment crosses the window boundary. The pair of branching segments whose orientation difference is closest to  $180^\circ$  remains connected; all other branches are severed such that they loose 8-pixel connectivity (Fig. 3.15b). The function was found to be most successful with an interrogation window size of 7 and 9 px for  $3 \times 10^5$  and  $4 \times 10^5$  magnifications, respectively.

### *Small Segment Removal*

The last image processing step was the removal of small segments below a size threshold. This was accomplished using MATLAB's *bwareaopen* function. The size threshold used was approximately 0.3 nm, which corresponds to 7 and 10 px

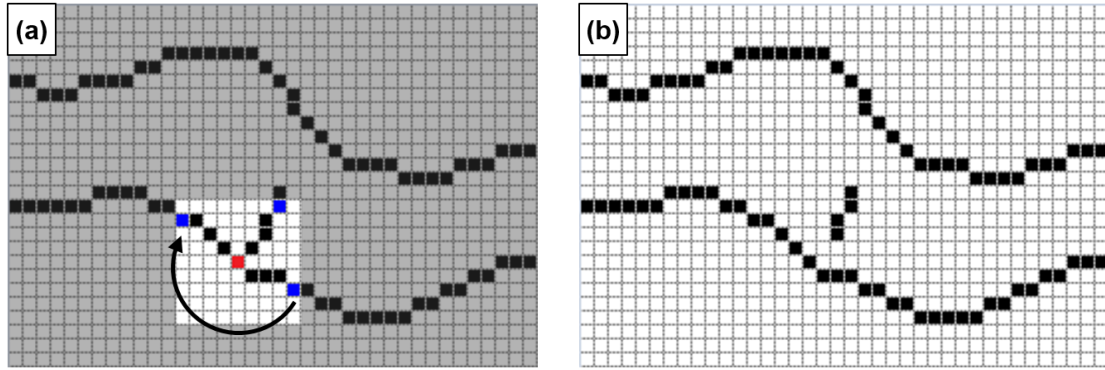


Figure 3.15: Severing a branched line segment. For clarity, pixel colors have been inverted. (a) Angles between each branching segment are measured at the border (blue pixels) of an interrogation window centered on the branch point (red pixel). The pair of branches closest to  $180^\circ$  apart and will remain connected. (b) The spurious branch is severed in the resulting image.

for images magnified  $3 \times 10^5$  and  $4 \times 10^5$ , respectively. It should be noted that the size threshold here refers simply to the number of pixels in a segment, and is only equivalent to the fringe length in the case of a perfectly horizontal or vertical fringe.

### 3.5.7.2 HRTEM Fringe Measurement

#### *Individual Fringes*

Before the skeletonized fringe image can be measured, the primary particle to which the fringes belong must be identified. This was performed manually on the original HRTEM image using Aerosol Image Analyzer's manual circle measurement tool, as shown in Fig. 3.16a. Defining the primary particle enables the computation of each fringe's orientation and radial location within the primary.

Figure 3.16 illustrates the measurements of fringe radial location, non-concentricity,

length, and tortuosity. These quantities were obtained using the *MeasureFringes* code provided in Appendix A.3.3. The function begins by calculating the centroid and orientation of each fringe object not touching the ROI border. Radial location,  $r_f$ , is then simply the distance between the primary particle’s center point and the fringe centroid. Non-concentricity,  $\theta_{f,c}$ , as defined here, is a fringe’s angular deviation from an orientation perpendicular to a radial line running through its centroid, (Fig. 3.16b). This is consistent with the definition used in the work of Shim et. al [175], although they they went further to define a polar order parameter. The measure of non-concentricity was found to be sufficient for the present work. Fringe length,  $L_f$ , is calculated as the sum of the distances between the center points of adjacent pixels in a fringe, which can be either 1 px or  $\sqrt{2}$  px, (Fig. 3.16c). Fringes shorter than a user-specified minimum length are not considered. For this study, a minimum fringe length of 0.483 nm was chosen, as it corresponds to the length of two aromatic rings [210]. Lastly, fringe tortuosity,  $\tau_f$ , is the fringe length divided by the linear distance between the fringe’s endpoints. For a perfect line,  $\tau_f = 1$ , while for all other geometries,  $\tau_f > 1$ .

#### *Fringe Separation Distance*

To calculate the separation distances between stacked lattice fringes, the function *GetFringeSeps* was developed. The code is given in Appendix A.3.4. The function only considers fringe pairs separated within a user-specified range. A separation range of 0.3 - 0.6 nm was used in the current work because this range was found to encompass the distribution of fringe separation values without truncation

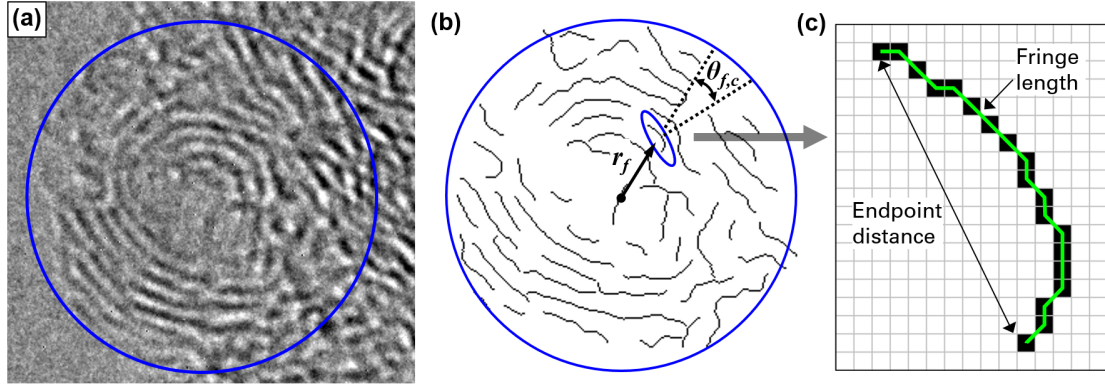


Figure 3.16: (a) Primary particle identified on the original image. (b) The given fringe is located at  $r_f$  within the primary particle, and its orientation deviates from perfect concentricity by angle  $\theta_{f,c}$ . (c) Fringe length (green line) is approximated by segments connecting pixel centers. Tortuosity is the ratio of fringe length to endpoint distance.

or inclusion of outliers. In addition, as others have noted [24,169,210], 0.6 nm marks a good upperbound, since van der Waals forces are negligible beyond this distance.

For each fringe identified in the prior step of fringe measurement, the algorithm determines the fringe's major axis (i.e. the axis defining its orientation) and isolates a region the width of the maximum allowed separation distance (i.e. 0.6 nm) on either side of the major axis as shown in Fig. 3.17a and b. The Euclidean distance of each pixel within this region to the nearest pixel of the reference fringe is computed. Then, the locations of the pixels of each neighboring fringe are determined within this Euclidean distance map (EDM). This is illustrated in Fig. 3.17c, where the Euclidean distance of each pixel away from the reference fringe is displayed as a grayscale intensity. A fringe's overall separation distance from the reference fringe is calculated as the average of the Euclidean distances of its pixels. The separation distance between a given fringe pair is the average of the two separation distances

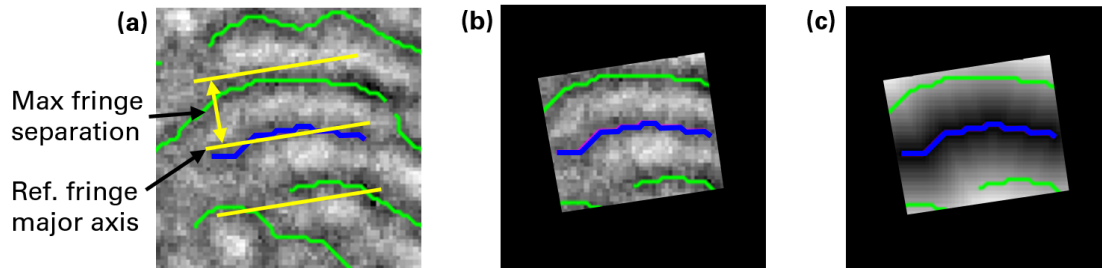


Figure 3.17: (a) Fringes identified on the original image. (b) Isolated region for analysis around the reference fringe (blue). (c) Neighboring fringes (green) superimposed over a grayscale map of the Euclidean distance from the reference fringe.

calculated when each fringe in a pair serves as the reference fringe.

Fringe pairs must also meet two criteria for parallelism. First, the orientations of the reference fringe and of the neighboring fringe may differ by no more than a user-supplied tolerance. If part of the neighboring fringe extends beyond the measurement window, only the portion of the fringe within the window is considered in the analysis. An orientation tolerance of  $\pm 30^\circ$  was used in the present study. A second measure of parallelism comes from the fact that the calculated distance from fringe  $i$  to fringe  $j$  will generally not be the same as that of  $j$  to  $i$ . To illustrate this, consider the two artificial fringes shown in Fig 3.18a. While the overall orientation of the two fringes' major axes is parallel, the contours of the two fringes clearly are not. Consequently, the fringe separation distance is 46% larger when calculated from fringe  $i$  to  $j$  than when calculated from  $j$  to  $i$ . If this artificial fringe image were to represent an image obtained at a magnification of  $4 \times 10^5$ , this would be a 0.14 nm difference in the fringe separation distance. This discrepancy can be visualized in the different Euclidean distance map images that are generated depending on which

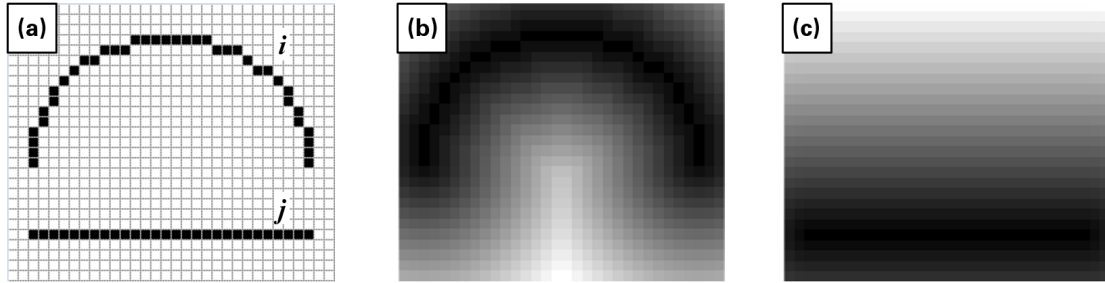


Figure 3.18: (a) The major axes fringes  $i$  and  $j$  are parallel however their contours are not. (b) Visualization of the EDM from fringe  $i$ . (c) Visualization of the EDM from fringe  $j$ .

of the two fringes is serving as the reference fringe (Fig. 3.18b and c). In the present work, for a fringe separation measurement to be retained, the fringe pair must reciprocally calculate the same separation distance within a tolerance of  $\pm 0.05$  nm.

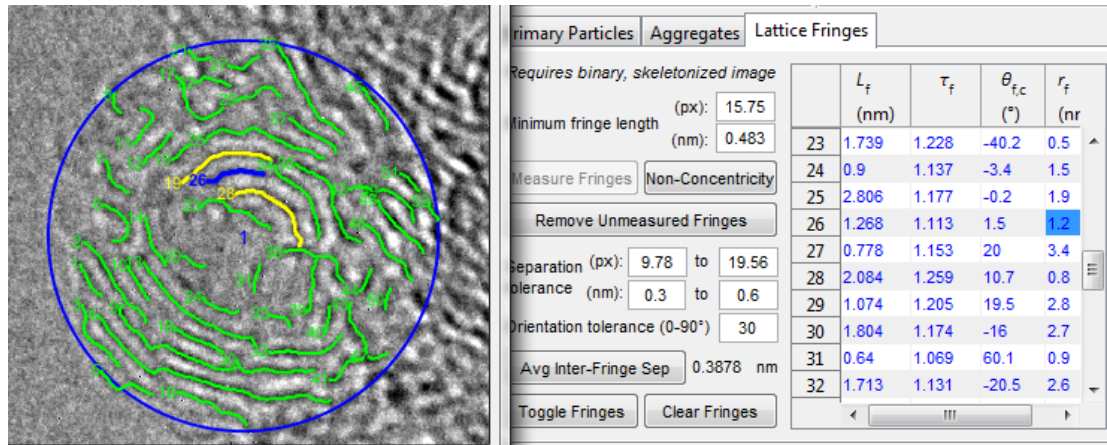


Figure 3.19: Final measured fringes as displayed in the Aerosol Image Analyzer software. The program identified the fringes in yellow as neighbors to the fringe shown in blue.

If a given fringe pair meets all of the above criteria (separation distance, orientation difference, and reciprocal separation difference all within allowable ranges

and tolerances), the fringe separation between the two fringes is included in the output of the *GetFringeSeps* function. An example of the final fringe measurements displayed by the AIA program are seen in Fig. 3.19. The user can verify the results of *GetFringeSeps* by clicking on a fringe object within the AIA program. The program highlights in yellow the neighboring fringes that meet the criteria for pairing with the clicked fringe (in blue), as shown in the figure.

### 3.6 Soot Oxidation Rate

Once measurements within the soot flame have been obtained per this Methods section, the soot oxidation rate may be determined and analyzed with respect to changing soot morphology, nanostructure, temperature and gas composition. The soot oxidation rate is derived as follows. Consider a control volume (CV) around the soot flame as depicted in Fig. 3.20. Soot enters the CV with a mass flow rate of  $\dot{m}_{s,1}$ , resides within the CV for time  $\Delta t$ , and then exits with mass flow rate  $\dot{m}_{s,2}$ . The change in soot mass within the CV is given by:

$$\Delta m_s = (\dot{m}_{s,1} - \dot{m}_{s,2})\Delta t \quad (3.21)$$

The radius of the control volume,  $R_{CV}$ , is constant and is sufficiently large to radially encompass all of the soot at each axial location within the soot flame. The height of the CV is simply the product of the soot velocity  $v_s$  and  $\Delta t$ .

The volume of soot within the control volume is:

$$V_{s,CV} = \Delta t v_s \int_0^{R_{CV}} 2\pi r f_s(r) dr \quad (3.22)$$

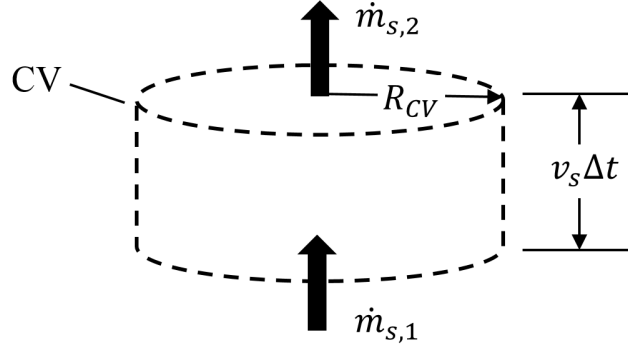


Figure 3.20: The soot flame control volume used in soot oxidation rate analysis.

The integral term in Eq. 3.22 is the sectional integrated soot volume fraction,  $F_s$ , whose value is experimentally determined via Eq. 3.2. The surface area of soot within the CV is then given by:

$$S_{s,CV} = \Delta t V_{s,CV} S_V \quad (3.23)$$

where  $S_V$  is the volume specific surface area, determined from Eq. 3.10.

The soot oxidation rate per unit of soot surface area within the control volume can be expressed as:

$$\dot{w}_{ox} = \lim_{\Delta t \rightarrow 0} \frac{-\Delta m_s}{S_{s,CV} \Delta t} \quad (3.24)$$

Recognizing that  $\dot{m}_s = \rho_s v_s F_s$ , combining Eq. 3.21-3.24, and taking the limit  $\Delta t \rightarrow 0$  the expression for the soot oxidation rate per unit surface area becomes:

$$\dot{w}_{ox} = \frac{-\rho_s}{v_s F_s S_V} \frac{d(v_s F_s)}{dt} \quad (3.25)$$

Once the overall soot oxidation rate is known, the next task is to determine the reaction kinetic parameters for the two principal oxidizers,  $O_2$  and  $OH$ . Owing to the small size of soot primary particles, the rate of soot oxidation is thought to

be limited by the chemical kinetics of the heterogeneous reactions, rather than by the rate of diffusion of gas phase oxidizers to the soot surface [247]. The reactions for soot oxidation by O<sub>2</sub> and OH are:



Rate expressions will be sought for these two reactions. Assuming that oxidizing species  $i$  has a constant activation energy  $E_{A,i}$  and a constant collision efficiency  $\eta_i$  with the soot surface, the reaction rate can be written in the Arrhenius form:

$$\dot{w}_{ox,i} = \frac{\eta_i [i] \bar{v}_i m_{C,i}}{4} \exp\left(\frac{-E_{A,i}}{R_u T}\right) \quad (3.28)$$

where  $[i]$  and  $\bar{v}_i$  are respectively the mole concentration and mean molecular velocity of species  $i$ ,  $m_{C,i}$  is the mass of carbon removed per mole of reactive collision between  $i$  and the soot surface (e.g. 12 g/mol for OH),  $T$  is temperature, and  $R_u$  is the universal gas constant. Assuming species velocities follow a Maxwell-Boltzmann distribution,  $\bar{v}_i$  is:

$$\bar{v}_i = \left(\frac{8R_u T}{\pi M_i}\right)^{1/2} \quad (3.29)$$

where  $M_i$  is the species  $i$  molar mass. After applying the ideal gas law, combining Eq. 3.28 and 3.29, and grouping constants, the following expression is obtained for the oxidation of soot by species  $i$ :

$$\dot{w}_{ox,i} = A_i p_i T^{-1/2} \exp\left(\frac{-E_{A,i}}{R_u T}\right) \quad (3.30)$$

where  $A_i$  is the Arrhenius pre-factor, and  $p_i$  is the partial pressure of species  $i$ . In the case of OH, the activation energy is understood to be zero [46], and the OH

collision efficiency is commonly written separately from the rest of the Arrhenius pre-factor. In this case, Eq. 3.30 reduces to:

$$\dot{w}_{ox,OH} = \eta_{OH} A_{OH} p_{OH} T^{-1/2} \quad (3.31)$$

For OH, the remaining pre-factor term,  $A_{OH}$ , is equal to 0.0127 s-K<sup>1/2</sup>/m. Note that the assumption of constant collision efficiency for both oxidizers implies a constant surface concentration of active sites (i.e.  $C_s = \text{const.}$  in Eq. 2.1). However, this is by no means a given, as evidenced by the multitude of studies indicating changing soot reactivities depending on factors such as nanostructure, prevalence of heteroatoms, etc. (See Sec. 2.4.4). For the present study, a constant  $\eta_i$  shall be treated as a null hypothesis, which will be evaluated in light of nanostructural measurements and of the goodness-of-fit of proposed reaction rate expressions.

In experiments involving only one oxidizer, typically molecular oxygen, the reaction rate parameters  $E_{A,i}$  and  $A_i$  may be obtained from the slope and intercept of a plot of  $K_i$  vs.  $1/T$  obtained by rearranging Eq. 3.30:

$$K_i = \ln \left( \frac{\dot{w}_{ox,i} T^{1/2}}{p_i} \right) = \frac{-E_{A,i}}{R_u} \frac{1}{T} + \ln A_i \quad (3.32)$$

However, in flames, the presence of multiple oxidizers complicates straightforward determination of the reaction rate parameters. For the present study, the measured soot oxidation rate will be compared against predictions of a combination of the Nagle and Strickland-Constable mechanism for O<sub>2</sub> [42] and the OH mechanism of Neoh et al [43], as well as the optimized expressions suggested by Guo et al. [46]. Then, an attempt will be made at determining rate expressions optimized against only the measurements in the present study. This will be done by varying the values

of  $E_{O_2}$ ,  $A_{O_2}$ , and  $\eta_{OH}$  across the ranges of published values for these parameters and maximizing the coefficient of determination between measured and predicted oxidation rates.

### 3.7 Uncertainty Analysis

The uncertainty of a quantity calculated from a data reduction equation that combines multiple independent variables, is obtained from the Taylor Series method (TSM) of uncertainty propagation [248, 249]:

$$u^2(y) = \sum_i \left( \frac{\partial y}{\partial x_i} \right)^2 u^2(x_i) \quad (3.33)$$

Here,  $u(y)$  is the combined standard uncertainty for a result  $y = y(x_1, x_2, \dots, x_n)$ , and  $u(x_i)$  is the elemental standard uncertainty of each independent variable  $x_i$ . The TSM method assumes a symmetric confidence interval around  $y$ , and requires that all elemental uncertainty distributions are known and symmetric. In cases in which these assumptions or requirements cannot be met, the Monte Carlo method (MCM) of uncertainty propagation is used instead [249, 250].

Regardless of whether TSM or MCM is used, the elemental uncertainty of each independent variable must include both random (precision) and systematic (bias) uncertainties. As discussed earlier in Sec. 2.2.3, uncertainties stemming from operator bias and sample variation are difficult to estimate because a measurement capability analysis of TEM-derived aerosol morphology is currently lacking from the literature. To address this gap in knowledge, and to generate a robust estimate of measurement uncertainties in the current work, a detailed repeatability and

reproducibility study (Gage R & R) is presented in Chapter 4.

Whenever possible, the uncertainties obtained from Gage R & R analysis will be used in the confidence intervals reported in the present work. When this cannot be done,  $u(x_i)$  will be obtained from a statistical analysis of multiple measurements. Other uncertainties will be adopted from the best available estimates in the literature. All uncertainties in the present work are reported at the 95% confidence level unless preceded by the modifier *standard*, indicating the value represents a single standard deviation.

## Chapter 4: Repeatability and Reproducibility of TEM Measurements and Surface Area Validation

This chapter presents a study of the repeatability and reproducibility of soot primary particle and surface area measurements obtained from TEM image analysis. The purpose is fourfold. First, although TEM is used widely to measure the size and structure of aerosols, a measurement system analysis of TEM used for this purpose is lacking from the literature. This study fills this gap in knowledge. Second, the present work employs several methods intended to reduce operator bias, (see Sec. 3.5.2.1), and an assessment of their efficacy is needed. Third, multiple methods of automating the measurement of primary particle size distributions from TEM images have been presented in the literature. If these methods are reliable, they would greatly accelerate one of the more time-consuming components of TEM aerosol analysis. This study evaluates their capabilities. Lastly, validation of the soot surface area measurement method presented in Sec. 3.5.3 is needed. Validation is performed here against the BET surface adsorption method.

## 4.1 Non-Bias-Controlled Results and Study Motivation

Prior to the development of the Aerosol Image Analyzer software (see Sec. 3.5.1), measurements of soot primary particle diameter from TEM images were performed manually in ImageJ [237]. In the course of performing these measurements, substantial discrepancies were observed in the results obtained by two equally-qualified operators. Figure 4.1a shows the results of measurements performed by the two operators on the same five image sets. No attempts were made to randomize which images were analyzed, which regions within each image to measure, or how many measurements to make; all such decisions were left to the judgment of the operator. The error bars shown in Fig. 4.1 represent the uncertainty at 95% confidence that can be attributed to non-operator effects (i.e. image resolution and statistical variance). The percent difference in the mean primary particle size for each sample ranged from 11% - 33%, and a consistent operator bias is readily observable.

To test that this observation was repeatable, and to better gage its magnitude, a formal follow-up test was performed with three operators. The operators measured primary particle diameters on image sets of two samples collected from the soot flame at a 13 mm height above burner. The operators were instructed to measure at least 300 primary particles per image set, but were not told which images within each set to select, or which regions therein to measure. The results, shown in Fig. 4.1b, again demonstrate considerable variability that cannot be attributed to statistical precision alone. Indeed, there is no overlap of 95% confidence intervals among any of the operators for any of the 7 samples considered across both tests, and

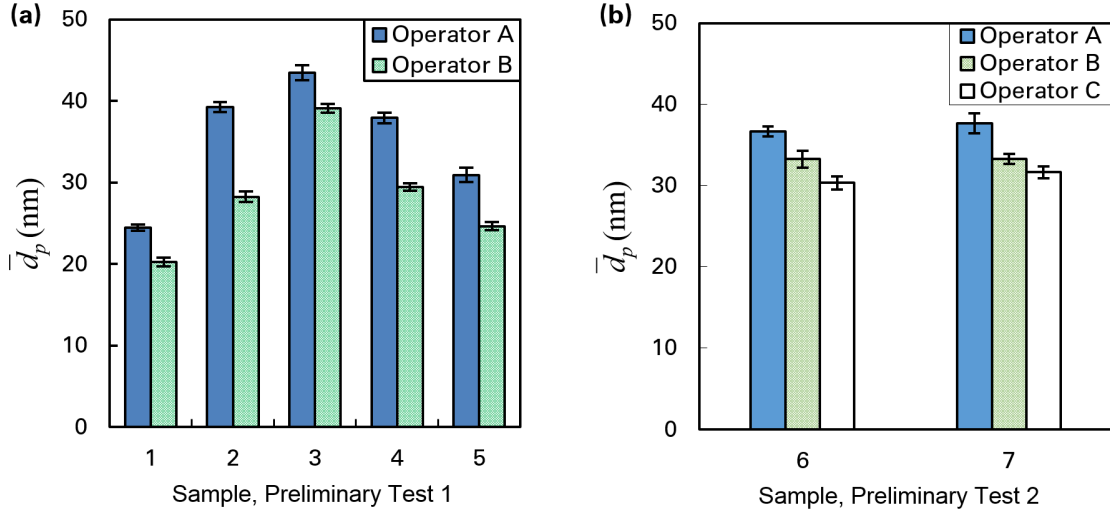


Figure 4.1: Preliminary measurements of mean primary particle diameter without bias controls. Both an initial test (a), and a follow-up test (b) show substantial variability between operators, and a consistent operator bias. Error bars reflect the precision of the mean at the 95% confidence level.

the consistent relative trend among the operators confirms the significant between-operator effect. In the follow-up test (Fig. 4.1b), the overall fluctuation, calculated as the measurement range over its average, was 18.9% and 17.6% for samples 6 and 7, respectively. This is comparable with the fluctuation of primary particle measurements across all operators reported by Kondo et al. [150].

Since operator bias is clearly present in primary particle measurements obtained using traditional methods, it is fair to inquire into the efficacy of the bias mitigation techniques employed in the present work (Sec. 3.5.2.1). Moreover, it would be valuable to quantify the overall uncertainty of TEM-measured primary particle size distributions, accounting for repeatability as well as variation across samples and operators. To these ends, a gage repeatability and reproducibility (Gage R & R) study was undertaken to produce a statistically robust estimate of

the true uncertainty associated with TEM measurements of soot primary particles.

We are also interested in evaluating the ability of several automated measurement methods presented in the literature to accurately measure soot primary particle size distributions. Using the Gage R & R results as the baseline, three automated methods are evaluated: two employing a Circular Hough Transform (CHT) algorithm and one utilizing Euclidean distance mapping (EDM).

Finally, with a firm understanding of the sources and magnitudes of TEM measurement uncertainties, analysis is extended to the important measurement of soot surface area. The mass-specific surface areas derived from TEM analysis are compared to results obtained by the BET method, which is a widely-recognized standard for measuring nanoparticle surface area.

## 4.2 Methods

### 4.2.1 Bias-controlled measurements

With the ring burner used to produce the ternary flame removed, three soot samples were thermophoretically drawn from the propylene/air co-flow diffusion flame on separate days at a height of 10 cm above the co-flow fuel port. The soot was deposited onto 200 mesh copper TEM grids with a standard carbon support film (Electron Microscopy Sciences CF200-Cu). Coordinates for imaging on the TEM grid plane were randomly generated. If soot was present at a coordinate, an image was recorded with no attempt to center the viewing window on any particular image element. Individual aggregates were identified in the images and then

randomly chosen for analysis. Four independent operators, three of whom made the preliminary measurements, performed image analysis using the Aerosol Image Analyzer program. The program randomly selected  $100 \times 100$  pixel regions of interest (ROIs) on each soot aggregate image. To ensure that more weight was not given to primary particles of smaller aggregates, the number of ROIs was proportional to an automated estimate of the aggregate's projected area. Operators were directed to measure every element within these ROIs they considered to reasonably constitute a primary particle using the semi-automated CSES algorithm, detailed in Sec. 3.5.2.2. If not satisfied with the algorithm's output, the operator could reject it and remeasure by selecting a different pixel or restricting the diameter range. The semi-automated measurement therefore reflects an operator's best judgment, but is also expected to reduce bias since it quantifies image features uniformly. The instruction to measure every discernible primary particle within an ROI was included to both inhibit selection bias by the operator, and to get the best estimate of primary particle overlap. Each operator performed 2 replicate measurements on each sample's image set, yielding a total of 24 measurement sets with an average of 290 measured primary particles per set. The randomly chosen images and ROIs used for a given replicate were the same for all operators.

#### 4.2.2 Gage R & R Analysis

The true uncertainty of the TEM measurement method described above and the extent to which it eliminates operator bias, was assessed through analysis of

variance (ANOVA) gage repeatability and reproducibility analysis. Since operators performed the measurement the same number of times on the same set of samples, and assuming the operators represent random selections from a population of all possible operators, the appropriate Gage R & R model is a balanced two-factor crossed random model with interaction [251]:

$$Y_{ijk} = \mu_Y + P_i + O_j + (PO)_{ij} + E_{ijk} \quad (4.1)$$

Here,  $Y_{ijk}$  is the measured value of sample  $i$ , by operator  $j$ , the  $k^{\text{th}}$  time, and  $\mu_Y$  is the true mean of the measurand  $Y$  from the population of all samples producible by the given process (in this case, the co-flow flame). The terms  $P_i$ ,  $O_j$ ,  $(PO)_{ij}$ , and  $E_{ijk}$ , are jointly independent normal random variables with means of zero and variances  $\sigma_P^2$ ,  $\sigma_O^2$ ,  $\sigma_{PO}^2$ , and  $\sigma_E^2$ . These correspond to the variation away from  $\mu_Y$  due to effects of sample, operator, sample-operator interaction, and random error, respectively. If an F-test determines the sample-operator interaction to be negligible, the term  $(PO)_{ij}$  may be dropped from Eq. 4.1, and one may assume  $\sigma_{PO}^2 = 0$ . This model is termed a balanced two-factor crossed random model with *no* interaction.

The variances  $\sigma_O^2$  and  $\sigma_{PO}^2$  sum to yield the reproducibility,  $\sigma_{\text{Repro}}^2$ , while  $\sigma_E^2$  is the repeatability,  $\sigma_{\text{Repeat}}^2$ . The variance of the measurement system,  $\sigma_M^2$  (also referred to as the Total Gage R & R), is then:

$$\sigma_M^2 = \sigma_{\text{Repro}}^2 + \sigma_{\text{Repeat}}^2 \quad (4.2)$$

and the total observed variance can be written as:

$$\sigma_{\text{Tot}}^2 = \sigma_P^2 + \sigma_M^2 \quad (4.3)$$

The model given in Eq. 4.1 assumes overall repeatability uncertainty is greater than measurement resolution. The measurands here are the mean,  $\overline{d}_p$ , and standard deviation,  $s_{d_p}$ , of the distribution, *not* the individual primary particle measurements. The resolution of  $\overline{d}_p$  and  $s_{d_p}$  estimated from  $n$  measured primary particle diameters are given by their respective standard deviations:  $s_{\overline{d}_p} = s_{d_p}/\sqrt{n}$  and  $s_{s_{d_p}} = s_{d_p}/\sqrt{2(n-1)}$ . The latter expression assumes a normal distribution of primary particles, however uncertainty due to any divergence from normality is expected to be negligible compared to other sources of uncertainty.

The values of these variances and  $\mu_Y$  found with Gage R & R analysis are point estimators (so denoted  $\hat{\sigma}^2$ ) of the true values, and are themselves subject to uncertainty. Uncertainty distributions for these terms were simulated following the generalized inference approach of Hamada and Weerahandi [252]. Sampling from these distributions, Monte Carlo methods were employed following the approach outlined in Ref. [253] to compute confidence intervals for the both the means and standard deviations of the measured size distributions.

To combine operator measurements and obtain confidence intervals for each sample, a balanced one factor random ANOVA model is used:

$$Y_{Ajk} = \mu_{Y_A} + O_{Aj} + E_{Ajk} \quad (4.4)$$

For a given sample  $A$ ,  $Y_{Ajk}$  is the  $k^{\text{th}}$  replicate measurement by operator  $j$ , and  $\mu_{Y_A}$  is the true mean of the measurand  $Y_A$ . The terms  $O_{Aj}$  and  $E_{Ajk}$  represent the deviation of the measurement away from the true mean of sample  $A$  due to operator and random effects, respectively. Since the sample is fixed, and  $O_{Aj}$  and  $E_{Ajk}$  are

assumed to be normally distributed about a mean of zero,  $\mu_{Y_A}$  also represents the true value of  $\mu_{Y_A}$ , for which the best estimate,  $\hat{\mu}_{Y_A}$ , is the mean of all measurements,  $\overline{Y_{A^{**}}}$ , for the sample. The confidence interval for  $Y_A$  is then found from

$$Y_A = \hat{\mu}_{Y_A} \pm \sqrt{s_O^2 F_{1-\alpha;1,o-1}/ro}, \quad (4.5)$$

where  $s_O^2 = (r/(o-1)) \sum_{j=1}^o (\overline{Y_{Aj^*}} - \overline{Y_{A^{**}}})^2$  is the mean squares for  $o$  operators each performing  $r$  replicates,  $\overline{Y_{Aj^*}}$  is the mean of measurements by operator  $j$ , and  $F_{1-\alpha;1,o-1}/ro$  is the  $F$ -statistic at significance level  $\alpha$ , having 1 and  $o-1$  degrees of freedom [251].

### 4.2.3 A simplified approach to obtaining sample confidence intervals

As a practical matter, it would be desirable to estimate the uncertainty of a sample's primary particle distribution without the relatively large number of replicates required by ANOVA. One approach treats the combination of operator results as an inter-laboratory evaluation in which operators are equally competent and subject to independent random and systematic effects [254]. The measurements of each operator  $j$  for a given sample are pooled, and the resulting distribution will have a mean and standard deviation with standard random uncertainties, equal to  $s_{\overline{d_p},j}$  and  $s_{s_{d_p},j}$ , as given in Section 4.2.2. For a given sample  $A$ , the measured value  $Y_{Aj}$  (here either  $\overline{d_p}$  or  $s_{d_p}$ ) from each operator  $j$  may then be combined using a weighted mean, where the weight is defined as  $w_{Aj} = 1/s_{Y_{Aj}}^2$ . The combined result,  $Y_{A,C}$ , is then:

$$Y_{A,C} = \frac{\sum_j w_{Aj} Y_{Aj}}{\sum_j w_{Aj}} \quad (4.6)$$

for which the standard uncertainty is:

$$u_{Y_{A,C}} = \frac{1}{\sqrt{\sum_j w_{Aj}}} \quad (4.7)$$

If the interval  $2u_{Y_{A,C}}$  of this combined mean fails to encompass a non-negligible fraction of operator results, an expanded confidence interval that includes an additive bias correction with its own expectation value and uncertainty distribution is appropriate. Since each operator's results are believed to be equally probable, this correction is assumed to follow a rectangular distribution on the interval  $(-a_1, a_2)$ , where  $-a_1 = \min_j(Y_{Aj}) - Y_{A,C}$  and  $a_2 = \max_j(Y_{Aj}) - Y_{A,C}$ . The expected value for this correction is  $B = (a_2 - a_1)/2$  with a standard uncertainty  $u_B = (a_2 + a_1)/\sqrt{12}$ . Finally, the confidence interval for the measurand  $Y_A$  is:

$$Y_A = (Y_{A,C} + B) \pm k(u_{Y_{A,C}}^2 + u_B^2)^{1/2} \quad (4.8)$$

where a value of 2 for the coverage factor  $k$  corresponds to a 95% confidence level.

## 4.2.4 Automated Measurements

### 4.2.4.1 Circular Hough Transform

The different methods proposed in the literature for automating primary particle measurement was touched upon in Sec. 2.2.2.3. Here, three different automated measurement methods were applied to the TEM image sets obtained in Sec. 4.2.1. The first, proposed by Grishin et al. [134], applies CHT to binarized images of soot aggregates, and will be referred to as the binary-CHT method. Techniques for automating the image binarization step have been proposed [134,244], however, as with

the soot sampled on carbon lacey grids (3.5.4), automated procedures were found to be incapable of reliably separating aggregate from background. The greatest success was obtained with a general procedure that employed edge-preserved smoothing (e.g., median filtering) and contrast enhancement followed by background removal via a rolling-ball transform and then manual thresholding. Grishin et al., [134] used a modified CHT algorithm to reduce processor load and eliminate falsely identified primary particles produced by convex fragments on the aggregate border. As these were not issues in our implementation, we used the unmodified CHT found in MATLAB's *imfindcircles* function.

The second method, suggested by Kook et al. [135], also uses the CHT algorithm, however with different pre-processing. First, the image undergoes inversion and self-subtraction to enhance contrast between aggregate and background. Primary particle edges are then enhanced by negative Laplacian filtering, after which Canny edge detection is applied. We used the MATLAB script provided by Kook et al. [135], which also utilizes the *imfindcircles* function. This method is referred to here as the Canny-CHT method.

Both CHT methods require the user to specify a diameter range and a sensitivity level. The sensitivity level is a value between 0 to 1, where higher sensitivities interpret more image features as circular. The Canny-CHT method also requires specified values for self-subtraction level and negative Laplacian filter shape parameter. Kook et al. [135] observed that parameter values, especially the lower-bound diameter, and CHT sensitivity, substantially affected results. Without knowledge of the primary particle size distribution *a priori*, the choice of parameter values

represents a source of uncertainty for all CHT methods. In practice, one would likely estimate the diameter range manually before performing automated analysis. Therefore, the diameter ranges found from the Gage R & R measurements were used as inputs to both CHT algorithms. For the binary-CHT method, the sensitivity value was varied, based on personal experience, between 0.8 and 0.92. For the Canny-CHT method, parameter ranges were adopted from those that Kook and co-workers [135] found to optimally detect soot primary particles produced by five different diesel combustion facilities. Sensitivity ranged from 0.75–0.79, self-subtraction level ranged from 0.8–1.2, and alpha was 0.1. Each of the input parameters to both CHT algorithms were then varied individually to assess sensitivity of the response variables.

#### 4.2.4.2 Euclidean Distance Mapping

The EDM method of Bescond et al. [133] was evaluated. This approach has the advantage of requiring no input parameters, however results must be calibrated and a distribution shape assumed. Bescond and co-workers assumed a lognormal distribution and computed calibration parameters that adequately fit EDM results from soot produced by both an aircraft engine and an ethylene laminar diffusion flame. Given the very different types of soot produced by these systems, the calibration is expected to be robust and was applied to the present study. Measurement was performed in the NIH software ImageJ using the plug-in provided by Bescond

et al. [133]. The resulting measurements were expected to follow a sigmoidal curve:

$$\frac{S(d)}{S(0)} = \left\{ 1 + \exp \left[ \frac{\frac{\ln d - \ln \overline{d_{pg}}}{\ln \sigma_{pg}} - \beta}{\Omega} \right] \right\}^{-1} \quad (4.9)$$

The left-hand side of this equation is the normalized average aggregate surface area after the EDM transformation at scale diameter,  $d$ , itself a function of the EDM threshold value. The calibration constants are  $\beta = 1.90 \pm 0.03$  and  $\Omega = 0.80 \pm 0.03$  [133]. The geometric mean,  $\overline{d_{pg}}$ , and geometric standard deviation,  $\sigma_{pg}$ , were determined from a fit of the sigmoidal curve to the data, and were then converted to their arithmetic values for comparison to results from other methods.

#### 4.2.5 TEM-Derived Mass Specific Surface Area

To obtain robust confidence intervals for the mass specific surface area (MSSA) of each of the three samples, the Gage R & R analysis presented in Sec. 4.2.2 was extended to two additional measurands: the skewness of the primary particle size distribution,  $\gamma_{d_p}$  and the mean projected overlap coefficient,  $\overline{C_{ov,p}}$ . To compare the two different methods presented in Sec. 3.5.3 for calculating the lost surface area and volume due to overlap,  $F_S$  and  $F_V$ , were calculated using both Eq. 3.14, and Eq. 3.19. As an additional comparison, MSSA was also calculated using the two simplifications common in the literature: primary particles in single point contact (i.e. no overlap), and monodisperse primary particles in single point contact. After obtaining the volume specific surface area,  $S_V$ , per Eq. 3.10, or via the simplified Eqs. 3.7 and 3.8, the MSSA is simply:

$$S_m = S_V / \rho_s \quad (4.10)$$

The soot density,  $\rho_s$ , represents an additional source of uncertainty. In the surveyed literature, which considers soot from a range of fuels and flame types, the value of  $\rho_s$  varies between 1.46 and 2.05 g/cm<sup>3</sup> [127,128,255–259]. No studies report the density of soot from a propylene/air flame, however a good estimate can be obtained using soot from flames of unsaturated aliphatic hydrocarbons. Combining the values from such studies (i.e. Refs. [127,255–258]) in an inter-laboratory evaluation as described in Sec. 4.2.3, yields  $\rho_s = 1.85 \pm 0.15$  g/cm<sup>3</sup>. The MSSA confidence intervals were obtained by propagating the independent elemental uncertainties (i.e. those corresponding to  $\overline{d_p}$ ,  $s_{d_p}$ ,  $\gamma_{d_p}$ ,  $\overline{C_{ov,p}}$ , and  $\rho_s$ ) obtained either from Gage R & R analysis or from literature using the law of uncertainty propagation, (Eq. 3.33).

#### 4.2.6 BET-Derived Mass Specific Surface Area

BET analysis was employed to characterize the porosity of the mature soot produced by the co-flow flame and to validate the method of measuring soot surface area from TEM images. To collect soot in bulk for BET analysis, a square copper plate, 1.6 mm thick with 12.7 cm sides, was suspended 10 cm above the co-flow fuel port, the same location from which the samples for TEM analysis were drawn. A 6 mm hole in the center of the plate was positioned on the soot column axis. Ultrafine particulates followed exhaust gas streamlines through the hole and onto a 0.2  $\mu\text{m}$  filter (Sigma-Aldrich Z269212) connected to a vacuum pump, while larger soot particles accumulated on the cold plate. For each of three samples taken, approximately 200 mg of soot was collected from the filter and plate. Attempts were

made to collect soot at the exit of the soot flame as well, however, the quantity of soot available at this location was insufficient for BET analysis. Bulk soot collection was performed at the same time that TEM samples were obtained.

BET surface area and t-plot external surface area measurements by adsorption of  $N_2$  were performed on a Micrometrics ASAP 2020 porosimeter at the University of Maryland NanoCenter’s FabLab. The t-plot external surface area method is based on the assumption that in a certain region of the adsorption isotherm, micropores ( $<2$  nm) are already filled, and the remaining external surface follows a linear pressure dependence. Absent any micropores in the aggregates, these two surface areas should show good agreement [260].

The porosimeter t-plot analysis also estimates the specific volume of surface micropores, which can then be used to calculate the porosity (i.e. the void fraction) of the sample.

The uncertainties of BET and t-plot surface areas reported by commercial porosimeters typically only consider the goodness of fits to the plotted isotherm data. However, there are far more sources of error beyond this [261]. For the work here, adsorption-derived MSSA values will be assigned either the combined uncertainty of the porosimeter and soot mass (via Eq. 3.33), or the known relative

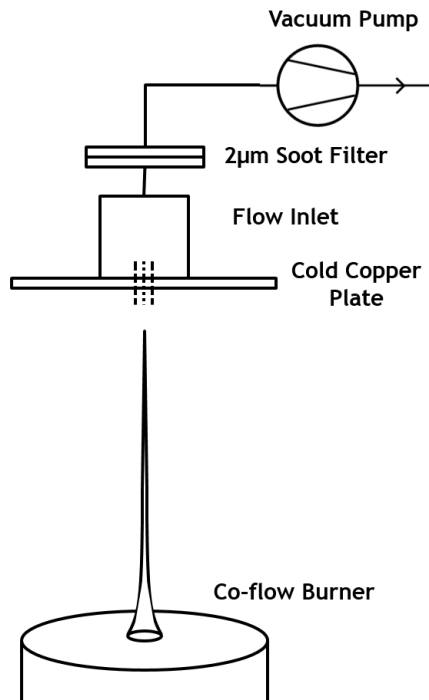


Figure 4.2: Soot collection apparatus for BET measurement.

standard uncertainty for adsorption methods of  $\pm 5\%$  [262], whichever is greater.

## 4.3 Results

### 4.3.1 Gage R & R Results

The mean primary particle diameter,  $\overline{d_p}$ , and standard deviation,  $s_{d_p}$ , for each measurement replicate is given in Fig 4.3, with the corresponding Gage R & R results in Table 4.1. An F-test ( $\alpha = 5\%$ ), determined that sample-operator interaction was negligible for both  $\overline{d_p}$ , and  $s_{d_p}$ , ( $p = 0.156$  and  $0.102$ , respectively). Hence, a balanced two-factor crossed random model with no interaction holds. Repeatability variances exceeded the variance due to individual measurement precisions which were  $s_{d_p}^2 \approx 0.6$  and  $s_{s_{d_p}}^2 \approx 0.3$ . This justifies the assumption that measurement resolution is subsumed within overall repeatability [263]. It is also clear from the differences in replicate measurements in Fig 4.3 that inhomogeneities in the sample account for some of the repeatability uncertainty. A follow-up test, in which 2 operators performed 5 replicate measurements on the same group of ROIs on successive days, found that inhomogeneities accounted for about two-thirds of the overall repeatability variance. In contrast to the finding of Kondo et al. [150], there was no discernible trend in results based on the experience level of the operator.

Sampling from the variance distributions produced by the generalized inference method, Monte Carlo simulations were used to construct 95% confidence intervals for key metrics. The true mean of all primary particle diameter means producible by this process, (that is, the mean of means),  $\mu_{\overline{d_p}}$ , is  $32.5 \pm 5.9$  nm ( $\pm 18\%$ ), and

Table 4.1: Components of variance in the measurement of primary particle diameter mean and standard deviation as quantified by Gage R & R analysis.

Variance Component	$\hat{\mu}_{d_p}$		$\hat{\sigma}_{d_p}$	
	Variance	% Variance	Variance	% Variance
$\hat{\sigma}_P^2$	4.82	57.4%	2.03	48.1%
$\hat{\sigma}_O^2$	0.53	6.3%	1.82	43.1%
$\hat{\sigma}_E^2$	3.05	36.3%	0.37	8.8%
$\hat{\sigma}_M^2$	3.58	42.6%	2.19	51.9%
$\hat{\sigma}_{Tot}^2$	8.4	100%	4.22	100%

the true mean of the standard deviation,  $\mu_{s_{dp}}$ , is  $12.3 \pm 4.3$  nm ( $\pm 35\%$ ). The values of  $\mu_{d_p}$  and  $\sigma_{d_p}$  of a *specific* sample for which a single measurement has been performed may be known within  $\pm 14\%$ , and  $\pm 33\%$ , respectively. The confidence intervals for  $\mu_{d_p}$  and  $\sigma_{d_p}$  for any *unmeasured* sample produced by this process are  $32.5 \pm 8.9$  nm ( $\pm 27\%$ ) and  $12.3 \pm 6.7$  nm ( $\pm 54\%$ ), respectively, however a larger number of samples beyond the three used here would likely narrow these intervals.

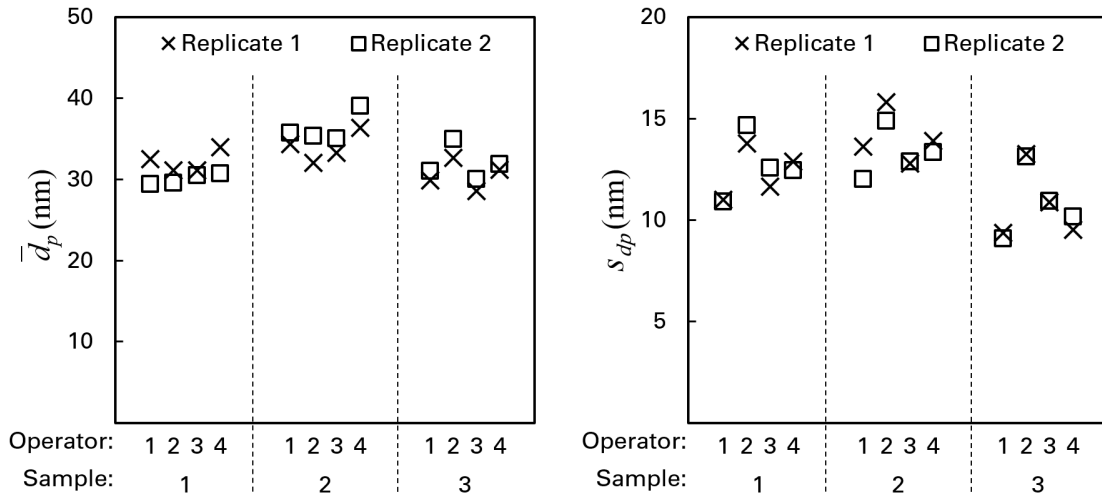


Figure 4.3: Primary particle diameter mean and standard deviation for each Gage R & R replicate.

For both  $\overline{d_p}$ , and  $s_{d_p}$ , the total variance is almost evenly split between sample and measurement system effects. Nearly all the measurement system variation for  $\overline{d_p}$  is due to repeatability - only 6.3% of the overall variance is attributable to operator effect. This is strong evidence that randomization and CSES semi-automation were effective in reducing operator bias. This claim is bolstered through a direct comparison of the fluctuation in measurements with and without bias controls. As reported earlier in Sec. 4.1, the non-bias controlled measurements of 2<sup>nd</sup> preliminary test fluctuated 18.9% and 17.6% for each of two samples across three operators. With bias-controls in place for the Gage R & R study, however, measurements by these same operators (Gage R & R operators 1,3 and 4) fluctuated only 4.9%, 9.8%, and 7.5% for each of the three samples. This amounts to a 59.5% reduction in the average fluctuation of measurements across the same set of operators.

In contrast, operator effects account for 43.1% of the overall variance of  $s_{d_p}$ . An inspection of operator measurements on identical image regions revealed that operators showed a clear preference for the range of primary particle diameters that they were willing to consider. This makes sense considering that primary particle range is the only user-adjustable parameter involved in CSES.

The two methods for combining operator measurements for each sample, produced comparable results as shown in Table 4.2. The approach outlined in Eqs. 4.6-4.8 therefore offers a way to estimate the values and uncertainties of  $\mu_{d_p}$  and  $\sigma_{d_p}$  in the absence of a large number of measurement replicates. Additionally, if measurements by multiple operators cannot be obtained, replicate measurements by a single operator utilizing bias limiting methods may serve as an adequate surrogate.

Table 4.2: Primary particle diameter mean and standard deviation of each sample using two methods for combining operator measurements. Intervals are at the 95% confidence level.

Sample	$\overline{d_p}$		$s_{d_p}$	
	Eq. 4.5	Eqs. 4.6-4.8	Eq. 4.5	Eqs. 4.6-4.8
1	31.1 ± 4.3%	31.3 ± 4.4%	12.5 ± 17.1%	12.6 ± 15.0%
2	35.1 ± 8.1%	35.7 ± 6.5%	13.6 ± 13.8%	13.7 ± 14.4%
3	31.3 ± 9.8%	31.5 ± 8.4%	10.8 ± 25.7%	11.2 ± 20.7%

The overall uncertainty of the combined result of  $r$  replicates on given sample  $A$ , could then be estimated following Sec. 4.2.3, by combining  $\sigma_O^2$  from Table 4.1 with Eq. 4.7, yielding:

$$u_{Y_{A,C}} = \left( 1 / \sum_{k=1}^r w_{Ak} + \hat{\sigma}_O^2 \right)^{1/2} \quad (4.11)$$

where now, the term in the summation corresponds to  $w_{Ak} = 1/\hat{\sigma}_E^2$ . If  $\hat{\sigma}_E^2$  can be considered to be constant across replicates, as is often the case, then Eq. 4.11 simplifies to:

$$u_{Y_{A,C}} = \left( \frac{\hat{\sigma}_E^2}{r} + \hat{\sigma}_O^2 \right)^{1/2} \quad (4.12)$$

As before, if  $2u_{Y_{A,C}}$  does not encompass the value of  $Y_A$  from most measurement replicates, Eq. 4.8 can be applied.

### 4.3.2 Automated Results

The three automated methods were applied to each of the 37, 41, and 73 aggregate images of samples 1, 2, and 3, respectively. The Gage R & R measurements found diameters ranging 6 – 79 nm, 8 – 86 nm, and 8 – 82 nm for these three samples. These ranges were supplied as inputs to the two CHT-based algorithms. The re-

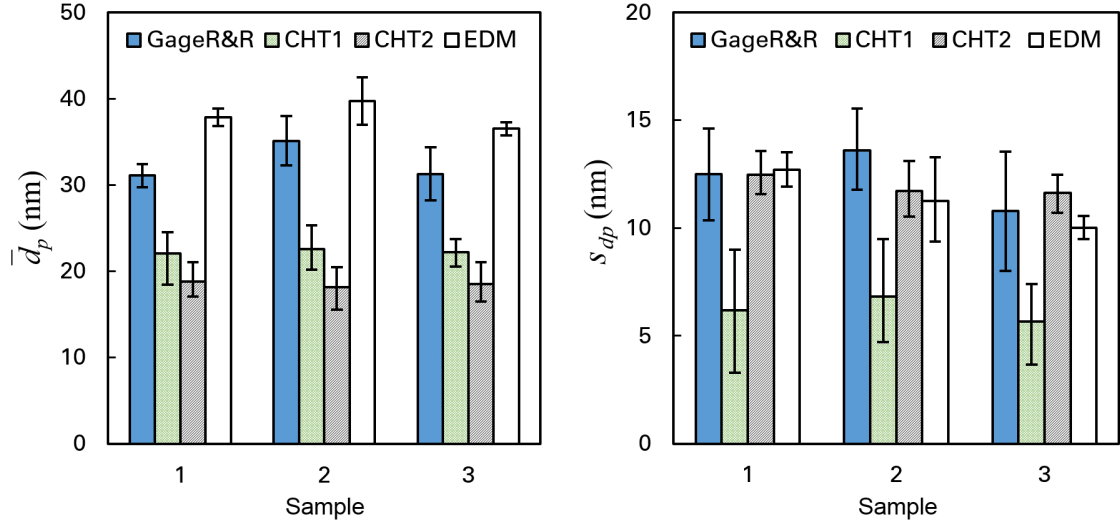


Figure 4.4: Primary particle diameter mean and standard deviation for each sample as found by CSES (Gage R & R), binary-CHT (CHT1), Canny-CHT (CHT2), and Euclidean distance mapping (EDM) methods.

maining parameters for each algorithm were varied as discussed in Sec. 4.2.4.1. The results of all three automated measurements are shown in Fig. 4.4 alongside the Gage R & R results combined across operators using Eq. 4.5. Both CHT-based algorithms drastically underpredicted  $\hat{\mu}_{d_p}$  for all three samples. The binary-CHT method also substantially underestimated  $\hat{\sigma}_{d_p}$ , while the Canny-CHT method generally matched the Gage R & R  $\hat{\sigma}_{d_p}$  results. While performing better than CHT, the EDM method consistently overpredicted  $\hat{\mu}_{d_p}$ . For  $\hat{\sigma}_{d_p}$ , the results are statistically equivalent to the Canny-CHT results. Inaccuracy of the EDM results can be credited to the model's assumed calibration values and lognormal distribution. The latter is questionable given that the distributions found from the semi-automated measurements almost uniformly failed standard tests for both normality and lognormality.

The error bars in Fig. 4.4 are at the 95% confidence level. For the CHT

results, the error bars reflect the statistical precision of the mean combined with uncertainty caused by varying input parameters other than diameter range. Error bars for the EDM method include the published uncertainty of the calibration constants [133], and uncertainty in the sigmoidal fits, but do not consider repeatability and reproducibility uncertainty of the calibration.

The two CHT methods showed sensitivity to several of the input parameters, most prominently, the lower-bound diameter. For the binary-CHT method, the value of  $\hat{\mu}_{d_p}$  rose 1 nm for each 1 nm increase in  $d_{p,\min}$ , and for Canny-CHT,  $\hat{\mu}_{d_p}$  increased at twice that rate. This large dependence on  $d_{p,\min}$  is problematic. To force either CHT method to yield a value for  $\hat{\mu}_{d_p}$  that matches the Gage R & R results for all three samples, a value for  $d_{p,\min}$  between 17 and 19 nm must be specified. There is no practical reason to choose an input value within this range without having foreknowledge of the distribution. Choice of such a value would also truncate the bottom 16% of the distribution. One possibility for overcoming this difficulty is through a weighted scoring scheme for the Hough Transform that is a function of diameter.

### 4.3.3 Mass Specific Surface Area Results

The Gage R & R results for the skewness of the primary particle size distribution,  $\gamma_{d_p}$ , and the mean projected overlap coefficient  $\overline{C_{ov,p}}$  are given in Table 4.3. As was the case with  $\overline{d_p}$  and  $s_{d_p}$ , sample-operator interaction was found to be negligible for both  $\gamma_{d_p}$  and  $\overline{C_{ov,p}}$ , ( $p = 0.055$  and  $0.255$ , respectively). Hence,  $\hat{\sigma}_{PO}^2$  is not

Table 4.3: Components of variance in the skewness of the primary particle size distribution and the mean projected overlap coefficient, as quantified by Gage R & R analysis.

Variance Component	$\hat{\gamma}_{d_p}$		$\overline{C_{ov,p}}$	
	Variance	% Variance	Variance	% Variance
$\hat{\sigma}_P^2$	0.016	14.8%	$5.7 \times 10^{-6}$	0.7%
$\hat{\sigma}_O^2$	0.031	29.6%	$7.4 \times 10^{-4}$	83.5%
$\hat{\sigma}_E^2$	0.059	55.6%	$1.4 \times 10^{-4}$	15.8%
$\hat{\sigma}_M^2$	0.090	85.2%	$8.8 \times 10^{-4}$	99.4%
$\hat{\sigma}_{Tot}^2$	0.106	100%	$8.9 \times 10^{-4}$	100%

included in the analysis. Sample effects have a much weaker impact on the overall variance here than what was found for  $\overline{d_p}$  and  $s_{d_p}$ , and in the case of  $\overline{C_{ov,p}}$ , sample effects are essentially zero. Another striking result is the heavy influence of operator on  $\overline{C_{ov,p}}$  measurements, where  $\hat{\sigma}_O^2$  accounts for nearly 84% of the overall variance. Clearly, the magnitude of primary particle overlap that can be interpreted from a TEM image varies greatly from one operator to the next. The true mean of the primary particle distribution skewness,  $\mu_{\gamma_{dp}}$ , is  $0.717 \pm 0.485$  ( $\pm 67\%$ ), while the true mean of the mean projected overlap coefficient,  $\mu_{\overline{C_{ov,p}}}$ , is  $0.277 \pm 0.045$  ( $\pm 16\%$ ).

Mass specific surface area was measured for each of the three soot samples using two nitrogen adsorption methods, and four TEM methods, as previously introduced. The results are presented in Fig. 4.5. The external surface area measured by the t-plot method for each sample was 9%, 12%, and 12% lower than the BET surface area for each respective sample. In other words, on average, 11% of the total surface area accessible to the adsorbing  $N_2$  molecules, came from micropores on the soot surface. The porosities (i.e. void fraction) determined by t-plot analysis were

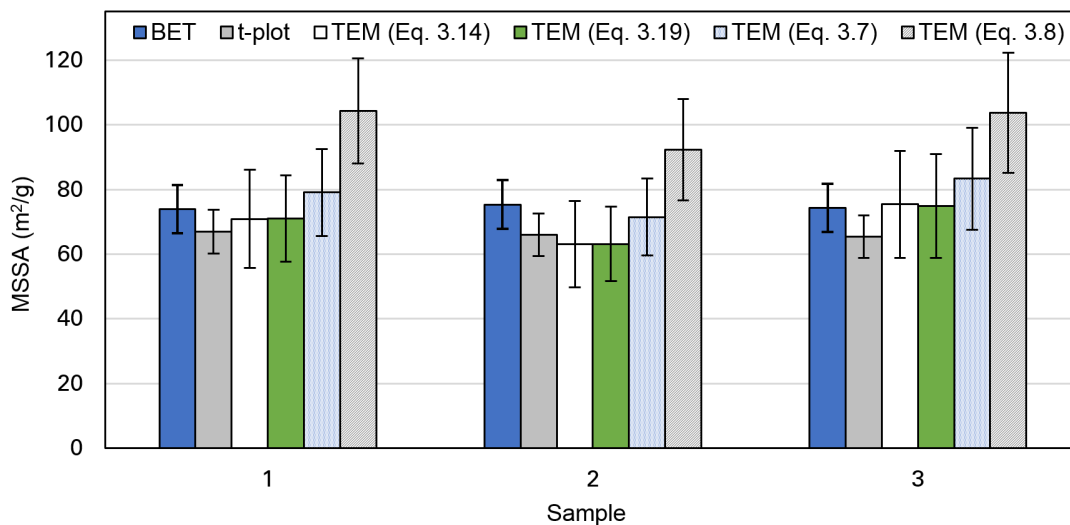


Figure 4.5: Mass specific surface area of the 3 soot samples as determined from the BET and t-plot adsorption methods, and from 4 different TEM methods.

relatively low; 1.5%, 1.7%, and 1.7%, for samples 1, 2, and 3, respectively.

Of the TEM-based methods, two approaches modeled soot as partially-sintered, polydisperse primary particles (Eq. 3.10). The only difference was how each calculates the reduction in VSSA due to overlap. The method utilizing Eq. 3.14, was derived from monodisperse simulations and assumed no volume lost to overlap, while the method of Eq. 3.19 calculated both the surface area and volume lost within each overlapping primary particle pair. There was a negligible difference ( $< 1\%$ ) between the MSSA results from these two methods, so for all practical purposes they are equivalent. The two remaining TEM methods modeled soot as non-sintered primary particles that were and either polydisperse, (Eq. 3.7), or monodisperse, (Eq. 3.8). Both methods produced MSSA results that were substantially larger than the models taking overlap into account. On average, MSSA derived from Eq. 3.7 and Eq. 3.8 were respectively 12% and 44% greater than the models with overlap.

While the monodisperse model (Eq. 3.8) clearly overstates the true soot surface area, the remaining models warrant greater scrutiny. The model of polydisperse primary particles in point-contact (Eq. 3.7) gives a result that is, on average, 5% greater than the BET surface area and 18% greater than the t-plot external surface area. The MSSA values calculated from the models of partially-sintered polydisperse primary particles fall, on average, in between those from BET and t-plot methods: (6% below BET and 5% above t-plot). Since pores on aggregate surfaces are not included in models for image derived surface area, one might expect the TEM results to hew more closely to the t-plot values, however no such trend is apparent here.

For the purpose of modeling soot oxidation, we are most interested in the surface area that is accessible to oxidizing gases. At high flame temperatures ( $>1000$  K) oxidizing gases are not expected to fully penetrate micropores [30], defined as pores less than 2 nm wide [260]. Hence the available surface area for oxidation in the soot flame is expected to fall somewhere between the values reported by BET and t-plot analyses. The TEM measurements incorporating overlap and polydispersity of primary particles best meet this criteria, and are therefore assessed as the best TEM-based method for evaluating soot surface area. At the same time, broad statements about the "correctness" of this approach are cautioned against. For one, even with operator bias minimized, TEM-based MSSA measurements consistently have uncertainties of  $\pm \sim 20\%$ , when repeatability and reproducibility is included. This is reflected in the error bars of Fig. 4.5. Hence, for the measurement performed here, all polydisperse models are "valid" in a statistical sense, even if models accounting for overlap are preferable on both empirical and theoretical grounds. Additionally, if

oxidation should result in the further opening of surface pores, or make the interior of soot particles available to oxidizers, the validity of any TEM-based method falls into question.

## 4.4 Conclusions

The method of Gage R & R was applied to the measurement of soot primary particle size distributions from TEM images. Uncertainties stemming from the sample, operator, and random effect were quantified, and the effectiveness of bias minimization was assessed. The Gage R & R results also served as the baseline against for evaluating the performance of different automated TEM measurement methods. Lastly, soot surface area was determined from TEM images using four different models and compared to the BET and t-plot adsorption methods. This study revealed several important findings:

1. **Uncertainties in TEM soot measurements are substantially greater than generally acknowledged.** Monte Carlo sampling of Gage R & R variance distributions found that 95% confidence intervals for a single estimate of  $\mu_{d_p}$  and  $\sigma_{d_p}$  for a given sample were  $\pm 14\%$  and  $\pm 33\%$ , respectively. If sample-to-sample variation is taken into account, these uncertainties grow to  $\pm 18\%$  and  $\pm 35\%$ . These are substantially greater than the  $< \pm 3\%$  [22, 119, 126, 133] and  $< \pm 5\%$  [115, 133] often reported for  $\mu_{d_p}$  and  $\sigma_{d_p}$ , respectively, which do not consider variation due to the measurement method. The 95% confidence of  $\mu_{d_p}$  and  $\sigma_{d_p}$  for any single *unmeasured* sample producible by

the co-flow flame is  $\pm 27\%$  and  $\pm 54\%$ , respectively. Uncertainties can be reduced by combining measurements across operators (Eqs. 4.6-4.8) or across replicates of a single operator (Eq. 4.11). Doing so incorporates an estimate of repeatability and reproducibility uncertainties without demanding a large number of replicates.

- 2. Bias minimization was successful.** Efforts to minimize operator bias through randomized image regions and use of the CSES algorithm were largely successful, especially for measurements of mean primary particle diameter. Operator effect accounted for only 6.3% of the total variance of  $\hat{\mu}_{d_p}$ , and the measurement fluctuation of  $\overline{d_p}$ , which averaged 18% without bias controls, dropped to 7.4% among the same operators once bias controls were in place. For  $\hat{\sigma}_{d_p}$ , operator effects still accounted for 43.1% of the overall variance, indicating that even with bias controls, operators showed a preference in the *range* of primary particles they were willing to consider.
- 3. Automated methods of primary particle size distribution measurements were unreliable.** All three automated methods that were considered failed to produce results consistent with the Gage R & R measurements. The EDM method came closest, but consistently overestimated  $\hat{\mu}_{d_p}$ . A calibration tailored to the soot produced by a specific process might improve this method's performance, although the need to assume a distribution shape will remain a source of uncertainty. On the other hand, both CHT methods greatly underestimated  $\hat{\mu}_{d_p}$  and the binary-CHT method also underestimated  $\hat{\sigma}_{d_p}$ . In-

accuracies in the CHT methods are mostly attributable to a high sensitivity to the algorithms' lower-bound diameter input. Less sensitivity to this and other input parameters is needed to make this approach robust enough to use broadly. Given the difficulties presented by existing automated techniques, the semi-automated CSES algorithm (or if unavailable, manual measurements), with randomization to reduce bias, constitutes the best method for evaluating soot primary particle size distributions from TEM images.

4. **TEM image measurement of primary particles, accounting for polydispersity and overlap, is a valid method for estimating soot surface area.** The soot surface area accessible to flame oxidizers is expected to fall between the t-plot external surface area, which does not include additional area within micropores, and the BET surface area, which does. Both TEM methods modeling primary particles as partially-sintered and polydisperse (i.e. utilizing Eq. 3.14 or Eq. 3.19) met this criterion. Modeling primary particles as polydisperse, but not partially sintered (i.e. no overlap), also gave reasonable results, but were consistently higher than the target range for validity. The model of monodisperse primary particles in single point contact, though prevalent in the literature, vastly overstated the soot surface area and should be dispensed with.

## Chapter 5: Results

### 5.1 Axial Flame Velocity Results

Soot flame velocity was determined by tracking the axial motion of a deliberate perturbation to the flame using high frame rate video. Videos were captured on four different occasions, and three disturbances were analyzed from each video for a total of 12 video sections analyzed. From this, a total of 135 data points were obtained. The axial location vs. time data was most accurately represented by a 2nd order polynomial fit. The corresponding plot of velocity vs. height above burner (HAB) is presented in Fig. 5.1.

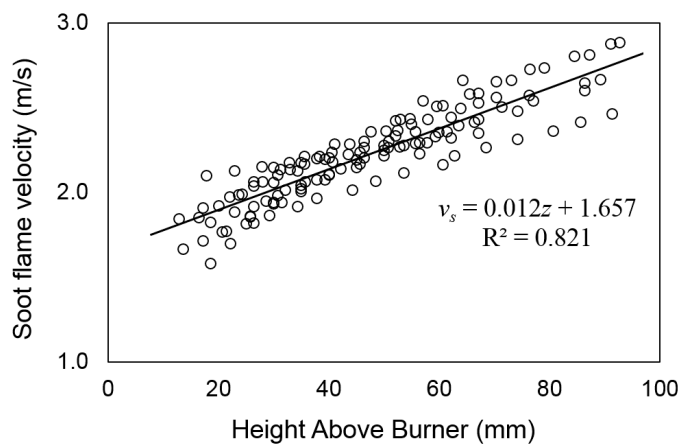


Figure 5.1: Soot flame velocity vs. height above burner.

Soot flame velocity is seen to increase with height above burner due to buoyancy. The soot velocity,  $v_s$  at a given height above burner,  $z$ , is then determined from the linear best fit of the data,  $v_s = az + b$ , where  $a = 0.012 \pm 0.0021$  and  $b = 1.657 \pm 0.168$ . Velocities calculated in this manner have an uncertainty of  $\pm 9\%$ .

## 5.2 Temperature, Soot Volume Fraction, and Gas Species Concentration Results

Measurements within the soot flame of temperature, soot volume fraction, and gas species concentrations were reported in detail in the dissertation of Guo [224]. Key results and additional discussion relevant to the preset study are provided here.

### 5.2.1 Temperature and Soot Volume Fraction

Figure 5.2 shows the radial profiles of temperature and soot volume fraction at selected locations within the soot flame. At a given HAB, temperatures were nearly uniform in the radial direction. At a given height, the radial temperature differed by no more than 150 K. Temperatures are somewhat lower where soot volume fractions peak, due to soot radiative heat loss. The soot volume fraction results indicate a hollow soot column.

Figure 5.3 plots soot flame temperature and integrated soot volume fraction against height above burner. Temperatures at each height were taken as the radial average of temperatures at locations whose soot volume fraction exceeded half the local maximum. This can be considered the temperature at which most soot oxi-

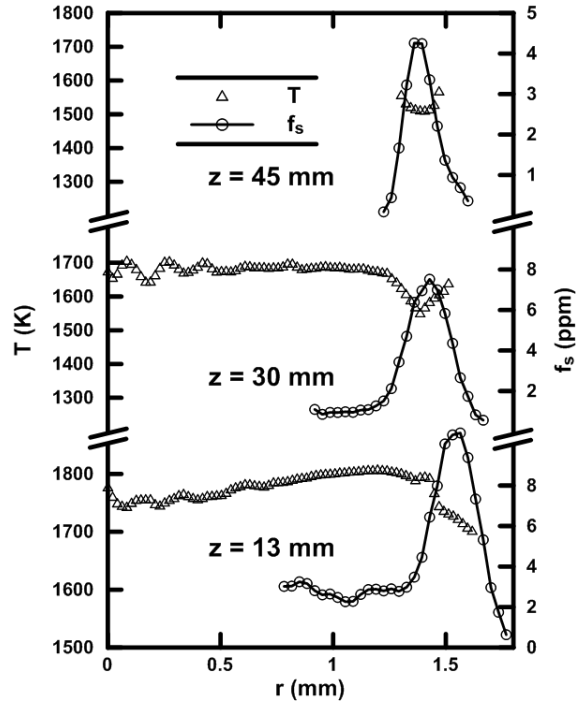


Figure 5.2: Radial temperature and soot volume fraction at heights of 13, 30, and 45 mm. Figure from Ref. [224].

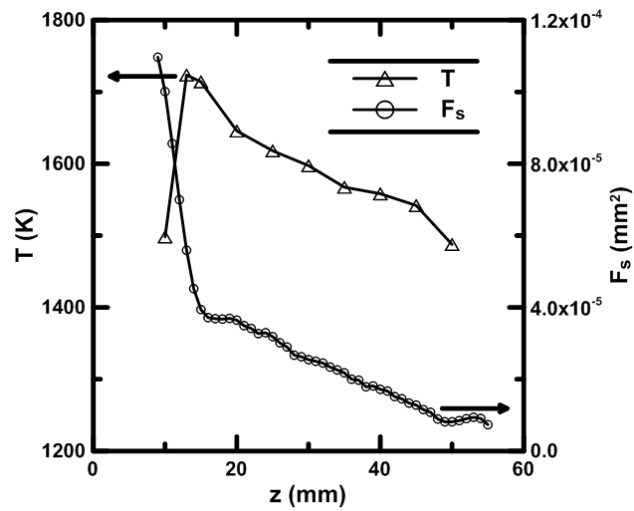


Figure 5.3: Temperature and integrated soot volume fraction at each HAB. Figure from Ref. [224].

ation occurred at each height. Values ranged from 1500 K at 50 mm to a peak of 1725 K at 13 mm. Integrated soot volume fraction,  $F_s$ , continuously decreased with height due to oxidation, dropping from  $1.1 \times 10^{-4}$  to  $8.1 \times 10^{-6}$  mm<sup>2</sup>. Normalizing  $F_s$  by the soot flame cross-sectional area yields an average soot volume fraction,  $f_s$ , between 1-15 ppm.

## 5.2.2 Gas Species Concentrations

Major species concentrations measured by gas chromatography and radical species, estimated from an assumption of full equilibrium, are provided in Fig. 5.4. Critical to the present study are concentrations of O<sub>2</sub> and OH. The former has a peak mole fraction of 10% at an HAB of 10 mm due to the entrained air from co-flow flame below. It quickly drops to its minimum of 0.8% at a height of 20 mm due to consumption by the hydrogen flame and soot. It climbs steadily thereafter as O<sub>2</sub> diffuses from the air.

The OH radical reaches a peak mole fraction of 0.055% at heights of 13 and 15 mm above the ring burner, corresponding with the peak flame temperatures. Thereafter it falls steadily until reaching a mole fraction of 0.007% at 50 mm. Uncertainty in OH concentration is estimated at  $\pm 40\%$  as propagated from temperature and species measurement uncertainties.

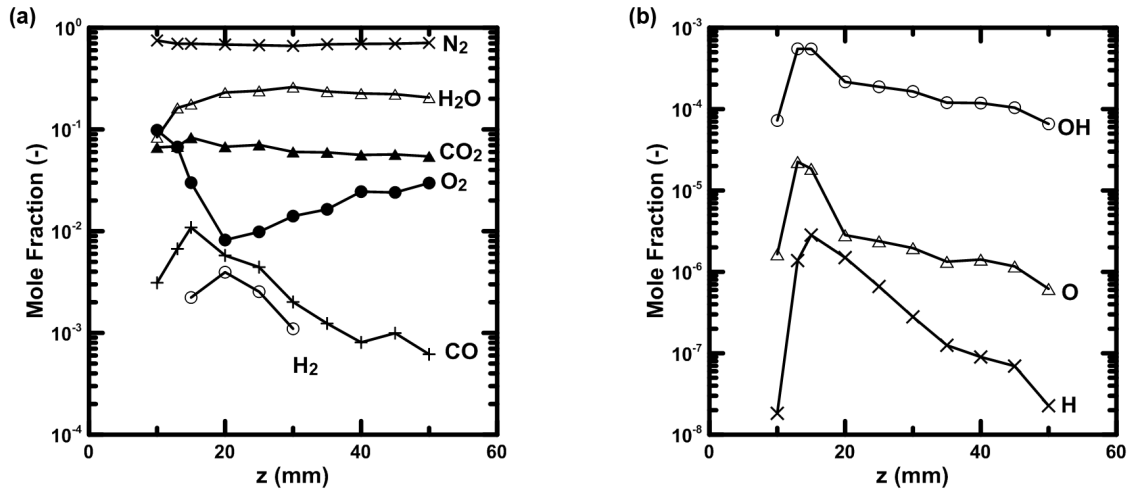


Figure 5.4: Species concentrations vs. height above burner. (a) Measured stable species. (b) Estimated radical species. Figures from Ref. [224].

## 5.3 TEM Measurement Results

### 5.3.1 Primary Particle Measurements

Soot primary particles underwent both qualitative and quantitative changes as oxidation progressed with increasing height above burner. TEM images representative of soot at heights of 10, 15, 25, and 50 mm are shown in Figure 5.5, and illustrate a clear progression in primary particle structure. The primary particles at  $HAB = 10$  mm are large, spherical, and well-defined, As height increases, they grow progressively smaller, and more poorly defined. By  $HAB = 50$  mm, there is a clear loss of sphericity, which some have suggested corresponds to exposure of the amorphous primary particle core [264].

Primary particle measurements were performed on TEM images obtained at each sampled location within the soot flame. An average of 495 primary particles,

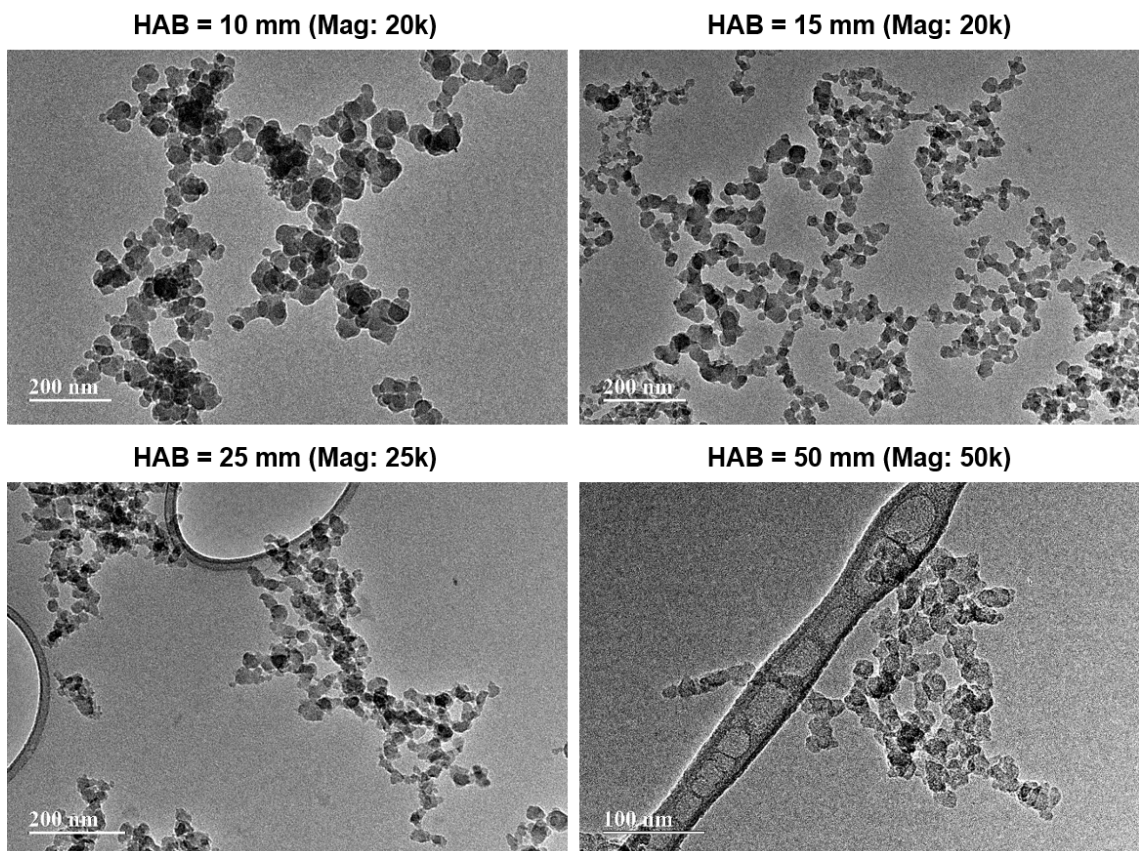


Figure 5.5: Representative images of primary particles obtained at HABs of 10, 15, 25, and 50 mm.

and no fewer than 355, were measured on each image set. At several locations in the flame, multiple samples were obtained; four were taken at HAB = 10 mm, while two samples were retrieved at both HAB = 13 and 40 mm. Values reported are the sample averages at these locations. The sample-to-sample variation was consistent with that reported in the Gage R & R study (Ch. 4).

The primary particle size distributions (PPSD) for samples obtained at each HAB are provided in Figs. 5.6 and 5.7. PPSDs shift downward with increasing HAB, as primary particles of all sizes shrink from oxidation. The shape of the

distribution also changes. An Anderson-Darling test for normality, which is robust for both symmetric and asymmetric distributions [265], was administered for each data set. At flame locations 20 mm and below, PPSDs most closely follow a normal distribution while above 20 mm, with the exception of HAB = 45 mm, distributions are better characterized as lognormal.

The distributions of primary particle diameters are summarized by their mean, standard deviation, and skewness, while distributions of overlap between primary particles are summarized by the mean projected overlap coefficient. The best estimates for each of these measured terms, respectively denoted  $\hat{\mu}_{d_p}$ ,  $\hat{\sigma}_{d_p}$ ,  $\hat{\gamma}_{d_p}$ , and  $\overline{C_{ov,p}}$ , are plotted against height above burner Fig. 5.8.

As the soot column travels upward, mean primary particle diameter and standard deviation steadily decrease due to surface oxidation. Distribution skewness shows an increasing trend with HAB, consistent with the evolution from normal to lognormal shape. Primary particle overlap shows a slight decreasing trend as oxidation proceeds. This suggests that primary particles are oxidizing in place with respect to each other, rather than compacting due to oxidative sintering. This contrasts with a study of furnace-oxidized soot which did observe compaction [52].

The uncertainties reflected in the error bars in Fig. 5.8, were obtained from the results of Gage R & R analysis and thus take into consideration variation due to different samples, operators, and replicate measurements. The relative standard uncertainties for  $\hat{\mu}_{d_p}$ ,  $\hat{\sigma}_{d_p}$ ,  $\hat{\gamma}_{d_p}$ ,  $\overline{C_{ov,p}}$  from a single measurement on a single sample are 9.0%, 17.5%, 34%, and 8.1%, respectively. Note that applying Gage R & R results in this way assumes Gage linearity, which is a reasonable, but not assured, assumption.

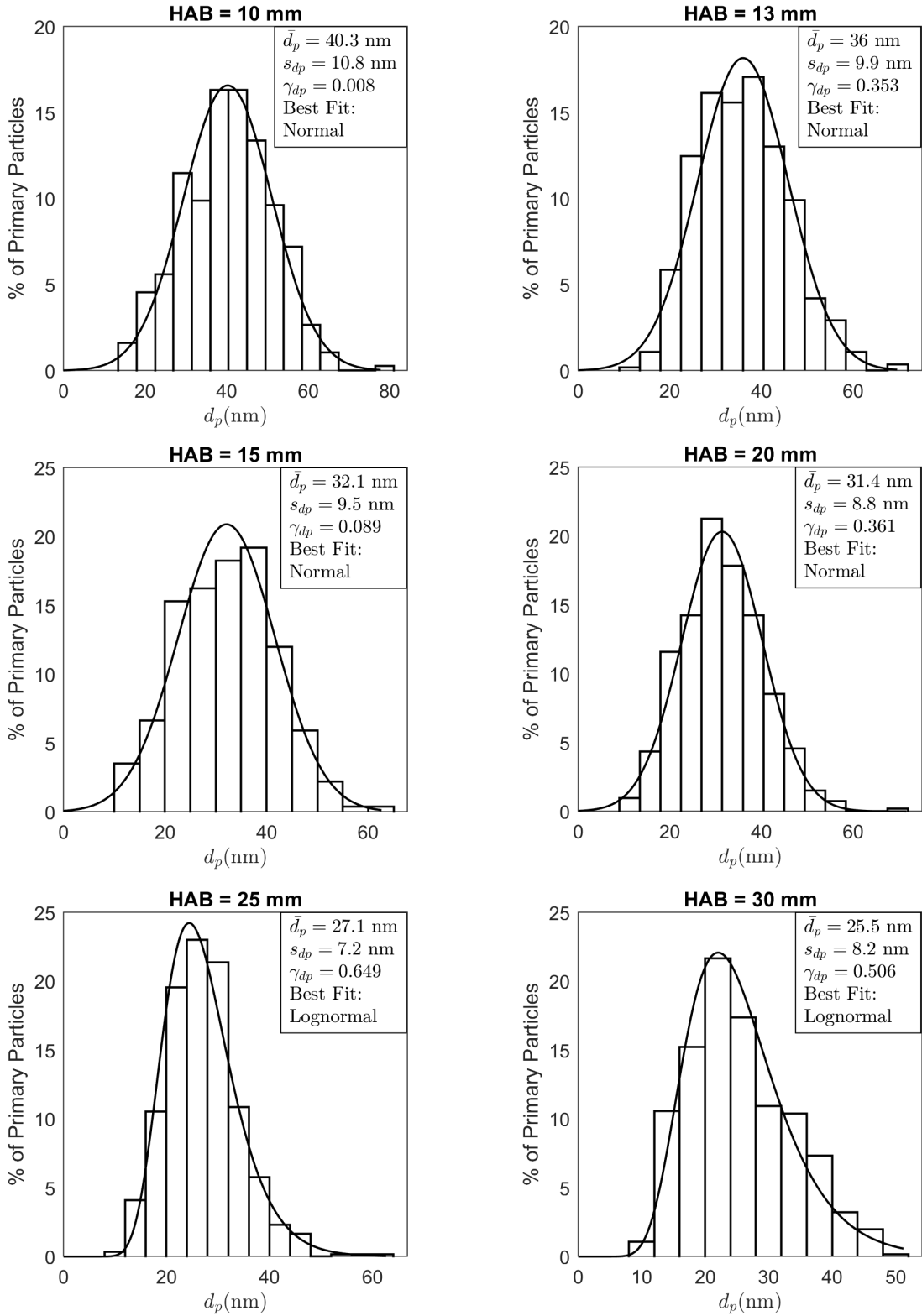


Figure 5.6: PPSDs at heights above burner of 10 to 30 mm.

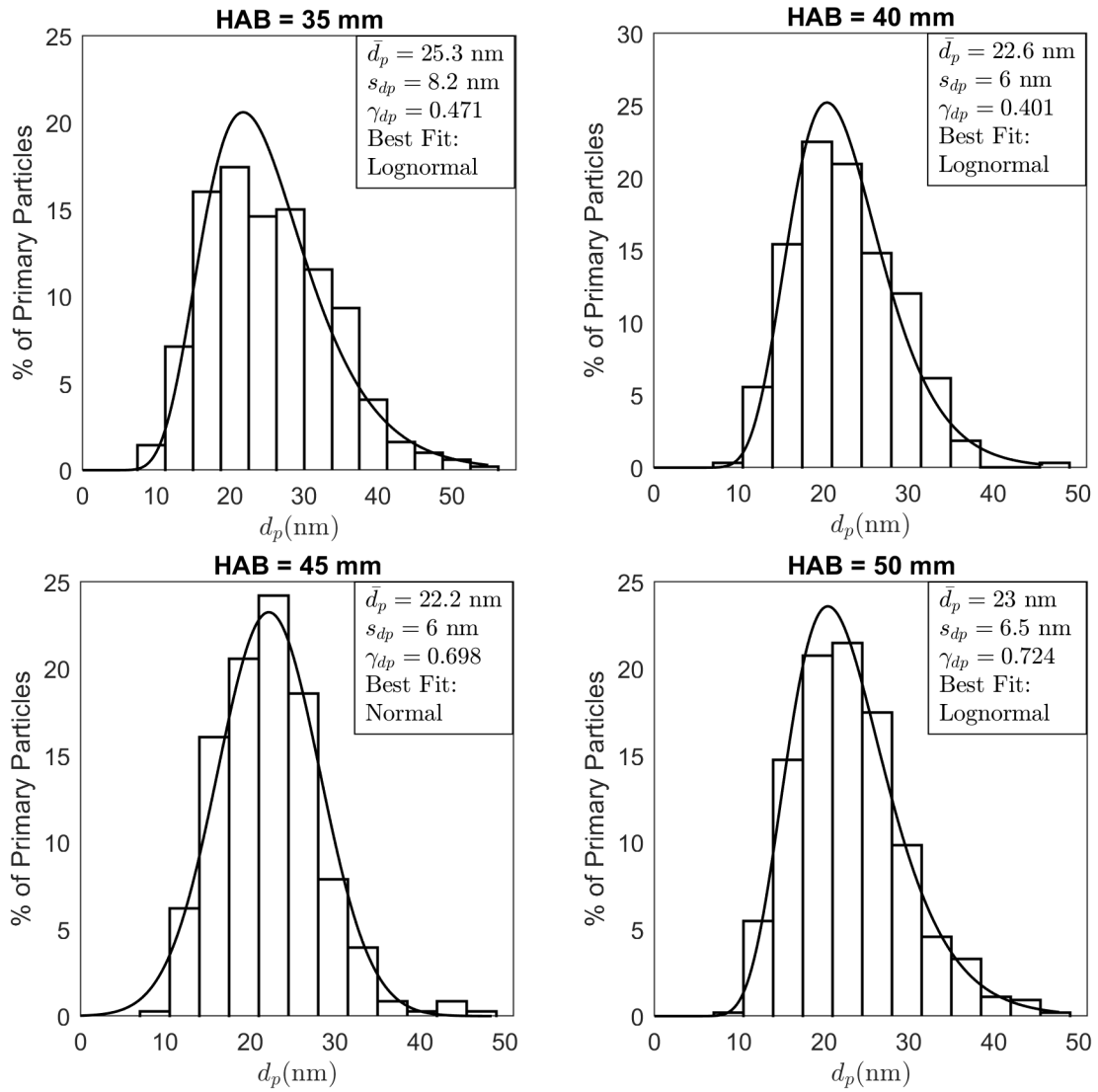


Figure 5.7: PPSDs at heights above burner of 35 to 50 mm.

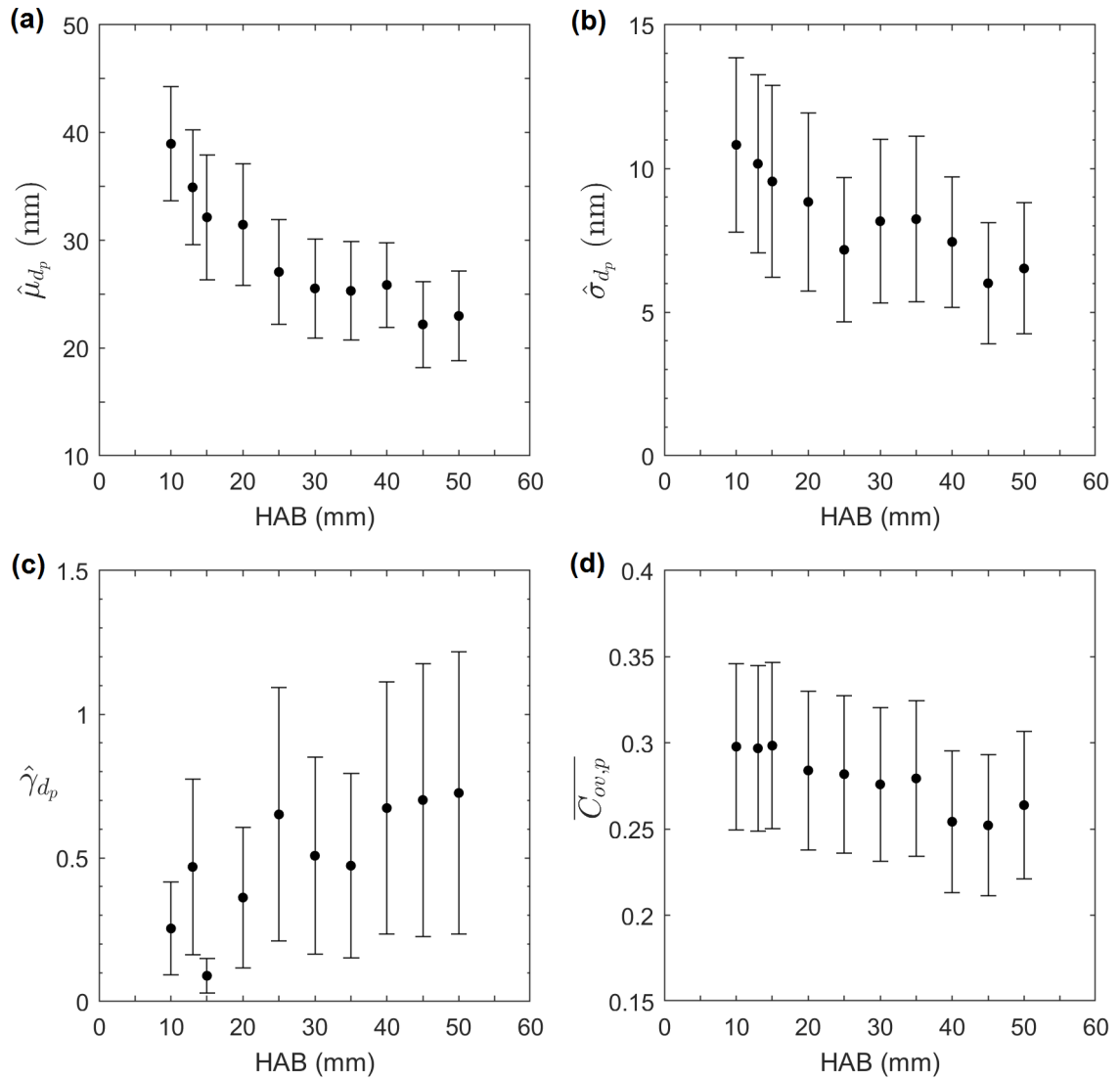


Figure 5.8: Primary particle measurements vs. height above burner. (a) Mean primary particle diameter. (b) Standard deviation of primary particle diameter. (c) Skewness of primary particle diameter. (d) Mean projected overlap coefficient.

tion. The proportions of these uncertainties stemming from sample, replicate, and operator are those given in Tables 4.1 and 4.3. For flame locations in which multiple samples were obtained, the uncertainty was reduced following Eq. 4.11, but with  $\hat{\sigma}_p^2$  now used to compute the summation term. The error bars for  $\hat{\gamma}_{d_p}$ , and  $\overline{C_{ov,p}}$  appear particularly large, owing to the relatively narrow range of results and to the large repeatability and reproducibility uncertainties inherent in these measurements.

### 5.3.2 Soot Surface Area

Volume specific surface area (VSSA) was calculated assuming a model of partially sintered, polydisperse primary particles (Eq. 3.10). This model was shown in Ch. 4 to best match results obtained from well-established surface adsorption methods. That chapter also showed the equivalence of the two approaches (Eq. 3.14 vs. 3.19) for calculating the terms in the VSSA overlap factor,  $F_{ov}$  (Eq. 3.9). The approach of Eq. 3.14 was used here due to its mathematical simplicity.

The VSSA along with the associated mass specific surface area (MSSA) are plotted against HAB in Fig. 5.9, and  $F_{ov}$  vs. HAB is given in Fig. 5.10. Specific surface area increases with height above burner due to the steady reduction in primary particle size. MSSA rises from 62 g/m<sup>2</sup> at HAB = 10 mm, a value comparable to those measured in Chapter 4, to a peak of 119 g/m<sup>2</sup> at HAB = 45 mm. Specific surface area drops going from 45 mm to 50 mm. The difference is certainly within the experimental error, so this drop may simply be statistical. Another possibility is that primary particles are coalescing into larger units as has been observed by stud-

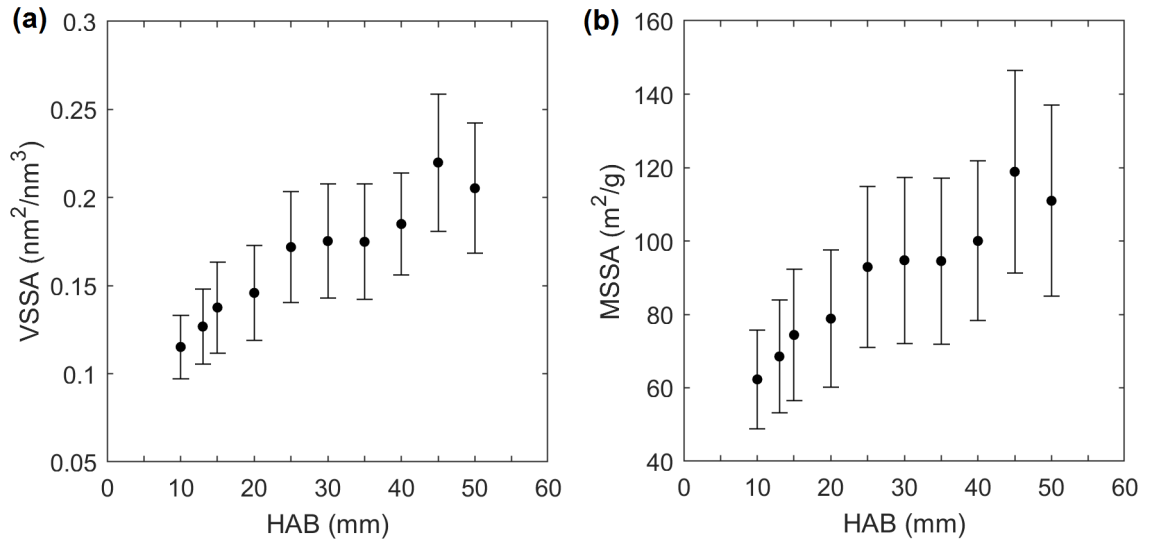


Figure 5.9: (a) Volume specific surface area, and (b) Mass specific surface area vs. height above burner.

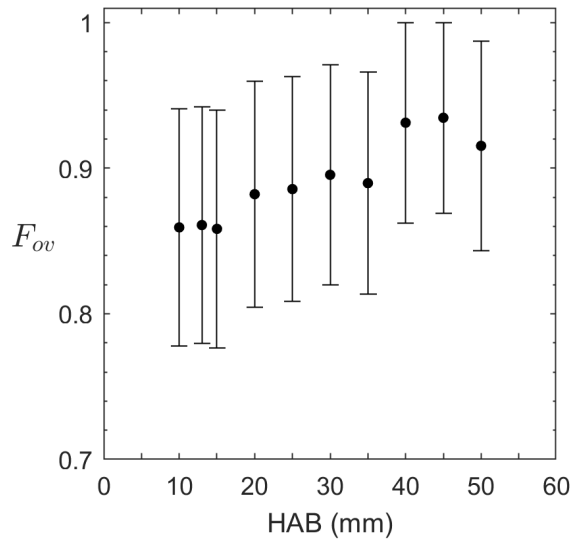


Figure 5.10: Specific surface area overlap factor vs. height above burner.

ies in an environmental TEM [264]. The error bars shown account for repeatability and reproducibility and are about  $\pm 18\%$  for VSSA and  $\pm 23\%$  for MSSA.

Looking at Fig. 5.10, overlap factor increases with HAB, consistent with the drop of overlap coefficient seen in Fig. 5.8).  $F_{ov}$  grows from 0.86 low in the flame to a peak of 0.93 at HAB = 40 and 45 mm. In other words, the reduction in specific surface area goes from 14% to 7% with respect to a point-contact, model of primary particles. Uncertainty in  $F_{ov}$  at the 95% confidence level is  $\sim \pm 9\%$ .

### 5.3.3 Soot Aggregate Morphology

Soot morphology was measured from TEM images obtained at each sampled location within the soot flame. At least 279 aggregates were analyzed from each sample's image set, with the exception of the sample at HAB = 40 mm, from which only 104 aggregates were measured due to their sparse deposition on the TEM grid. In the case of HAB = 50 mm, the TEM grid was too sparsely populated to obtain a sufficient number of aggregate images, so this flame location was omitted from soot morphology analysis.

To estimate the sources and magnitudes of the uncertainties of TEM-derived morphology, the operators and samples used in the Gage R & R study of Chapter 4 were again employed. Sets of 12, 15, and 20 aggregate images were randomly selected from each of the three respective samples. Each operator was instructed to create a binary image of each aggregate using the image processing tools available in the Aerosol Image Analyzer program. Some guidance was given to the operators in this

regard, but the image processing procedure and parameters used were ultimately left to the operator's best judgment. Once a binary representation of each aggregate was produced to the satisfaction of the operator, the maximum projected length,  $L$ , and projected aggregate area  $A_a$  were measured.

Gage R & R analysis of these measurements revealed that the magnitude of uncertainties due to random and operator effects were negligible ( $< 2\%$ ) compared to sample variation. Knowing this, a single operator measured the balance of aggregate images for the three samples, a total of 37, 41, and 73 aggregates, respectively. From this, standard uncertainties of 5% and 10% were determined for the means of  $L$  and  $A_a$ , respectively. These elemental uncertainties, combined with the published uncertainties of empirical constants, were used to derive the 95% confidence intervals given in the results below, following the methodology of Sec. 3.7.

Using the maximum projected length as the characteristic aggregate size, histograms of the soot aggregate size distribution at each HAB were generated, and are presented in Fig. 5.11. Without exception, the size distributions were lognormal. Hence, a lognormal fit to each histogram is also plotted, and the geometric mean,  $\overline{L}_g$ , is listed with each plot. No major trend stands out, however there does appear to be a shift in the distributions at heights of 35 mm and above. In these locations, the size distributions are bunched toward lower values of  $L$ . Likewise,  $\overline{L}_g$ , though fluctuating across flame locations, appears to be systematically lower for HAB = 35 to 45 mm than elsewhere in the flame. The significance of this will be examined further when fragmentation is discussed in Sec. 5.3.4.

Figure 5.12 presents the geometric mean of the radius of gyration, calculated

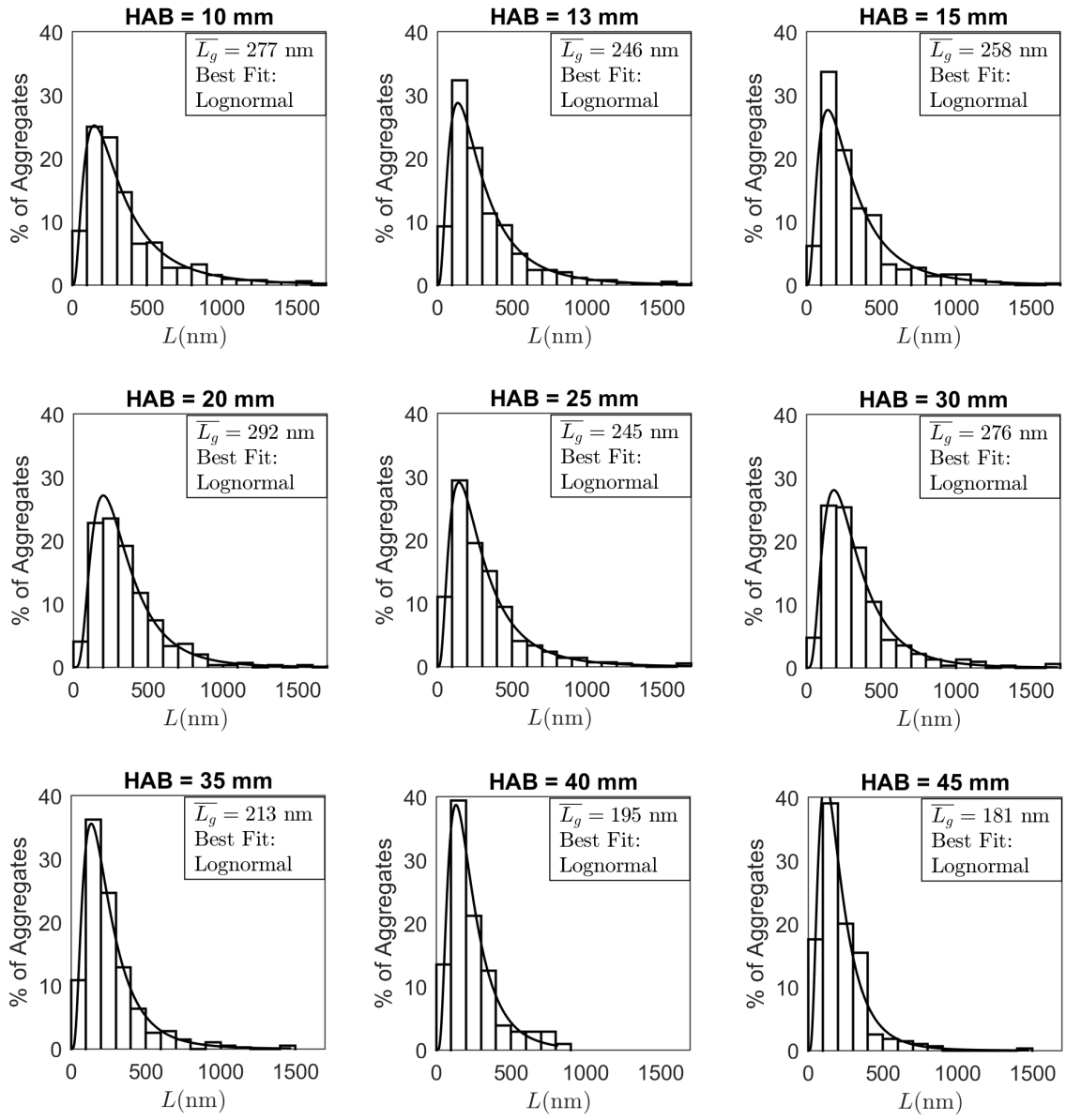


Figure 5.11: Soot aggregate size distributions based on the maximum projected length, at different heights above burner.

at each HAB using the three methods presented in Sec. 2.2.1.2. The first method, (denoted  $2DR_g$ ) simply calculates the 2-dimensional radius of gyration from a binary image of the aggregate, according to Eq. 2.5. The two other methods estimate a 3-dimensional value of  $R_g$  using the empirical formulas:  $R_g = \sqrt{LW}/\beta$ , (Eq. 2.6), where  $\beta = 2.34$  and  $R_g = L/2C$ , (Eq. 2.7), where  $C = 1.5$ . Uncertainties are  $\pm 11\%$ . From Fig. 5.12, the two empirical formulas give essentially the same result, and are consistently higher than the value of  $2DR_g$  by a factor of  $1.2 \pm 0.02$ . This is very near the factor of 1.24 found from simulated aggregates by Köylü et al. [90]. In general, the radius of gyration is essentially constant from  $HAB = 10$  to  $30$  mm, and then decreases steadily beginning at  $HAB = 35$  mm.

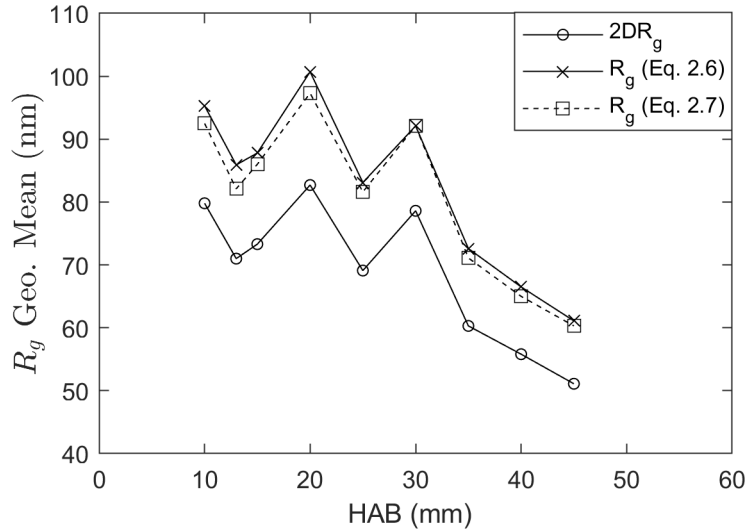


Figure 5.12: Radius of gyration geometric mean vs. height above burner.

The number of primary particles in each aggregate,  $N_{p,a}$ , was determined using Eq. 2.4. Then, for each HAB, the fractal dimension,  $D_f$ , and pre-factor,  $k_f$ , as defined by Eq. 2.3, were determined from the slope and intercept of a least-squares

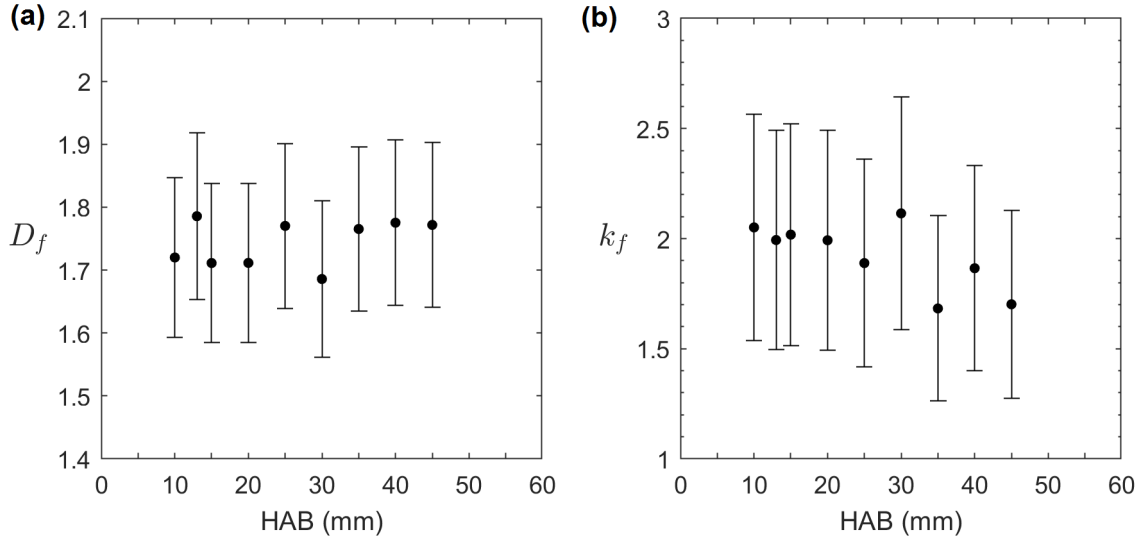


Figure 5.13: (a) Soot aggregate fractal dimension, and (b) pre-factor vs. height above burner.

fit of  $\ln(N_{p,a})$  vs.  $\ln(R_g/\bar{r}_p)$ . The fitted plots at each HAB are provided in Appendix C.1. The value of  $R_g$  calculated from Eq. 2.7 was used in this analysis. The fractal parameters at each HAB are shown in Fig. 5.13. Both  $D_f$  and  $k_f$  are very typical for flame generated soot [96, 98, 112, 115, 118, 123, 125–127]. The mean value of  $D_f$  is 1.74, which is very close to 1.78, the theoretical value for diffusion limited cluster aggregation [103].  $D_f$  is essentially constant, with a percent difference no greater than 5.7% between any two points in the flame. This is in contrast with groups such as Li et al. [118], who found fractal dimension to increase as soot matured and began to oxidize in a co-flowing flame. They interpreted this as compaction of the aggregates. Ma et al. [52] similarly observed aggregate compaction due to oxidation in a flow reactor, although a fractal analysis was not performed. The pre-factor,  $k_f$ , may trend mildly downward as HAB increases, with the most

pronounced drop at HAB = 35 mm. This corresponds with the reductions in  $L$  and  $R_g$  already noted at this flame location.

### 5.3.4 Soot Fragmentation

If soot aggregates undergo fragmentation at a particular point within the flame, this should be detected as drop in the geometric mean number of primary particles per aggregate,  $\overline{N_{pg,a}}$ , and should coincide with a shift in the probability distribution of  $N_{p,a}$ . Additionally, the total number flow rate of aggregates,  $\dot{N}_a$ , should increase at the same flame location.

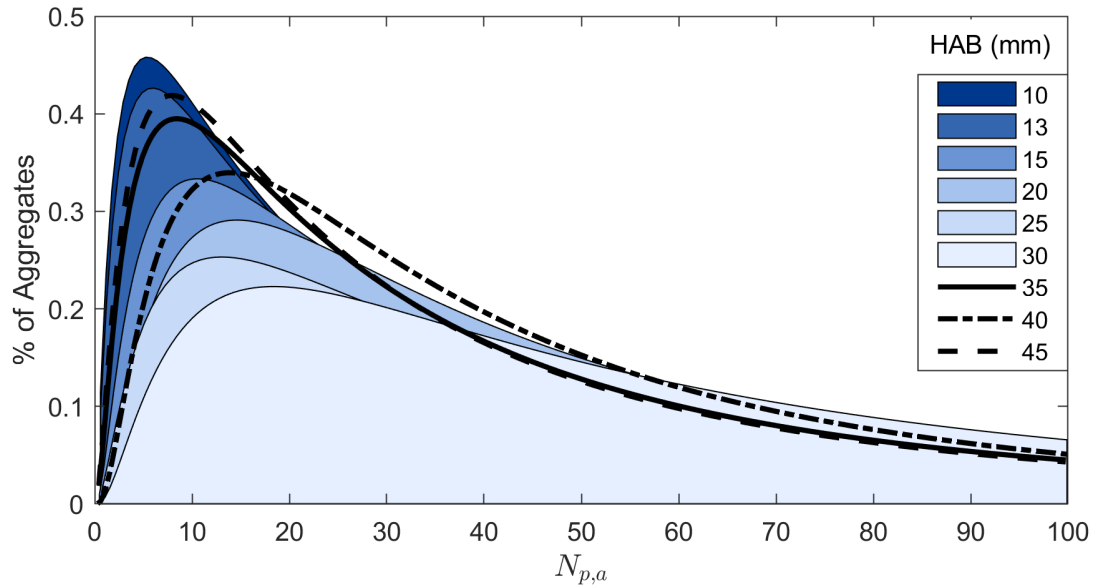


Figure 5.14: Probability distribution of the number of primary particles per aggregate at each height above burner.

The probability distributions of  $N_{p,a}$  at each sampled flame location are given in Fig. 5.14. The plotted distributions are shaded from dark to light as HAB increases from 10 to 30 mm. Within this range, the distribution becomes steadily less

weighted toward aggregates with small  $N_{p,a}$  and more weighted towards aggregates with greater  $N_{p,a}$ . However, the trend is broken at a height of 35 mm and thereafter, which are plotted as lines in Fig. 5.14. At HAB = 35 mm the distribution shifts back toward a greater percentage of aggregates with a small number of primary particles. This is indicative of large-scale fragmentation occurring across the aggregate population.

The pattern is mirrored in the plot of  $\overline{N_{pg,a}}$  vs. HAB in Fig. 5.15a, which exhibits a large drop in  $\overline{N_{pg,a}}$  at 35 mm. Figure 5.15b paints a corroborating picture, with a jump in  $\dot{N}_a$  beginning at 35 mm.

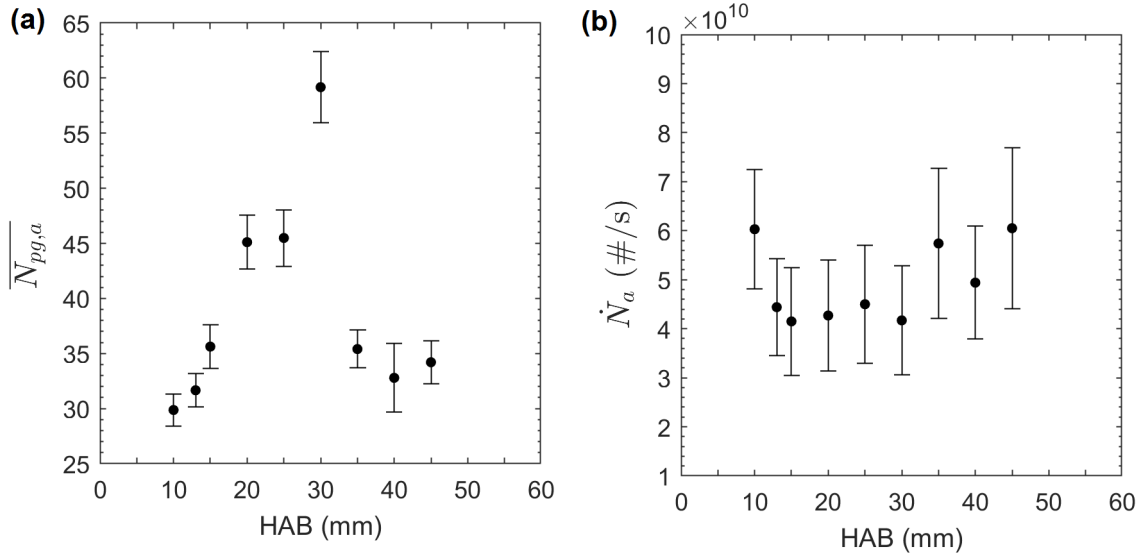


Figure 5.15: (a) Geometric mean number of primary particles per aggregate vs. height above burner. (b) Total number flow rate of aggregates vs. height above burner.

The increase in  $\overline{N_{pg,a}}$ , seen here in the lower regions of the soot flame, has also been observed by Li et al. [118] who attributed the trend to agglomeration by

aggregates, though offered no justification for this interpretation. Given that the large drop in  $\dot{N}_a$  from HAB 10 - 13 mm coincides with the region of greatest soot oxidation (see Fig. 5.3), this drop (and the attendant increase in  $\overline{N_{pg,a}}$ ) would seem to have more to do with the burnout of very small aggregates, than with aggregate agglomeration.

The decrease in  $\overline{N_{pg,a}}$ ,  $\overline{L_g}$ ,  $\overline{R_g}$ , and  $k_f$ , along with the increase in  $\dot{N}_a$ , all beginning at HAB = 35 mm is strong evidence that this location in the flame marks the onset of large-scale aggregate fragmentation. The residence time at this point in the flame is 19 ms. It is unclear why this should be the critical point for fragmentation to occur, as there are no major shifts in temperature or species concentrations at this location. However, given the lack of evidence for internal burning of soot primary particles (see Sec. 5.3.7), we can surmise that the mode of fragmentation is through the destruction of structurally weak points in the aggregate through surface oxidation, rather than through internal burning by O<sub>2</sub> that consumes material between primary particles from the inside out. To the best of the author's knowledge, this is the first successful detection of soot fragmentation from the statistical analysis of TEM images.

### 5.3.5 Primary Particle Number Flow Rate

Though an analysis of the number flow rate of soot primary particles was not originally planned, and investigation yielded results that merit attention. The primary particle number flow rate,  $\dot{N}_p$  is simply the product of the number flow rate

of aggregates and the mean number of primaries per aggregate:

$$\dot{N}_p = \dot{N}_a \overline{N_{p,a}} \quad (5.1)$$

Generally, we should expect  $\dot{N}_p$  to continuously decrease as soot is consumed during its upward journey above the ring burner. Indeed, this is the trend from HAB = 10 to 20 mm, as seen in Fig. 5.16. However, an unexpected jump in  $\dot{N}_p$  occurs at HAB = 25 mm, after which the downward trend resumes, but now at systematically higher values of  $\dot{N}_p$ . This would suggest that individual primary particles begin to break apart into smaller primaries beginning at HAB = 25 mm. Moreover, the remnants of this sundering would have to retain a sphere-like character enough for an operator to perceive them as primary particles. There is no obvious mechanism for this sort of fragmentation at the primary particle level. One might expect that this phenomenon would be preceded by some form of internal burning, however no evidence of this is apparent in the HRTEM images (see Sec. 5.3.7). Nonetheless, some circumstantial evidence for primary particle fragmentation does exist. There is a sizable drop in  $\hat{\mu}_{d_p}$  at HAB = 25 mm (Fig. 5.8a), and this location in the flame does mark the shift from a normal to a lognormal primary particle size distribution (Fig. 5.6). Qualitatively, primary particle asphericity becomes visually more pronounced beginning at 25 mm above the ring burner, which might be the result of spherical primary particles being broken apart.

Looking for other possible explanations, one might investigate the validity of the assumptions employed in the calculation of  $\dot{N}_p$ , namely, the assumptions of non-porous spherical primary particles, and of constant dimensionless extinction

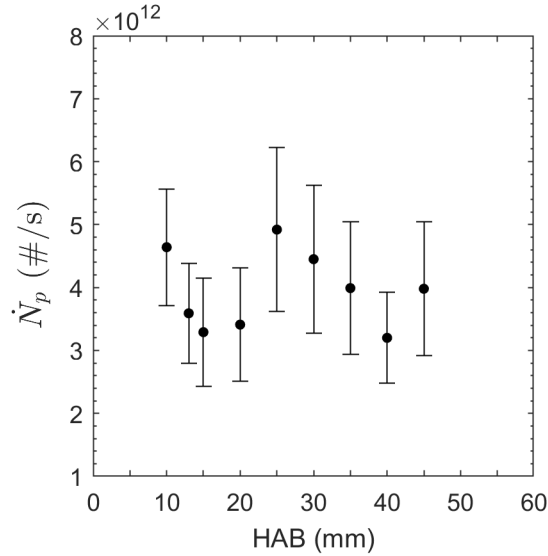


Figure 5.16: Primary particle number flow rate vs. height above burner.

coefficient,  $K_e$ . If primary particles have a high level of porosity, the volume per primary particle as determined from TEM images as the diameter of average volume,  $d_{pv}$ , will be overstated. This would lead to fewer observed primary particles for a given soot volume fraction than are actually present. However, for this to be the origin of the trends in Fig. 5.16, porosity would need to be high near the base of the flame, with primary particles suddenly becoming non-porous at  $\text{HAB} = 25$  mm and above. Apart from violating common sense, this scenario does not comport with the available data. Adsorption measurements of the mature soot generated by co-flow burner showed void fractions less than 2% (Sec. 4.3.3), therefore, soot below  $\text{HAB} = 25$  mm is unlikely to be highly porous. Moreover, HRTEM images show little evidence of primary particle porosity at any point in the flame.

Turning to the 2nd assumption, for variations in the dimensionless extinction coefficient to explain the jump in  $\dot{N}_p$ , the value of  $K_e$  would need to increase

sharply at HAB = 25 mm. That is, if  $K_e$  is greater than was assumed at 25 mm and above, the soot volume fraction at those locations is actually smaller than what was measured. Recall that  $K_e = 6\pi E(m)(1 + \rho_{sa})$ , (Eq. 3.3), where  $\rho_{sa}$  is the ratio of scattering-to-absorption cross-section. An increase in  $K_e$  could come about though an increase in the relative influence of scattering of the incoming laser light. The inclusion of scattering in the soot extinction model can be accommodated through Rayleigh-Debye-Gans Polydisperse Fractal Aggregate theory (RDG-PFA), which considers the effects not only of individual primary particles, but also of their membership within aggregates of various sizes and fractal dimensions [79–81, 229, 266]. Unfortunately, RDG-PFA predicts that  $\rho_{sa}$  will increase with greater aggregate size, which would exacerbate, rather than resolve the present issue. Indeed, if one assumes that aggregates meet the size criterion of  $2\pi R_g/\lambda \leq 3$  [80], which for the present case is quite reasonable, RDG-PFA predicts a value of  $\rho_{sa}$  at HAB = 25 mm that is almost 60% less than at HAB = 10 mm.

Other factors that may affect  $K_e$ , include the extent of primary particle overlap and between-particle necking, [145], intra-aggregate multiple scattering, [267], primary particle asphericity, [268], and degree of graphitization [269]. However, the effects of such factors is generally much smaller than the first-order scattering effects predicted by RDG-PFA. At this point, the inconsistencies in the measured number of primary particles will have to remain an avenue for future research.

### 5.3.6 Selected Area Electron Diffraction

A total of 8 diffraction pattern images were taken from soot samples obtained at HABs of 10, 15, 25, and 50 mm in the soot flame. Figure 5.17 shows representative SAED images from each location, and Fig. 5.18 plots the d-spacings and integral breadths for the  $d_{002}$ ,  $d_{100}$ , and  $d_{110}$  lattice spacings at each HAB. Error bars were calculated by pooling the relative variances across measurements at each HAB.

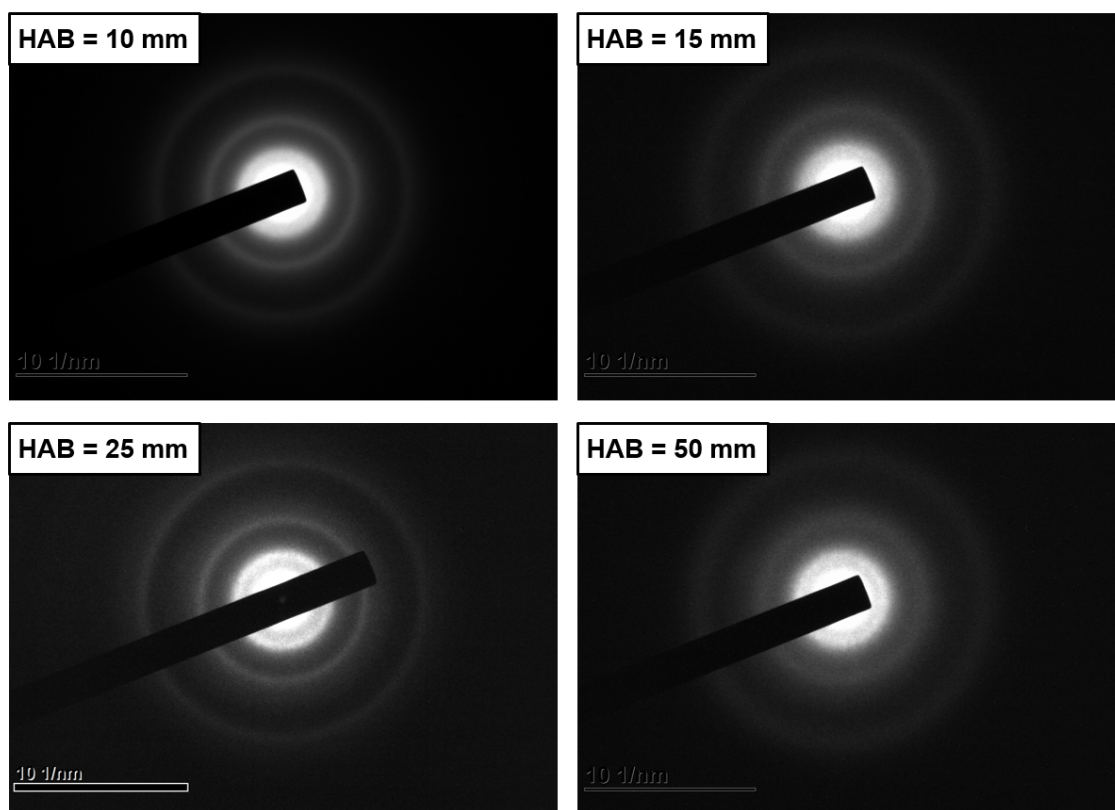


Figure 5.17: Representative SAED images obtained at HABs of 10, 15, 25, and 50 mm.

Figure 5.18a shows that overall, the d-spacings are constant throughout the soot flame. The average values for the  $d_{002}$ ,  $d_{100}$ , and  $d_{110}$  lattice spacings are 3.85,

2.08, and 1.21 Å. The interlayer  $d_{002}$  spacing is near the higher end of the 3.5 Å–3.9 Å range that is typical for soot [76, 161, 162, 164–170, 189, 193, 201]. The  $d_{110}$ , and  $d_{100}$  spacings respectively correspond to first and second-neighbor interatomic distances of 1.4 Å and 2.42 Å, which is just slightly below the interatomic distances in crystalline graphite, but is not uncommon in soot due to the presence of bond-shortening 5-membered carbon rings [201].

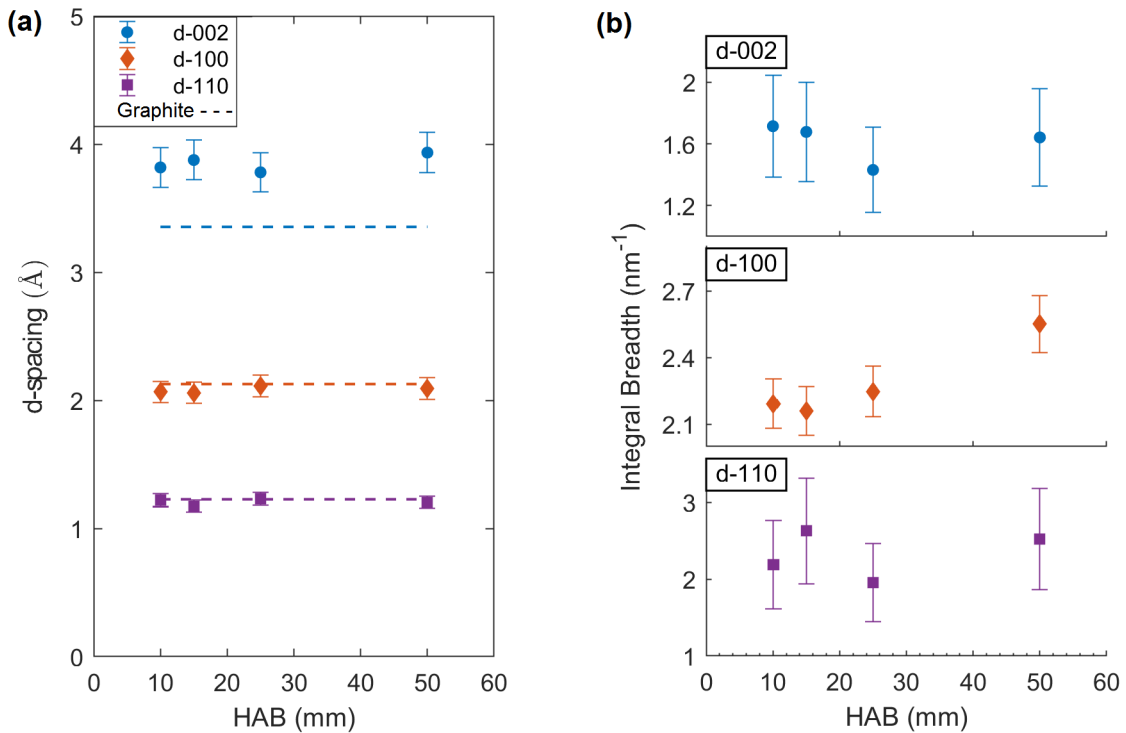


Figure 5.18: (a) d-spacings and (b) integral breadths for the  $d_{002}$ ,  $d_{100}$ , and  $d_{110}$  lattice spacings obtained at HABs of 10, 15, 25, and 50 mm.

Qualitatively, the rings in the SAED image at 25 mm appear more sharply defined than in the other images. This may correspond to the lower  $d_{002}$  and  $d_{110}$  integral breadths at this height. However, the only difference in Fig. 5.18b that has statistical significance is the  $d_{100}$  increase from HAB = 25 to 50 mm. In principal, an

increased integral breadth can indicate a broadening of the probability distribution of lattice plane spacings. This could correspond to an increasing percentage of the soot exhibiting an amorphous-like nanostructure. However, a single data point showing a statistically significant shift is scant evidence for a change in the soot nanostructure. In summary, the SAED images do not indicate any sort of global change to the soot nanostructure as it undergoes oxidation in the soot flame.

### 5.3.7 HRTEM Lattice Fringe Analysis Results

Lattice fringe analysis was performed on 6 randomly selected high resolution images from each sampled height above burner (HAB). Typically, only one primary particle was present in each image, although in some cases two or three could be clearly identified. The lattice fringes from each individually identifiable primary particle were measured separately, following the image processing and fringe measurement procedures detailed in Sec. 3.5.7.

By this method, between 2,000 and 7,500 lattice fringes were measured at each HAB, from a total of 87 different primary particles. Having been randomly selected, the measured primary particles cover a broad range of diameters as shown in Fig. 5.19.

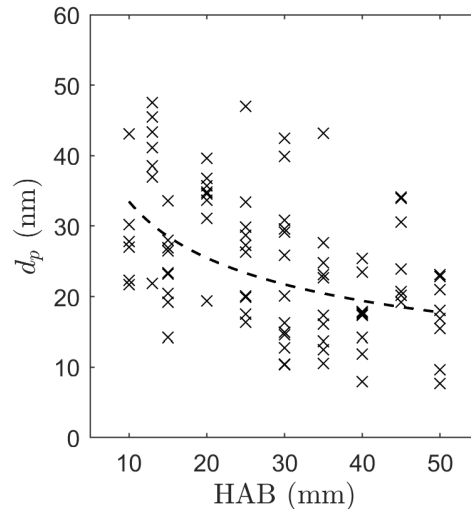


Figure 5.19: Diameters of primary particles used for fringe analysis at each HAB. The fitted line serves to guide the eyes.

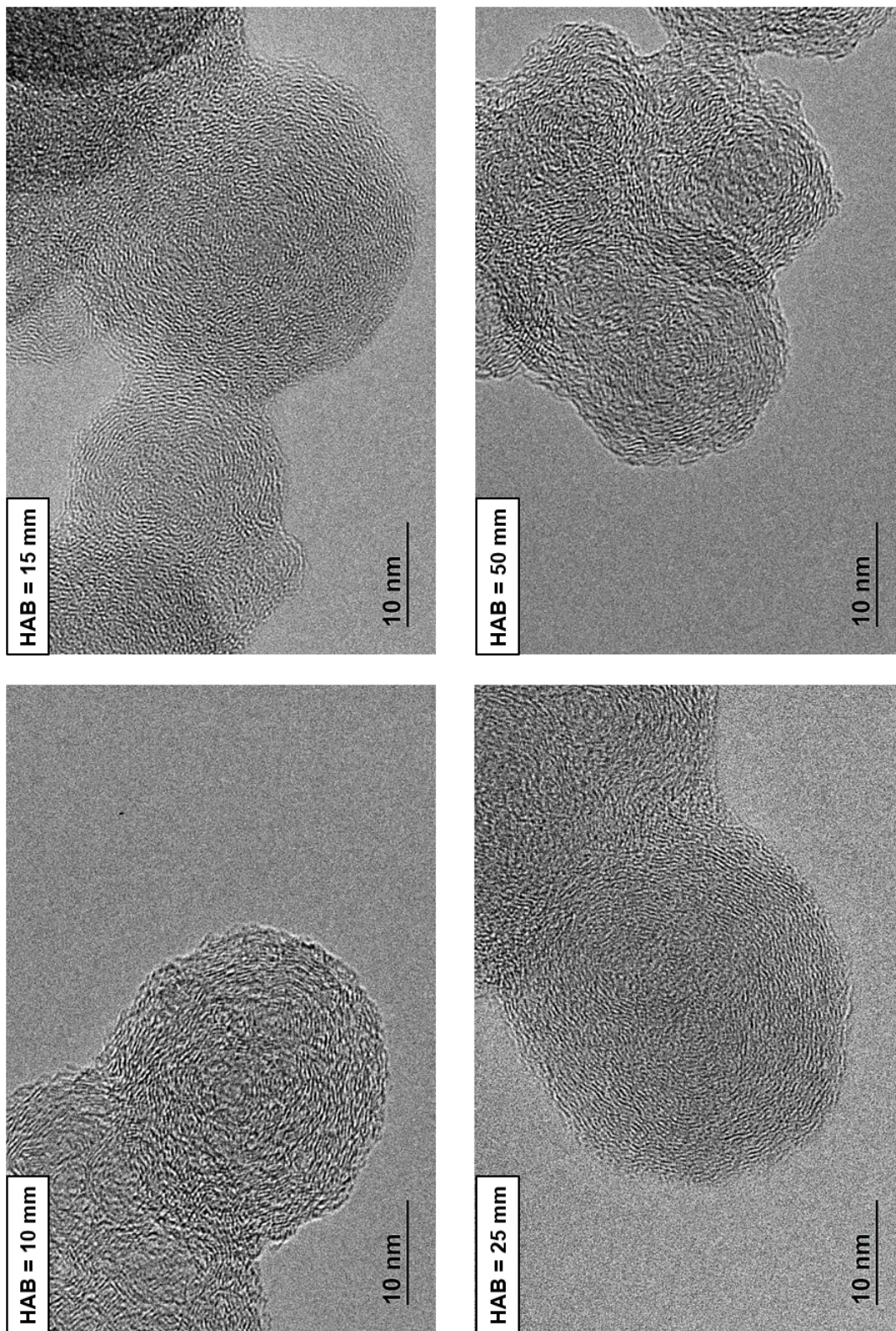


Figure 5.20: Representative HRTEM images of soot obtained at heights above burner of 10, 15, 20, and 50 mm. Magnification is 400,000 for all images.

However, the overall trend matches that of the formal measurement of  $\overline{d_p}$  vs. HAB reported in Sec. 5.3.1.

Figure 5.20 shows HRTEM images representative of soot at heights of 10, 15, 25, and 50 mm. A number of general observations can be made of the images obtained at all sampled flame locations. For all samples, lattice fringes are generally oriented concentrically and increase in average length as one moves radially outward. Fringes near the primary particle core show less order in their arrangement. As is somewhat evident in the image at HAB = 50 mm, primary particles higher in the flame are less-perfectly circular than at lower locations. There were no images that showed evidence of internal burning; (compare to Fig. 2.3).

### 5.3.7.1 Fringe Length

Lattice fringe length distributions were right-skewed and could be best approximated as lognormal, although lognormal fits uniformly underpredicted the sharpness of the distribution peak as exemplified in Fig. 5.21a. Fringe length distributions, as a whole, remained largely unchanged from one HAB to another. The most dissimilar distributions, as determined from a pairwise Kruskal-Wallis test, were those at HAB = 25 and 45 mm, which are plotted together in Fig. 5.21a. Figure 5.21b reveals no obvious overarching relationship between median fringe length,  $\tilde{L}_f$ , and HAB, although there is a statistically significant rise in  $\tilde{L}_f$  from 35 to 45 mm above the burner, followed by a significant drop from 45 to 50 mm. Since the uncertainty of the median is poorly defined for non-normal distributions, the 95% confidence

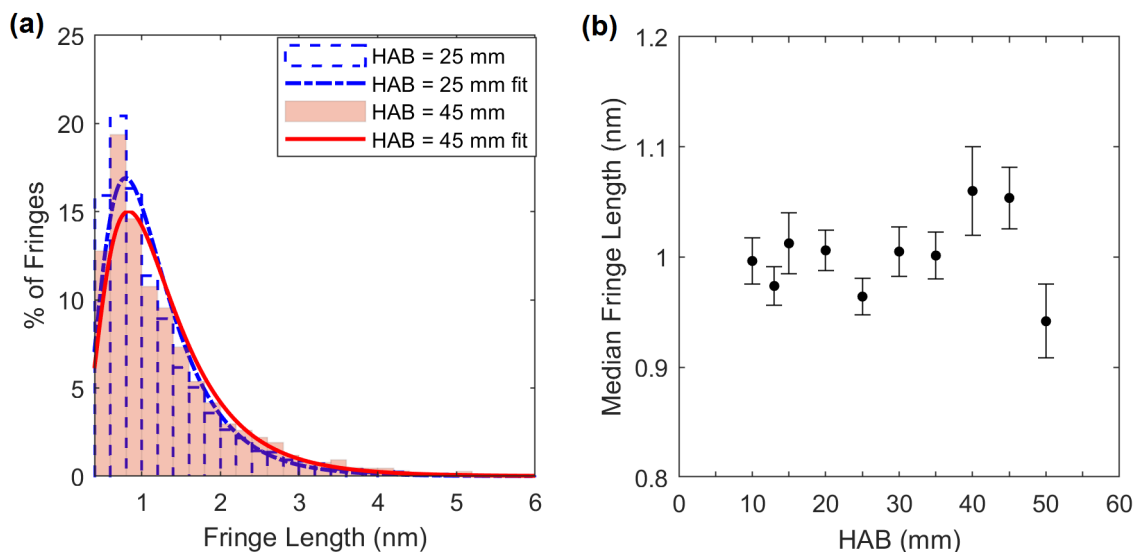


Figure 5.21: (a) Histograms and lognormal fits of the two most dissimilar fringe length distributions illustrate the range of  $L_f$  variation within the soot flame. (b) Median fringe length vs. height above burner.

intervals reported in Fig. 5.21b, and for all other medians in this Results section, were determined by bootstrapping the sample data [270].

Things become more interesting when fringes are scrutinized with respect to their host primary particles. Consider Fig. 5.22a which shows, at three different HABs, how the median fringe length changes with respect to radial location,  $r_f$ , within the host primary particle. To calculate medians, fringes were radially grouped into successive 1 nm-wide rings. Only radial locations with at least 30 measurements were included in the plot. While there is considerable random variability from one radial location to the next, the general trend is of increasing  $\tilde{L}_f$  as one moves farther from the primary particle center, followed by decreasing  $\tilde{L}_f$  at larger radial locations. Grouping results by HAB obscures the correlation between fringe length and radial location, due to the diversity of primary particle sizes analyzed.

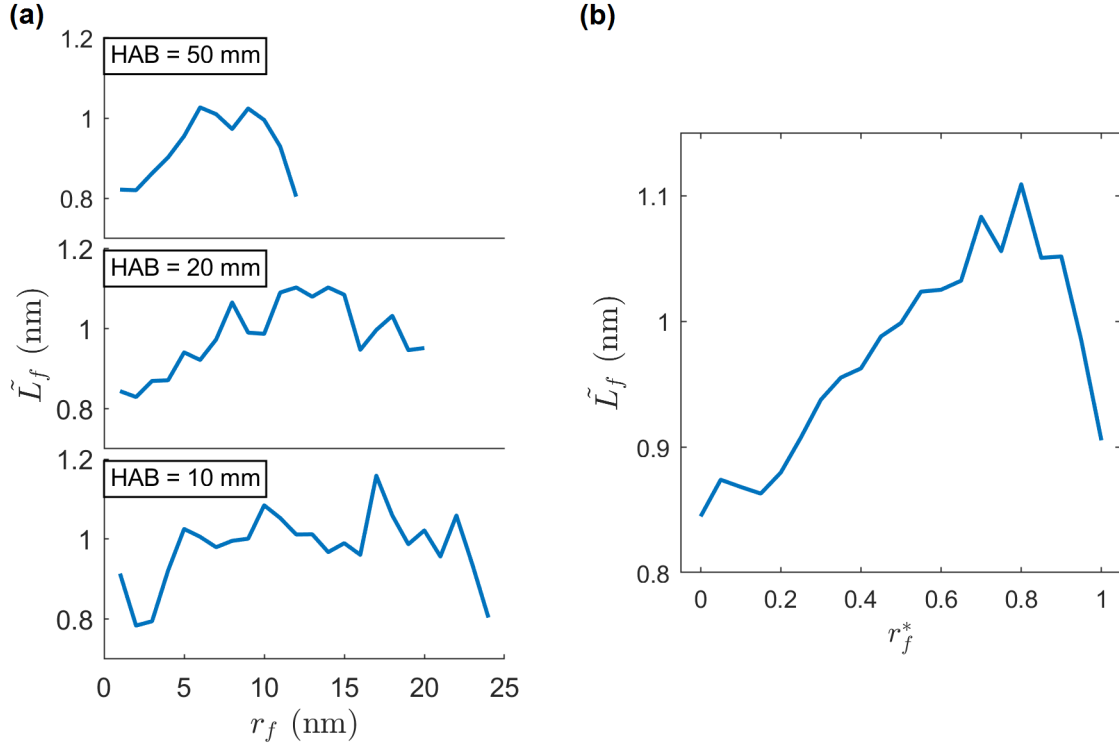


Figure 5.22: (a) Plots from 3 different HABs showing typical contours of median fringe length vs. radial fringe location. (b) Median fringe length vs. radial fringe location normalized by primary particle radius. Fringe length drops near a primary particle's outer edge due to surface oxidation.

A clearer picture is obtained when the radial location of each fringe is normalized by the radius of its host primary particle. Figure 5.22b shows  $\tilde{L}_f^*$  measured at each normalized radial location,  $r_f^*$ . For this calculation, fringes were grouped together in successive rings with normalized widths of 0.05. At a given value of  $r_f^*$ , there was no significant difference in the fringe lengths based on height above burner, therefore measurements from all HABs were combined to form the plot. Fringes at radial locations outside the user-identified primary particle (due to noncircularity) were included in the  $r_f^* = 1$  median calculation. Figure 5.22b shows that fringe length grows with increasing radial distance, up 80% of the primary particle radius. Fringe

length drops sharply, however, within the outer 20% of the primary particle. This can be interpreted as the shortening of the carbon layers due to surface oxidation.

If the lengths of non-surface fringes grow with radius, but their median value remains essentially constant (Fig. 5.21b) even as primary particles shrink (Fig. 5.19), it must be that fringes within the bulk of the primary particle grow as the surface oxidizes. To investigate this, the median fringe length at each radial location between 1 and 15 nm was evaluated against the diameter of the host primary particle,  $d_p$ . For the analysis, diameters were rounded to the nearest nm and the outer 20% of each primary particle, where fringe length was clearly affected by oxidation, was excluded. Figure 5.23a plots  $\tilde{L}_f$  against  $d_p$  for radial locations of 2, 6, 11, and 15 nm. Two trends are apparent. First, for any given radial location, fringe length generally increases as primary particle size decreases. Second, the sensitivity of this relationship becomes more pronounced at larger radial locations.

Figure 5.23b plots the average rate of change of  $\tilde{L}_f$  with respect to  $d_p$  at each radial location. Not only is the relationship between  $\Delta\tilde{L}_f$  and  $\Delta d_p$  uniformly negative, but the further one gets from the center of the primary particle, the more greatly fringe length grows in response to a reduction in primary particle size. Moreover there appears to be two regimes of fringe length growth. The first occurs within the core of a primary particle ( $r_f$  between  $\sim 0$  and 12 nm), where  $\Delta\tilde{L}_f/\Delta d_p$  decreases modestly as  $r_f$  increases. The second regime shows a much steeper change of  $\Delta\tilde{L}_f/\Delta d_p$  with respect to  $r_f$  and occurs nearer to the primary particle surface, which is undergoing oxidation.

The two regimes point to two modes of carbon layer graphitization. The first

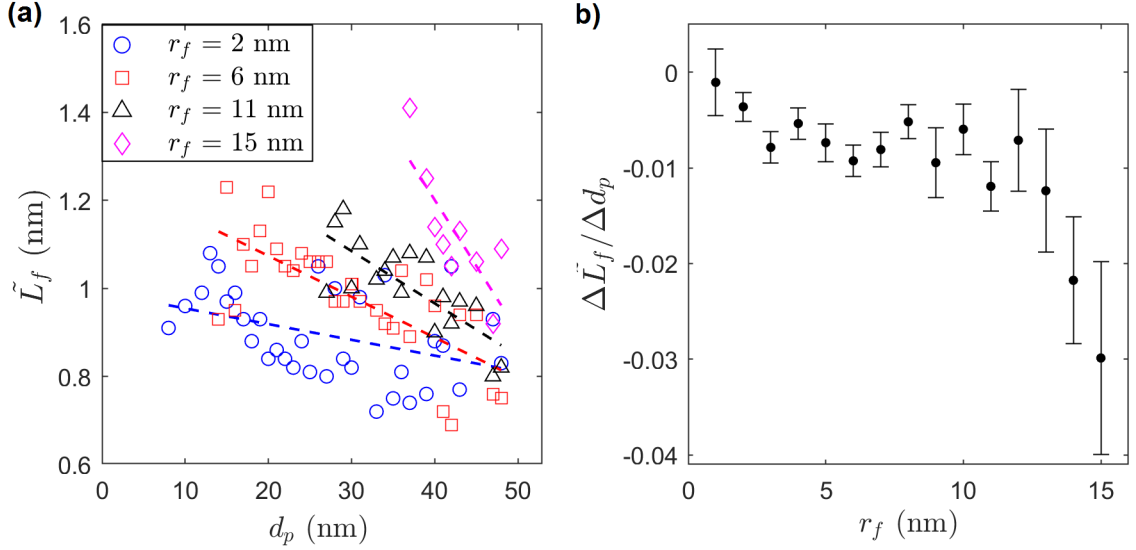


Figure 5.23: (a) Median fringe length vs. primary particle diameter for selected fringe radial locations. (b) Change in median fringe length with respect to primary particle diameter at each fringe radial location. To exclude surface oxidation effects, only fringes within the core 80% of the primary particle were used in the analysis.

arises everywhere within the primary particle as a result of thermal annealing. The effect appears to be weaker near the particle core where the atomic structure is more securely locked into place within the carbon matrix - an observation also made in the flame studied by Botero et al. [215]. The second mode is induced by surface oxidation, which removes cross-links and interstitial material at the outer shell of the particle, freeing the carbon planes beneath it to realign and expand while still out of reach of oxidizing gases.

### 5.3.7.2 Fringe Tortuosity

Fringe tortuosity at each height above burner exhibited a highly skewed distribution. While some authors have attempted to fit a lognormal curve to tortuosity

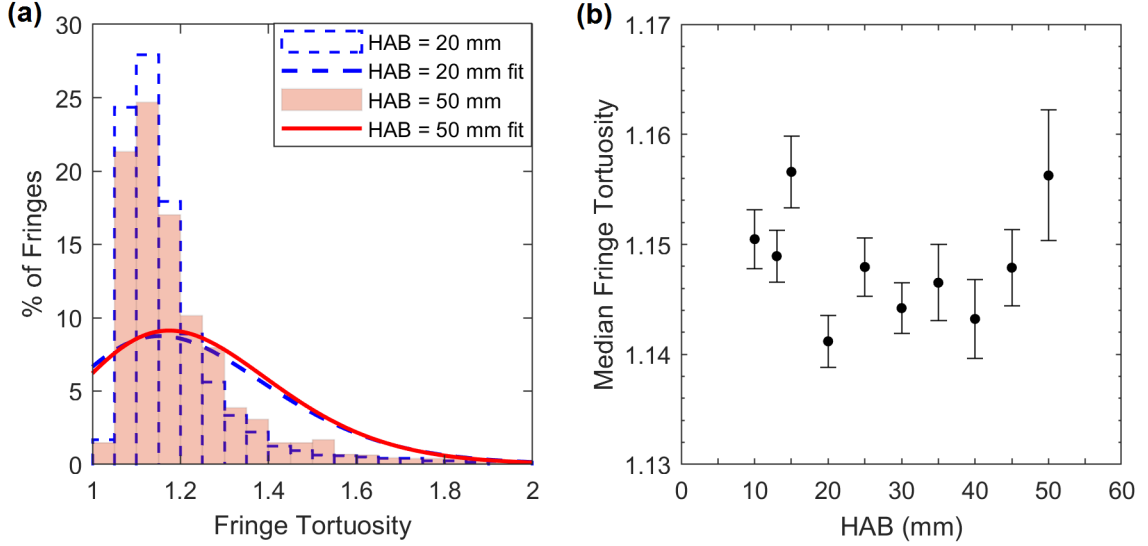


Figure 5.24: (a) Histograms and lognormal fits of the two most dissimilar fringe tortuosity distributions illustrate the range of variation of  $\tau_f$  within the soot flame (b) Median fringe tortuosity vs. height above burner.

data [118, 210], in the current work, no distribution shape could be found that reasonably fit the data. As with fringe length, the tortuosity distribution held relatively unchanged within the soot flame. Histograms for the two most dissimilar distributions, (at HAB = 20 and 50 mm as determined by a pairwise Kruskal-Wallis test), are shown in Fig. 5.24a. Lognormal fits are also plotted for comparison. Substantial scatter is seen in the plot of median tortuosity,  $\tilde{\tau}_f$  vs. HAB given in Fig. 5.24b. A statistically significant spike in  $\tilde{\tau}_f$  occurs at HAB = 15 mm, followed by an even greater drop at HAB = 20 mm. There also may be an upward trend in  $\tilde{\tau}_f$  from HAB = 40 to 50 mm. Possible explanations for these features will be discussed below.

At all locations in the soot flame, a strong relationship exists between fringe tortuosity and fringe radial location within the host primary particle. Figure 5.25

plots median tortuosity against fringe radial location,  $r_f$ , at select HABs, as well as against normalized radial location,  $r_f^*$ . Radial groupings for the calculation of medians were the same as those used in the fringe length analysis. Fringe tortuosity consistently decreases with increasing distance from the primary particle core, although a slight upturn may occur at the very surface. This indicates that the degree of graphitization increases with increasing radius, consistent with fringe length results. However, unlike fringe lengths, which dropped sharply near the primary particle surface due to oxidation, there is no dramatic change in tortuosity within the outer shell. This difference is understandable considering the mechanisms responsible for each effect. Fringe lengths are reduced predominantly by oxidation of highly reactive edge site carbons. An increase in curvature, on the other hand, would come about through the removal of a far less reactive basal plane carbon, followed by a re-alignment of the carbon plane to incorporate the new 5-carbon ring. At the same time, curvature reducing mechanisms would also be in effect, such as the removal of a carbon from a 5- or 7-membered ring, both of which would tend to relax the curvature of the carbon plane. Due to the bond strain present in these odd-numbered rings, these carbons are also more reactive than basal carbon. The cumulative effect is that tortuosity, overall, changes very little due to oxidation. The slight increase in  $\tilde{\tau}_f$  at the primary particle surface is therefore most likely an artifact of decreasing fringe length rather than a result of increasing curvature.

The median fringe tortuosity at each radial location between 1 and 15 nm was evaluated against the diameter of the host primary particle,  $d_p$ . Consistent with the analysis performed on fringe lengths, diameters were rounded to the nearest nm, and

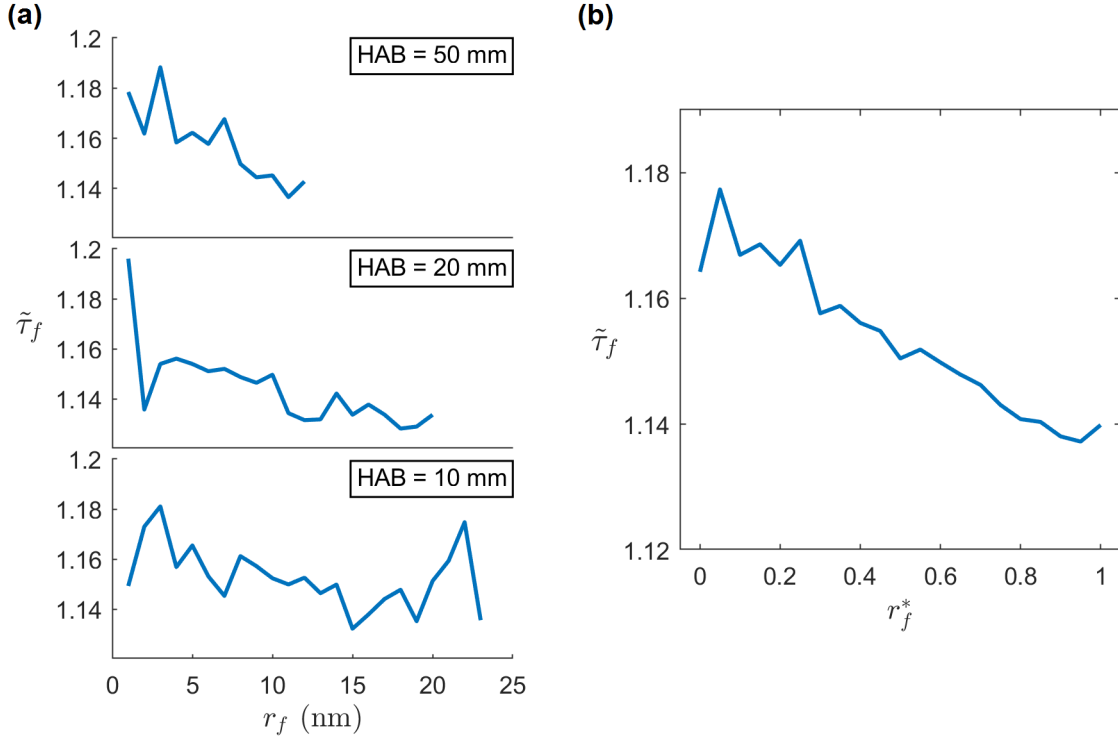


Figure 5.25: (a) Plots from 3 different HABs showing typical contours of median fringe tortuosity vs. radial fringe location. (b) Median fringe tortuosity vs. radial fringe location normalized by primary particle radius.

the outer 20% of each primary particle was excluded to avoid confounding trends due to surface oxidation. Figure 5.26 plots the average rate of change of  $\tilde{\tau}_f$  with respect to  $d_p$  at each radial location. The plot shows that throughout the bulk of the primary particle,  $\Delta\tilde{\tau}_f/\Delta d_p$  is small, but generally in positive territory. This means that at any given radial location, fringes tend to straighten (i.e.  $\tau_f$  decreases) as primary particle size is reduced. This corroborates the graphitization by thermal annealing already observed, in which fringe elongation accompanied decreasing particle size. The data point at  $r = 15$  nm may indicate that the effect on tortuosity is heightened nearer to the surface oxidation zone, but there is insufficient data to make a strong

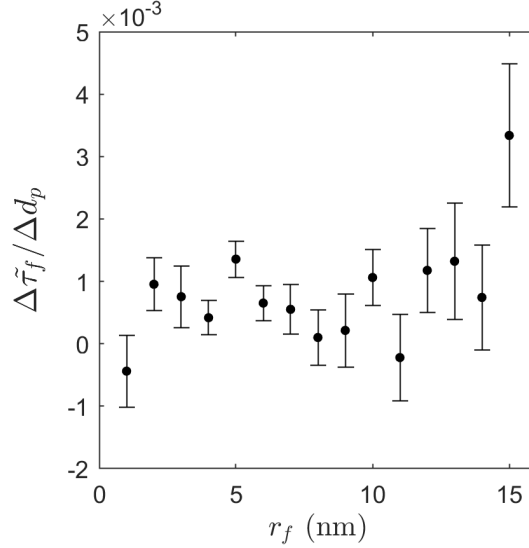


Figure 5.26: Change in median fringe tortuosity with respect to change in primary particle diameter at different fringe radial locations. To exclude surface oxidation effects, only fringes within the core 80% of the primary particle were used in the analysis.

claim. Similarly, the two negative data points at  $r_f = 1$  and 11 nm are more likely the result of statistical variation than to any special factors occurring at these locations.

### 5.3.7.3 Fringe Orientation

The soot produced by the propylene co-flow diffusion flame exhibited a loosely concentric arrangement of lattice fringes about the primary particle core. This structure is common among combustion soot from short-chained hydrocarbons [119, 158, 162, 175]. The histograms in Fig. 5.27a are for the two most dissimilar distributions of non-concentricity, which occur at HAB = 15 and 25 mm as determined by a pairwise Kruskal-Wallis test. Distributions changed very little within the soot flame, and all HABs displayed a distribution peak near  $0^\circ$ , which is indicative of a

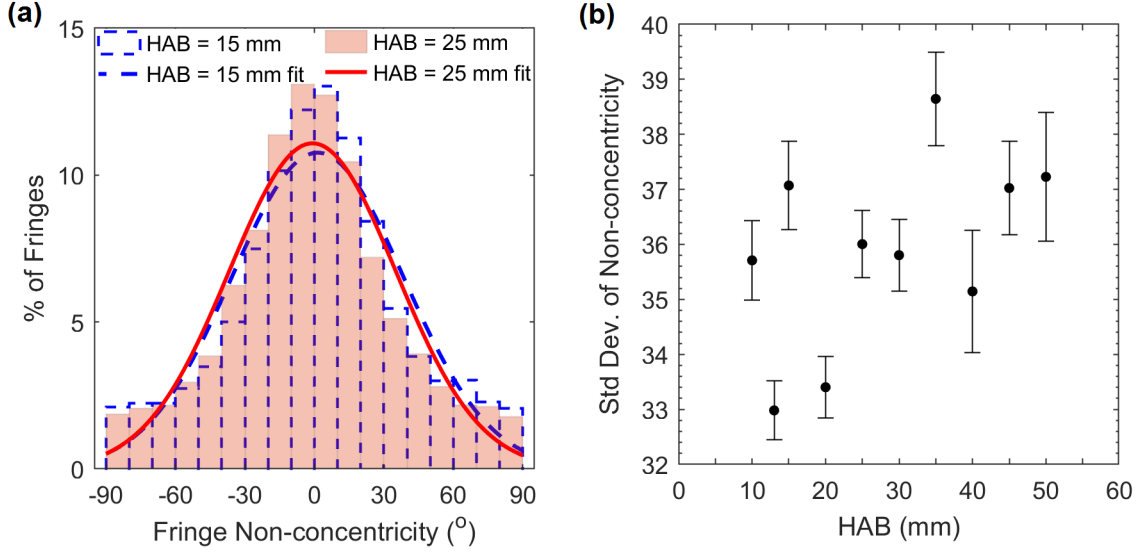


Figure 5.27: (a) Histograms and normal fits of the two the most dissimilar fringe non-concentricity distributions illustrate the variation of  $\theta_{f,c}$  distributions within the soot flame. (b) Standard deviation of fringe non-concentricity vs. height above burner.

concentric fringe arrangement. The distributions can be reasonable approximated as normal, as shown by the plotted fits, although the approximation is worse near the distribution tails.

The extent of orientational order within this concentric fringe arrangement can be quantified by the standard deviation of the fringe non-concentricity, with lower standard deviations signifying greater order. The standard deviation of fringe non-concentricity,  $s_{\theta_{f,c}}$  at each HAB is plotted in Fig. 5.27b. The data is fairly well scattered about a mean  $s_{\theta_{f,c}}$  of about 36. Although there may appear to be a subtle trend of rising  $s_{\theta_{f,c}}$  as HAB increases, the correlation is not significant ( $p=0.14$ ).

All measured samples exhibited a reduction in  $s_{\theta_{f,c}}$  as one moves radially outward within the host primary particle. This is exemplified in Fig. 5.28a for

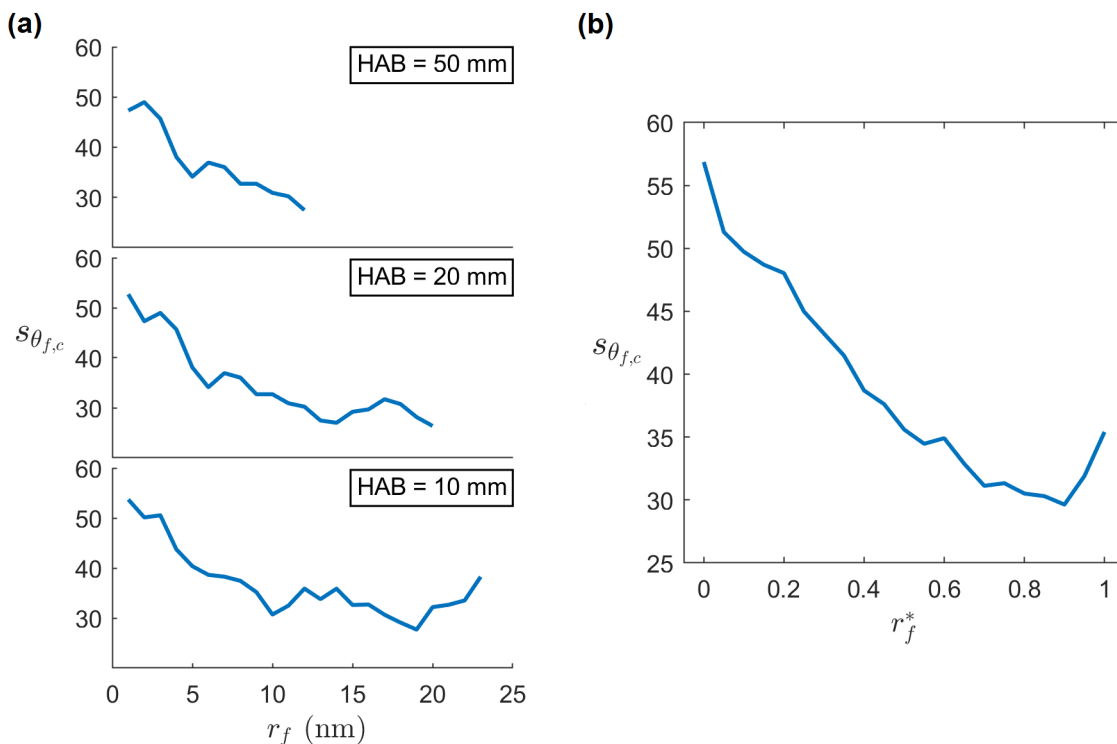


Figure 5.28: (a) Plots from 3 different HABs showing typical contours of the standard deviation of fringe non-concentricity vs. radial fringe location. (b) Standard deviation of fringe non-concentricity vs. radial fringe location normalized by primary particle radius.

three heights above burner. Statistics were calculated within the same radial groupings as was done for fringe length and tortuosity analysis. Measurements from all HABs were combined and normalized against host primary particle radius to create Fig. 5.28b. Here,  $s_{\theta_{f,c}}$  trends downward as  $r_f^*$  increases. This matches observations by Shim et. al [175] who reported a higher polar order parameter as one moved radially from the particle nucleus. The downward slope continues until  $r_f^* = 0.9$ , at which point, the trend reverses. The higher orientational disorder near the primary particle center is consistent with randomly distributed PAH clusters, typical in the cores of flame-generated soots [158, 181, 271]. A small but unmistakable increase in

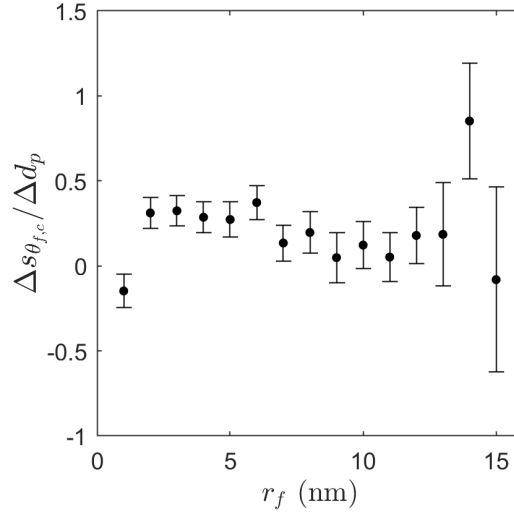


Figure 5.29: Change in the standard deviation of fringe non-concentricity with respect to change in primary particle diameter at each fringe radial location. To exclude surface oxidation effects, only fringes within the core 80% of the primary particle were used in the analysis.

disorder is present at the oxidizing outer shell of the primary particle. This indicates an increase in carbon plane mobility near the surface, as well as a weakening attachment to the underlying layers. The mobility of carbon planes near the primary particle surface is both consistent with and necessary for the oxidation-induced graphitization inferred from fringe length measurements in Sec. 5.3.7.1.

To see the effect of primary particle size on fringe orientation, the standard deviation of fringe non-concentricity,  $s_{\theta_{f,c}}$ , at radial locations from 1 to 15 nm was evaluated with respect to diameter of the host primary particle,  $d_p$ . As was done for fringe length and tortuosity analysis, diameters were rounded to the nearest nm, and the outer 20% of each primary particle was excluded to eliminate surface oxidation effects. Figure 5.29 plots the average rate of change of  $s_{\theta_{f,c}}$  with respect to  $d_p$  at each radial location. Similar to the tortuosity results,  $\Delta s_{\theta_{f,c}} / \Delta d_p$ , is small but positive

in in most locations. This means that in response to a reduction in primary particle size, fringes at a given radial location become more concentric (i.e.  $\Delta s_{\theta_{f,c}} < 0$ ). This is consistent with the picture painted thus far of thermally-induced graphitization within the bulk of the primary particle. The jump in  $\Delta s_{\theta_{f,c}}/\Delta d_p$  at  $r_f = 14$  nm is also consistent with the oxidation-induced graphitization suspected just below the surface layers. As cross-links between layers are removed by oxidation, the carbon layers beneath are free to grow and concentrically realign. Although the data point at  $r_f = 15$  nm casts doubt on this interpretation, it may be close enough to the surface here for carbon plane mobility to increase orientational disorder, as discussed in the paragraphs above.

#### 5.3.7.4 Fringe Separation Distance

The final HRTEM measurement to consider is the fringe separation distance,  $d_f$ . Distributions of  $d_f$  appeared nearly symmetric, although lognormal fits were uniformly superior to normal fits. Nonetheless, means will be used as the summary statistic, consistent with existing literature (e.g. [118, 208, 210, 210, 214]). Figure 5.30a shows the histograms and lognormal fits of  $d_f$  from HAB = 13 and 20 mm, which were the least similar data sets as determined from a pairwise Kruskal-Wallis test. The plot of  $\overline{d_f}$  vs. HAB in Fig. 5.30b shows large amount of statistical scatter without any obvious trend. The overall mean value of  $d_f$  across all samples was 0.427 nm, which is falls right in the middle of the range of typical values [24, 118, 199, 207, 210, 215].

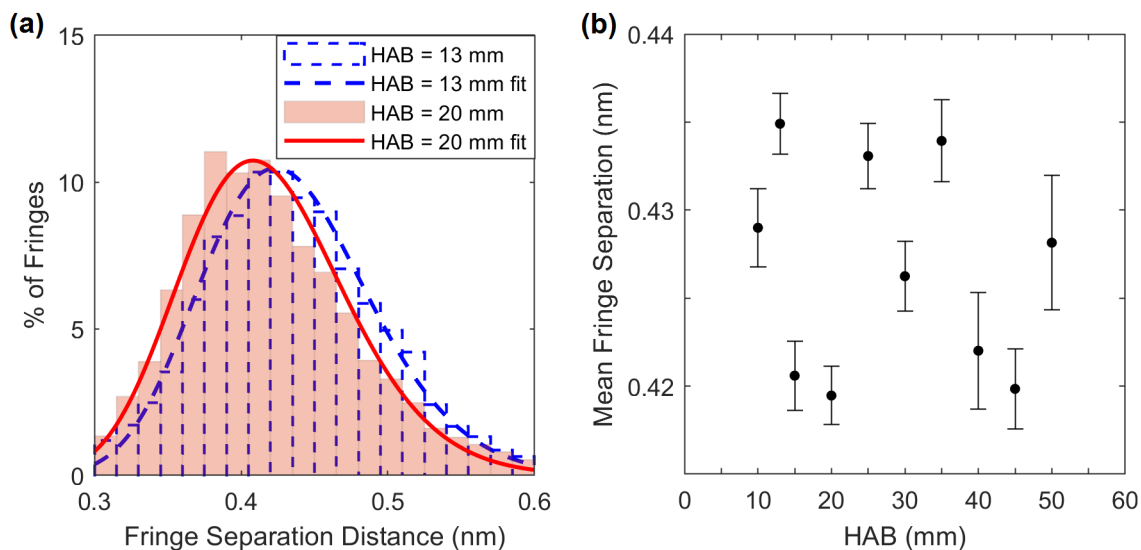


Figure 5.30: (a) Histograms and lognormal fits of the two the most dissimilar fringe separation distributions illustrate the range of  $d_f$  variation within the soot flame. (b) Mean fringe separation distance vs. height above burner.

Clearer patterns are observable when fringe separation distance is shown with respect to fringe radial location, which was taken as the average radial location of the fringes in each pair. As with prior analyses, fringes were radially grouped into successive 1 nm-wide rings, and only radial locations with at least 30 measurements were considered. Figure. 5.31a shows the relationship between  $\overline{d}_f$  and radial  $r_f$  at three different heights above burner, and Fig. 5.31b shows  $\overline{d}_f$  combined across HABs vs. radial location normalized by primary particle radius. The basic pattern that emerges is of  $\overline{d}_f$  that is high near the primary particle core, but that drops with increasing  $r_f$  until  $r_f^* = 0.8$  at which point  $\overline{d}_f$  rises until reaching the particle surface.

Relatively large fringe separations near the primary particle center followed by closer fringes away from the center, again aligns with the core-shell soot model in which an amorphous nucleus is surrounded by increasingly graphitized carbon

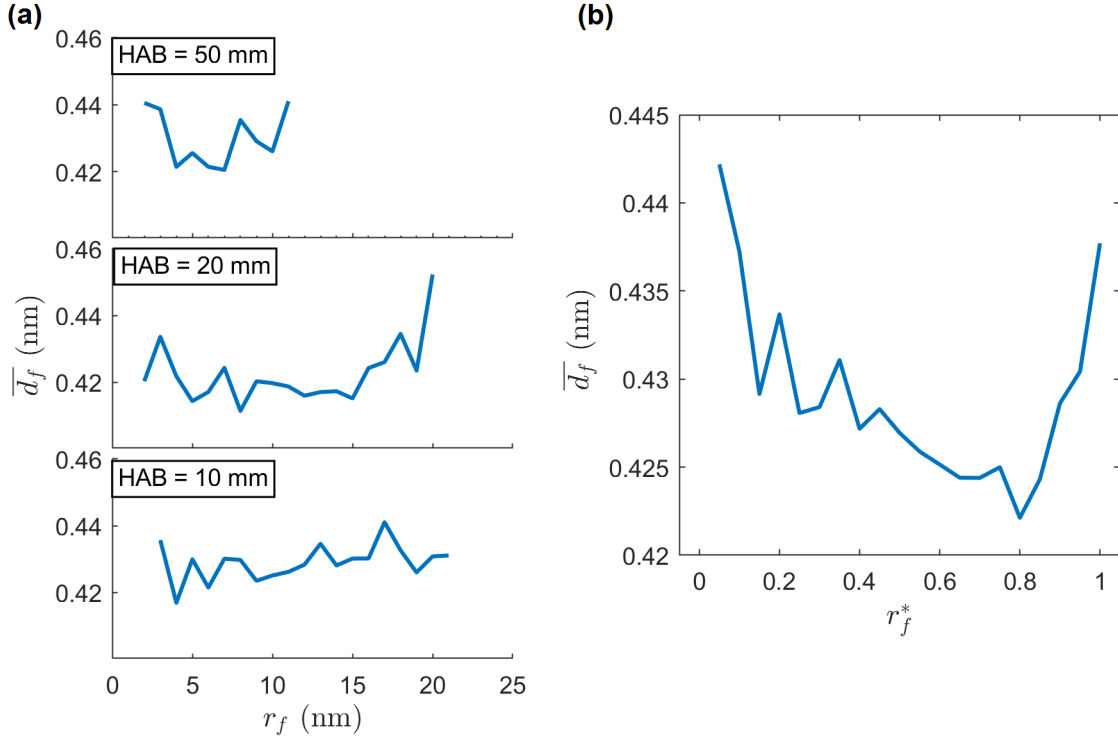


Figure 5.31: (a) Plots from 3 different HABs showing typical contours of the mean fringe separation distance vs. radial fringe location. (b) Mean fringe separation distance vs. radial fringe location normalized by primary particle radius.

layers (e.g. [119, 158, 161, 162, 166, 172, 173]). This model holds until the inflection point at  $r_f^* = 0.8$ , which precisely matches the start of the surface oxidation region ascertained from fringe length analysis. Here we see that the effect of oxidation is a widening distance between carbon layers. This would result in weaker coupling to neighboring layered planes, permitting greater fringe mobility, as was concluded from fringe orientation measurements. This lends further support to the theory of oxidation-induced graphitization just below the oxidation region, since fringe mobility is an ingredient of this graphitization mode.

The mean fringe separation distance at each radial location between 1 and

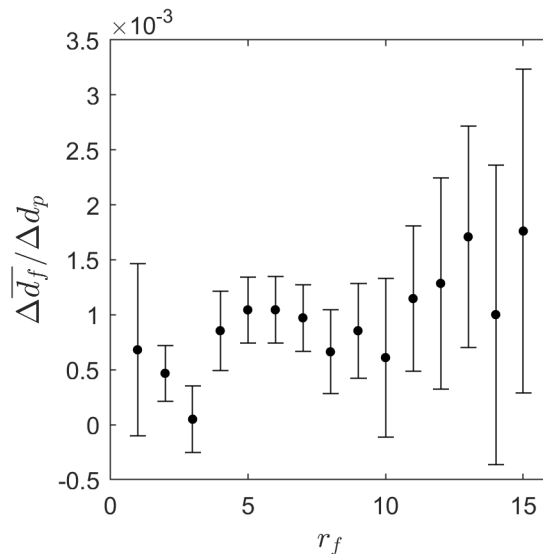


Figure 5.32: Change in the mean fringe separation distance with respect to change in primary particle diameter at each fringe radial location. To exclude surface oxidation effects, only fringes within the core 80% of the primary particle were used in the analysis.

15 nm was evaluated against the primary particle diameter,  $d_p$ . As before, diameters were rounded to the nearest nm, and the outer 20% of each primary particle was excluded to avoid surface oxidation effects. Figure 5.32 plots the average rate of change of  $\bar{d}_f$  with respect to  $d_p$  at each radial location. For each plotted point,  $\Delta \bar{d}_f / \Delta d_p$  is positive, meaning that as  $d_p$  shrinks,  $\bar{d}_f$  decreases as well. This comports with results of  $L_f$ ,  $\tau_f$ , and  $\theta_{f,c}$ , which indicate thermally-induced graphitization within the bulk of the primary particle, as oxidation proceeds on the surface.

Lastly, several authors have argued that fringes with greater tortuosity will produce larger fringe separation distances by inhibiting stacked layer development [209, 214]. While we observe regions in which both tortuosity and separation distance decrease due to graphitization, an analysis of individual fringes found no

correlation between tortuosity and separation distance.

### 5.3.7.5 Nanostructure at the Particle Surface

A threefold summary of the HRTEM data analyzed thusfar can now be made. First, there is no evidence of internal burning or major pore openings within soot primary particles. Instead, oxidation appears to proceed inward from the particle surface in a shrinking sphere manner. Second, primary particles can be divided into an inner radial 80%, in which lattice fringes display greater order and graphitization with increasing radius, and an outer 20% in which this trend reverses due to surface oxidation. Third, while oxidation is happening at the soot surface, shrinking the primary particles, graphitization is occurring in the particle interior, as evidenced by the growing, straightening, re-orienting, and compaction of lattice fringes.

We now turn our attention to the affects of oxidation on nanostructure within the outer 20% of the primary particles. Section [2.4.4](#) detailed the myriad ways in which soot nanostructure affects its ability to be oxidized. Not only does the nanostructure dictate how carbons with varying reactivities become accessible to gas-phase oxidizers, but changes to the nanostructure can alter these reactivities. Since oxidation is essentially isolated to the outer primary particle shell, changes to nanostructure within this region will directly inform the approach that should be taken in analyzing chemical kinetics with the gas phase.

For fringe lengths, a different picture emerges at the primary particle surface than in the bulk. As was done in Sec. [5.3.7.1](#), Fig. [5.33a](#) plots the median fringe

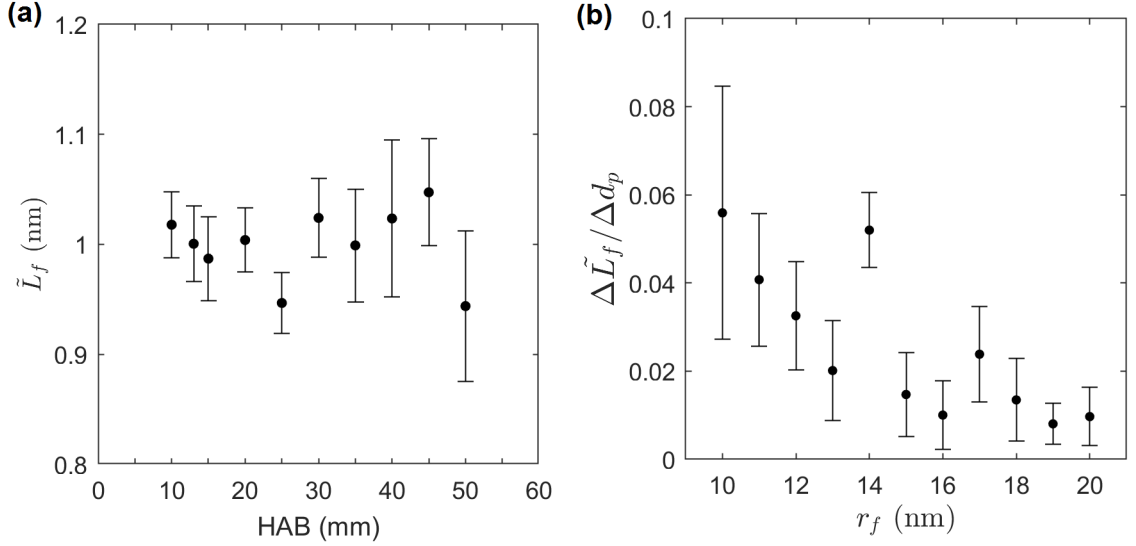


Figure 5.33: Fringe lengths near the primary particle surface. To highlight surface oxidation effects, only fringes within the outer 20% of the primary particle were used in the analysis. (a) Median fringe length vs. height above burner. (b) Change in median fringe length with respect to primary particle diameter at each fringe radial location.

length against height above burner and Fig. 5.33b plots the average rate of change of  $\tilde{L}_f$  with respect to  $d_p$  at each radial location. However, now only the outer 20% of each primary particle is included in the analysis. Figure 5.33a shows no correlation between  $\tilde{L}_f$  and HAB, and notwithstanding the dips at heights of 25 and 50 mm,  $\tilde{L}_f$  stays essentially constant at about 1.0 nm. In contrast to Fig. 5.23, in Fig. 5.33b, values for  $\Delta\tilde{L}_f/\Delta d_p$  are uniformly *positive*, indicating that fringes at a given radial location near the particle surface shorten in response to a drop in primary particle size. This means, for example, that at a radial location of 10 nm,  $\tilde{L}_f$  will be greater in a 12 nm radius primary particle than in one with an 11 nm radius. This is consistent with an environment of surface oxidation. The effect appears to lessen in magnitude with increasing radial fringe location. One possible explanation for this

is that for primary particles with larger radii, the outer 20% includes some regions that are undergoing graphitization, thereby offsetting the fringe shortening effect of oxidation. Indeed, if the analysis is restricted to the outer 2 nm of each primary particle, the downward trend in Fig. 5.33b largely disappears, (Fig. 5.34).

The other lattice fringe measurements are equally independent of both soot flame location and primary particle size. These results are included in Appendix C.2. Taken together, the data shows that while fringe lengths are shorter as one moves radially inward, the character of the carbon layers encountered by the gas phase at the surface remains essentially constant due to prior thermal and oxidation-induced graphitization, even as the primary particles shrink.

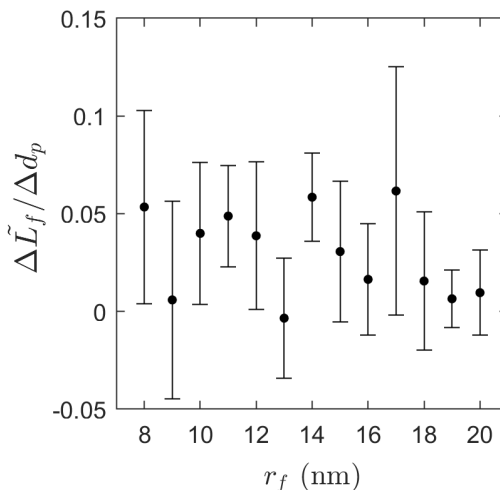


Figure 5.34: Change in median fringe length with respect to primary particle diameter at each fringe radial location. Analysis restricted to the outer 2 nm of each primary particle.

Obviously, this trend cannot continue indefinitely. Eventually, the primary particles will be so small that one or more of the following will be forced to occur:

1. The carbon layers decrease in size, increasing the percentage of edge to basal plane carbons;
2. Curvature of the carbon layers increases, raising the proportion of the more reactive odd-member-ring carbons;
3. The primary particles lose their spherical shape, increasing the specific surface area.

All of these transformations would result in an increase of the effective soot reactivity. In a shrinking-sphere

situation, these effects should become especially pronounced as the primary particle diameter approaches the lattice fringe length. In the flame system investigated here, the ratio of mean primary particle diameter to median fringe length never goes below about 20. Only the 3rd effect, increasing asphericity, has been qualitatively observed. Interestingly, the presence of this effect may be responsible for the other two having *not* been observed. That is, the loss of sphericity may precede the curving and shortening of fringes such that primary particles exhibiting these latter features are no longer recognizable as such by a TEM operator.

#### 5.4 Soot Oxidation Rate Expressions

From the TEM measurements, there are several key results of direct relevance to the analysis of the chemical kinetics of soot oxidation. First, there are no changes to the soot morphology or global nanostructure that would greatly affect soot optical properties. Second, for the current flame system, observations are best represented by a shrinking sphere model, with oxidation restricted to the outer soot surface. Third, the nanostructure encountered by the gas-phase is effectively constant, even as material is removed through oxidation.

The first two results align with assumptions embedded in the measurements of soot volume fraction and specific surface area. This should strengthen confidence in these measurements, and in the soot oxidation rates derived from them. The third result comports with the assumption of a constant concentration of active sites on the soot surface. From this, we conclude that the null hypothesis of constant collision

efficiencies between oxidizers and the soot surface cannot be rejected. The soot oxidation analysis can therefore proceed as presented in Sec. 3.6 without alteration.

The overall soot oxidation rate at each sampled location in the soot flame, is presented in Fig. 5.35a. These results update those reported by Guo [224], based on refinements to the specific surface area and soot flame velocity measurements in the present work. The soot oxidation rate reaches a peak of 5.7 g/m<sup>2</sup>-s at 13 mm, coinciding with the location of peak temperature and OH concentration. Oxidation rate falls to a low of 0.3 g/m<sup>2</sup>-s shortly thereafter, at HAB = 20 mm which coincides with the location of minimum O<sub>2</sub>. Uncertainties in the values of  $\dot{w}_{ox}$  ranged between  $\pm 20\%$  and  $\pm 60\%$ , and were calculated from the elemental uncertainties of each of the terms in Eq. 3.25 following the method outlined in Ref. [272].

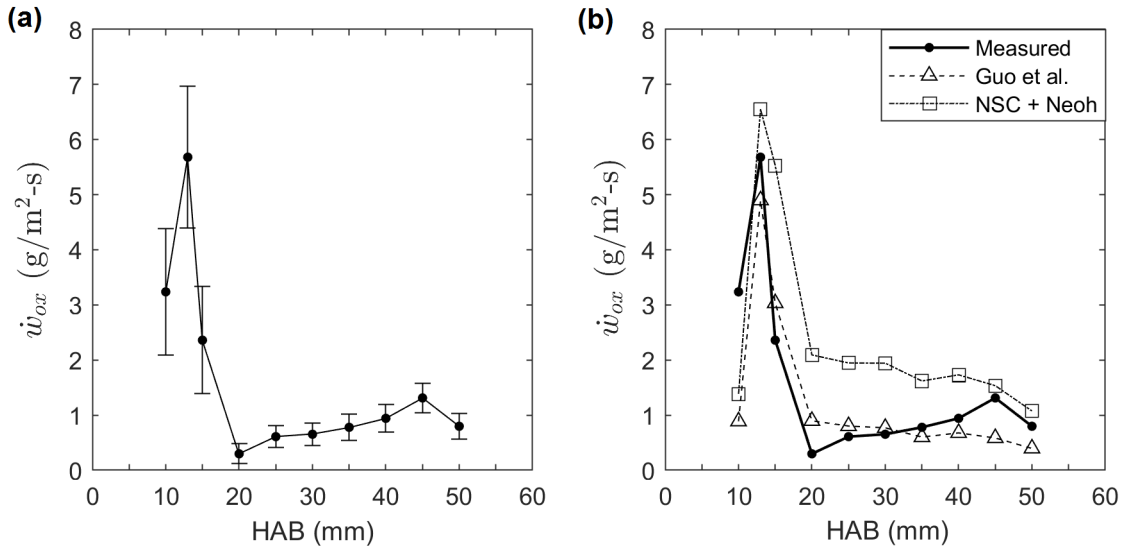


Figure 5.35: (a) Measured soot oxidation rate vs. height above burner. (b) Comparison of measured soot oxidation rates with those predicted by mechanisms of NSC + Neoh et al. [42, 43], and the optimized mechanism of Guo et al. [46]

In Fig. 5.35b, the measured oxidation rate is plotted alongside the predicted rates of two different mechanisms. The first prediction combines of the two most commonly used mechanisms for oxidation by  $O_2$  and OH, which are those by Nagle and Strickland-Constable (NSC) [42] and Neoh et al. [43], respectively. For all but the data point at 10 mm, NSC + Neoh greatly overpredicts the oxidation rate. Apart from the extreme difference at HAB = 20 mm (600%), the largest overprediction is 220% occurring at 25 mm. Overall, the average prediction is 137% greater than the measured values. The optimized expression derived from the meta-analysis of Guo et al, [46], does substantially better. The largest underprediction is 73% at at 10 mm, and apart from the overshoot at 20 mm (200%), the largest overprediction is only 30%, occurring at 25 mm.

Table 5.1 lists these mechanisms, as well as two others, with the  $R^2$  value of a fit of the predicted oxidation rates to the line of  $\dot{w}_{ox,meas} = \dot{w}_{ox,predict}$ . The combined prediction of Lee + Neoh [43, 47], yields a very similar result to that of Guo et al. [46].

Table 5.1: Comparison of oxidation mechanism predictions with measured oxidation rates.

Mechanism	$\eta_{OH}$	$A_{O_2}$ (s-K <sup>1/2</sup> /m)	$E_{A,O_2}$ (kJ/mol)	$R^2$
NSC + Neoh [42, 43]	0.13	(multiple sub-expressions)		0.11
Lee + Neoh [43, 47]	0.13	1.071	164.4	0.60
Guo et al. [46]	0.1	15.8	195	0.69
$O_2$ only	0	0.03	97	0.99

Interestingly, an optimum fit to the data is obtained when oxidation by OH is ignored entirely. The resulting O<sub>2</sub> pre-factor and activation energy are far below literature values suggested for mature soot. (See values and reviews in Refs. [47, 50, 51, 273–275]. The value for  $E_{A,O_2}$  of 31.3 kJ/mol used by the ABF soot formation model [13] is derived from reactions with phenyl, not soot [276]).

A far more likely scenario is that OH is at superequilibrium quantities at the lowest points in the soot flame, and higher in the flame, the available surface area begins to deviate from that of hard, spherical primary particles. Indeed, differences between measured and predicted rates disappear at heights of 10 and 13 mm if OH exists at superequilibrium ratios of 10 and 1.5, at these respective locations. Even in the presence of soot, these are common superequilibrium ratios, especially near the flame sheet [69, 70, 277]. Likewise, beginning at a height of 35 mm, if the specific surface area increases by only 30% above the hard sphere model due to loss of sphericity and the opening of micropores, then discrepancies between predicted and measured values are largely rectified. This too is reasonable - recall, the BET surface area was 11% greater than the external surface area even *before* entering the soot flame, (Sec. 4.3.3). If OH superequilibrium and increased specific surface are present in the soot flame as described here, the Guo et al. mechanism [46] would yield an R<sup>2</sup> value of 0.95, while the R<sup>2</sup> from the Lee + Neoh mechanism would be 0.93. Intriguingly, in this hypothesized scenario, the location where the specific surface area begins to increase, corresponds with the onset of aggregate fragmentation.

## Chapter 6: Conclusions and Recommendations

### 6.1 Summary and Conclusions

A study has been performed investigating the nanostructure, morphology and gas-phase kinetics of soot oxidized in a unique ternary flame system. In this system, a column of soot is generated to maturity in a propylene-air co-flow diffusion flame, after which it enters a hydrogen diffusion flame. This creates a soot flame where, owing to the absence of hydrocarbons, soot oxidation may be observed without competing soot formation processes, a confounding factor which past studies of soot oxidation in flames have had to account for.

Within the soot flame, detailed measurements were performed, tracking the evolving soot structure, oxidation rate, temperature, and gas species concentrations. Transmission electron microscopy (TEM) was instrumental in characterizing soot structure at three levels of increasing resolution. At the lowest magnifications, soot particles appeared as fractal aggregates comprised of sphere-like primary particles. At the next level, size distributions and partial sintering of primary particles were measured. Lastly, at the highest resolutions, lattice fringes were measured, revealing the organization of carbon layered planes with respect to height in the soot flame and position within the primary particles.

To efficiently process and measure TEM images of soot across this broad scale, a program was developed in MATLAB called the Aerosol Image Analyzer (AIA). The program provides a convenient environment to rapidly test, optimize, and save image processing procedures needed for repeatable quantitative analysis. It also contains several new algorithms used to improve the speed and accuracy of measurements relevant to soot and other aerosols. An innovative algorithm, known as Center-Selected Edge Scoring (CSES) was used to semi-automatically measure the diameters of individual primary particles. CSES operates as an inverse to traditional circle detection algorithms which depend on accurate edge detection. CSES instead begins with a user-estimated center point and measures the gradients of all pixels on a candidate circle's circumference, not just those detectable as edges. The algorithm gives accurate results that represent an operator's best judgment, but is also five times faster than manual measurement.

Early on, large discrepancies in TEM measurements showed a clear need to reduce operator bias, obtain better estimates of TEM measurement uncertainties, and validate the proposed method for determining specific surface area from TEM images. This prompted the gage repeatability and reproducibility study presented in Chapter 4. This study produced four key results. First, robust uncertainty estimates for primary particle size distributions and specific surface areas were calculated, accounting for variations among samples, operators, and measurements replicates. These uncertainties, which were substantially greater than generally acknowledged in literature, were put to use thereafter in the analysis of soot flame measurements. Second, the study revealed that efforts to minimize bias through randomization and

use of the CSES algorithm were successful. Third, automated methods from the literature for measuring primary particle size distributions were found to be unreliable. Lastly, through comparison with surface area measurements by  $N_2$  adsorption, it was determined that measurement of primary particles on TEM images was a valid method for estimating soot surface area, provided that polydispersity and overlap among primary particles was taken into consideration.

Measurements in the soot flame found that the primary particle diameter mean and standard deviation decreased with increasing height in the flame, as a result of surface oxidation. In addition, primary particle asphericity became more apparent at higher flame locations. A shift in the size distributions from a normal to lognormal shape was observed, beginning a height of at 25 mm. Partial sintering between primary particles, observed as overlap on the TEM images, was seen to slightly decrease as height above burner increased, indicating in-place oxidation of primary particles rather than compaction due to oxidative sintering.

Primary particle size distribution and overlap was also used to determine the volume specific surface area (VSSA) of soot at each sampled location in the flame. Distribution-agnostic expressions for VSSA were derived that accounted for polydispersity of the primary particle population as well as the volume and surface area consumed by partial sintering. Two methods for estimating the volume and surface area lost to overlap were evaluated and found to give equivalent results. VSSA increased by as much as 90% with increasing height in the soot flame.

Soot aggregates were characterized by their maximum projected length  $L$ , radius of gyration  $R_g$ , number of constituent primary particles  $N_{p,a}$ , fractal dimension

$D_f$ , and pre-factor  $k_f$ . Aggregate size distributions were found to be consistently lognormal. Two different methods for calculating 3-dimensional  $R_g$  were found to be in agreement, and their relation to 2-dimensional  $R_g$  was consistent with past studies. The fractal dimension was essentially constant throughout the soot flame with a mean value of 1.74, which is typical for soot.

Several morphological metrics pointed to the onset of soot fragmentation beginning at a height of 35 mm. At this location in the flame, there was a shift in the distribution of  $L$ , a sharp drop in the geometric mean value of  $R_g$ , and a mild drop in  $k_f$ . However, even more direct evidence for soot fragmentation came from two complementary methods. From TEM imaging alone, the number of primary particles per aggregate was found to dramatically drop at a height of 35 mm. A second method combined TEM, soot volume fraction, and velocity measurements to compute the total number flow rate of aggregates, which was seen to suddenly increase at 35 mm. Taken together, this is strong evidence for soot fragmentation, and is the first detection of this phenomenon using the methods presented here.

An interesting result was found in the overall number flow rate of primary particles, which sees a sharp, unexpected increase at 25 mm in the soot flame. This observation is surprising, as it would imply that in addition to aggregate fragmentation, primary particle fragmentation also occurs, but in such a way that the its remnants retain enough sphericity to be detected as primary particles by an operator. While this seems implausible, alternative possibilities, including changes in porosity or to soot optical properties, could not explain the observations. This curious result therefore remains an open question.

High magnification TEM analysis was performed in both selected area electron diffraction (SAED) mode, and bright field HRTEM mode. The two methods are complementary in that the former reveals information about the specimen-averaged distribution of atomic spacings that cannot be observed by HRTEM, while the latter provides information about soot nanostructure that is spatially resolved within the projected image. The d-spacings and integral breadths determined at four flame locations by SAED were typical for soot and did not indicate a changing nanostructure on a global scale.

HRTEM lattice fringe analysis provided a wealth of information about how soot nanostructure changes with respect to the location within the primary particle and in the soot flame. Measurements of fringe length, tortuosity, orientation, and separation distance revealed that primary particles could be radially divided into two regions: an inner 80% where nanostructural order increases as one moves radially outward from the center of a primary particle, and an outer 20% where this trend reverses. Greater nanostructural order was interpreted from longer fringe lengths, lower tortuosities, greater fringe concentricity, and shorter fringe separation distances. These are all hallmarks of mature soot that has already undergone graphitization.

Since primary particles decreased in diameter with increasing height above burner, and the nanostructure showed greater disorder near the primary particle core, it was expected that the fringe analysis would also show an average decrease in the indicators of graphitization with increasing height in the flame. Surprisingly this was not the case; median and average values of fringe measurements showed little

correlation with location in the soot flame. Instead, analysis found that within the outer 20% of primary particles, oxidation by the gas phase stripped away material in a shrinking-sphere manner, while the inner 80%, which was out of reach of oxidizing gases, underwent further graphitization. Additionally, there was evidence for two graphitization modes. The first occurred within the bulk of the primary particle due to thermal annealing. The second mode was more dramatic and occurred just below the oxidizing surface. This was interpreted as graphitization induced by oxidation at the outer shell, which removed cross links and interstitial material, allowing carbon planes beneath it to grow and realign. Analysis of HRTEM images found no evidence of internal burning or major pore openings within soot primary particles, however a deviation from perfect sphericity did appear to accompany increasing height in the soot flame.

The ongoing graphitization within primary particle interiors is consistent with the unchanging overall nanostructure suggested by SAED measurements. It also challenges the assumption that once soot reaches maturity, the nanostructure is essentially "locked in," and cannot be altered at typical flame temperatures and residence times. Instead, while the overall *character* of the nanostructure remains unaltered (i.e. the soot retains concentric layers of increasing order), graphitization remains ongoing, even in mature soot, in ways that are consequential to the reactive chemistry. In this study, ongoing graphitization in the primary particle core resulted in an unchanging nanostructure being presented to the oxidizing gas phase. Consequently, analysis of oxidation kinetics proceeded with an assumption of a constant surface concentration of active sites, implying constant collision efficiencies for the

oxidizers  $O_2$  and OH.

Soot oxidation rates per unit of soot surface area were obtained by combining measurements of soot volume fraction, velocity, and specific surface area. The integrated soot volume fraction at each height within the soot flame was measured using laser extinction at 632.8 nm. Velocity was determined using high frame rate video to track perturbations to the soot flame as they traveled axially upward. Specific surface area was obtained from measured TEM images of primary particles as described above. The resulting soot oxidation rates ranged from 0.3 - 5.7  $g/m^2\cdot s$  within the soot flame.

Soot flame temperatures were found using ratio pyrometry with a modified commercial digital camera at wavelengths of 450, 650, and 900 nm, followed by Abel deconvolution. Gas chromatography was used to derive major species concentrations from isokinetically sampled gases, while water concentration was determined from desiccant gravimetry. Radical concentrations were estimated from full equilibrium at local temperatures and stoichiometry.

Measured soot oxidation rates were compared to predictions of several mechanisms. The combined mechanism of Nagle and Strickland-Constable (NSC) [42] for  $O_2$ , and of Neoh et al., [43] for OH, though arguably the most prevalent rate expressions in the literature, gave very poor predictions of the oxidation observed in the present study. Most of this difference can be ascribed to the NSC expression's overprediction of oxidation by  $O_2$ . The mechanisms of Lee et al. [47] combined with Neoh [43], gave far better predictions, and the optimized rate expressions by Guo [46], did better still. In addition, very reasonable changes to the assumptions

of equilibrium OH low in the flame and hard-sphere surface areas high in the flame would largely reconcile observations with the predictions of these latter two mechanisms.

## 6.2 Recommendations for Future Study

There are several avenues worthy of further investigation. First, the present work has assumed soot optical properties and density to be constant. However, this may not be the case. For example, first order calculations using RDG-PFA theory suggest that scattering may play a larger role in laser extinction than was assumed here. If so, changes to primary particle and aggregate sizes could lead to changing optical properties, which would in-turn affect observed oxidation rates. This line of inquiry may also shed light on the increase in primary particle number flow rate observed in Sec. 5.3.5.

Second, it would be useful to investigate whether the hard-sphere assumption in calculating soot surface area holds after substantial oxidation. One way this could be determined is by increasing soot production in the co-flow flame, or by lowering the intensity of the hydrogen flame such that sufficient quantities of soot for BET analysis could be obtained at the soot flame exit. Moreover, if increases in BET specific surface area could be correlated to changes in TEM images, for example by changes in the ratio of projected image perimeter to area, this could provide a valuable means of refining surface area estimations from TEM images.

Third, as was discussed in the literature review, soot nanostructure is known

to be a function fuel type. An investigation using the same ternary flame system but with soot generated from different fuels (e.g. aromatics), producing very different nanostructures would be valuable toward understanding how nanostructure affects oxidation behavior. Similarly, the ternary flame system could be used to examine the oxidation of soot at varying degrees of maturity. Less mature soot could be produced by placing a wire mesh into the co-flow flame to quench it.

Lastly, a direct measurement of the OH radical in the soot flame, such as by laser induced fluorescence, would be invaluable. If deviations from the assumed equilibrium condition were observed, this would go a long way toward validating or invalidating some of the oxidation mechanisms considered in the present work.

## Appendix A: MATLAB Code

### A.1 Center-Selected Edge Scoring

```
function [CenterPt,Radius,Score]= CSES(Img, DiaRange, Polarity, ClickedPt)
% CSES Fit the best circle to an image using Center-Selected Edge Scoring
%
% Uses Center-Selected Edge Scoring (CSES) to find the best-fit circle on
% the input image with a diameter within DiaRange and a centerpoint in the
% neighborhood of ClickedPt
%
% Input arguments:
% Img           The image matrix on which a circle is to be found
% DiaRange      A vector array giving the range of diameters to evaluate
%               for a best-fit circle on IMG.
% Polarity      Intensity of the image foreground with respect to the
%               background. Allowed values: 'bright' or 'dark'
% ClickedPt     A vector array [x, y] of the point clicked in the Image by
%               the user. This will be the center of the pixel neighborhood
%               that will serve as candidate centerpoints for the best fit
%               circle. Note: x increases from left to right, y increases
%               from top to bottom of the image
%
% Output arguments:
% CenterPt      Center point of the best fit circle
% Radius        Radius of the best fit circle
% Score         CSES goodness-of-fit score of the best fit circle
%
% Date          Version      Author          Notes
% 10/02/14     1.00         Paul M. Anderson  Initial release
% 12/15/16     1.01         Paul M. Anderson  Utilizes circle masks generated by
%                  midpoint circle algorithm
% 01/28/18     1.02         Paul M. Anderson  Circle masks referenced with
%                  linear indexing to improve speed
%                  and memory. Circles with even
%                  diameters centered at pixel
%                  corners.
```

```

load( 'CSESCircleMasks.mat', 'Masks' )

if strcmp(Polarity, 'bright') % If foreground is bright, first invert image
    Img = imcomplement(Img);
end
[ImgGrads.Mag, ImgGrads.Orient] = CalcEdges(Img);

% Get original image dimensions
[h,w] = size(ImgGrads.Mag);

RadRange = DiaRange./2;
r_min = min(RadRange);
r_max = max(RadRange);

% Size of the pixel neighborhood surrounding the ClickedPt.  Pixels within
% the neighborhood will be evaluated as centerpoints for a best fit circle.
% Example: CenterPtNeighb = 1 will consider a 3x3 matrix with ClickedPt at
% its center, 2 will consider a 5x5 matrix, etc.  From experience, the
% following expression yields a CenterPtNeighb that meets user intuition.
CtrPtNeighb = round(0.05*r_max+1);

% r_max will be the smaller of the input r_max or the radius of the largest
% circle that can be drawn at a center of (ClickedPt +/- CtrPtNeighb)
% without going beyond the image boundaries
r_max = min([ ClickedPt(1)-CtrPtNeighb-0.5, w-ClickedPt(1)-CtrPtNeighb+0.5, ...
    ClickedPt(2)-CtrPtNeighb-0.5, h-ClickedPt(2)-CtrPtNeighb+0.5, r_max]);

d_min = ceil(2*r_min);
d_max = floor(2*r_max);

if d_min > d_max
    PromptText = 'The minimum radius is too large for this image location.';
    uiwait(msgbox(PromptText, 'CSES_Error', 'modal'));
    Radius = -1; CenterPt = []; Score = 0;
    return
end

nDiams = d_max - d_min + 1; %Number of diameters that will be evaluated

% Calculate distance from ClickedPt needed for evaluation window
Offset = int16(min([ ClickedPt(1)-1, w-ClickedPt(1), ClickedPt(2)-1, ...
    h-ClickedPt(2), (Masks.Size(1)-1)/2, (Masks.Size(2)-1)/2]));

% Make sub-matrices of the image's magnitude and orientation matrices
SubMatMags = ImgGrads.Mag(ClickedPt(2)-Offset:ClickedPt(2)+Offset, ...
    ClickedPt(1)-Offset:ClickedPt(1)+Offset);

```

```

SubMatOrient = ImgGrads.Orient(ClickedPt(2)-Offset:ClickedPt(2)+Offset, ...
    ClickedPt(1)-Offset:ClickedPt(1)+Offset);

[hSub,wSub]=size(SubMatMags);

% If the sub-matrices are smaller than the circle mask matrices, pad the
% sub-matrices to equal the dimensions of the circle mask matrices
if hSub < Masks.Size(1)
    xPad = (Masks.Size(2)-wSub)/2;
    yPad = (Masks.Size(1)-hSub)/2;
    SubMatMags = padarray(SubMatMags,[yPad,xPad], 'both');
    SubMatOrient = padarray(SubMatOrient,[yPad,xPad], 'both');
    hSub=size(SubMatMags,1);
end

kMin = find(Masks.Diams==d_min);
kMax = find(Masks.Diams==d_max);

PixIdx = Masks.PixIdx(kMin:kMax);
Orient = Masks.Thetas(kMin:kMax);
Diams = Masks.Diams(kMin:kMax);
nPixels = Masks.nPixels(kMin:kMax);

% Variables to hold the best-fit circle data
BestScore = 0; BestCtrDel = [0,0]; BestDiam = 0;

% For each possible centerpoint (i.e. all points in neighborhood)
for xDel = -CtrPtNeighb : CtrPtNeighb
    for yDel = -CtrPtNeighb : CtrPtNeighb

        for k = 1:nDiams
            % shift columns that indices to refer to
            TheseIdx = PixIdx{k} + hSub*xDel + yDel;

            EdgeMags = SubMatMags(TheseIdx);
            EdgeOrient = SubMatOrient(TheseIdx);

            DeltaTheta = EdgeOrient - Orient{k};
            OrientScores = cos(DeltaTheta);
            ThisCircleScore = (sum(EdgeMags.* OrientScores))/nPixels(k);

            if ThisCircleScore > BestScore
                BestScore = ThisCircleScore;
                BestCtrDel = [xDel,yDel];
                BestDiam = Diams(k);
            end
        end
    end
end

```

```
        end
    end

    CenterPt = [ClickedPt(1)+BestCtrDel(1), ClickedPt(2)+BestCtrDel(2)];
    if mod(BestDiam, 2) == 0 % if best circle has even diameter
        CenterPt = CenterPt + 0.5;
    end

    Radius = BestDiam/2;
    Score = BestScore;
```

## A.2 SAED Image Analysis Code

```
function [DP]= AnalyzeDiffPatt(CtrPt,PadImgTF,CurveFitType,DiffImg,MaskImg)
% ANALYZEDIFFPATT Measure features of a concentric-ring diffraction pattern

% Input Arguments
% CtrPt      Center point [px] of the original diffraction pattern image
% PadImgTF   1 if you want to pad the diffraction pattern image to make it
%            square prior to analysis, 0 to keep it as-is.
% DiffImg    The diffraction pattern image
% MaskImg    Beam blocker image mask
% Scale      Diffraction pattern image scale [nm-1/px]

% Output Arguments
% DP         A structure variable with the following fields:
%   r        Each radius [px] at which the intensity of the raw
%            diffraction pattern is circumferentially averaged,
%            yielding DP_gross
%   gross     The gross diffraction pattern profile: the average
%            intensity of the raw diffraction pattern image at each r
%   rr       Only those values of r larger than the location of the
%            first inflection point in DP_gross
%   r_BkgPts Radius values of the selected points of the backgrnd signal
%   A_BkgPts Values of the background intensity at each r_BkPts
%   BkgFit    Curve fit object fitted to the selected background points
%   BkgCurve  The best fit background image curve, evaluated at each rr
%   net       The diffraction pattern profile with the background removed
%   pks       The values of DP_net at each local peak
%   locs      The values of rr at which pks occur [px]
%   FWHM      The full-width, half-maximums of each peak [nm-1]
%   dSpacing  The lattice d-spacing (in Angstroms) corresponding to the
%            location of each peak
%   Intensity The integrated intensity of each peak [a.u.]
%   Breadth   The integral breadth of each peak [nm-1]

% Paul M. Anderson, 2018

warning('off','images:initSize:adjustingMag');

RefineFitTF = true; % Refine initial fit with a spline fit
NumValleys = 2;    % Number of local minima to be found in DiffImg

load('CSESCircleMasks.mat','Masks')
dMax = 1500;
DiaRange = [10, dMax];
```

```

% Get original image dimensions
[h,w] = size(DiffImg);

if PadImgTF
    % Pad the image to make it square
    PadSize = round((w-h)/2);
    DiffImg = padarray(DiffImg,[PadSize,0],'both');
    MaskImg = padarray(MaskImg,[PadSize,0],255,'both');
    [h,w] = size(DiffImg);
    CtrPt(2) = CtrPt(2)+PadSize;
else
    PadSize = 0;
end

RadRange = DiaRange./2;
r_min = min(RadRange);
r_max = max(RadRange);

% r_max is smaller of input r_max or radius of the largest circle that can
% be drawn centered at CtrPt without going beyond the image boundaries
r_max=min([CtrPt(1)-0.5,w-CtrPt(1)+0.5,CtrPt(2)-0.5,h-CtrPt(2)+0.5,r_max]);

d_min = ceil(2*r_min);
d_max = floor(2*r_max);

if d_min > d_max
    PromptText = 'The minimum radius is too large for this image location.';
    uiwait(msgbox(PromptText,'Error','modal'));
    return
end

nDiams = d_max - d_min + 1; %Number of diameters that will be evaluated

% Calculate distance from CtrPt needed for evaluation window
Offset = int16(min([CtrPt(1)-1,w-CtrPt(1),CtrPt(2)-1,h-CtrPt(2), ...
    (Masks.Size(1)-1)/2, (Masks.Size(2)-1)/2]));

% Make sub-matrices of the Diffraction pattern image and beam blocker mask
SubDiffImg = DiffImg(CtrPt(2)-Offset:CtrPt(2)+Offset, ...
    CtrPt(1)-Offset:CtrPt(1)+Offset);
SubMaskImg = MaskImg(CtrPt(2)-Offset:CtrPt(2)+Offset, ...
    CtrPt(1)-Offset:CtrPt(1)+Offset);

[hSub,wSub]=size(SubDiffImg);

% If the sub-matrices are smaller than the circle mask matrices, pad the
% sub-matrices to equal the dimensions of the circle mask matrices

```

```

if hSub < Masks.Size(1)
    xPad = (Masks.Size(2)-wSub)/2;
    yPad = (Masks.Size(1)-hSub)/2;
    SubDiffImg = padarray(SubDiffImg,[yPad,xPad], 'both');
    SubMaskImg = padarray(SubMaskImg,[yPad,xPad], 'both');
    hSub=size(SubDiffImg,1);
end

kMin = find(Masks.Diams==d_min);
kMax = find(Masks.Diams==d_max);

PixIdx = Masks.PixIdx(kMin:kMax);
Diams = Masks.Diams(kMin:kMax);
r = zeros(nDiams,1);
DP_gross = zeros(nDiams,1);

for k = 1:nDiams
    DiffImgVals = SubDiffImg(PixIdx{k});
    MaskImgVals = SubMaskImg(PixIdx{k});

    MaskedDiffImgVals = uint32(DiffImgVals).*uint32(MaskImgVals);
    nPixels = numel(find(MaskedDiffImgVals));
    r(k) = Diams(k)/2;

    DP_gross(k) = sum(MaskedDiffImgVals)/nPixels;
end

% Force program to ignore false minima near the direct beam
DP_gross(1:170)=max(DP_gross);

MaxDP=255;
rScaled = r*Scale;

% Get the loctions of local minima between peaks as well as the inflection
% point of the curve near the direct electron beam
[ValleyIdx,InflxPtIdx] = GetValleys(DP_gross,NumValleys);

EndIdx = find(r==600); % Perform analysis out to r=600:

%Use inflection point, valley points, & end point as points for curve fit
r_BkgPts = vertcat(r(InflxPtIdx),r(ValleyIdx),r(EndIdx));
A_BkgPts = vertcat(DP_gross(InflxPtIdx),DP_gross(ValleyIdx), ...
    DP_gross(EndIdx));

switch CurveFitType
    case 'Lognorm'
        % Use a lognormal curve to fit the background

```

```

    opts = fitoptions('Method','NonlinearLeastSquares',...
                    'Lower',[0,-Inf,-Inf],...
                    'Upper',[Inf,Inf,Inf],...
                    'Startpoint',[10^11,-25,10]);
    f = fitype('(a/x)*exp(-((log(x)-b)/c)^2)', 'options', opts);
    BkgFit = fit(r_BkgPts, A_BkgPts, f);
    b = feval(BkgFit, r);

case 'PowerLaw'
    % Use a power law curve to fit the background
    BkgFit = fit(r_BkgPts, A_BkgPts, 'power2');
    b = feval(BkgFit, r); % evaluate the curve at each value of r

case 'Spline'
    % Use a spline to fit the background
    BkgFit = fit(r_BkgPts, A_BkgPts, 'smoothingspline', ...
                'SmoothingParam', 0.001);
    b = feval(BkgFit, r); % evaluate the curve at each value of r
otherwise
    msgbox('We did not recognize that curve fit type ID. Aborting.')
    return
end

StartIdx = InflxPtIdx;

% Only analyze the relevant portions of the diffraction pattern
rr = r(StartIdx:EndIdx); rrScaled = rr*Scale;
AA = DP_gross(StartIdx:EndIdx);
BkgCurve1 = b(StartIdx:EndIdx);

% Difference between diffraction pattern image & 1st background estimate
DP_net1 = AA-BkgCurve1;

if RefineFitTF
    % Find the minima of the 1st estimate of the net diffraction pattern
    ValleyTF = islocalmin(DP_net1, 'MaxNumExtrema', 2, 'MinSeparation', 80);
    ValleyIdx = find(ValleyTF);

    r_BkgPts2 = vertcat(rr(1), rr(ValleyIdx), rr(end));
    A_BkgPts2 = vertcat(DP_net1(1), DP_net1(ValleyIdx), DP_net1(end));

    % Use a spline to fit the background
    BkgFit2 = fit(r_BkgPts2, A_BkgPts2, 'smoothingspline', ...
                'SmoothingParam', 0.1);
    BkgCurve2 = feval(BkgFit2, rr); % evaluate the curve at each rr

    % Difference between net diffraction pattern & background

```

```

    DP_net2 = DP_net1-BkgCurve2;
    DP_net2(DP_net2<0)=0; % Set negative net values to zero
else
    BkgCurve2 = zeros(size(BkgCurve1));
    DP_net2 = DP_net1;
end

% Get locations and FWHMs of diffraction peaks
[pks,locs,widths,proms] = findpeaks(DP_net2,rr,'MinPeakDistance',50, ...
    'MinPeakProminence',2,'Annotate','extents','WidthReference','halfprom');
npks = length(pks);

% Get the locations of minima between peaks, for use as integration limits
ValleyTF = islocalmin(DP_net2,'MaxNumExtrema',2,'MinSeparation',80);
ValleyIdx = find(ValleyTF);

IntLimIdx = vertcat(1,ValleyIdx,length(DP_net2));

dSpacing = 10./(locs(1:length(pks)).*Scale); %d-spacing in Angstroms
FWHM = widths.*Scale; % Full-width half-maximums in nm-1

% Calculate the integrated intensity, integral breadth
Intensity = zeros(length(pks),1);
Breadth = zeros(length(pks),1);
for k = 1:length(pks)
    Intensity(k) = trapz(DP_net2(IntLimIdx(k):IntLimIdx(k+1)))*Scale;
    Breadth(k) = (Intensity(k)/pks(k));
end

% Output everything as a structure variable
DP = struct('r',r,'gross',DP_gross,'rr',rr,'r_BkgPts',r_BkgPts, ...
    'A_BkgPts',A_BkgPts,'BkgFit',BkgFit,'BkgCurve',BkgCurve1, ...
    'net',DP_net2,'pks',pks,'locs',locs,'dSpacing',dSpacing, ...
    'FWHM',FWHM,'Intensity',Intensity,'Breadth',Breadth);

% Plot everything all on one giant amazing plot!
TotBkgCurve = BkgCurve1 + BkgCurve2;
figure; hAx4 = axes;
plot(hAx4,rScaled,DP_gross/MaxDP,'b',r_BkgPts*Scale,A_BkgPts/MaxDP, ...
    '*r',rrScaled,TotBkgCurve/MaxDP,'-r'); hold on;
plot(hAx4,rrScaled,DP_net2/MaxDP,'k');
plot(hAx4,locs*Scale,(pks+1)/MaxDP,'vb','MarkerFaceColor','g');
plot(hAx4,rrScaled(IntLimIdx(1:npks+1)), ...
    DP_net2(IntLimIdx(1:npks+1))/MaxDP,'or');
title(ImgID,'Interpreter','none');
legend('Gross_Diffraction_Pattern','Background_Points', ...
    'Background_Fit','Net_Diffraction_Pattern', ...

```

```

'Diffraction_Peak_Maxima', 'Limits_of_Integration', 'Gaussian_Fit');
end

function [ValleyIdx,InflxPtIdx] = GetValleys(A,NumValleys)

% Input arguments
% A          The diffraction pattern intensity profile
% NumValleys The total number of minima expected in the diff pattern

% Output arguments
% ValleyIdx  Indices of the locations of minima in A
% InflxPtIdx Index of the location of the 1st inflection point in the
%            diffraction pattern curve

KeepLooping = true;
n = 0;
while KeepLooping

    % Keep smoothing raw data until there are no false minima
    A = smoothdata(A, 'movmean',2+n);

    ValleyTF = islocalmin(A);
    n = n+1;
    if sum(ValleyTF) <= NumValleys || n == 100
        KeepLooping = false;
    end
end

ValleyIdx = find(ValleyTF);

Y = diff(A,2); % 2nd derivative of the curve
InflxPtIdx = find(Y>0,1); % Find the first inflection point in the curve

end

```

## A.3 Lattice Fringe Analysis Code

### A.3.1 BridgeGaps Function

```
function BridgedImg = BridgeGaps(BWImg, Prox, AngTol)
% BRIDGEGAPS Connect line segments meeting criteria
% Connects line segments whose endpoints are within a given proximity
% and whose orientations are within a given tolerance
%
% Input Arguments:
% BWImg          A binary image of skeletonized line segments
% Prox           The maximum proximity between endpoints within which
%               line segments will be considered for connection
% AngTol        The maximum difference in angles made by the ends of
%               each line segment allowed for connection
%
% Output Arguments:
% BridgedImg     The original image with lines drawn connecting line
%               segments meeting criteria
%
% Paul M. Anderson, 2017

% Covert angle tolerance to radians
AngTol = AngTol*pi/180;

% Orientations around a 5x5 bounding box
Ang = [2.3562  2.0344  1.5708  1.1071  0.7854; ...
       2.6779   0       0       0       0.4636; ...
       3.1416   0       0       0       0; ...
       3.6052   0       0       0       5.8195; ...
       3.9270  4.2487  4.7124  5.1760  5.4978];

% Create a mask within which neighboring endpoints will be evaluated for
% bridging. Note that since endpoints are evaluated in order of ascending
% linear index, to avoid evaluating the same endpoint pair twice, the mask
% only covers those points representing linear indicies greater than the
% candidate endpoint. This gives the mask a semicircle-like shape
hMask = 2*Prox+1; wMask = hMask;
[xx,yy] = meshgrid(1:wMask,1:hMask);
ProxMask = false(hMask,wMask);
% Create a mask with 1's at pixels within Prox of the centerpoint
ProxMask = ProxMask | hypot(xx - (Prox+1), yy - (Prox+1)) <= Prox;
% Zero-out the right half of the circular mask
ProxMask(:,1:Prox)=0;
% Zero-out the pixels directly above above and including the center
```

```

ProxMask(1:Prox+1,Prox+1)=0;

% Don't evaluate line segments smaller than 4 pixels
Img = bwareaopen(BWImg,4,8);

% Pad image to accomodate masking near image boundaries
BridgedImg = padarray(Img,[Prox,Prox],'both');
EndPtImg = bwmorph(BridgedImg,'endpoint',inf);

% For reasons unknown, bwmorph occasionally finds endpoints at black pixels
EndPtImg = EndPtImg & BridgedImg;

% Identify endpoints and label each segment
[row,col] = find(EndPtImg);
[h,w] = size(EndPtImg);
Ind = sub2ind([h,w],row,col);
LabMat = labelmatrix(bwconncomp(BridgedImg));

% Determine the orientation of the end of each line segment
EndAng = zeros(numel(row),1);
for n=1:numel(row)
    EndSegImg = BridgedImg(row(n)-2:row(n)+2,col(n)-2:col(n)+2);
    D = bwdistgeodesic(EndSegImg,3,3);
    D(~isfinite(D))=0; % Zero out any NaN and Inf
    D(2:end-1,2:end-1)=0; % Interested in only the border pixels
    % Orientation of the 1st pixel that traces back to the sub image border
    EndAng(n) = Ang(find(D==min(D(D>0)),1));
end

% Evaluate each endpoint for bridging
for n=1:numel(row)
    SubImg = BridgedImg(row(n)-Prox:row(n)+Prox,col(n)-Prox:col(n)+Prox);
    SubEndPtImg = EndPtImg(row(n)-Prox:row(n)+Prox,col(n)-Prox:col(n)+Prox);
    SubEndPtImg(SubEndPtImg==0) = 0; % mask the sub endpoint image
    [SubRow,SubCol] = find(SubEndPtImg);
    for m = 1:numel(SubRow)
        % Convert back to rows & cols of padded image
        r = row(n)+(SubRow(m)-(Prox+1));
        c = col(n)+(SubCol(m)-(Prox+1));
        % If the 2 endpoints aren't part of the same segment, evaluate
        if LabMat(r,c)~=LabMat(row(n),col(n))
            Idx = sub2ind([h,w],r,c);
            Ang2 = EndAng(find(Ind==Idx));
            AngDiff = abs(EndAng(n)-Ang2);
            if abs(AngDiff - pi) <= AngTol % Meets connection criteria
                BridgedImg=linept(BridgedImg,r,c,row(n),col(n));
            end
        end
    end
end

```

```
        end
    end
end

% Remove padding from BridgedImg
BridgedImg = BridgedImg(Prox+1:h-Prox, Prox+1:w-Prox);

% Add back in the small line segments that were removed
BridgedImg = BridgedImg | BImg;
```

### A.3.2 SeverBranches Function

```
function [OutImg,BranchMarkers] = SeverBranches(BWImg,SubImgSize)
% SEVERBRANCHES Sever spurious branches from line segments
% Compares line segment orientations at each branchpoint of a
% skeletonized image to determine which segments are spurious branches
% from the primary line segment. Severs the branches and marks the
% remaining portion.
%
% Input arguments:
% BWImg          The binary skeletonized image to be evaluated
% SubImgSize     The length of a side of the square region centered
%                at each branchpoint. The angle between the region's
%                center and a segment's location on the region's
%                border determines its orientation. Must be odd.
%
% Output Arguments:
% OutImg         BWImg with branches severed (no branch 8-connectivity)
% BranchMarkers  A binary matrix the same size as OutImg with 1's
%                marking a pixel within each severed branch
%
% Paul M. Anderson, 2017

OutImg = BWImg;
BranchMarkers = false(size(BWImg));

% Create an image containing only branchpoints, and get their coordinates
BranchPtImg = bwmorph(BWImg,'branchpoints');
[row,col] = find(BranchPtImg);

% Ensure the interrogation window is always the correct size
c = 0.5+SubImgSize/2;
a = floor(c)-1;
b = ceil(c)-1;

% Create a matrix the size of SubImg in which each cell's value
% is its angle with respect the the matrix center
[X,Y] = meshgrid(-(c-1):(c-1),-(c-1):(c-1));
Ang = flip(atan2(Y,X));
Ang(Ang<0)=Ang(Ang<0)+2*pi;

nBranchPts = numel(row);
nPrevBranchPts = 0;

%Keep looping until the number of branchpoints in the image stops changing
while nBranchPts ~= nPrevBranchPts
```

```

nPrevBranchPts = nBranchPts;

for Ind=1:nBranchPts

    % If the interrogation window does not cross the image boundaries
    if row(Ind)-a > 0 && row(Ind)+b <= size(BWImg,1) && col(Ind)-a ...
        > 0 && col(Ind)+b <= size(BWImg,2)

        % Create a sub-image centered at the given branchpoint
        SubImg=OutImg(row(Ind)-a:row(Ind)+b, col(Ind)-a:col(Ind)+b);

        % Identify and index the endpoint of each segment in SubImg
        SegmtEnds = bwmorph(SubImg, 'endpoints', inf);
        EndInds = find(SegmtEnds);

        % The angle of each segment at the edge of the SubImg
        SegmtAngs = Ang(EndInds);

        % Calculate the difference between the orientations of each
        % pairing of SubImg segments
        n = numel(SegmtAngs);
        AngDiffs = zeros(n);
        for i = 1:n-1
            for j = i+1:n
                AngDiffs(i, j)=abs(SegmtAngs(i)-SegmtAngs(j));
            end
        end
        Orients = abs(AngDiffs - pi);

        % Retain the segment pair whose angle diff is closest to pi
        [~, MinInd]=min(Orients (:));
        [i, j]=ind2sub([n, n], MinInd);
        KeptInds = false(n, 1);
        KeptInds(i) = true; KeptInds(j) = true;

        % Calc the dist from the endpoints of the retainable segments
        % to all other pts on line
        D = bwdistgeodesic(SubImg, EndInds(KeptInds));
        SubD = D(c-1:c+1, c-1:c+1); % The center 3x3 pixels of D
        SubD(SubD>=D(c, c))=0; % Sever the spurious branches in D
        SubD = SubD>0; % Convert center pixels to binary
        SubImg(c-1:c+1, c-1:c+1) = SubD; % replace severed center pixels
        SubImg(c, c)=true; %Make sure the branchpoint itself is retained
        SubMarker = false(size(SubImg));
        SubMarker(EndInds(~KeptInds))=1; % Mark the spurious branches

        % Insert the broken SubImg into the original image and the

```

```

        % marker into the BranchMarkers matrix
        OutImg(row(Ind)-a:row(Ind)+b, col(Ind)-a:col(Ind)+b) = SubImg;
        BranchMarkers(row(Ind)-a:row(Ind)+b, col(Ind)-a:col(Ind)+b) ...
            = SubMarker;
    end
end

% Check the number of branchpoints remaining in the image
BranchPtImg = bwmorph(OutImg, 'branchpoints');
[row, col] = find(BranchPtImg);
nBranchPts = numel(row);
end

end

```

### A.3.3 MeasureFringes Function

```
function [FringeData, FringeCoords] = MeasureFringes(BWImg, ...
    MinFringeLength, PolyLines, ImgAxes, CtrPt)
% MEASUREFRINGES Perform measurements on skeletonized lattice fringes
%
% Input Arguments:
% BWImg          A binary image of the skeletonized fringe segments
% MinFringeLength In pixels. Segments shorter than this will not be
%                included in the output measurement
% PolyLines      Line objects representing the ROI
% ImgAxes        The axes object currently displaying the image
% CtrPt          Centerpoint of the primary particle to which the fringe
%                segments belong
%
% Output Arguments:
% FringeData     A matrix containing the computed length, tortuosity,
%                non-concentricity, and radial location of each fringe
% FringeCoords   Coordinates of each fringe's pixels
%
% Paul M. Anderson, 2017

% Ignore all the b&w objects touching the ROI if there is an ROI, or
% touching the image border if there is no ROI
if isempty(PolyLines)
    BWImg = imclearborder(BWImg);
else
    % Coordinates of ROI vertices
    Pos = horzcat(PolyLines.XData', PolyLines.YData');
    hPoly = impoly(ImgAxes, Pos);
    LineMask = createMask(hPoly);
    delete(hPoly);
    LineMask = bwmorph(LineMask, 'remove'); % Just ROI polygon border
    BWImg(LineMask)=1; %Burn the ROI polygon border into the image
    Marker = false(size(BWImg));
    [I, J] = find(LineMask, 1); %Coords of 1st pixel on ROI polygon border
    Marker(I, J)=true; % Tag the ROI border pixel
    % Img of only the white pixels on or 8-connected to the ROI border
    BorderFringeImg = imreconstruct(Marker, BWImg);
    % Img with the white pixels on or 8-connected to the ROI border removed
    BWImg = logical(BWImg - BorderFringeImg);
end

% Identify each unique fringe in the skeletonized image
CC = bwconncomp(BWImg, 8);
s = regionprops(CC, 'Centroid', 'Orientation', 'Extrema');
```

```

% Create a label matrix
LMat = labelmatrix(CC);

%Preallocate
EndPtDists = zeros(CC.NumObjects,1);
FringeLengths = zeros(CC.NumObjects,1);
gDists = cell(CC.NumObjects,1);
FringeCoords = cell(CC.NumObjects,1);
FringeOrients = zeros(CC.NumObjects,1);
FringeRadDists = zeros(CC.NumObjects,1);

UserCancelled = false;

% If indeed we have fringes...
if CC.NumObjects > 0

    wb = waitbar(0, '', 'Name', 'Measuring_fringes...', ...
        'CreateCancelBtn', 'setappdata(gcf, ''canceling'',1)');

    RightTopPts = zeros(CC.NumObjects,2);

    % Loop through each unique fringe object
    for f = 1:CC.NumObjects

        % Check for click of waitbar's Cancel button
        if getappdata(wb, 'canceling')
            UserCancelled = true;
            break;
        end

        % Update waitbar every 5th time through the loop
        if mod(f,5)==0
            waitbar(f/CC.NumObjects,wb, sprintf ...
                ('%d_of_%d_candidate_fringes_evaluated',f,CC.NumObjects));
        end

        % Find the endpoints of fringe f
        TempImg = LMat == f;
        [row, col]=find(bwmorph(TempImg, 'endpoints'));
        RightTopPts(f,:) = s(f).Extrema(8,:);

        % Ignore single pixels and objects lacking endpoints (e.g. circles)
        if numel(row) > 1
            % Calculate the fringe length
            gDists{f} = bwdistgeodesic(TempImg, col(1),row(1), ...
                'quasi-euclidean');
        end
    end
end

```

```

gDists{f} = gDists{f}(~isnan(gDists{f}));

% Sort the Fringe pixel indices so that they are in order of
% increasing distance from the starting pixel
[~,SortIdx]=sort(gDists{f});
[i,j] = ind2sub(CC.ImageSize,CC.PixelIdxList{f}(SortIdx));

% Since bwdistgeodesic terminates at the centers of the
% endpoint pixels, must extend to the true fringe termina
i = [1.5*i(1)-0.5*i(2); i; 1.5*i(end)-0.5*i(end-1)];
j = [1.5*j(1)-0.5*j(2); j; 1.5*j(end)-0.5*j(end-1)];
FringeLengths(f) = max(gDists{f}) + sqrt((i(1)-i(2))^2 ...
    + (j(1)-j(2))^2) + sqrt((i(end)-i(end-1))^2 ...
    + (j(end)-j(end-1))^2);

% Compute the distance between the fringe termina
EndPtDists(f) = sqrt((i(1)-i(end))^2+(j(1)-j(end))^2);

FringeCoords{f} = [i,j]; %Record this fringe's x,y coordinates

% Fringe centroid
c = s(f).Centroid;
x = c(1)-CtrPt(1); y = CtrPt(2)-c(2);

% Radial dist of fringe from CtrPt of primary particle
FringeRadDists(f) = hypot(x,y);

% Compute the fringe's deviation from perfect concentricity
Theta=atand(y/x); % Angle of the radial vector from the x-axis
if (y*x)>0 % If fringe is in 1st or 3rd unit circle quadrant
    % Angle between the radial vector and this fringe
    FringeOrients(f) = 90 - Theta + s(f).Orientation;
else % If fringe is in 2nd or 4th unit circle quadrant
    FringeOrients(f) = s(f).Orientation - Theta - 90;
end
% Ensure angle btwn +/-90
if FringeOrients(f) > 90
    FringeOrients(f) = FringeOrients(f) - 180;
elseif FringeOrients(f) < -90
    FringeOrients(f) = FringeOrients(f) + 180;
end
end
end

delete(wb); % delete the waitbar figure

if UserCancelled

```

```

        set(hObject, 'Enable', 'on'); % re-enable the Measure Fringes button
    else
        % Retain data of only those objects meeting fringe criteria
        KeptFringes = FringeLengths >= MinFringeLength;
        FringeLengths = FringeLengths(KeptFringes);
        FringeOrients = FringeOrients(KeptFringes);
        FringeRadDists = FringeRadDists(KeptFringes);
        EndPtDists = EndPtDists(KeptFringes);
        FringeTorts = FringeLengths ./ EndPtDists;
        FringeData = horzcat(FringeLengths, FringeTorts, FringeOrients, ...
            FringeRadDists);
        FringeCoords = FringeCoords(KeptFringes);
    end
end
end

```

### A.3.4 GetFringeSeps Function

```
function FringeSeps = GetFringeSeps(CC, MinFringeLength, SepTol, ...
    OrientTol, RecipTol)
% GETFRINGESEPS Calculate fringe separation distances
%
% Input Arguments:
% CC                Connected components structure of objects on image
% MinFringeLength  Minimum allowable fringe length, [px]
% SepTol           A two-element array with the allowable range [min max]
%                 of fringe separation distances [px]
% OrientTol        Fringe orientation difference tolerance (degs)
% RecipTol         Tolerance w/in which fringe pairs must reciprocally
%                 calculate the same separation dist [px]
%
% Output Arguments:
% FringeSeps       A matrix containing the ID numbers of identified fringe
%                 pairs and their separation distances in pixels
%
% Paul M. Anderson, 2017

% Create a label matrix
LMat = labelmatrix(CC);
FringeImg = LMat > 0; % Image containing only the measured fringes
FringeSeps = [];

W = 2*max(SepTol)+1; % Mask width for identifying neighboring fringes

% Calculate geometric properties of each fringe
s = regionprops(CC, 'Centroid', 'Orientation', 'MajorAxisLength');

wb = waitbar(0, '', 'Name', 'Calculating_fringe_separation_distances...', ...
    'CreateCancelBtn', 'setappdata(gcf, ''canceling'', 1)');

n = 0;
for f = 1:CC.NumObjects % for each fringe in the image

    % Check for click of waitbar's Cancel button
    if getappdata(wb, 'canceling')
        FringeSeps = 0;
        break;
    end
    % Update waitbar every 5th time through the loop
    if mod(f,5)==0
        waitbar(f/CC.NumObjects, wb, sprintf('...
            (%d_of_%d_fringes_evaluated', f, CC.NumObjects));
```

```

end

% Create an image with just this fringe
ThisFringeImg = LMat == f;
% Get the Euclidian distance of all pixels from this fringe
dImg = bwdist(ThisFringeImg);
% Create a rectangular mask symetrically centered on the major axis
% of the given fringe
L = s(f).MajorAxisLength;
theta = s(f).Orientation;
x = s(f).Centroid(1) + 0.5*(L*cosd(theta)*[-1;1;1;-1] ...
    + W*sind(theta)*[-1;-1;1;1]);
y = s(f).Centroid(2) + 0.5*(L*sind(theta)*[1;-1;-1;1] ...
    + W*cosd(theta)*[-1;-1;1;1]);
FringeMask = poly2mask(x,y,CC.ImageSize(1),CC.ImageSize(2));
NeighbFringes = FringeImg;
NeighbFringes(FringeMask == 0) = 0;
% Eliminate the current fringe keeping only its neighboring fringes
NeighbFringes(ThisFringeImg == 1) = 0;
NeighbLMat = LMat;
NeighbLMat(NeighbFringes == 0) = 0;
% get the lengths of each masked neighbor fringe
NeighbIDs = unique(NeighbLMat);
NeighbIDs = NeighbIDs(NeighbIDs>0);
NeighbLengths = zeros(numel(NeighbIDs),1);
gDists = cell(numel(NeighbIDs),1);
for j = 1:numel(NeighbIDs)
    % Image of just this masked neighbor fringe
    ThisNeighbImg = NeighbLMat == NeighbIDs(j);
    % Shortest dist from each pixel in this neighbor to ref fringe
    SepDists = dImg(ThisNeighbImg);
    MeanSepDist = mean(SepDists);
    [row,col]=find(bwmorph(ThisNeighbImg,'endpoints'));
    % Ignore single pixels and objects lacking endpoints (e.g. circles)
    if numel(row) > 1
        % Calculate the fringe length
        gDists{j} = bwdistgeodesic(ThisNeighbImg,col(1),row(1), ...
            'quasi-euclidean');
        gDists{j} = gDists{j}(~isnan(gDists{j}));
        NeighbLengths(j) = max(gDists{j})+1;
    end

    ThisNeighb = regionprops(ThisNeighbImg,'Orientation');
    if length(ThisNeighb) > 1
        % If the FringeMask cuts the neighboring fringe into multiple
        % sections, use the entire neighboring fringe to measure the
        % orientation difference

```

```

        OrientDiff = abs(s(NeighbIDs(j)).Orientation - s(f).Orientation);
    else
        % Otherwise use only the portion of the neighboring fringe
        % that is within the FringeMask
        OrientDiff = abs(ThisNeighb.Orientation - s(f).Orientation);
    end

    % if this neighboring fringe is longer than MinFringeLength,
    % is w/in the orientation tolerance with respect to the reference
    % fringe, and has an avg separation distance w/in the tolerance,
    % record the average fringe dist & the IDs of the two fringes
    if NeighbLengths(j) >= MinFringeLength && MeanSepDist >= SepTol(1) .
        && MeanSepDist <= SepTol(2) && OrientDiff <= OrientTol
        n=n+1;
        FringeSeps(n,:) = [f, double(NeighbIDs(j)), MeanSepDist];
    end
end
end

delete(wb); % delete the waitbar figure

% If fringes were found and the user didn't cancel...
if ~isempty(FringeSeps) && ~FringeSeps(1)==0

    % Sort so that the larger ID# of each fringe pairs is in column 2
    FringeSeps = horzcat(min(FringeSeps(:,1:2), [], 2), ...
        max(FringeSeps(:,1:2), [], 2), FringeSeps(:,3));
    FringeSeps = sortrows(FringeSeps); % Sort ascending based on column 1

    % Get the row ID of each reciprocal fringe pair
    [~, ia1, ~] = unique(FringeSeps(:,1:2), 'rows', 'first');
    [~, ia2, ~] = unique(FringeSeps(:,1:2), 'rows', 'last');

    % Average the fringe separations of each reciprocal fringe pair
    AvgFringeSeps = (FringeSeps(ia1,3) + FringeSeps(ia2,3))/2;

    % Eliminate any fringe pairs that do not reciprocally calculate
    % the same separation distance within a specified tolerance
    k = abs(FringeSeps(ia1,3) - FringeSeps(ia2,3)) < RecipTol;
    AvgFringeSeps = AvgFringeSeps(k);

    % Return the unique fringe pairs with averaged separation distances
    FringeIDs = FringeSeps(ia1,1:2);
    FringeSeps = horzcat(FringeIDs(k,:), AvgFringeSeps);
end

```

## Appendix B: Mathematical Derivations

### B.1 Expressions for the Diameters of Average Surface Area and Volume

The  $i^{\text{th}}$  moment of a continuous distribution function of random variable  $x$  is defined as:

$$M_i \equiv \int_{-\infty}^{\infty} x^i f(x) dx \quad (\text{B.1})$$

Now consider a discrete size distribution function of a population of primary particle diameters,  $f(d_p)$ , defined such that  $f(d_p)$  equals the number of primary particles in the population with diameter  $d_p$ . The zeroth moment of  $f(d_p)$  then is simply the total number of primary particles:

$$M_0 = \sum_{d_p} f(d_p) = N_p \quad (\text{B.2})$$

The mean primary particle diameter is by definition:

$$\mu_{d_p} = \frac{1}{N_p} \sum_{d_p} d_p f(d_p) \quad (\text{B.3})$$

which is simply the ratio of the first to the zeroth moments:

$$\mu_{d_p} = \frac{M_1}{M_0} \quad (\text{B.4})$$

The diameters of average surface area and volume can be similarly defined using the second and third moments of the distribution, respectively [141]:

$$\mu_{d_{pS}} = \left( \frac{M_2}{M_0} \right)^{1/2} \quad (\text{B.5})$$

and

$$\mu_{d_{pV}} = \left( \frac{M_3}{M_0} \right)^{1/3} \quad (\text{B.6})$$

The general equation for the  $i^{\text{th}}$  central moment  $CM_i$ , of a continuous distribution of random variable  $x$  was given in Eq. 3.11:

$$CM_i = \int_{-\infty}^{\infty} (x - \mu)^i f(x) dx \quad (\text{B.7})$$

In discrete form with  $f(d_p)$  defined as above, the second central moment is simply the variance of the population of primary particles:

$$\sigma_{d_p}^2 = CM_2 = \frac{1}{N_p} \sum_{d_p} (d_p - \mu_{d_p})^2 f(d_p) \quad (\text{B.8})$$

Expanding the polynomial and rearranging, Eq. B.8 can be written as:

$$\sigma_{d_p}^2 = \frac{1}{N_p} \left[ \sum_{d_p} d_p^2 f(d_p) - 2\mu_{d_p} \sum_{d_p} d_p f(d_p) + \mu_{d_p}^2 \sum_{d_p} f(d_p) \right] \quad (\text{B.9})$$

which from the definition of the moments of the distribution is:

$$\sigma_{d_p}^2 = \frac{1}{N_p} \left[ M_2 - 2\mu_{d_p} M_1 + \mu_{d_p}^2 M_0 \right] \quad (\text{B.10})$$

Using the relationships given by Eq. B.2 - B.5, and solving for  $\mu_{d_{pS}}$ :

$$\mu_{d_{pS}} = (\sigma_{d_p}^2 + \mu_{d_p}^2)^{1/2} \quad (\text{B.11})$$

Writing this in terms of the sample population variables defined in the text yields Eq. 3.12:

$$d_{pS} = (s_{d_p}^2 + \bar{d}_p^2)^{1/2} \quad (\text{B.12})$$

Now consider that the skewness of a distribution is defined as the third central moment divided by the standard deviation cubed. For the distribution of primary particles this is:

$$\gamma_{d_p} = \frac{CM_3}{\sigma_{d_p}^3} = \frac{1/N_p \sum_{d_p} (d_p - \mu_{d_p})^3 f(d_p)}{\sigma_{d_p}^3} \quad (\text{B.13})$$

Expanding the polynomial and applying the definitions of the moments of the distribution, as was done for  $\sigma_{d_p}$  above gives:

$$\gamma_{d_p} \sigma_{d_p}^3 = \frac{1}{N_p} \left[ M_3 - 3\mu_{d_p} M_2 + 3\mu_{d_p}^2 M_1 - \mu_{d_p}^3 M_0 \right] \quad (\text{B.14})$$

Using the relationships given by Eq. [B.2](#) - [B.6](#), and solving for  $\mu_{d_{pV}}$ :

$$\mu_{d_{pV}} = (\gamma_{d_p} \sigma_{d_p}^3 + 3\mu_{d_p} \sigma_{d_p}^2 + \mu_{d_p}^3)^{1/3} \quad (\text{B.15})$$

Writing this in terms of sample population variables defined in the text yields Eq. [3.13](#):

$$d_{pV} = (\gamma_{d_p} s_{d_p}^3 + 3\bar{d}_p s_{d_p}^2 + \bar{d}_p^3)^{1/3} \quad (\text{B.16})$$

## B.2 Expressions for Spherical Cap Height

Begin with the spherical cap and overlapping primary particle schematic:

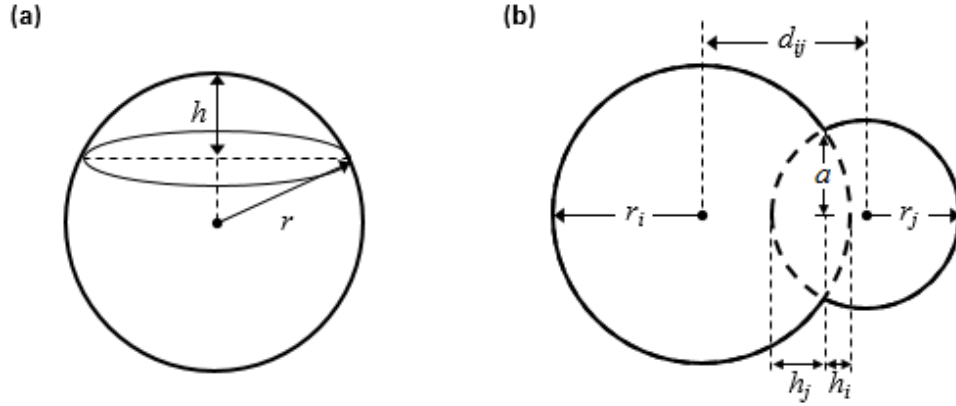


Figure B.1: (a) Spherical cap (b) Overlapping primary particles of different sizes.

Assuming the centers of spheres  $i$  and  $j$  are both situated on a plane normal to the viewer, then the overlap coefficient,  $C_{ov}$  is equivalent to the projected overlap coefficient in Eq. 2.8:

$$C_{ov} = \frac{\bar{d}_p - d_{ij}}{\bar{d}_p} \quad (\text{B.17})$$

Since the mean primary particle diameter  $\bar{d}_p$  for spheres  $i$  and  $j$  is simply  $r_i + r_j$ , Eq. B.17 can be rewritten solving for  $d_{ij}$ :

$$d_{ij} = (r_i + r_j)(1 - C_{ov}) \quad (\text{B.18})$$

which from Fig. B.1 is also:

$$d_{ij} = r_i - h_i + r_j - h_j \quad (\text{B.19})$$

equating Eq. B.18 and B.19 and solving for  $h_j$  yields Eq. 3.18:

$$h_j = C_{ov}(r_i + r_j) - h_i \quad (\text{B.20})$$

Next, by the Pythagorean theorem, the following two expressions are both equivalent to length  $a$ , and therefore to each other:

$$r_i^2 - (r_i - h_i)^2 = r_j^2 - (r_j - h_j)^2 \quad (\text{B.21})$$

Expanding the polynomials and rearranging gives:

$$2r_i h_i - h_i^2 = 2r_j h_j - h_j^2 \quad (\text{B.22})$$

Substituting  $h_j$  from Eq. B.20 into Eq. B.22, solving for  $h_i$ , and simplifying produces equation Eq. 3.17:

$$h_i = \frac{C_{ov}^2(r_i + r_j) - 2r_j C_{ov}}{2(C_{ov} - 1)} \quad (\text{B.23})$$

## Appendix C: Supplemental Figures

This page intentionally left blank

## C.1 Fractal Dimension and Pre-factor from Fitted Data

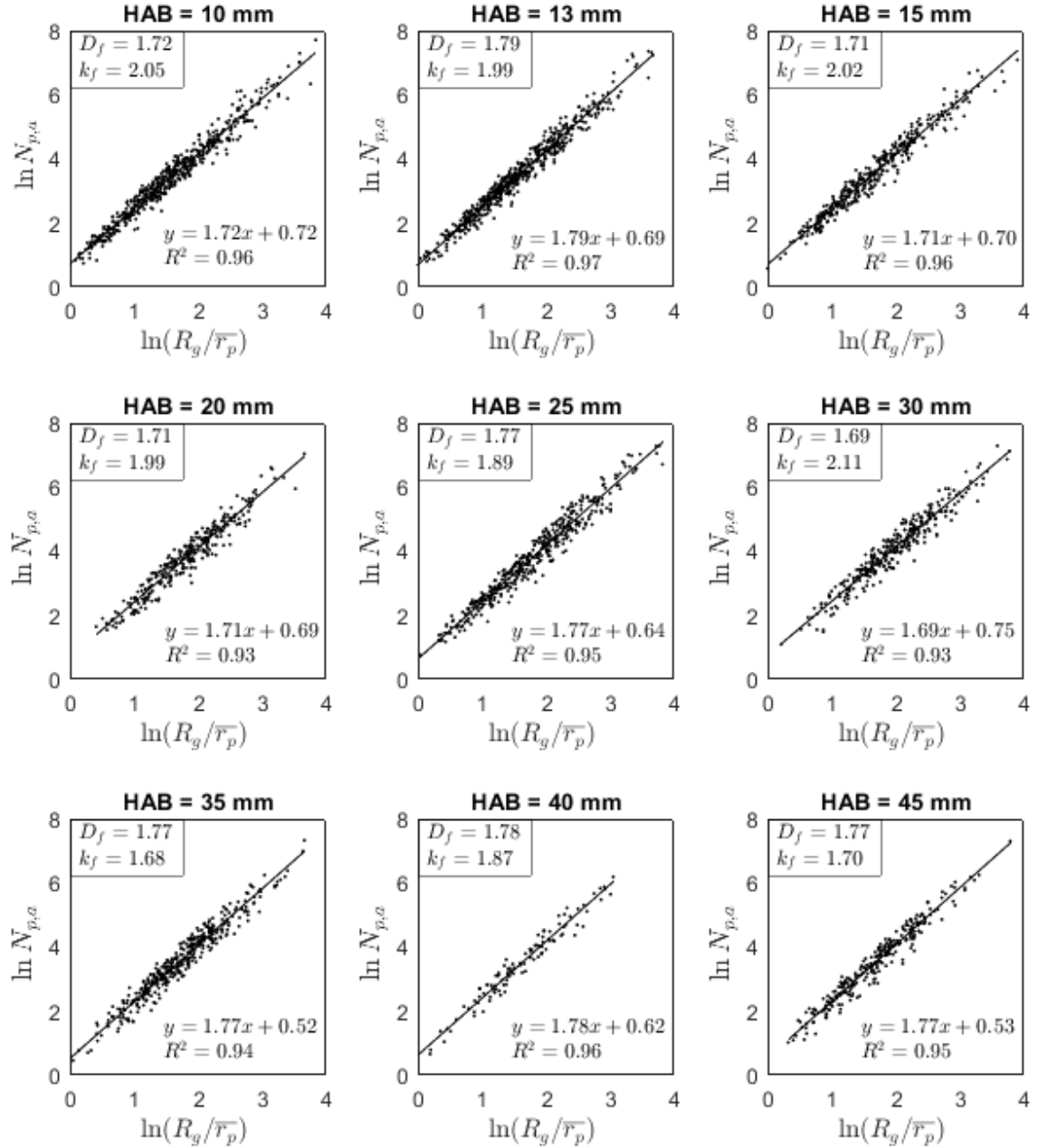


Figure C.1: Least-squares fits of  $\ln(N_{p,a})$  vs.  $\ln(R_g/\bar{r}_p)$  data, yielding a global aggregate fractal dimension,  $D_f$  and pre-factor,  $k_f$ , at each height above burner.

## C.2 Additional Fringe Measurements at the Primary Particle Surface

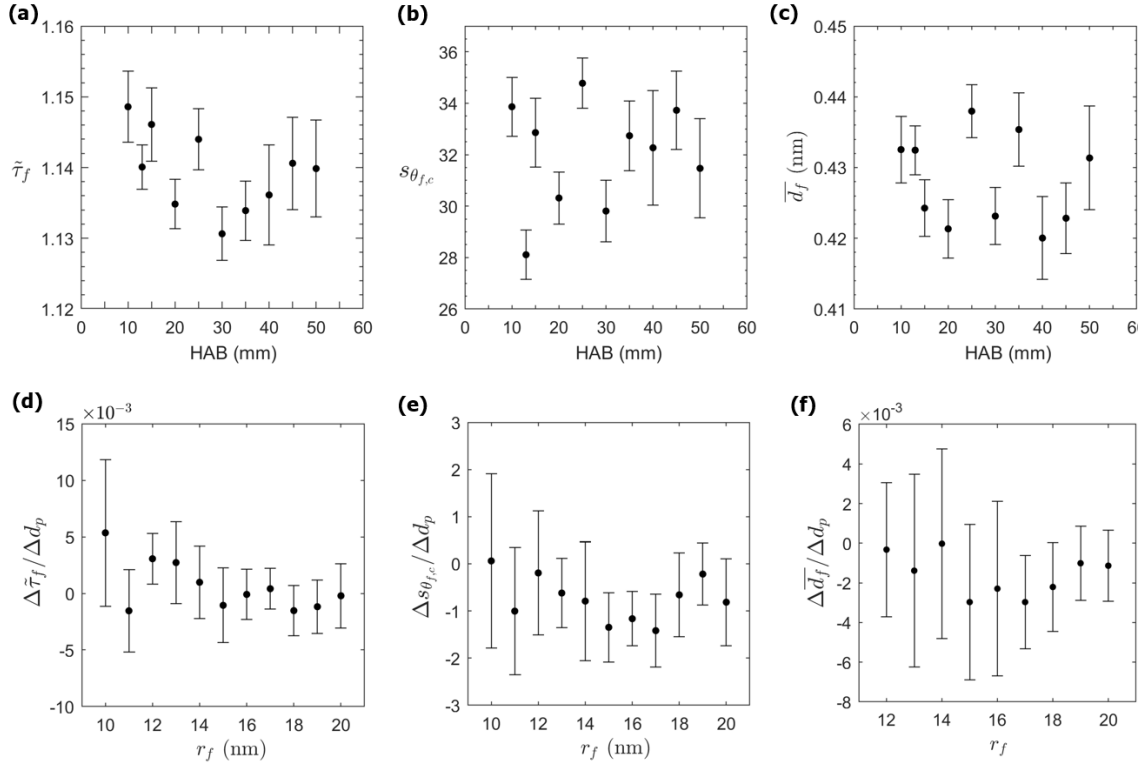


Figure C.2: Additional lattice fringe measurements. To highlight surface oxidation effects, only fringes within the outer 20% of the primary particle were used in the analysis. (a)-(c) Median fringe tortuosity, standard deviation of fringe non-concentricity, and mean fringe separation distance vs. height above burner. (e)-(f) Change in median fringe tortuosity, standard deviation of fringe non-concentricity, and mean fringe separation distance with respect to primary particle diameter vs. fringe radial location.

## Bibliography

- [1] C. Arden Pope, Richard T. Burnett, Michael J. Thun, Eugenia E. Calle, Daniel Krewski, Kazuhiko Ito, and George D. Thurston. Lung cancer, cardiopulmonary mortality, and long-term exposure to fine particulate air pollution. *JAMA*, 287(9):1132–1141, March 2002.
- [2] Lotte Risom, Marianne Dybdahl, Jette Bornholdt, Ulla Vogel, Håkan Wallin, Peter Møller, and Steffen Loft. Oxidative DNA damage and defence gene expression in the mouse lung after short-term exposure to diesel exhaust particles by inhalation. *Carcinogenesis*, 24(11):1847–1852, November 2003.
- [3] B. Kumfer and I. Kennedy. The role of soot in the health effects of inhaled airborne particles. In Henning Bockhorn, editor, *Combustion Generated Fine Carbonaceous Particles: Proceedings of an International Workshop Held in Villa Orlandi, Anacapri, May 13-16, 2007*, pages 1–15. KIT Scientific Publishing, 2009.
- [4] Jessica Evans, Aaron van Donkelaar, Randall V. Martin, Richard Burnett, Daniel G. Rainham, Nicholas J. Birkett, and Daniel Krewski. Estimates of global mortality attributable to particulate air pollution using satellite imagery. *Environmental Research*, 120:33–42, January 2013.
- [5] World Health Organization. WHO — 7 million premature deaths annually linked to air pollution. <http://www.who.int/mediacentre/news/releases/2014/air-pollution/en/>, March 2014.
- [6] U.S. Environmental Protection Agency. EPA Announces Next Round of Clean Air Standards to Reduce Harmful Soot Pollution. [https://archive.epa.gov/epapages/newsroom\\_archive/newsreleases/a7446ca9e228622b85257a](https://archive.epa.gov/epapages/newsroom_archive/newsreleases/a7446ca9e228622b85257a), December 2012.
- [7] Mark Z. Jacobson. Strong radiative heating due to the mixing state of black carbon in atmospheric aerosols. *Nature*, 409:695–697, August 2001.

- [8] Christopher D. Cappa, Timothy B. Onasch, Paola Massoli, Douglas R. Worsnop, Timothy S. Bates, Eben S. Cross, Paul Davidovits, Jani Hakala, Katherine L. Hayden, B. Tom Jobson, Katheryn R. Kolesar, Daniel A. Lack, Brian M. Lerner, Shao-Meng Li, Daniel Mellon, Ibraheem Nuaaman, Jason S. Olfert, Tuukka Petäjä, Patricia K. Quinn, Chen Song, R. Subramanian, Eric J. Williams, and Rahul A. Zaveri. Radiative Absorption Enhancements Due to the Mixing State of Atmospheric Black Carbon. *Science*, 337(6098):1078–1081, August 2012.
- [9] J. Barrie Maxwell and Leonard A. Barrie. Atmospheric and Climatic Change in the Arctic and Antarctic. *Ambio*, 18(1):42–49, 1989.
- [10] T. C. Bond, S. J. Doherty, D. W. Fahey, P. M. Forster, T. Berntsen, B. J. DeAngelo, M. G. Flanner, S. Ghan, B. Kärcher, D. Koch, S. Kinne, Y. Kondo, P. K. Quinn, M. C. Sarofim, M. G. Schultz, M. Schulz, C. Venkataraman, H. Zhang, S. Zhang, N. Bellouin, S. K. Guttikunda, P. K. Hopke, M. Z. Jacobson, J. W. Kaiser, Z. Klimont, U. Lohmann, J. P. Schwarz, D. Shindell, T. Storelvmo, S. G. Warren, and C. S. Zender. Bounding the role of black carbon in the climate system: A scientific assessment. *Journal of Geophysical Research: Atmospheres*, 118(11):5380–5552, June 2013.
- [11] Randy L. Vander Wal and Aaron J. Tomasek. Soot oxidation: Dependence upon initial nanostructure. *Combustion and Flame*, 134(1-2):1–9, July 2003.
- [12] Andrei Kazakov, Hai Wang, and Michael Frenklach. Detailed Modeling of Soot Formation in Laminar Premixed Ethylene Flames at a Pressure of 10 Bar. *Combustion and Flame*, 100:111–120, 1995.
- [13] Jörg Appel, Henning Bockhorn, and Michael Frenklach. Kinetic modeling of soot formation with detailed chemistry and physics: Laminar premixed flames of C2 hydrocarbons. *Combustion and Flame*, 121(1):122–136, 2000.
- [14] M Smooke, M Long, B Connelly, M Colket, and R Hall. Soot formation in laminar diffusion flames. *Combustion and Flame*, 143(4):613–628, December 2005.
- [15] Seth B. Dworkin, Qingan Zhang, Murray J. Thomson, Nadezhda A. Slavinskaya, and Uwe Riedel. Application of an enhanced PAH growth model to soot formation in a laminar coflow ethylene/air diffusion flame. *Combustion and Flame*, 158(9):1682–1695, September 2011.
- [16] R.S. Mehta, D.C. Haworth, and M.F. Modest. An assessment of gas-phase reaction mechanisms and soot models for laminar atmospheric-pressure ethylene–air flames. *Proceedings of the Combustion Institute*, 32(1):1327–1334, January 2009.
- [17] R. Jullien and R. Botet. *Aggregation and Fractal Aggregates*. World Scientific, Singapore, 1987.

- [18] Hai Wang. Formation of nascent soot and other condensed-phase materials in flames. *Proceedings of the Combustion Institute*, 33(1):41–67, 2011.
- [19] K. O. Johansson, M. P. Head-Gordon, P. E. Schrader, K. R. Wilson, and H. A. Michelsen. Resonance-stabilized hydrocarbon-radical chain reactions may explain soot inception and growth. *Science*, 361(6406):997–1000, September 2018.
- [20] N. R. Laine, F. J. Vastola, and P. L. Walker. The Importance of Active Surface Area in the Carbon-Oxygen Reaction. *The Journal of Physical Chemistry*, 67(10):2030–2034, October 1963.
- [21] Kevin A. Davis, Robert H. Hurt, Nancy Y. C. Yang, and Thomas J. Headley. Evolution of char chemistry, crystallinity, and ultrafine structure during pulverized-coal combustion. *Combustion and Flame*, 100(1):31–40, January 1995.
- [22] Juhun Song, Mahabubul Alam, André L. Boehman, and Unjeong Kim. Examination of the oxidation behavior of biodiesel soot. *Combustion and Flame*, 146(4):589–604, September 2006.
- [23] Khalid Al-Qurashi and André L. Boehman. Impact of exhaust gas recirculation (EGR) on the oxidative reactivity of diesel engine soot. *Combustion and Flame*, 155(4):675–695, December 2008.
- [24] M. Alfè, B. Apicella, R. Barbella, J. N. Rouzaud, A. Tregrossi, and A. Ciajolo. Structure–property relationship in nanostructures of young and mature soot in premixed flames. *Proceedings of the Combustion Institute*, 32(1):697–704, January 2009.
- [25] Magín Lapuerta, Fermín Oliva, John R. Agudelo, and André L. Boehman. Effect of fuel on the soot nanostructure and consequences on loading and regeneration of diesel particulate filters. *Combustion and Flame*, 159(2):844–853, February 2012.
- [26] Lin Wang, Chonglin Song, Jinou Song, Gang Lv, Huating Pang, and Wei Zhang. Aliphatic C–H and oxygenated surface functional groups of diesel in-cylinder soot: Characterizations and impact on soot oxidation behavior. *Proceedings of the Combustion Institute*, 34(2):3099–3106, January 2013.
- [27] Michaela Nicole Ess, Henrike Bladt, Wolfgang Mühlbauer, Simone Isabelle Seher, Christian Zöllner, Sebastian Lorenz, Dieter Brüggemann, Ulrich Nieken, Natalia P. Ivleva, and Reinhard Niessner. Reactivity and structure of soot generated at varying biofuel content and engine operating parameters. *Combustion and Flame*, 163:157–169, January 2016.
- [28] Sk Bhatia and Dd Perlmutter. A Random Pore Model for Fluid-Solid Reactions: I. Isothermal, Kinetic Control. *Aiche Journal*, 26(3):379–386, 1980. WOS:A1980JW25900007.

- [29] John P. A. Neeft, T. Xander Nijhuis, Erik Smakman, Michiel Makkee, and Jacob A. Moulijn. Kinetics of the oxidation of diesel soot. *Fuel*, 76(12):1129–1136, 1997.
- [30] Brian R. Stanmore, Jean-Francois Brillhac, and Patrick Gilot. The oxidation of soot: A review of experiments, mechanisms and models. *Carbon*, 39(15):2247–2268, 2001.
- [31] Lakshitha Pahalagedara, Hom Sharma, Chung-Hao Kuo, Saminda Dharmarathna, Ameya Joshi, Steven L. Suib, and Ashish B. Mhadeshwar. Structure and Oxidation Activity Correlations for Carbon Blacks and Diesel Soot. *Energy & Fuels*, 26(11):6757–6764, November 2012.
- [32] Mariano Sirignano, John Kent, and Andrea D’Anna. Further experimental and modelling evidences of soot fragmentation in flames. *Proceedings of the Combustion Institute*, 35(2):1779–1786, 2015.
- [33] Hossein Ghiassi, Pal Toth, Isabel C. Jaramillo, and JoAnn S. Lighty. Soot oxidation-induced fragmentation: Part 1: The relationship between soot nanostructure and oxidation-induced fragmentation. *Combustion and Flame*, 163:179–187, January 2016.
- [34] Hossein Ghiassi, Isabel C. Jaramillo, Pal Toth, and JoAnn S. Lighty. Soot oxidation-induced fragmentation: Part 2: Experimental investigation of the mechanism of fragmentation. *Combustion and Flame*, 163:170–178, January 2016.
- [35] Isabel C. Jaramillo, Chethan K. Gaddam, Randy L. Vander Wal, and JoAnn S. Lighty. Effect of nanostructure, oxidative pressure and extent of oxidation on model carbon reactivity. *Combustion and Flame*, 162(5):1848–1856, May 2015.
- [36] Kuen Yehliu, Randy L. Vander Wal, Octavio Armas, and André L. Boehman. Impact of fuel formulation on the nanostructure and reactivity of diesel soot. *Combustion and Flame*, 159(12):3597–3606, December 2012.
- [37] Abhijeet Raj, Seung Yeon Yang, Dongkyu Cha, Russell Tayouo, and Suk Ho Chung. Structural effects on the oxidation of soot particles by O<sub>2</sub>: Experimental and theoretical study. *Combustion and Flame*, 160(9):1812–1826, September 2013.
- [38] André L. Boehman, Juhun Song, and Mahabubul Alam. Impact of Biodiesel Blending on Diesel Soot and the Regeneration of Particulate Filters. *Energy & Fuels*, 19(5):1857–1864, September 2005.
- [39] Michael Frenklach, Zhenyuan Liu, Ravi I. Singh, Galiya R. Galimova, Valeriy N. Azyazov, and Alexander M. Mebel. Detailed, sterically-resolved modeling of soot oxidation: Role of O atoms, interplay with particle nanostructure, and emergence of inner particle burning. *Combustion and Flame*, 188(Supplement C):284–306, February 2018.

- [40] Jack B. Howard. Carbon addition and oxidation reactions in heterogeneous combustion and soot formation. In *Symposium (International) on Combustion*, volume 23, pages 1107–1127. Elsevier, 1991.
- [41] Ian M. Kennedy. Models of soot formation and oxidation. *Progress in Energy and Combustion Science*, 23(2):95–132, 1997.
- [42] J. Nagle and R.F. Strickland-Constable. Oxidation of Carbon Between 1000–2000°C. *Proceedings of the Fifth Conference on Carbon*, 1:154–164, 1961.
- [43] K. G. Neoh, J. B. Howard, and A. F. Sarofim. Neoh\_1981\_Soot Oxidation in Flames\_Part particulate Carbon.pdf. In *Particulate Carbon, Formation during Combustion*, pages 261–282. Plenum Press, New York, 1981.
- [44] W. Felder, S. Madronich, and D. B. Olson. Oxidation kinetics of carbon blacks over 1300–1700 K. *Energy & Fuels*, 2(6):743–750, November 1988.
- [45] Philip Cadman and Ronald J. Denning. Oxidation rates of soot particulates by oxygen in the temperature range 1500–3500 K determined using a shock tube. *Journal of the Chemical Society, Faraday Transactions*, 92(21):4159–4165, January 1996.
- [46] Haiqing Guo, Paul M. Anderson, and Peter B. Sunderland. Optimized rate expressions for soot oxidation by OH and O<sub>2</sub>. *Fuel*, 172:248–252, May 2016.
- [47] K. B. Lee, M. W. Thring, and J. M. Beer. On the rate of combustion of soot in a laminar soot flame. *Combustion and Flame*, 6:137–145, 1962.
- [48] C. Park and Jp Appleton. Shock-Tube Measurements of Soot Oxidation Rates. *Combustion and Flame*, 20(3):369–379, 1973. WOS:A1973P810000010.
- [49] P. Roth, O. Brandt, and S. Von Gersum. High temperature oxidation of suspended soot particles verified by CO and CO<sub>2</sub> measurements. *Symposium (International) on Combustion*, 23(1):1485–1491, January 1991.
- [50] M. L. Chan, K. N. Moody, J. R. Mullins, and A. Williams. Low-temperature oxidation of soot. *Fuel*, 66(12):1694–1698, December 1987.
- [51] Kelly J. Higgins, Heejung Jung, David B. Kittelson, Jeffrey T. Roberts, and Michael R. Zachariah. Size-Selected Nanoparticle Chemistry: Kinetics of Soot Oxidation. *The Journal of Physical Chemistry A*, 106(1):96–103, January 2002.
- [52] X. Ma, C. D. Zangmeister, and M. R. Zachariah. Soot Oxidation Kinetics: A Comparison Study of Two Tandem Ion-Mobility Methods. *The Journal of Physical Chemistry C*, 117(20):10723–10729, May 2013.
- [53] Joaquin Camacho, Yujie Tao, and Hai Wang. Kinetics of nascent soot oxidation by molecular oxygen in a flow reactor. *Proceedings of the Combustion Institute*, 35(2):1887–1894, 2015.

- [54] Jinou Song, Chonglin Song, Gang Lv, Lin Wang, and Feng Bin. Modification to Nagle/Strickland-Constable model with consideration of soot nanostructure effects. *Combustion Theory and Modelling*, 16(4):639–649, August 2012.
- [55] Rahul Puri, Marlow Moser, Robert J. Santoro, and Kermit C. Smyth. Laser-induced fluorescence measurements of OH• concentrations in the oxidation region of laminar hydrocarbon diffusion flames. *Proceedings of the Combustion Institute*, 1992.
- [56] M. Haudiquert, A. Cessou, D. Stepowski, and A. Coppalle. OH and Soot Concentration Measurements in a High-Temperature Laminar Diffusion Flame. *Combustion and Flame*, 111:338–349, 1997.
- [57] Hemant P. Mungekar and Arvind Atreya. Flame Radiation and Soot Emission From Partially Premixed Methane Counterflow Flames. *Journal of Heat Transfer*, 128(4):361, 2006.
- [58] R Lockett and R Woolley. Instabilities and soot formation in high-pressure, rich, iso-octane-air explosion flames1. Dynamical structure. *Combustion and Flame*, 151(4):601–622, December 2007.
- [59] Roger C. Millikan. Non-equilibrium soot formation in premixed flames. *The Journal of Physical Chemistry*, 66(5):794–799, 1962.
- [60] F. Xu, A. M. El-Leathy, C. H. Kim, and G. M. Faeth. Soot surface oxidation in hydrocarbon/air diffusion flames at atmospheric pressure. *Combustion and Flame*, 132(1):43–57, 2003.
- [61] C.H. Kim, A.M. El-Leathy, F. Xu, and G.M. Faeth. Soot surface growth and oxidation in laminar diffusion flames at pressures of 0.1–1.0 atm. *Combustion and Flame*, 136(1-2):191–207, January 2004.
- [62] C.H. Kim, F. Xu, and G.M. Faeth. Soot surface growth and oxidation at pressures up to 8.0 atm in laminar nonpremixed and partially premixed flames. *Combustion and Flame*, 152(3):301–316, February 2008.
- [63] R. E. Mitchell, A. F. Sarofim, and L. A. Clomburg. Partial equilibrium in the reaction zone of methane-air diffusion flames. *Combustion and Flame*, 37:201–206, 1980.
- [64] R. E. Mitchell. *Nitrogen Oxide Formation in Laminar Methane-Air Diffusion Flames*. PhD thesis, Massachusetts Institute of Technology, 1975.
- [65] Kermit C. Smyth, Paul J. H. Tjossem, Anthony Hamins, and J. Houston Miller. Concentration measurements of OH• and equilibrium analysis in a laminar methane-air diffusion flame. *Combustion and Flame*, 79(3):366–380, March 1990.

- [66] C.P. Fenimore and G.W. Jones. Oxidation of soot by hydroxyl radicals. *Journal of Physical Chemistry*, 71(3):593–597, February 1967.
- [67] Jürgen Warnatz. Hydrocarbon Oxidation at High Temperatures. *Berichte der Bunsengesellschaft für physikalische Chemie*, 87(11):1008–1022, November 1983.
- [68] A. Garo, G. Prado, and J. LaHaye. Chemical Aspects of Soot Particles Oxidation in a Laminar Methane-Air Diffusion Flame. *Combustion and Flame*, 79:226–233, 1990.
- [69] Rahul Puri, Robert J. Santoro, and Kermit C. Smyth. The oxidation of soot and carbon monoxide in hydrocarbon diffusion flames. *Combustion and Flame*, 97(2):125–144, 1994.
- [70] Rahul Puri, Robert J. Santoro, and Kermit C. Smyth. Erratum. *Combustion and Flame*, 102(1):226–228, 1995.
- [71] M. F. R. Mulcahy and B. C. Young. The reaction of hydroxyl radicals with carbon at 298 K. *Carbon*, 13(2):115–124, April 1975.
- [72] T. Mendiara, M. U. Alzueta, A. Millera, and R. Bilbao. Oxidation of Acetylene Soot: Influence of Oxygen Concentration. *Energy & Fuels*, 21(6):3208–3215, November 2007.
- [73] Chenxi Sun, Jonathan Martin, and André L. Boehman. Nanostructure and reactivity of soot produced from a turbodiesel engine using post injection. *Proceedings of the Combustion Institute*, July 2018.
- [74] Chethan K. Gaddam, Randy L. Vander Wal, Xu Chen, Aleksey Yezerets, and Krishna Kamasamudram. Reconciliation of carbon oxidation rates and activation energies based on changing nanostructure. *Carbon*, 98:545–556, March 2016.
- [75] Pal Toth, Daniel Jacobsson, Martin Ek, and Henrik Wiinikka. Real-time, in situ, atomic scale observation of soot oxidation. *Carbon*, 145:149–160, April 2019.
- [76] Tomoji Ishiguro, Noritomo Suzuki, Yoshiyasu Fujitani, and Hidetake Morimoto. Microstructural Changes of Diesel Soot During Oxidation. *Combustion and Flame*, 85(1):1–6, 1991.
- [77] K. G. Neoh, J. B. Howard, and A. F. Sarofim. Effect of oxidation on the physical structure of soot. In *Symposium (International) on Combustion*, volume 20, pages 951–957, 1984.
- [78] Carlos A. Echavarria, Isabel C. Jaramillo, Adel F. Sarofim, and JoAnn S. Lighty. Studies of soot oxidation and fragmentation in a two-stage burner under fuel-lean and fuel-rich conditions. *Proceedings of the Combustion Institute*, 33(1):659–666, 2011.

- [79] Richard A. Dobbins and Constantine M. Megaridis. Absorption and scattering of light by polydisperse aggregates. *Applied Optics*, 30(33):4747–4754, November 1991.
- [80] C. M. Sorensen. Light Scattering by Fractal Aggregates: A Review. *Aerosol Science and Technology*, 35(2):648–687, January 2001.
- [81] T. C. Williams, C. R. Shaddix, K. A. Jensen, and J. M. Suo-Anttila. Measurement of the dimensionless extinction coefficient of soot within laminar diffusion flames. *International Journal of Heat and Mass Transfer*, 50(7–8):1616–1630, April 2007.
- [82] Arka Soewono and Steven Rogak. Morphology and Raman Spectra of Engine-Emitted Particulates. *Aerosol Science and Technology*, 45(10):1206–1216, October 2011.
- [83] Xerxes López-Yglesias, Paul E. Schrader, and Hope A. Michelsen. Soot maturity and absorption cross sections. *Journal of Aerosol Science*, 75:43–64, September 2014.
- [84] Chao Liu, Yan Yin, Fangchao Hu, Hongchun Jin, and Christopher M. Sorensen. The Effects of Monomer Size Distribution on the Radiative Properties of Black Carbon Aggregates. *Aerosol Science and Technology*, 49(10):928–940, October 2015.
- [85] S. Bau, B. Zimmermann, R. Payet, and O. Witschger. A laboratory study of the performance of the handheld diffusion size classifier (DiSCmini) for various aerosols in the 15–400 nm range. *Environmental Science: Processes & Impacts*, 17(2):261–269, February 2015.
- [86] Matthew F. Chandler, Yingwu Teng, and Umit O. Koylu. Diesel engine particulate emissions: A comparison of mobility and microscopy size measurements. *Proceedings of the Combustion Institute*, 31(2):2971–2979, January 2007.
- [87] Rouzbeh Ghazi, Hugo Tjong, Arka Soewono, Steven N. Rogak, and Jason S. Olfert. Mass, Mobility, Volatility, and Morphology of Soot Particles Generated by a McKenna and Inverted Burner. *Aerosol Science and Technology*, 47(4):395–405, April 2013.
- [88] Anshuman Amit Lall and Sheldon K. Friedlander. On-line measurement of ultrafine aggregate surface area and volume distributions by electrical mobility analysis: I. Theoretical analysis. *Journal of Aerosol Science*, 37(3):260–271, March 2006.
- [89] S. Bau, O. Witschger, F. Gensdarmes, O. Rastoix, and D. Thomas. A TEM-based method as an alternative to the BET method for measuring off-line the specific surface area of nanoaerosols. *Powder Technology*, 200(3):190–201, June 2010.

- [90] ÜÖ Köylü, G. M. Faeth, T. L. Farias, and M. G. Carvalho. Fractal and projected structure properties of soot aggregates. *Combustion and Flame*, 100(4):621–633, 1995.
- [91] Kihong Park, David B. Kittelson, and Peter H. McMurry. Structural Properties of Diesel Exhaust Particles Measured by Transmission Electron Microscopy (TEM): Relationships to Particle Mass and Mobility. *Aerosol Science and Technology*, 38(9):881–889, September 2004.
- [92] Magín Lapuerta, Jesús Sánchez-Valdepeñas, Javier Barba, David Fernández-Rodríguez, Juan Pedro Andrés, and Tomás García. Analysis of Soot from the Use of Butanol Blends in a Euro 6 Diesel Engine. *Energy & Fuels*, 33(3):2265–2277, March 2019.
- [93] S. R. Forrest and T. A. Witten Jr. Long-range correlations in smoke-particle aggregates. *Journal of Physics A: Mathematical and General*, 12(5):L109, 1979.
- [94] Rj Santoro, Hg Semerjian, and Ra Dobbins. Soot Particle Measurements in Diffusion Flames. *Combustion and Flame*, 51(2):203–218, 1983. WOS:A1983QR48000007.
- [95] J. Cai, N. Lu, and C.M. Sorensen. Comparison of Size and Morphology of Soot Aggregates As Determined by Light Scattering and Electron Microscope Analysis. *Langmuir*, 9(11):2861–2867, 1993.
- [96] Ümit O. Köylü, Yangchuan Xing, and Daniel E. Rosner. Fractal morphology analysis of combustion-generated aggregates using angular light scattering and electron microscope images. *Langmuir*, 11(12):4848–4854, 1995.
- [97] S. De Iuliis, S. Maffi, F. Cignoli, and G. Zizak. Three-angle scattering/extinction versus TEM measurements on soot in premixed ethylene/air flame. *Applied Physics B*, 102(4):891–903, December 2010.
- [98] R. J. Samson, George W. Mulholland, and J. W. Gentry. Structural analysis of soot agglomerates. *Langmuir*, 3(2):272–281, 1987.
- [99] Bon Ki Ku and Andrew D. Maynard. Comparing aerosol surface-area measurements of monodisperse ultrafine silver agglomerates by mobility analysis, transmission electron microscopy and diffusion charging. *Journal of Aerosol Science*, 36(9):1108–1124, September 2005.
- [100] Kuk Cho and Pratim Biswas. Sintering Rates for Pristine and Doped Titanium Dioxide Determined Using a Tandem Differential Mobility Analyzer System. *Aerosol Science and Technology*, 40(5):309–319, June 2006.
- [101] Sin Young Lee, Hankwon Chang, Takashi Ogi, Ferry Iskandar, and Kikuo Okuyama. Measuring the effective density, porosity, and refractive index of

- carbonaceous particles by tandem aerosol techniques. *Carbon*, 49(7):2163–2172, June 2011.
- [102] Bon Ki Ku and Douglas E. Evans. Investigation of Aerosol Surface Area Estimation from Number and Mass Concentration Measurements: Particle Density Effect. *Aerosol Science and Technology*, 46(4):473–484, April 2012.
- [103] C. M. Sorensen. The Mobility of Fractal Aggregates: A Review. *Aerosol Science and Technology*, 45(7):765–779, July 2011.
- [104] Stephen Brunauer, Paul Hugh Emmett, and Edward Teller. Adsorption of gases in multimolecular layers. *Journal of the American Chemical Society*, 60(2):309–319, 1938.
- [105] Af Ahlstrom and Cui Odenbrand. Combustion Characteristics of Soot Deposits from Diesel-Engines. *Carbon*, 27(3):475–483, 1989. WOS:A1989U934400019.
- [106] Hans Darmstadt and Christian Roy. Comparative investigation of defects on carbon black surfaces by nitrogen adsorption and SIMS. *Carbon*, 39(6):841–848, 2001.
- [107] Zhiyou Du. *Kinetic Modeling of Carbon Oxidation.Pdf*. PhD thesis, Massachusetts Institute of Technology, 1990.
- [108] D. Pan, M. Jaroniec, and J. Klinik. Thermogravimetric evaluation of the specific surface area and total porosity of microporous carbons. *Carbon*, 34(9):1109–1113, 1996.
- [109] Carlos A. Echavarría, Isabel C. Jaramillo, Adel F. Sarofim, and JoAnn S. Lighty. Burnout of soot particles in a two-stage burner with a JP-8 surrogate fuel. *Combustion and Flame*, 159(7):2441–2448, July 2012.
- [110] R. A. Dobbins and C. M. Megaridis. Morphology of flame-generated soot as determined by thermophoretic sampling. *Langmuir*, 3(2):254–259, 1987.
- [111] C. Oh and C.M. Sorensen. The Effect of Overlap between Monomers on the Determination of Fractal Cluster Morphology. *Journal of Colloid and Interface Science*, 193:17–25, 1997.
- [112] Constantine M. Megaridis and Richard A. Dobbins. Morphological Description of Flame Generated Materials. *Combustion Science and Technology*, 71:95–109, 1990.
- [113] A. I. Medalia and F. A. Heckman. Morphology of aggregates—II. Size and shape factors of carbon black aggregates from electron microscopy. *Carbon*, 7(5):567–582, October 1969.

- [114] A. M. Brasil, T. L. Farias, and M. G. Carvalho. A recipe for image characterization of fractal-like aggregates. *Journal of Aerosol Science*, 30(10):1379–1389, 1999.
- [115] Patience Gwaze, Otmar Schmid, Harold J. Annegarn, Meinrat O. Andreae, Joachim Huth, and Günter Helas. Comparison of three methods of fractal analysis applied to soot aggregates from wood combustion. *Journal of Aerosol Science*, 37(7):820–838, July 2006.
- [116] Francisco J. Martos, Magín Lapuerta, Juan José Expósito, and Enrique Sanmiguel-Rojas. Overestimation of the fractal dimension from projections of soot agglomerates. *Powder Technology*, 311:528–536, April 2017.
- [117] J. Morán, J. Cuevas, F. Liu, J. Yon, and A. Fuentes. Influence of primary particle polydispersity and overlapping on soot morphological parameters derived from numerical TEM images. *Powder Technology*, 330:67–79, May 2018.
- [118] Zhongqiu Li, Liang Qiu, Xiaobei Cheng, Ying Li, and Hui Wu. The evolution of soot morphology and nanostructure in laminar diffusion flame of surrogate fuels for diesel. *Fuel*, 211:517–528, January 2018.
- [119] ÜÖ Köylü and Gerard M. Faeth. Structure of overfire soot in buoyant turbulent diffusion flames at long residence times. *Combustion and Flame*, 89(2):140–156, 1992.
- [120] Rajan K. Chakrabarty, Hans Moosmüller, W. Patrick Arnott, Mark A. Garro, Guoxun Tian, Jay G. Slowik, Eben S. Cross, Jeong-Ho Han, Paul Davidovits, Timothy B. Onasch, and Douglas R. Worsnop. Low Fractal Dimension Cluster-Dilute Soot Aggregates from a Premixed Flame. *Physical Review Letters*, 102(23):235504, June 2009.
- [121] M. Wozniak, F.R.A. Onofri, S. Barbosa, J. Yon, and J. Mroczka. Comparison of methods to derive morphological parameters of multi-fractal samples of particle aggregates from TEM images. *Journal of Aerosol Science*, 47:12–26, May 2012.
- [122] R. Puri, T.F. Richardson, R.J. Santoro, and R. A. Dobbins. Aerosol Dynamic Processes of Soot Aggregates in a Laminar Ethene Diffusion Flame. *Combustion and Flame*, 92(3):320–333, February 1993.
- [123] Rajan K. Chakrabarty, Hans Moosmüller, W. Patrick Arnott, Mark A. Garro, and John Walker. Structural and Fractal Properties of Particles Emitted from Spark Ignition Engines. *Environmental Science & Technology*, 40(21):6647–6654, November 2006.
- [124] Soleiman Bourrous, Quentin Ribeyre, Laura Lintis, Jérôme Yon, Sébastien Bau, Dominique Thomas, Cécile Vallières, and François-Xavier Ouf. A semi-automatic analysis tool for the determination of primary particle size, overlap

- coefficient and specific surface area of nanoparticles aggregates. *Journal of Aerosol Science*, 126:122–132, December 2018.
- [125] Jian Cai, Ninglong Lu, and Christopher M. Sorensen. Analysis of Fractal Cluster Morphology Parameters: Structural Coefficient and Density Autocorrelation Function Cutoff. *Journal of Colloid and Interface Science*, 171(2):470–473, May 1995.
- [126] Bing Hu, Bo Yang, and Ümit Ö Köylü. Soot measurements at the axis of an ethylene/air non-premixed turbulent jet flame. *Combustion and Flame*, 134(1-2):93–106, July 2003.
- [127] François-Xavier Ouf, Jacques Vendel, Alexis Coppalle, Marc Weill, and Jérôme Yon. Characterization of Soot Particles in the Plumes of Over-Ventilated Diffusion Flames. *Combustion Science and Technology*, 180(4):674–698, February 2008.
- [128] Kihong Park, David B. Kittelson, Michael R. Zachariah, and Peter H. McMurry. Measurement of inherent material density of nanoparticle agglomerates. *Journal of Nanoparticle Research*, 6(2):267–272, 2004.
- [129] Randy L. Vander Wal, Thomas M. Ticich, and A. Brock Stephens. Can soot primary particle size be determined using laser-induced incandescence? *Combustion and Flame*, 116(1–2):291–296, January 1999.
- [130] Boris F. Kock, Benjamin Tribalet, Christof Schulz, and Paul Roth. Two-color time-resolved LII applied to soot particle sizing in the cylinder of a Diesel engine. *Combustion and Flame*, 147(1–2):79–92, October 2006.
- [131] E. Cenker, K. Kondo, G. Bruneaux, T. Dreier, T. Aizawa, and C. Schulz. Assessment of soot particle-size imaging with LII at Diesel engine conditions. *Applied Physics B*, 119(4):765–776, June 2015.
- [132] Mohammad Reza Kholghy, Yashar Afarin, Anton D Sediako, Javier Barba, Magín Lapuerta, Carson Chu, Jason Weingarten, Bobby Borshanpour, Victor Chernov, and Murray J Thomson. Comparison of multiple diagnostic techniques to study soot formation and morphology in a diffusion flame. *Combustion and Flame*, 176:567–583, February 2017.
- [133] A. Bescond, J. Yon, F. X. Ouf, D. Ferry, D. Delhaye, D. Gaffié, A. Coppalle, and C. Rozé. Automated Determination of Aggregate Primary Particle Size Distribution by TEM Image Analysis: Application to Soot. *Aerosol Science and Technology*, 48(8):831–841, August 2014.
- [134] Igor Grishin, Kevin Thomson, Francesca Migliorini, and James J. Sloan. Application of the Hough transform for the automatic determination of soot aggregate morphology. *Applied Optics*, 51(5):610–620, 2012.

- [135] Sanghoon Kook, Renlin Zhang, Qing Nian Chan, Tetsuya Aizawa, Katsufumi Kondo, Lyle M. Pickett, Emre Cenker, Gilles Bruneaux, Oivind Andersson, Joakim Pagels, and Erik Z. Nordin. Automated Detection of Primary Particles from Transmission Electron Microscope (TEM) Images of Soot Aggregates in Diesel Engine Environments. *SAE International Journal of Engines*, 9(1):279–296, January 2016.
- [136] P. B. Sunderland, Ü. Ö. Köylü, and G. M. Faeth. Soot Formation in Weakly Buoyant Acetylene-Fueled Laminar Jet Diffusion Flames Burning in Air. *Combustion and Flame*, 100:310–322, 1995.
- [137] P. B. Sunderland and G. M. Faeth. Soot Formation in Hydrocarbon/Air Laminar Jet Diffusion Flames. *Combustion and Flame*, 105:132–146, 1996.
- [138] Magín Lapuerta, Francisco J. Martos, and José M. Herreros. Effect of engine operating conditions on the size of primary particles composing diesel soot agglomerates. *Journal of Aerosol Science*, 38(4):455–466, April 2007.
- [139] M. Wentzel, H. Gorzawski, K. H. Naumann, H. Saathoff, and S. Weinbruch. Transmission electron microscopical and aerosol dynamical characterization of soot aerosols. *Journal of Aerosol Science*, 34(10):1347–1370, October 2003.
- [140] F. X. Ouf, J. Yon, P. Ausset, A. Coppalle, and M. Maillé. Influence of Sampling and Storage Protocol on Fractal Morphology of Soot Studied by Transmission Electron Microscopy. *Aerosol Science and Technology*, 44(11):1005–1017, September 2010.
- [141] Sheldon K. Friedlander. *Smoke, Dust, and Haze: Fundamentals of Aerosol Dynamics*. Oxford University Press, New York, 2nd edition, 2000.
- [142] Ramin Dastanpour and Steven N. Rogak. The effect of primary particle polydispersity on the morphology and mobility diameter of the fractal agglomerates in different flow regimes. *Journal of Aerosol Science*, 94:22–32, April 2016.
- [143] Magín Lapuerta, Juan José Expósito, and Francisco J. Martos. Effect of sintering on the fractal prefactor of agglomerates. *Powder Technology*, 271:141–154, February 2015.
- [144] J. Johnsson, H. Bladh, N.-E. Olofsson, and P.-E. Bengtsson. Influence of soot aggregate structure on particle sizing using laser-induced incandescence: Importance of bridging between primary particles. *Applied Physics B*, 112(3):321–332, September 2013.
- [145] J. Yon, A. Bescond, and F. Liu. On the radiative properties of soot aggregates part 1: Necking and overlapping. *Journal of Quantitative Spectroscopy and Radiative Transfer*, 162:197–206, September 2015.

- [146] Paul V.C. Hough. Method and means for recognizing complex patterns, 1962.
- [147] Cheng Wang, Qing N. Chan, Renlin Zhang, Sanghoon Kook, Evatt R. Hawkes, Guan H. Yeoh, and Paul R. Medwell. Automated determination of size and morphology information from soot transmission electron microscope (TEM)-generated images. *Journal of Nanoparticle Research*, 18(5):127, May 2016.
- [148] J. Canny. A Computational Approach to Edge Detection. *IEEE Transactions on Pattern Analysis and Machine Intelligence*, PAMI-8(6):679–698, November 1986.
- [149] Pieter-Jan De Temmerman, Eveline Verleysen, Jeroen Lammertyn, and Jan Mast. Semi-automatic size measurement of primary particles in aggregated nanomaterials by transmission electron microscopy. *Powder Technology*, 261:191–200, July 2014.
- [150] Katsufumi Kondo, Tetsuya Aizawa, Sanghoon Kook, and Lyle Pickett. Uncertainty in Sampling and TEM Analysis of Soot Particles in Diesel Spray Flame. SAE Technical Paper 2013-01-0908, SAE International, Warrendale, PA, April 2013.
- [151] Magín Lapuerta, Francisco J. Martos, and Juan José Expósito. Morphological characterization of diesel soot agglomerates based on the Beer–Lambert law. *Measurement Science and Technology*, 24(3):035405, 2013.
- [152] P. Toth, J.K. Farrer, A.B. Palotas, J.S. Lighty, and E.G. Eddings. Automated analysis of heterogeneous carbon nanostructures by high-resolution electron microscopy and on-line image processing. *Ultramicroscopy*, 129:53–62, June 2013.
- [153] Hossein Ghiassi, Isabel C. Jaramillo, Pal Toth, and JoAnn S. Lighty. Experimental Investigation of the Mechanism of Soot Oxidation-Induced Fragmentation. In *9th U.S. National Combustion Meeting*, Cincinnati, OH, 2015.
- [154] Renlin Zhang and Sanghoon Kook. Structural evolution of soot particles during diesel combustion in a single-cylinder light-duty engine. *Combustion and Flame*, 162(6):2720–2728, June 2015.
- [155] Stephen J. Harris and M. Matti Maricq. The role of fragmentation in defining the signature size distribution of diesel soot. *Journal of Aerosol Science*, 33(6):935–942, 2002.
- [156] M.E. Mueller, G. Blanquart, and H. Pitsch. Modeling the oxidation-induced fragmentation of soot aggregates in laminar flames. *Proceedings of the Combustion Institute*, 33(1):667–674, 2011.

- [157] Fabian Mauss, Bernhard Trilken, Hermann Breitbach, and Norbert Peters. Soot Formation in Partially Premixed Diffusion Flames at Atmospheric Pressure. In Professor Dr Henning Bockhorn, editor, *Soot Formation in Combustion*, number 59 in Springer Series in Chemical Physics, pages 325–349. Springer Berlin Heidelberg, 1994.
- [158] Robert H. Hurt, Gregory P. Crawford, and Hong-Shig Shim. Equilibrium nanostructure of primary soot particles. *Proceedings of the Combustion Institute*, 28(2):2539–2546, January 2000.
- [159] Mariano Sirignano, Angelo Collina, Mario Commodo, Patrizia Minutolo, and Andrea D’Anna. Detection of aromatic hydrocarbons and incipient particles in an opposed-flow flame of ethylene by spectral and time-resolved laser induced emission spectroscopy. *Combustion and Flame*, 159(4):1663–1669, April 2012.
- [160] J. Biscoe and B. E. Warren. An X-Ray Study of Carbon Black. *Journal of Applied Physics*, 13(6):364–371, June 1942.
- [161] J. Lahaye and G. Prado. Morphology and Internal Structure of Soot and Carbon Blacks. In Donald C. Siegla and George W. Smith, editors, *Particulate Carbon: Formation During Combustion*, pages 33–55. Springer US, Boston, MA, 1981.
- [162] Randall L. Vander Wal. A TEM Methodology for the Study of Soot Particle Structure. *Combustion Science and Technology*, 126(1-6):333–351, July 1997.
- [163] A. D. H. Clague, J. B. Donnet, T. K. Wang, and J. C. M. Peng. A comparison of diesel engine soot with carbon black. *Carbon*, 37(10):1553–1565, 1999.
- [164] C. R. Kinney, R. C. Nunn, and P. L. Walker. Carbonization of Anthracene and Graphitization of Anthracene Carbons. *Industrial & Engineering Chemistry*, 49(5):880–884, May 1957.
- [165] Árpád B. Palotás, Lenore C. Rainey, Adel F. Sarofim, John B. Vander Sande, and Paolo Ciambelli. Effect of Oxidation on the Microstructure of Carbon Blacks. *Energy & Fuels*, 10(1):254–259, January 1996.
- [166] Tomoji Ishiguro, Yoshiki Takatori, and Kazuhiro Akihama. Microstructure of diesel soot particles probed by electron microscopy: First observation of inner core and outer shell. *Combustion and Flame*, 108(1):231–234, January 1997.
- [167] Rubén H. Muñoz and T. T. Charalampopoulos. Evolution of compositional and structural properties of soot in premixed alkane flames. *Symposium (International) on Combustion*, 27(1):1471–1479, January 1998.
- [168] L.E. Murr and K.F. Soto. A TEM study of soot, carbon nanotubes, and related fullerene nanopolyhedra in common fuel-gas combustion sources. *Materials Characterization*, 55(1):50–65, July 2005.

- [169] M. Alfè, B. Apicella, J. N. Rouzaud, A. Tregrossi, and A. Ciajolo. The effect of temperature on soot properties in premixed methane flames. *Combustion and Flame*, 157(10):1959–1965, October 2010.
- [170] Carmela Russo, Michela Alfè, Jean-Noël Rouzaud, Fernando Stanzione, Antonio Tregrossi, and Anna Ciajolo. Probing structures of soot formed in premixed flames of methane, ethylene and benzene. *Proceedings of the Combustion Institute*, 34(1):1885–1892, January 2013.
- [171] Pal Toth, Arpad B. Palotas, Terry A. Ring, Eric G. Eddings, Randy Vander Wal, and JoAnn S. Lighty. The effect of oxidation pressure on the equilibrium nanostructure of soot particles. *Combustion and Flame*, 162(6):2422–2430, June 2015.
- [172] F. A. Heckman and D. F. Harling. Progressive Oxidation of Selected Particles of Carbon Black: Further Evidence for a New Microstructural Model. *Rubber Chemistry and Technology*, 39(1):1–13, March 1966.
- [173] H. X. Chen and R. A. Dobbins. Crystallogensis of Particles Formed in Hydrocarbon Combustion. *Combustion Science and Technology*, 159(1):109–128, October 2000.
- [174] Jean-Baptiste Donnet. Fifty years of research and progress on carbon black. *Carbon*, 32(7):1305–1310, January 1994.
- [175] Hong-Shig Shim, Robert H. Hurt, and Nancy Y. C. Yang. A methodology for analysis of 002 lattice fringe images and its application to combustion-derived carbons. *Carbon*, 38(1):29–45, January 2000.
- [176] Pr Buseck, Bj Huang, and Lp Keller. Electron-Microscope Investigation of the Structures of Annealed Carbons. *Energy & Fuels*, 1(1):105–110, January 1987. WOS:A1987L637900020.
- [177] K. Kaneko, C. Ishii, M. Ruike, and H. Kuwabara. Origin of Superhigh Surface-Area and Microcrystalline Graphitic Structures of Activated Carbons. *Carbon*, 30(7):1075–1088, 1992. WOS:A1992JX72700019.
- [178] Michael Frenklach and Hai Wang. Twenty-Third Symposium (International) on Combustion Detailed modeling of soot particle nucleation and growth. *Symposium (International) on Combustion*, 23(1):1559–1566, January 1991.
- [179] Michael Frenklach. Reaction mechanism of soot formation in flames. *Physical Chemistry Chemical Physics*, 4(11):2028–2037, 2002.
- [180] Richard A Dobbins. Soot inception temperature and the carbonization rate of precursor particles. *Combustion and Flame*, 130(3):204–214, August 2002.

- [181] Mohammad Reza Kholghy, Armin Veshkini, and Murray John Thomson. The core-shell internal nanostructure of soot – A criterion to model soot maturity. *Carbon*, 100:508–536, April 2016.
- [182] Randy L Vander Wal and Aaron J Tomasek. Soot nanostructure: Dependence upon synthesis conditions. *Combustion and Flame*, 136(1):129–140, January 2004.
- [183] Randy L. Vander Wal, Aaron J. Tomasek, Kenneth Street, David R. Hull, and William K. Thompson. Carbon Nanostructure Examined by Lattice Fringe Analysis of High-Resolution Transmission Electron Microscopy Images. *Applied Spectroscopy*, 58(2):230–237, February 2004.
- [184] Norio Iwashita and Michio Inagaki. Relations between structural parameters obtained by X-Ray powder diffraction of various carbon materials. *Carbon*, 31(7):1107–1113, January 1993.
- [185] Randy L. Vander Wal, Mun Young Choi, and Kyeong-ook Lee. The effects of rapid heating of soot: Implications when using laser-induced incandescence for soot diagnostics. *Combustion and Flame*, 102(1):200–204, July 1995.
- [186] R. A. Dobbins, R. A. Fletcher, and W. Lu. Laser microprobe analysis of soot precursor particles and carbonaceous soot. *Combustion and Flame*, 100(1):301–309, January 1995.
- [187] Randall L. Vander Wal. Soot precursor carbonization: Visualization using LIF and LII and comparison using bright and dark field TEM. *Combustion and Flame*, 112(4):607–616, March 1998.
- [188] B. Apicella, A. Ciajolo, A. Tregrossi, J. Abrahamson, R. L. Vander Wal, and C. Russo. HRTEM and EELS investigations of flame-formed soot nanostructure. *Fuel*, 225:218–224, August 2018.
- [189] Mihir Patel, Cristy Leonor Azanza Ricardo, Paolo Scardi, and Pranesh B. Aswath. Morphology, structure and chemistry of extracted diesel soot—Part I: Transmission electron microscopy, Raman spectroscopy, X-ray photoelectron spectroscopy and synchrotron X-ray diffraction study. *Tribology International*, 52:29–39, August 2012.
- [190] F. Tuinstra and J. L. Koenig. Raman Spectrum of Graphite. *The Journal of Chemical Physics*, 53(3):1126–1130, August 1970.
- [191] A. C. Ferrari and J. Robertson. Interpretation of Raman spectra of disordered and amorphous carbon. *Physical Review B*, 61(20):14095–14107, May 2000.
- [192] B. Apicella, P. Pré, M. Alfè, A. Ciajolo, V. Gargiulo, C. Russo, A. Tregrossi, D. Deldique, and J.N. Rouzaud. Soot nanostructure evolution in premixed flames by High Resolution Electron Transmission Microscopy (HRTEM). *Proceedings of the Combustion Institute*, 35(2):1895–1902, 2015.

- [193] P. Parent, C. Laffon, I. Marhaba, D. Ferry, T. Z. Regier, I. K. Ortega, B. Chazallon, Y. Carpentier, and C. Focsa. Nanoscale characterization of aircraft soot: A high-resolution transmission electron microscopy, Raman spectroscopy, X-ray photoelectron and near-edge X-ray absorption spectroscopy study. *Carbon*, 101:86–100, May 2016.
- [194] A. Sadezky, H. Muckenhuber, H. Grothe, R. Niessner, and U. Pöschl. Raman microspectroscopy of soot and related carbonaceous materials: Spectral analysis and structural information. *Carbon*, 43(8):1731–1742, July 2005.
- [195] J.-O. Müller, D. S. Su, R. E. Jentoft, U. Wild, and R. Schlögl. Diesel Engine Exhaust Emission: Oxidative Behavior and Microstructure of Black Smoke Soot Particulate. *Environmental Science & Technology*, 40(4):1231–1236, February 2006.
- [196] Randy L. Vander Wal, Vicky M. Bryg, and Michael D. Hays. Fingerprinting soot (towards source identification): Physical structure and chemical composition. *Journal of Aerosol Science*, 41(1):108–117, January 2010.
- [197] Randy L. Vander Wal, Vicky M. Bryg, and Michael D. Hays. XPS Analysis of Combustion Aerosols for Chemical Composition, Surface Chemistry, and Carbon Chemical State. *Analytical Chemistry*, 83(6):1924–1930, March 2011.
- [198] K. A. Katrinak, P. Rez, and P. R. Buseck. Structural variations in individual carbonaceous particles from an urban aerosol. *Environmental Science & Technology*, 26(10):1967–1976, October 1992.
- [199] Aymeric Galvez, Nathalie Herlin-Boime, Cécile Reynaud, Christian Clinard, and Jean-Noël Rouzaud. Carbon nanoparticles from laser pyrolysis. *Carbon*, 40(15):2775–2789, January 2002.
- [200] Jeremy P. Cain, Paul L. Gassman, Hai Wang, and Alexander Laskin. Micro-FTIR study of soot chemical composition—evidence of aliphatic hydrocarbons on nascent soot surfaces. *Physical Chemistry Chemical Physics*, 12(20):5206, 2010.
- [201] Viktória Kovács Kis, Mihály Pósfai, and János L. Lábár. Nanostructure of atmospheric soot particles. *Atmospheric Environment*, 40(29):5533–5542, September 2006.
- [202] János L. Lábár. Electron Diffraction Based Analysis of Phase Fractions and Texture in Nanocrystalline Thin Films, Part I: Principles. *Microscopy and Microanalysis*, 14(4):287–295, August 2008.
- [203] David B. Williams and C. Barry Carter. *Transmission Electron Microscopy: A Textbook for Materials Science*. Springer, Boston, MA, 2009.

- [204] A. Oberlin. High-Resolution TEM Studies of Carbonization and Graphitization. In Peter A. Thrower, editor, *Chemistry and Physics of Carbon*, volume 22, pages 1–143. Marcel Dekker, New York, June 1989.
- [205] Árpád B. Palotás, Lenore C. Rainey, Christian J. Feldermann, Adel F. Sarofim, and John B. Vander Sande. Soot morphology: An application of image analysis in high-resolution transmission electron microscopy. *Microscopy Research and Technique*, 33(3):266–278, February 1996.
- [206] A. Sharma, T. Kyotani, and A. Tomita. A new quantitative approach for microstructural analysis of coal char using HRTEM images. *Fuel*, 78(10):1203–1212, August 1999.
- [207] Jean-Noël Rouzaud and Christian Clinard. Quantitative high-resolution transmission electron microscopy: A promising tool for carbon materials characterization. *Fuel Processing Technology*, 77-78:229–235, June 2002.
- [208] Kuen Yehliu, Randy L. Vander Wal, and André L. Boehman. Development of an HRTEM image analysis method to quantify carbon nanostructure. *Combustion and Flame*, 158(9):1837–1851, September 2011.
- [209] Randy L. Vander Wal, Aaron J. Tomasek, Michael I. Pamphlet, Christina D. Taylor, and William K. Thompson. Analysis of HRTEM images for carbon nanostructure quantification. *Journal of Nanoparticle Research*, 6(6):555–568, December 2004.
- [210] Maria L. Botero, Dongping Chen, Silvia González-Calera, David Jefferson, and Markus Kraft. HRTEM evaluation of soot particles produced by the non-premixed combustion of liquid fuels. *Carbon*, 96(Supplement C):459–473, January 2016.
- [211] Chethan K. Gaddam, Chung-Hsuan Huang, and Randy L. Vander Wal. Quantification of nano-scale carbon structure by HRTEM and lattice fringe analysis. *Pattern Recognition Letters*, 76(Supplement C):90–97, June 2016.
- [212] Chang’an Wang, Thomas Huddle, Edward H. Lester, and Jonathan P. Mathews. Quantifying Curvature in High-Resolution Transmission Electron Microscopy Lattice Fringe Micrographs of Coals. *Energy & Fuels*, 30(4):2694–2704, April 2016.
- [213] Pascaline Pré, Guillaume Huchet, Dominique Jeulin, Jean-Noël Rouzaud, Mohamed Sennour, and Alain Thorel. A new approach to characterize the nanostructure of activated carbons from mathematical morphology applied to high resolution transmission electron microscopy images. *Carbon*, 52(Supplement C):239–258, February 2013.
- [214] Kuen Yehliu, Randy L. Vander Wal, and André L. Boehman. A comparison of soot nanostructure obtained using two high resolution transmission electron

- microscopy image analysis algorithms. *Carbon*, 49(13):4256–4268, November 2011.
- [215] Maria L. Botero, Yuan Sheng, Jethro Akroyd, Jacob Martin, Jochen A.H. Dreyer, Wenming Yang, and Markus Kraft. Internal structure of soot particles in a diffusion flame. *Carbon*, 141:635–642, January 2019.
- [216] Harry Marsh, editor. *Introduction to Carbon Science*. Butterworths, London, 1st edition, 1989.
- [217] Juhun Song, Mahabubul Alam, and André L. Boehman\*. Impact of alternative fuels on soot properties and DPF Regeneration. *Combustion Science and Technology*, 179(9):1991–2037, August 2007.
- [218] D.E. Rosner and H. D. Allendorf. Comparative studies of the attack of pyrolytic and isotropic graphite by atomic and molecular oxygen at high temperatures. *AIAA Journal*, 6(4):650–654, 1968.
- [219] M. S. Dresselhaus, G. Dresselhaus, and P. C. Eklund. *Science of Fullerenes and Carbon Nanotubes: Their Properties and Applications*. Elsevier, March 1996.
- [220] Joseph M. Hornback. *Organic Chemistry*. Cengage Learning, January 2005.
- [221] R. H. Hurt, D. R. Dudek, J. P. Longwell, and A. F. Sarofim. The phenomenon of gasification-induced carbon densification and its influence on pore structure evolution. *Carbon*, 26(4):433–449, January 1988.
- [222] Randy L. Vander Wal, Aleksey Yezerets, Neal W. Currier, Do Heui Kim, and Chong Min Wang. HRTEM Study of diesel soot collected from diesel particulate filters. *Carbon*, 45(1):70–77, January 2007.
- [223] Hee Je Seong and André L. Boehman. Impact of Intake Oxygen Enrichment on Oxidative Reactivity and Properties of Diesel Soot. *Energy & Fuels*, 25(2):602–616, February 2011.
- [224] Haiqing Guo. *Soot Oxidation in Hydrocarbon Free Flames*. Dissertation, University of Maryland, College Park, MD, 2015.
- [225] Haiqing Guo, Paul M. Anderson, and Peter B. Sunderland. A Ternary Flame System for Soot Oxidation Studies. *Combustion Science and Technology*, 187(11):1836–1840, November 2015.
- [226] Haiqing Guo, Jose A. Castillo, and Peter B. Sunderland. Digital camera measurements of soot temperature and soot volume fraction in axisymmetric flames. *Applied Optics*, 52(33):8040, November 2013.
- [227] R. Starke, B. Kock, and P. Roth. Nano-particle sizing by laser-induced-incandescence (LII) in a shock wave reactor. *Shock Waves*, 12(5):351–360, March 2003.

- [228] Zeng-Guang Yuan. The filtered Abel transform and its application in combustion diagnostics. Technical Report NASA/CR-2003-212121, National Aeronautics and Space Administration, Glenn Research Center, Cleveland, Ohio, 2003.
- [229] Ü. Ö. Köylü and G. M. Faeth. Optical Properties of Overfire Soot in Buoyant Turbulent Diffusion Flames at Long Residence Times. *Journal of Heat Transfer*, 116(1):152–159, February 1994.
- [230] S. De Iuliis, M. Barbini, S. Benecchi, F. Cignoli, and G. Zizak. Determination of the Soot Volume Fraction in an Ethylene Diffusion Flame by Multiwavelength Analysis of Soot Radiation. *Combustion and Flame*, 115(1–2):253–261, October 1998.
- [231] Jing Lu, Chun Lou, and Huai-Chun Zhou. Experimental investigation on soot volume fraction in an ethylene diffusion flame by emission spectrometry without optically-thin assumption. *Journal of Physics: Conference Series*, 147:012084, February 2009.
- [232] C.R. Shaddix and T.C. Williams. Soot structure and dimensionless extinction coefficient in diffusion flames: Implications for index of refraction. In Henning Bockhorn, editor, *Combustion Generated Fine Carbonaceous Particles: Proceedings of an International Workshop Held in Villa Orlandi, Anacapri, May 13-16, 2007*, pages 17–33. KIT Scientific Publishing, 2009.
- [233] W. H. Dalzell, G. C. Williams, and H. C. Hottel. A light-scattering method for soot concentration measurements. *Combustion and Flame*, 14(2):161–169, April 1970.
- [234] Kevin A. Thomson, Matthew R. Johnson, David R. Snelling, and Gregory J. Smallwood. Diffuse-light two-dimensional line-of-sight attenuation for soot concentration measurements. *Applied Optics*, 47(5):694, February 2008.
- [235] F. Xu, P. B. Sunderland, and G. M. Faeth. Soot formation in laminar premixed ethylene/air flames at atmospheric pressure. *Combustion and Flame*, 108(4):471–493, March 1997.
- [236] R.J. Kee, F.M. Rupley, and J.A. Miller. CHEMKIN. Reaction Design, Inc., 2014.
- [237] W.S. Rasband. ImageJ. U. S. National Institutes of Health, 1997.
- [238] Theodore Hatch and Sarah P. Choate. Statistical description of the size properties of non uniform particulate substances. *Journal of the Franklin Institute*, 207(3):369–387, March 1929.
- [239] Jost Heintzenberg. Properties of the Log-Normal Particle Size Distribution. *Aerosol Science and Technology*, 21(1):46–48, January 1994.

- [240] A. D. Maynard. Estimating Aerosol Surface Area from Number and Mass Concentration Measurements. *Annals of Occupational Hygiene*, 47(2):123–144, March 2003.
- [241] John H. Seinfeld and Spyros N. Pandis. *Atmospheric Chemistry and Physics: From Air Pollution to Climate Change*. John Wiley & Sons, December 2012.
- [242] Kuo Tian, Kevin A. Thomson, Fengshan Liu, David R. Snelling, Gregory J. Smallwood, and Dashan Wang. Determination of the morphology of soot aggregates using the relative optical density method for the analysis of TEM images. *Combustion and Flame*, 144(4):782–791, March 2006.
- [243] Kuo Tian, Fengshan Liu, Kevin A. Thomson, Dave R. Snelling, Gregory J. Smallwood, and Dashan Wang. Distribution of the number of primary particles of soot aggregates in a nonpremixed laminar flame. *Combustion and Flame*, 138(1-2):195–198, July 2004.
- [244] C. Park, J. Z. Huang, J. X. Ji, and Y. Ding. Segmentation, Inference and Classification of Partially Overlapping Nanoparticles. *IEEE Transactions on Pattern Analysis and Machine Intelligence*, 35(3):1–1, March 2013.
- [245] János L. Lábár. Electron Diffraction Based Analysis of Phase Fractions and Texture in Nanocrystalline Thin Films, Part II: Implementation. *Microscopy and Microanalysis*, 15(1):20–29, February 2009.
- [246] E.R. Davies. *Computer and Machine Vision: Theory, Algorithms, Practicalities*. Elsevier, New York, 4th edition, 2012.
- [247] Koon Neoh, Gee. *Soot Burnout in Flames*. PhD thesis, Massachusetts Institute of Technology, 1980.
- [248] International Organization for Standardization. Evaluation of measurement data - Guide to the expression of uncertainty in measurement. Standard JCGM 100:2008, International Organization for Standardization, Genève, Switzerland, 2008.
- [249] Hugh W. Coleman and W. Glenn Steele. *Experimentation, Validation, and Uncertainty Analysis for Engineers*. John Wiley & Sons, Inc., Hoboken, NJ, 3rd edition, 2009.
- [250] International Organization for Standardization. Evaluation of measurement data — Supplement 1 to the “Guide to the expression of uncertainty in measurement” — Propagation of distributions using a Monte Carlo method. Standard JCGM 101:2008 E, International Organization for Standardization, Genève, Switzerland, 2008.
- [251] Richard K. Burdick, Connie M. Borrer, and Douglas C. Montgomery. *Design and Analysis of Gauge R&R Studies: Making Decisions with Confidence Intervals in Random and Mixed ANOVA Models*. ASA-SIAM Series on Statistics

and Applied Probability. Society for Industrial Applied Mathematics ; American Statistical Association, Philadelphia, Pa. : Alexandria, Va, 2005. OCLC: ocm58985799.

- [252] Michael Hamada and Sam Weerahandi. Measurement system assessment via generalized inference. *Journal of Quality Technology*, 32(3):241–253, July 2000.
- [253] M. Solaguren-Beascoa Fernández, J. M. Alegre Calderón, and P. M. Bravo Díez. Implementation in MATLAB of the adaptive Monte Carlo method for the evaluation of measurement uncertainties. *Accreditation and Quality Assurance*, 14(2):95–106, February 2009.
- [254] R. Kacker, R. Datla, and A. Parr. Combined result and associated uncertainty from interlaboratory evaluations based on the ISO Guide. *Metrologia*, 39:279–293, 2002.
- [255] M.Y. Choi, G.W. Mulholland, A. Hamins, and T. Kashiwagi. Comparisons of the soot volume fraction using gravimetric and light extinction techniques. *Combustion and Flame*, 102(1–2):161–169, July 1995.
- [256] R. P. Rossman and W. R. Smith. Density of Carbon Black by Helium Displacement. *Industrial & Engineering Chemistry*, 35(9):972–976, September 1943.
- [257] J.-S. Wu, S. S. Krishnan, and G. M. Faeth. Refractive Indices at Visible Wavelengths of Soot Emitted From Buoyant Turbulent Diffusion Flames. *Journal of Heat Transfer*, 119(2):230–237, May 1997.
- [258] S. di Stasio. Observation of restructuring of nanoparticle soot aggregates in a diffusion flame by static light scattering. *Journal of Aerosol Science*, 32(4):509–524, April 2001.
- [259] Magín Lapuerta, Rosario Ballesteros, and Francisco J. Martos. A method to determine the fractal dimension of diesel soot agglomerates. *Journal of Colloid and Interface Science*, 303(1):149–158, November 2006.
- [260] S. Lowell, Joan E. Shields, Martin A. Thomas, and Matthias Thommes. *Characterization of Porous Solids and Powders: Surface Area, Pore Size and Density*. Kluwer Academic Publishers, Netherlands, 2004.
- [261] Alexander Badalyan and Phillip Pendleton. Analysis of Uncertainties in Manometric Gas-Adsorption Measurements. I: Propagation of Uncertainties in BET Analyses. *Langmuir*, 19(19):7919–7928, September 2003.
- [262] F. Rouquerol, J. Rouquerol, K. S. W. Sing, P. Llewellyn, and G. Maurin, editors. *Adsorption by Powders and Porous Solids*. Academic Press, Oxford, 2nd edition, 1999.

- [263] International Organization for Standardization. Statistical methods in process management. Capability and performance. Capability of measurement processes. Technical Report BS/ISO 22514-7:2012, International Organization for Standardization, 2012.
- [264] Anton D. Sediako, Charles Soong, Jane Y. Howe, Mohammad Reza Kholghy, and Murray J. Thomson. Real-time observation of soot aggregate oxidation in an Environmental Transmission Electron Microscope. *Proceedings of the Combustion Institute*, 36(1):841–851, January 2017.
- [265] Nornadiah Mohd Razali and Yap Bee Wah. Power comparisons of Shapiro-Wilk, Kolmogorov-Smirnov, Lilliefors and Anderson-Darling tests. *Journal of Statistical Modeling and Analytics*, 2(1):21–33, 2011.
- [266] Ü. Ö. Köylü and G. M. Faeth. Optical Properties of Soot in Buoyant Laminar Diffusion Flames. *Journal of Heat Transfer*, 116(4):971–979, November 1994.
- [267] J. C. Ku. Correction for the extinction efficiency factors given in the Jones solution for the electromagnetic scattering by agglomerates of small spheres. *Journal of Physics D: Applied Physics*, 24(1):71–75, January 1991.
- [268] Yu Wu, Tianhai Cheng, Lijuan Zheng, and Hao Chen. Effect of morphology on the optical properties of soot aggregated with spheroidal monomers. *Journal of Quantitative Spectroscopy and Radiative Transfer*, 168:158–169, January 2016.
- [269] Christopher R. Shaddix, Árpád B. Palotás, Constantine M. Megaridis, Mun Y. Choi, and Nancy Y. C. Yang. Soot graphitic order in laminar diffusion flames and a large-scale JP-8 pool fire. *International Journal of Heat and Mass Transfer*, 48(17):3604–3614, August 2005.
- [270] Joseph W. McKean and Ronald M. Schrader. A comparison of methods for studentizing the sample median. *Communications in Statistics - Simulation and Computation*, 13(6):751–773, 1984.
- [271] Hiralal Bhowmick and S. K. Biswas. Relationship Between Physical Structure and Tribology of Single Soot Particles Generated by Burning Ethylene. *Tribology Letters*, 44(2):139, August 2011.
- [272] Peter B. Sunderland. *Soot Formation in Laminar Jet Diffusion Flames*. Dissertation, University of Michigan, Ann Arbor, MI, 1995.
- [273] Maria Kalogirou and Zissis Samaras. Soot oxidation kinetics from TG experiments. *Journal of Thermal Analysis and Calorimetry*, 99(3):1005–1010, February 2010.
- [274] I. W. Smith. The combustion rates of coal chars: A review. *Symposium (International) on Combustion*, 19(1):1045–1065, January 1982.

- [275] Hom N. Sharma, Lakshitha Pahalagedara, Ameya Joshi, Steven L. Suib, and Ashish B. Mhadeshwar. Experimental Study of Carbon Black and Diesel Engine Soot Oxidation Kinetics Using Thermogravimetric Analysis. *Energy & Fuels*, 26(9):5613–5625, September 2012.
- [276] C. Y. Lin and M. C. Lin. Kinetics of the  $C_6H_5 + O_2$  reaction. In *Eastern States Section of the Combustion Institute Fall Technical Meeting, Gaithersburg, MD, USA*, 1987.
- [277] M. D. Smooke, C. S. McEnally, L. D. Pfefferle, R. J. Hall, and M. B. Colket. Computational and experimental study of soot formation in a coflow, laminar diffusion flame. *Combustion and Flame*, 117(1):117–139, 1999.